

Towards understanding the electrogram: Theoretical & experimental multiscale modelling of factors affecting action potential propagation in cardiac tissue

A thesis submitted to Imperial College
for the degree of Doctor of Philosophy
by

Eugene Tze-Yeng Chang

Department of Bioengineering
Imperial College London

Declaration

I hereby declare that this submission is my own work and that it contains no material previously published or written by another person, nor material which to a substantial extent has been accepted for the award of any other degree or diploma of the university or other institute of higher learning, except where due acknowledgment has been made in the text.

Eugene Tze-Yeng Chang

The copyright of this thesis rests with the author and is made available under a Creative Commons Attribution Non-Commercial No Derivatives licence. Researchers are free to copy, distribute or transmit the thesis on the condition that they attribute it, that they do not use it for commercial purposes and that they do not alter, transform or build upon it. For any reuse or redistribution, researchers must make clear to others the licence terms of this work

Abstract

Conduction of electrical excitation in cardiac tissue is mediated by multiple physiological factors. Abnormal conduction may lead to onset of arrhythmia, and is correlated experimentally and clinically with electrogram fractionation. *In-silico* modelling studies seek to characterise and predict the biophysical phenomena underlying electrical excitation and conduction, and thus inform experiment design, and diagnostic and treatment strategies. Existing models assume syncytial or continuum behaviour, which may not be an accurate assumption in the disease setting. The aim of this thesis is to correlate simple theoretical and experimental models of abnormal cardiac conduction, and investigate the limits of validity of the theoretical models under critical parameter choices.

An experimental model of 1D continuum conduction is established in guinea pig papillary muscle to examine the relationship between mean tissue resistivity and electrical conduction velocity (CV). The relationship is compared with a monodomain tissue model coupled with the Luo Rudy I (LR1) guinea pig ventricular action potential, which obeys classical cable theory of conduction under pharmacological modulation. An experimental model of 1D discrete conduction is created via development of a micro-patterned culture model of the HL-1 atrial myocyte cell line on micro-electrode arrays, which has a lower baseline conduction velocity compared to conventional cardiomyocyte models. A novel 1D bidomain model of conduction of discrete cells coupled by gap junctions is proposed and validated, based on existing analytical and numerical studies, and coupled to the LR1 model.

Simulation of slow conduction under modulation of physiological parameters reveal differences in the excitation conduction between continuum and discrete models. Electrogram fractionation is observed in the discrete model, which may be a more realistic model of conduction in diseased myocardium. This work highlights possibilities and challenges in comparing and validating theoretical models with data from experiments, and the importance of choosing the appropriate modelling assumptions for the specific physiological question.

Acknowledgements

I would like to express my sincere thanks and gratitude to my supervisors, Dr Jennifer Siggers, Professor Spencer Sherwin and Professor Nicholas Peters. Their advice, guidance and suggestions at critical moments in my studies have helped to keep me on track, develop a coherent story and become an independent researcher. In particular, I would like to express thanks to Jennifer for her endless enthusiasm, to Spencer for his thoughtful and helpful insights, and to Nick for investing his faith and support in me, as a mathematician looking to do wet lab work and establish myself in the world of multidisciplinary research.

I gratefully acknowledge the British Heart Foundation Centre of Research Excellence at Imperial College London, for their financial support and for their excellent training programme. Their commitment to multidisciplinary research has influenced my thinking and development, and allowed me to meet and establish firm friendships with students and staff across the Centre. I would like to thank the Department of Bioengineering and the NHLI for hosting and supporting my studies, and to London Centre of Nanotechnology at University College London for use of their clean room facilities.

The work completed in this thesis would not have been possible without the support of my group members, to whom I am indebted. Dr Rasheda Chowdhury, Dr Chris Cantwell, Dr Fu Siong Ng and Dr Emmanuel Dupont have been incredible friends, teachers and mentors, teaching me about biological research, cell culture, immunohistochemistry, optical mapping and scientific computing. Caroline Roney has been a bastion of strength though my PhD, co-supervising projects, discussing ideas and working closely together over the last few years. She, Olga Korolkova, Rheeda Ali, and Dr Ani Setchi have been my sounding board and source of moral support through all the highs and lows. I am also incredibly grateful to Dr Junaid Zaman, Dr Chris Bell, Mrs Pravina Patel, Dr Mike Debney and Dr Sevil Payvandi for all their help in the initial stages of my research career.

My thanks must go to the many researchers with whom I have interacted during my PhD, for their invaluable guidance and many discussions. These include Professor Chris Fry, Dr Paramdeep Dhillon and Samantha Salvage for the guinea pig papillary muscle work, Dr Enno de Lange for teaching me the fundamentals of computational cardiac electrophysiology, Dr Thomas Desplantez and Professor Ken McLeod for the HL-1 work, and Dr Patrizia Camelliti for feedback on patterned culture. I would like to acknowledge insightful discussions and feedback from Professor Kim Parker, Professor Mauricio Bar-

hona, Professor Cesare Terranciano, Professor Darryl Holm, Professor Darryl Francis and Dr Darryl Overby.

My friends have been an incredible source of fun and support during this journey. I would like to acknowledge Racton flatmates and friends Veronique, Amalia, Daria, Chris and Silvia, my former wardening colleagues Marko, Dan, Joanna and Vero, and my fellow Lunch Club members Sietse, Yean, Agnes, Ani, Jason and Ed Brightman. Thank you to bioengineers and friends Lucas, Ioannis, Alex, Lucas, Jose, Jason, Reva, Kelly, Julius, Jenny, Ryan, Joe, Rob, Vero, Gemma and Mariea for nights out and lunches, to those from my MRes course Jen, Florian, Paul, Abdullah, Gurpreet, and Tom, to my wonderful Beijing summer school friends Michelle, Miguel, Myrsini, Nair, and Jade, to my Union and university friends Andy, Rachel, Alex B, Slobodan, Jenny, Lily, Lizzie, Min, Karim, Tim, Monica, Phil, and anyone else I have forgotten. I had fabulous times rehearsing, performing and touring with members of the Techtonics, Imperial College Sinfonietta and Symphony Orchestra, and training with Imperial College Wushu Society, which I look back upon with great fondness.

Finally and most importantly, I would like to thank my mum, dad and my sister Felicia for their unwavering support and encouragement throughout. I couldn't have got to where I am today without your love and sacrifice, and I would like to dedicate this thesis to you, my family.

Contents

Declaration	1
Abstract	2
Acknowledgements	3
List of Figures	10
List of Tables	13
List of Abbreviations	14
1 Introduction	16
1.1 Overview	16
1.2 Summary and key challenges	16
1.3 Aims and Outline of Thesis	18
2 Physiological background	20
2.1 The electrical conduction system of the heart	21
2.1.1 Cardiac arrhythmias	22
2.1.2 Cellular action potentials	28
2.1.3 Myocardial tissue structure and anatomy	34
2.1.4 Gap junctions	37
2.2 Effects of structure and function on initiation of arrhythmia	38
2.2.1 Initiation of action potential upstroke and conduction slowing	39
2.3 Detection and measurement of electrical activity	42
2.3.1 Unipolar, bipolar electrodes and cardiac catheters	43
2.3.2 Multi-electrode arrays	45
2.3.3 Microelectrodes	45
2.3.4 Optical mapping	46
2.4 Modelling in cardiac electrophysiology	47
2.4.1 Functional models of the single cardiac myocyte	47
2.4.2 Models of excitable cardiac tissue	49
2.4.3 Challenges of electrophysiology modelling	53

3 Numerical solution of cardiac electrophysiology equations	58
3.1 Introduction	58
3.2 Single cell action potential models	59
3.2.1 The Cherry–Fenton phenomenological model	59
3.2.2 The Luo–Rudy I ventricular myocyte model	62
3.3 Numerical integration of action potential models	63
3.3.1 The Rush–Larsen algorithm	64
3.4 Tissue models	67
3.4.1 Derivation of the cable equation	68
3.4.2 The monodomain model	70
3.4.3 The bidomain model	72
3.5 Numerical implementation	75
3.5.1 Numerical methods for continuum cardiac tissue models	75
3.5.2 Monodomain implementation	78
3.6 Post-processing	81
3.6.1 Calculation of the virtual electrogram	81
3.6.2 Determining electrical properties of the tissue	82
3.7 Discussion	83

I Measuring and calculating macroscopic conduction properties in intact myocardial tissue 85

4 Measuring conduction properties in a guinea pig papillary muscle model	87
4.1 Introduction	87
4.2 Materials and methods	88
4.2.1 Materials	88
4.2.2 Preparation of papillary muscle samples	89
4.2.3 Impedance dish design and setup	91
4.2.4 Protocol for measuring tissue impedance properties	93
4.3 Microelectrode recordings	97
4.3.1 Description of setup	99
4.3.2 Measurement of intracellular action potentials	100
4.3.3 Measurement of longitudinal conduction velocity	102
4.3.4 Calculation of intracellular resistivity	102
4.3.5 Effect of carbenoxolone on longitudinal conduction velocity	102
4.4 Results	103
4.4.1 Impedance measurements	103
4.4.2 Intracellular recordings	105
4.4.3 The effect of modulating resistivity on conduction velocity	106
4.5 Discussion	108
4.5.1 Measured passive tissue resistivity	109
4.5.2 Physiological range of resistivities from carbenoxolone modulation	110

4.5.3	Physiological range of conduction and breakdown of cable theory	110
5	The effect of modulating conductivity in a continuum model of conduction	112
5.1	Introduction	112
5.2	Methods	114
	5.2.1 Implementation of numerical model	114
5.3	Results	116
	5.3.1 Simulation duration and accuracy	116
	5.3.2 Modulation of physiological parameters	118
	5.3.3 Action potential foot τ_{ap}	122
	5.3.4 Electrogram	122
5.4	Discussion	123
	5.4.1 Numerical accuracy	123
	5.4.2 Modulation of physiological parameters	124
	5.4.3 Range of parameter modulation compared with experiment	125
II	Development of a framework to examine discrete models of conduction	126
6	Development of a 1D experimental cell culture model using the HL-1 cell line	129
6.1	Background	130
	6.1.1 Choice of a cell-line model	132
	6.1.2 The HL-1 cell line	132
6.2	Methods	134
	6.2.1 Maintenance of the HL-1 cell line	134
	6.2.2 Cryostorage of HL-1 cells	134
	6.2.3 Stimulating and recording of extracellular electrograms	135
	6.2.4 Cell culture protocol for monolayers on MEA plates	136
	6.2.5 Micro-contact printing for cell culture	137
	6.2.6 Immunocytochemistry	142
6.3	Results	144
	6.3.1 Control of cell seeding density	144
	6.3.2 Alignment with electrodes	145
	6.3.3 Quality of fibronectin transfer from stamp on to plate	145
	6.3.4 Stability of patterns	147
	6.3.5 Co-location and cell growth	147
	6.3.6 Cell shape and anisotropy	147
	6.3.7 Expression of Cx43 in patterned strands	151
	6.3.8 Electrical Recording	156
6.4	Discussion	157
	6.4.1 Summary of findings	157

6.5	Work in progress: Development of a mathematical model of the HL1–6 action potential	162
7	Developing a 1D mathematical model of conduction in discrete coupled myocytes	163
7.1	Introduction	163
7.2	The discrete cell chain model	165
7.2.1	Analytical solution: steady state passive problem, Dirichlet boundary conditions	167
7.2.2	Analytical solution: steady state passive problem, Neumann boundary conditions	168
7.2.3	Unsteady passive problem, no flux boundary condition with time dependent stimulus	170
7.2.4	Outline of the 1D discrete model with active ion channel kinetics	172
7.3	Results: Implementation and validation of the 1D discrete model	174
7.3.1	Implementation of the Keener and Sneyd model	174
7.3.2	The passive Dirichlet problem	175
7.3.3	The passive Neumann problem	181
7.3.4	No flux (Neumann) boundary conditions, time dependent forcing stimulus	185
7.3.5	Implementation of the full model with active ion channel kinetics	187
7.4	Results: Computation details and numerical sensitivity	187
7.5	Results: Determining physiological factors underlying conduction slowing	192
7.5.1	Gap junctional resistance	192
7.5.2	Cytoplasmic resistivity	195
7.5.3	Membrane capacitance	197
7.5.4	Sodium channel excitability	197
7.6	Results: Discrete model versus Continuum model	199
7.6.1	Effective diffusivity versus gap junction resistance	200
7.6.2	Sodium excitability and composite effects	204
7.6.3	Electrogram	205
7.7	Discussion	205
7.7.1	Summary of findings	205
7.7.2	Numerical sensitivity and stability of the discrete model	207
7.7.3	Physiological insights from the discrete model	208
7.7.4	Differences between the 1D discrete and the 1D cable model	211
7.7.5	Applicability and limitations of the discrete model	213
III	Conclusions and Comments	215
8	Discussion	216
8.1	Summary of key findings	216
8.2	Addressing the study aims	219

8.2.1	Developing an integrative theoretical and experimental approach for understanding cardiac conduction	219
8.2.2	Investigation of the physiological parameter range and limitations of experimental models	221
8.2.3	Developing and investigating a discrete framework and approach to understanding slow conduction	222
8.2.4	Assessing the numerical and physiological parameters for which continuum models produce physiologically meaningful predictions	224
8.3	Study limitations and future directions	225
8.3.1	Guinea pig work	225
8.3.2	Creating patterned strands in cell culture for electrogram recording	226
8.3.3	Development of an HL-1 sub clone action potential model	226
8.3.4	Discrete cell model	227
8.4	Concluding remarks	228
	Bibliography	230
A	The equations of the Luo-Rudy I model	243
B	Developing a mathematical model of the action potential for the HL-1 clone 6 cell line	246
B.1	Background	246
B.2	Methods: Determining components of the HL-1 action potential	247
B.2.1	Data from literature	247
B.2.2	Experimental HL1 subclone characterisation	248
B.3	Results	249
B.3.1	Description of initial model	249
B.3.2	Electrophysiological Properties	250
B.3.3	APD and restitution properties	250
B.3.4	Coupling to the monodomain model	252
B.4	Discussion	252
B.4.1	Choice of currents for the HL1-6 model	252
B.4.2	Restitution properties of the model	253
B.4.3	Conduction properties of the model	253
B.4.4	Summary	254
C	A simple mathematical model of discrete coupled cells	255
D	Additional activities	259

List of Figures

2.1	Electrical conduction system of the heart	21
2.2	Cellular mechanisms of arrhythmias	24
2.3	Anatomical re-entry	26
2.4	Schematic of a mammalian ventricular action potential	30
2.5	Variation of action potential shape in the heart	32
2.6	A typical cardiac restitution curve	35
2.7	Diagrammatic view of a gap junction channel	38
2.8	Distribution of Cx43 protein in healthy and diseased tissue	39
3.1	The Cherry–Fenton Model 2a	62
3.2	An example Luo–Rudy I action potential	64
3.3	The Rush–Larsen algorithm	67
3.4	Finite difference stencil	78
4.1	Dissection of the guinea pig papillary muscle	90
4.2	A papillary muscle preparation	91
4.3	The oil gap chamber	92
4.4	The impedance chamber dish with a preparation inserted	92
4.5	Intracellular impedance stimulation protocol	93
4.6	Canonical model of the experimental impedance system	95
4.7	Summary of the impedance measurement protocol	98
4.8	Schematic of the micro electrode setup	100
4.9	Calculation of τ_{ap} and V_{th}	101
4.10	Example impedance plots	104
4.11	Effect of carbenoxolone: time course effect and AP upstroke	107
4.12	Effect of resistivity on conduction velocity in guinea pig myocardium	108
5.1	Schematic of the implemented cable model	115
5.2	Numerical error for varying Δt	117
5.3	Numerical error for varying Δx	118
5.4	log-log graph of diffusion coefficient D vs CV	120
5.5	Graph of diffusion coefficient g_{Na} vs CV	121
5.6	Effect of modulating physiological parameters on max AP upstroke	122
5.7	Virtual electrogram of cable model	123

6.1	Micro electrode array schematic	136
6.2	Microelectrode array plates	137
6.3	The micro-contact printing protocol	139
6.4	Transparency marks design	140
6.5	Quality of fibronectin transfer on to MEA plate	146
6.6	Growth of patterned HL-1 cells on MEA plates	148
6.7	Single cell alignment on fibronectin patterns	149
6.8	HL-1: Patterned strand vs monolayer	149
6.9	Cell orientation in thin vs thick strands	150
6.10	Comparison of cell morphology in different strand thickness	152
6.11	Orientation of patterned cells from horizontal	153
6.12	Overgrowth of patterned cells	154
6.13	Cx43 labelling of patterned HL-1 myocytes on MEA plate	155
6.14	Z stack of Cx43 labelling in patterned strand	156
6.15	Z-projected, max intensity profile of Cx43 labelling	157
6.16	Overlaid image of Cx43 and N-Cadherin labelling	158
7.1	Analytical solution, Dirichlet boundary conditions	169
7.2	Analytical transmembrane solution, Neumann boundary conditions	171
7.3	Analytical steady state solution, Dirichlet boundary condition	176
7.4	Different steady state implementations against analytic solution	177
7.5	Transmembrane solutions for all cases, zoomed	178
7.6	Ln Δx (h) against Ln error (E)	179
7.7	Time dependent numerical solution against Steady State solution (V2).	181
7.8	Ln dt against Ln error, at steady state ($t=5\text{ms}$).	182
7.9	Log dt against Log error, for several time steps.	183
7.10	Steady state solution, transmembrane potential V_m . Compare with Figure 7.2.	184
7.11	Time dependent stimulus, transmembrane potential V_m	185
7.12	Time dependent stimulus, no flux boundary conditions, transmembrane potential V_m	186
7.13	Equivalent circuit diagram of the 1D discrete cell model	188
7.14	Spatial sensitivity: L2 error norm of discrete model	190
7.15	Temporal sensitivity: L2 error norm of discrete model	191
7.16	V_m spatial profile for different gap junctional resistivities	194
7.17	Effect of modulating R_j on V_m versus time	195
7.18	Morphology of the LR-1 AP in single cell versus discrete coupled cells	196
7.19	Effect of modulating R_c on V_m activation wavefront	198
7.20	log-log graph of diffusion coefficient g_{Na} versus CV	199
7.21	Conduction velocity (CV) against diffusion parameters for continuum and discrete models	201
7.22	Maximum dV/dt as a function of diffusivity	202
7.23	Simulated action potentials in cable, discrete cells and a single cell model	203

7.24	Discrete versus continuum – sodium excitability	204
7.25	Virtual ECGs generated from cable and discrete models	206
B.1	Schematic depiction of HL-1 features	247
B.2	HL1-6 action potential	249
B.3	Simulated HL1-6 AP	251
B.4	Simulated HL1-6 restitution curve	251

List of Tables

3.1	Intracellular and extracellular conductivity values in literature	83
4.1	Composition of Tyrode's solution	88
4.2	Guinea pig left ventricular papillary muscle resistivities	103
4.3	Guinea pig tissue resistivity following CBX modulation	105
4.4	Action potential parameters from guinea pig papillary muscle	106
5.1	Effect of conductivity D on conduction velocity	119
5.2	Effect of reducing peak sodium excitability g_{Na} on conduction velocity .	120
6.1	Summary of SU-8 photoresist properties and required times for each protocol step	141
6.2	Cell morphology in strands of different thickness	151
7.1	Parameters used in Keener and Sneyd [2009] for discrete model.	175
7.2	Effect of increasing R_j from baseline ($\times 1$).	193
7.3	Effect of increasing R_c from baseline ($\times 1$).	196
7.4	Effect of reducing peak sodium excitability g_{Na} on conduction velocity .	199
7.5	Effect of reducing peak sodium excitability g_{Na} on conduction velocity for $R_j \times 8$	200
A.1	Parameters within the Luo–Rudy I cell model	245

List of Abbreviations

AF	Atrial fibrillation
AP	Action potential
APD	Action potential duration
APD90	Time duration for action potential to recover 90% towards baseline resting membrane potential
AV	atrio-ventricular
BSA	Bovine serum albumin
CA	Cellular automata
CBX	Carbenoxolone
CFAE	Complex fractionated atrial electrogram
CL	Cycle length
CSA	Cross sectional area
CV	Conduction velocity
Cx	Connexin
DAD	Delayed after depolarisation
DI	Diastolic interval
EAD	Early after depolarisation
ECG	Electrocardiogram
EP	Electrophysiology
ERP	Effective Refractory Period
FDM	Finite difference method

FEM	Finite element method
FVM	Finite volume method
GJ	Gap junction
GP	Guinea pig
GP	Guinea pig
LA	Left atrium
LR-1	Luo-Rudy I ion channel model
LR-D	Luo-Rudy dynamic guinea pig ventricular action potential model
LV	Left ventricle
MEA	Micro electrode array
NCX	Sodium calcium exchanger
NRVM	Neonatal rat ventricular myocyte
PBS	Phosphate buffered saline
PDMS	Polydimethylsiloxane
PLL-PEG	Poly-L-Lysine-conjugated Polyethylene Glycol
RA	Right atrium
RC	Resistor capacitor
RP	Refractory period
RyR2	Ryanodine receptor
S.D.	Standard deviation
SA	Sino-atrial
SERCA	Sarco-endoplasmic reticulum Ca^{2+} -ATPase
SF	Safety factor
SR	Sarcoplasmic reticulum
vECG	virtual electrogram

Chapter 1

Introduction

1.1 Overview

The work in this thesis examines multi scale theoretical and experimental models of cardiac excitation under modulation of tissue conduction properties. Specifically, it assesses the factors affecting the validity of modelling assumptions in studies of excitation propagation. The ultimate aim is to improve understanding of the cardiac electrogram.

Section 1.2 determines the open challenges and questions which this thesis aims to address. Finally, the outline of the thesis is presented in Section 1.3, which formulates the main hypotheses and aims of this work.

1.2 Summary and key challenges

Chapter 2 introduces the background literature on cardiac arrhythmias and theoretical and experimental models developed, and outlines several existing modalities for measuring cell, tissue and organ electrophysiology. Each recording modality has specific advantages and disadvantages, such as spatial or temporal resolution, toxicity or capability to

record conduction over a large area. Certain techniques cannot easily be transferred to human studies, due to technical, ethical or financial barriers, yet are essential for gaining detailed electrophysiological information which cannot be simply obtained using the ECG or catheter recordings.

It is thus important to decipher as much biological detail as possible from limited *in-vivo* recording techniques, and to determine the electrophysiology of the substrate based on these limited details. Doing so requires a deeper understanding of how electrophysiological activity affects the signature of the unipolar electrogram, which remains the primary diagnostic tool in the hospital EP clinic. This requires a close interaction between experimental, theoretical and clinical *in-vivo* studies, as validated, detailed theoretical models have the capability to replicate and extrapolate experimental trends, and provide a platform to generate simulated electrograms which can be compared to clinical data. Conversely, if a theoretical relationship is established between a certain electrophysiological phenomenon and a particular clinical dataset, then an inverse theoretical problem may be solved when clinical data is recorded, which then has the potential to aid diagnosis and treatment.

In order to form correlations between experimental, theoretical and clinical results, it is important to understand the key limitations and assumptions of specific experimental techniques and also theoretical models. A model with a minimum spatial resolution to satisfy modelling assumptions may not produce physiologically relevant result at a finer spatial scale. The critical spatial and temporal resolutions at which a model breaks down may lead to incorrect conclusions, and care must be taken to ensure that theoretical and experimental work can justifiably be compared and correlated with each other.

1.3 Aims and Outline of Thesis

The aim of this thesis is to assess the factors affecting the validity of multi scale theoretical and experimental models of cardiac excitation under modulation of tissue conduction properties. The work in this thesis addresses this aim via the following sub aims:

- To develop an integrative approach towards understanding cardiac excitation via combining research in both experimental and theoretical models.
- To develop and investigate a discrete framework and approach to understanding slow electrical conduction, and understanding the subsequent local electrogram.
- To investigate the physiological parameter range in experimental models of cardiac conduction, and understand limitations of experimental models.
- To assess the numerical and physiological parameters for which continuum tissue models produce physiologically meaningful predictions.

These sub-aims will be addressed within this thesis is outlined as follows:

Chapter 2 describes the physiological background and current state-of-the-art underlying cardiac excitation and methods of detecting electrical activity in the laboratory and clinic. Chapter 3 describes the general numerical methods used, including a finite difference implementation of the monodomain cable model in Matlab. The action potential models used in the thesis are presented, along with the mathematical formulation of the virtual electrogram.

Chapter 4 concerns the experimental guinea pig papillary muscle data, acquired in and from the laboratory of Professor CH Fry at the University of Surrey. This is matched

in Chapter 5 with numerical simulation of excitation in a 1D continuum cable model of guinea pig papillary muscle using the Luo–Rudy I action potential model.

In Chapter 6, work to optimise an experimental technique to obtain linear strands and subsequent 1D conduction on micro electrode arrays at the discrete myocyte level is presented, using the HL–1 atrial myocyte cell line.

Based on the patterned cell strand setup from Chapter 6, Chapter 7 documents a novel implementation of a 1D mathematical bidomain model of discrete myocytes coupled by gap junctions and a physiological action potential. The numerical stability of this model is explored, and the discrete model is compared with the continuum cable model under modulation of physiological parameters, and for different levels of spatial discretisation to observe the critical resolution at which the continuum approximation deviates from the discrete model.

Initial work to carry out single cell characterisation of the HL–1 is presented in Appendix B, developing a mathematical action potential model for the HL–1 clone 6 cell line, and testing its properties when coupled to a continuum tissue model. This work, although carried out in parallel with the other research documented, is not presented towards results in the final thesis.

Chapter 8 summarises and discusses results obtained in the preceding chapters with relation to the aims of the thesis, and identifies potential avenues of further research.

Chapter 2

Physiological background

This chapter sets out the physiology background and current state-of-the-art experimental knowledge within cardiac electrophysiology. Section 2.1 is concerned with an introduction to cardiac arrhythmias, the gross structure of cardiac tissue and cardiac muscle cells (*cardio-myocytes*), and the electrical functionality of the cardio-myocytes due to *action potentials*. Section 2.2 explores the existing experimental literature on arrhythmia initiation, introducing the notion that a complex interaction of changes in both cardiac structure and function are responsible for arrhythmia initiation and maintenance. Accurately describing the complexity of excitable tissue is a key step towards understanding these interactions, both in the clinical and the laboratory environment. The clinical challenge of correctly detecting and diagnosing complex arrhythmias informs Section 2.3, which reviews several *in-vivo* and *in-vitro* electrical recording techniques, and introduces the difficulty of understanding the pathophysiology of arrhythmia based on limited clinical data (the inverse problem of electrophysiology). Section 2.4 examines the theoretical modelling literature, with a focus on reviewing the assumptions underlying the modelling of multi scale tissue and cellular electrical behaviour.

2.1 The electrical conduction system of the heart

The heart functions as a mechanical pump. Blood is pumped from the atria in to the ventricles, which then contract to circulate blood around the body. The mechanical contraction and relaxation of heart muscle is triggered by synchronised electrical activity in cardiac *myocytes*. Normal *sinus rhythm* starts in the sino-atrial (SA) node, sending a wavefront of electrical activity across the atrium, through the atrio-ventricular (AV) node, the bundle of His and the Purkinje fibres before spreading excitation in the ventricle from apex to base, leading to ventricular contraction (Fig. 2.1). The rate of sinus rhythm can be increased by the autonomic nervous system to accelerate the transport of blood through the body.

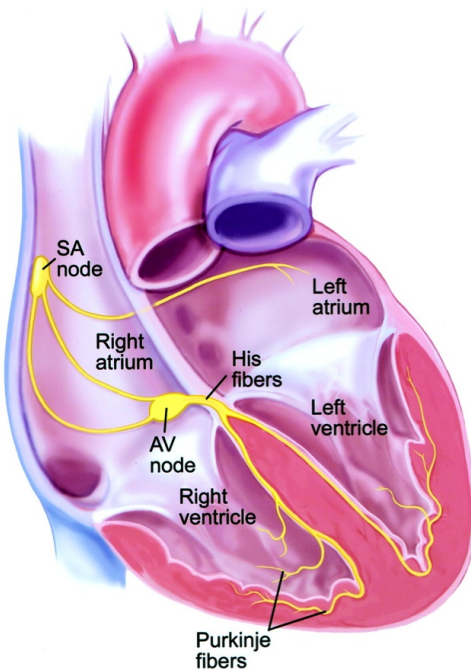


Figure 2.1: The heart and its electrical conduction system. Electrical impulses start in the sino-atrial (SA) node and travel via the atria to the AV node. From there, the electrical impulse travels through the His fibers and the Purkinje fibers to the left and right ventricles. (Reproduced from [Wang and Estes \[2002\]](#)).

The lumped electrical behaviour of the heart can be measured non-invasively using the *electrocardiogram* (ECG), a ‘first glance’ technique for diagnosis of arrhythmias [Hampton, 2003] via electrical recordings from pairs of external electrodes placed on the body surface. Output through a specific pair of electrodes is known as a *lead*, with 12 leads forming the standard ECG. In Lead I of the ECG measured between electrodes on the left and right arms, the *P* wave corresponds to atrial electrical depolarisation preceding atrial contraction, and the *QRS* complex, the ventricular depolarisation preceding ventricular contraction (the atrial re-polarisation is concealed within the *QRS* wave due to its relatively small amplitude). The *T* wave corresponds to ventricular re-polarisation. The ECG serves as a common technique for cardiovascular screening, and as an initial tool for diagnosing cardiac arrhythmias [Hampton, 2003]. For in-depth diagnosis and treatment of arrhythmias in specialised electrophysiology clinics, intra-cardiac *electrogram* signals are obtained, via insertion of specialised catheters in the heart, which can record electrical activity and deliver radio-frequency or cryo ablations to treat the arrhythmia.

2.1.1 Cardiac arrhythmias

Cardiac arrhythmias refer to non-sinus rhythm behaviour, which affects cardiac contraction and can lead to sudden death, or increased mortality from non-sudden cardiac deaths. Around 50% of cardiac related deaths are attributable to sudden death [Huikuri et al., 2001], with some 100,000 sudden cardiac deaths per year in the UK alone [Morgan et al., 2006].

Arrhythmias can be classified by the location, rate and frequency of occurrence, and its effect on cardiac contractility. *Tachyarrhythmias* are characterised by an abnormally

increased heart rate, and *bradyarrhythmias* by a slowed heart rate. Within this thesis, bradyarrhythmias are not investigated, with understanding the mechanisms underlying tachyarrhythmias the primary concern.

Common tachyarrhythmias include atrial flutter, ventricular tachycardia, atrial fibrillation and ventricular fibrillation. Biological mechanisms underlying simpler arrhythmias such as atrial flutter are well understood, and thus successful treatment of these in specialist electrophysiology centres is routine. However, atrial fibrillation and ventricular tachycardia are examples of arrhythmias that are not simple to diagnose or treat. These develop due to clinical cardiac pathologies, such as coronary artery disease, hypertrophic cardiomyopathy or congenital heart disease. As a result of these diseases, complex pathological changes may occur, such as structural and functional remodelling of cardiac tissue, which result in a complicated substrate that is more susceptible to initiation and maintenance of arrhythmias [Peters et al., 1997, Severs et al., 2008, Zou, 2005] .

Mechanisms leading to the onset of tachyarrhythmia can be classified in to three categories [Wolf and Berul, 2008]: automaticity, triggered activity and re-entry. These are described in Figure 2.2, briefly outlined below, and described in more detail in Section 2.2.

Automaticity

Electrical automaticity refers to the self-excitability of cells without external stimulus. It is a property found in cardiac myocytes located within the sinus node, AV node and the His-Purkinje fibres (see Figure 2.1) due to the existence of specific ionic currents such as the funny current or the T-type calcium channel (see Figure 2.2). Alterations in the ionic currents within these cells may lead to increased automaticity and subsequent

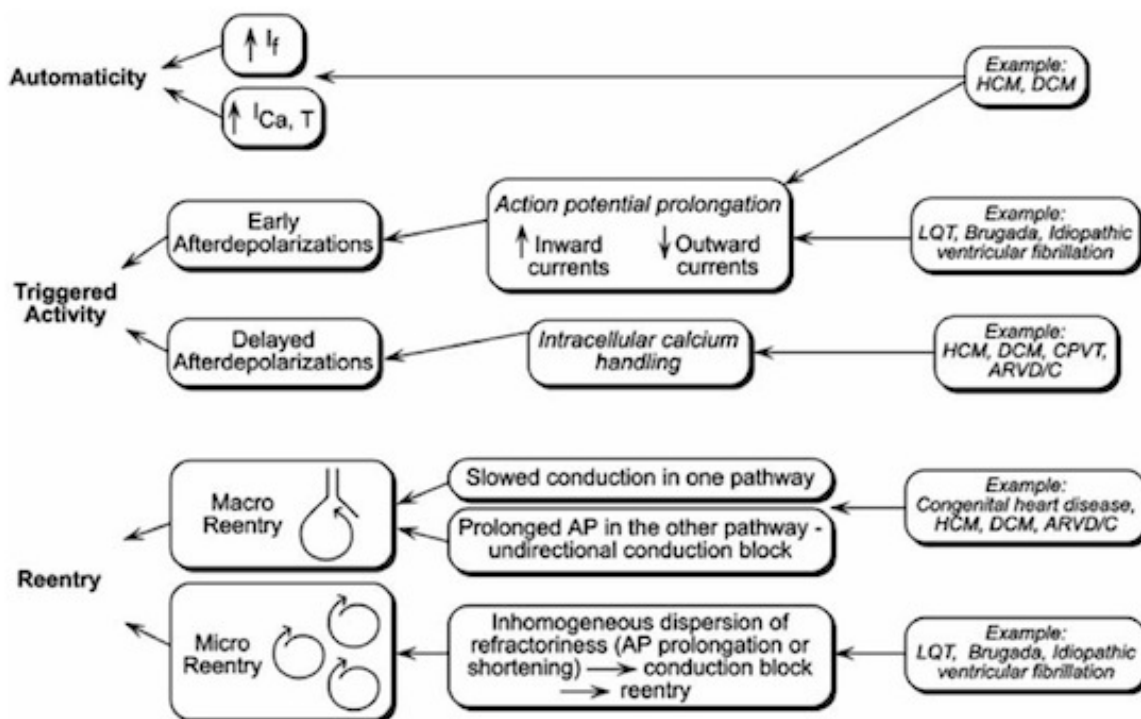


Figure 2.2: Three mechanisms, individually or in combination, are responsible for causing cardiac arrhythmia: automaticity, triggered activity and re-entry. Abbreviations as follows: AP action potential, HCM hypertrophic cardiomyopathy, DCM dilated cardiomyopathy, ARVD/C arrhythmogenic right ventricular dysplasia/cardiomyopathy, LQT: Long QT, CPVT: Catecholaminergic polymorphic ventricular tachycardia. (Re-produced from [Wolf and Berul \[2008\]](#))

arrhythmia.

Triggered Activity

Electrically activated cardiac myocytes are subject to a period of inexcitability or ‘refractoriness’, which is described more in Section 2.1.2. Alterations to the ionic currents within these cells may lead to a change of the electrical activation period within or beyond the time period of inexcitability. This mismatch of activation and inexcitation periods may trigger additional excitation in the myocytes outside of normal sinus rhythm. These triggers can be sub-classified into early after-depolarisation (EADs) and delayed

after-depolarisations (DADs) (Figure 2.2), which will be introduced in the following subsections.

Re-entry

Re-entry refers to a self-perpetuating electrical wavefront over a region of cardiac tissue that does not terminate, creating a circuit of electrical activity over which tissue continues to be re-excited independently of normal sinus rhythm stimulation. Re-entry can be further divided in to anatomical and functional re-entry.

Anatomical re-entry refers to movement around a structural obstacle of in-excitation, such as a region of infarcted or scarred tissue, or a pulmonary vein, and was elegantly described by Mines [[Mines, 1913](#)]. He demonstrated the principle of re-entrant behaviour around a fixed anatomical obstacle, based on the concept of *uni-conductational block* as a necessity for initiation. For a circuit of excitable tissue that is stimulated at a single point on the circuit, excitation will spread in both directions around the circuit, with the two wavefronts eventually colliding and cancelling. However, if just one side of the excitation wavefront is blocked, then this will allow the other wavefront to traverse the circuit forming a re-entrant loop.

Furthermore, Mines introduced the notion of the unexcitable *wavelength* of tissue, which is the product of the speed of excitation and the time period of unexcitability. He then compared the path length of the circuit versus the wavelength. If the former is larger, then an ‘*excitable gap*’ permits the wavefront to perpetuate around the circuit and re-entry successfully occurs, as depicted in Fig. 2.3.

A location of common anatomical re-entry is around the pulmonary veins in the

atrium, where there is a region of excitable tissue extending 1–2 cm in to the sleeves of the veins that can act as a source of reentrant behaviour.

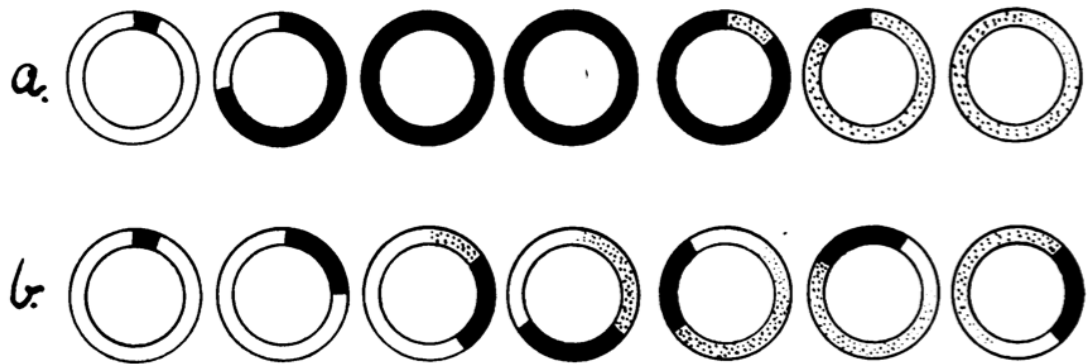


Figure 2.3: Mines described the relationship between speed of excitation and the period of unexcitability, introducing the concept of the unexcitable wavelength. In a), the unexcitable wavelength (in black) is greater than the path length and the excitation wavefront terminates when it encounters its tail. In b), the wavelength is shorter than the path length and this leads to a sustained reentrant circuit (Reproduced from [Mines \[1913\]](#)).

Functional re-entry occurs around normally excitable obstacles which are temporarily unexcitable in time, and again leads to self perpetuating wavefronts of activity. This was discovered by [Garrey \[1914\]](#) around the same time as Mines who described anatomical entry; he demonstrated that a fixed anatomical obstacle is not required for reentrant behaviour to be observed. This was further explained by [Allessie et al. \[1977\]](#), who described the ‘leading circle’ re-entrant circuit around an area of tissue in a permanently unexcitable state . In this re-entrant circuit, there is no excitable gap, and the excitation wavefront activates the tissue ahead, which has just recovered from excitation. If, instead, the re-entrant wavefront meets refractory tissue ahead, then it is described to encounter a line of *functional block* and this may lead to termination of the wavefront. A re-entrant wavefront may be initiated when a planar excitation wave encounters a partial line of functional block, causing the wavefront to change direction around the line of block.

Functional re-entry and lines of functional block are now commonly accepted mechanisms of arrhythmia initiation, and are thought to be the cause behind spiral wave and rotor activity measured in atrial arrhythmias [[Narayan et al., 2012b](#)]. These forms of electrical excitation therefore form the focus of many current mathematical modelling and experimental studies [[Fenton et al., 2002](#), [Jalife, 2003](#), [ten Tusscher and Panfilov, 2006](#)]

Of these three mechanisms, arrhythmogenesis of reentrant behaviour are least understood, with diagnosis and treatment of atrial fibrillation (AF) currently the primary challenge in the electrophysiology clinic [[José Jalife and Kalifa, 2009](#)]. Conduction slowing and conduction block are primary initiators of AF [[Kléber and Rudy, 2004](#)], and thus the study of mechanisms underlying conduction slowing and conduction block form the

primary interest of this thesis. This requires introduction to the cellular and sub-cellular mechanisms in cardiac myocytes, which is the focus of the next section.

2.1.2 Cellular action potentials

A cardiac myocyte stimulated from its resting transmembrane potential has an associated electrical *action potential* (AP) which is a change in electrical potential across the cell membrane over time. This change is due to the flow of ions via specialised *ion channels* - pore-forming proteins - which transport ions across the cell's plasma membrane via electro-chemical gradients. The electrochemical gradient across a cell membrane for a given ion type is determined by the Nernst equation :

$$V = \frac{RT}{zF} \ln \frac{C_o}{C_i} \quad (2.1)$$

- V is the transmembrane potential in Volts (conventionally defined as intracellular potential minus the extracellular),
- C_o, C_i denote the concentrations outside and inside the membrane respectively ,
- T is the absolute temperature in Kelvin,
- R is the gas constant and F Faradays constant respectively,
- z denotes the valence or charge of the ion in elementary units.

In the absence of other ions, the transmembrane current is zero when the ionic concentration inside and outside the cells are balanced. The transmembrane potential at which this occurs is referred to as the *reversal* or *Nernst potential* within the context of a single ion system. A small change in this transmembrane potential results in net movement of the ion across the cell membrane, resulting in a further change in potential.

Within a multiple ion channel system such as cardiomyocytes, the transmembrane potential is due to a contribution of activity from different ions. Alongside the regular ion channels which can be in the state of open, closed or inactivated, active *ion pumps* constantly transport ions against the concentration gradient, so there is an imbalance in potential across the cell membrane. The equilibrium resting potential of the cell is thus non-zero (conventionally written as negative). The resting potential of a myocyte due to all ions can be determined by the *Goldman–Hodgkin–Katz equation* which is a generalised form of the Nernst equation:

$$V = \frac{RT}{zF} \ln \frac{\sum_m p_{C_m^+} [C_m^+]_{out} + \sum_n p_{C_n^-} [C_n^-]_{in}}{\sum_m p_{C_m^+} [C_m^+]_{in} + \sum_n p_{C_n^-} [C_n^-]_{out}}, \quad (2.2)$$

where $p_{C_{m,n}}$ represents the permeability for ion $C_{m,n}$, and $[C_{m,n}^{+, -}]_{in,out}$ represents the concentration of that ion either inside or outside the cell.

A cardiac myocyte at a temporal steady state of its transmembrane potential is described to be at rest, and *excitable*. A typical resting transmembrane potential of cardiac myocytes would be around -70 to -85mV . Upon displacement from this resting potential above threshold, an action potential is triggered [Kléber and Rudy, 2004]. Ignoring the other ionic currents present in cardiac myocytes specific to a given species or cell type, which will be discussed further in Section 2.4.1, the major ions involved in the cardiac action potential are sodium (Na), potassium (K) and calcium (Ca). The mammalian ventricular action potential is divided in to 5 phases as outlined below, and depicted in Figure 2.4:

- Resting (Phase 4): The resting potential of the cardiac myocyte is between -70 to -85 mV , which is closest to the reversal potential of potassium. It is polarised,

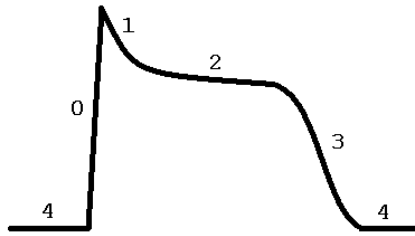


Figure 2.4: Schematic of a typical mammalian ventricular action potential against time. It can be divided into 5 phases which refer to distinct qualitative features.

excitable and responsive to stimuli.

- Rapid Depolarisation or Upstroke (Phase 0): A small super-threshold electrical stimulus causes a deviation from the resting potential, and causes rapid opening of sodium (Na^+) channels. This permits a large influx of sodium ions, which depolarises the cell. This typically occurs within 1-2 milliseconds.
- Initial Repolarisation (Phase 1): The inactivation of Na^+ channels, combined with the opening of the potassium (K^+) channel causing potassium ions to flow out of the membrane, begins the repolarisation of the cell.
- Plateau (Phase 2): The opening of L-type slow calcium (Ca^{2+}) channels (influx of calcium ions) balances with the efflux of potassium ions, which slows down the repolarisation process and gives rise to a plateau phase at around 0mV.
- Rapid Repolarisation (Phase 3): The closure of L-type Ca^{2+} channels disturbs the potential balance from the plateau phase, and creates a net outward current of the membrane which results in a drop in membrane potential. The K^+ channels close after the membrane potential is restored to resting state.

The upstroke of the AP has been studied in detail [Hille, 2001], and modelled mathematically. In the classic Hodgkin–Huxley formulation, sodium channel activity is de-

scribed by the equation:

$$I_{Na} = g_{Na}(V - E_{Na}), \quad (2.3)$$

where g_{Na} refers to the conductance of the sodium channels, and E_{Na} ($\sim 50mV$) is the reversal potential of the sodium current. More specifically, $g_{Na} = \overline{g_{Na}}m^3h$ is decomposed in to peak conductance $\overline{g_{Na}}$ (with all sodium channels fully open), multiplied by rate constants m^3 and h , where m and h are voltage dependent functions varying between 0 and 1, that effectively determine the probability of all the sodium channels being open or inactivated. Sodium channels open rapidly within several milliseconds, then typically undergo an extended period of inactivation before closing. It is known that the full AP upstroke can be triggered even under reduced sodium activity [Kléber and Rudy, 2004].

There are differences between characteristic cardiac action potentials in specific regions of the heart, due to specialist functions of myocytes in the region. Nodal (SA, AV node) cells do not exhibit a resting potential due to automaticity capabilities of these cells and have a slower AP upstroke, while the duration of atrial myocyte action potentials are shorter than that of ventricular myocytes. Figure 2.5 demonstrates typical action potentials in different regions of the heart. Furthermore, there are inter-species differences in cardiac action potentials. Variability of the action potential in different species will be discussed further in Section 2.4.1.

Initiation of the action potential causes myocyte contractility via *excitation-contraction coupling*. Ca^{2+} ions released from the sarcoplasmic reticulum (SR) within the myocytes induces the plateau (phase 2) of the AP. The released calcium ions bind with *troponin*, altering its shape and position, thus allowing *actin* and *myosin* to bind together. This causes shortening of the muscle fibres or myofibrils, on which actin filaments are aligned.

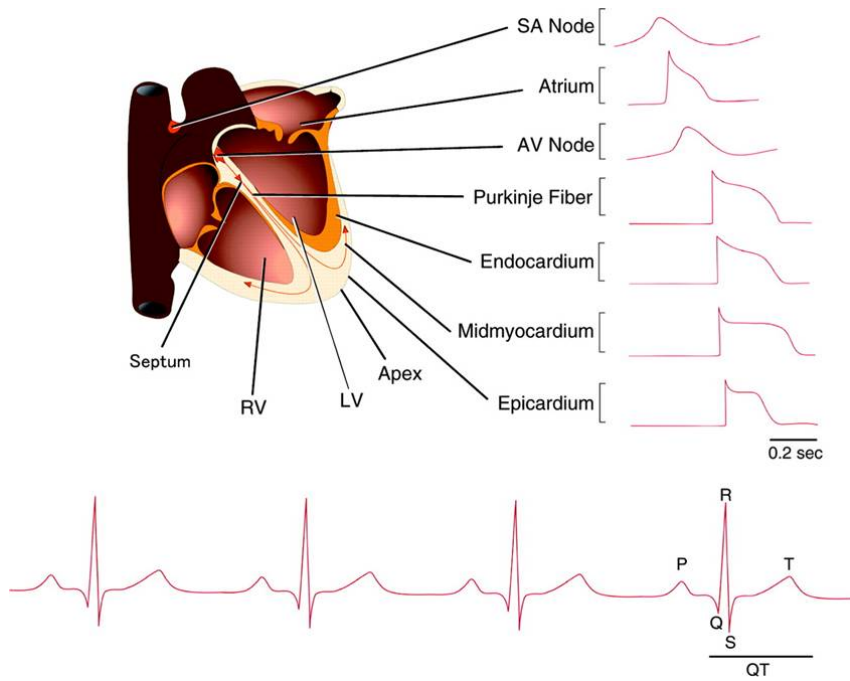


Figure 2.5: Variation in the typical action potential in regions of the heart are due to regional cardiac myocytes having specific roles within the conduction system. Overlaid in time with the lead I ECG, the SA and AV node cells exhibit a slower upstroke than other myocytes, and the lack of a plateau phase. An atrial action potential has a shorter temporal duration than a ventricular AP, whilst there are differences in AP shape within the thickness of the ventricular wall. (Reproduced from [Nerbonne and Kass \[2005\]](#))

After-depolarisations

A second stimulus delivered shortly after an AP is initiated (for example during phase 2, 3 or even 4) may not successfully trigger a second AP. If it does however, the second AP is known as an *after-depolarisation* and may have a shorter temporal duration. If this after-depolarisation occurs during phase 2 or 3, it is known as an *early after-depolarisation* (EAD). If triggered during phase 4, it is known as a *delayed after-depolarisation* (DAD). This second AP, if synchronised across the domain, leads to a second, weaker, contraction of the tissue. The presence of EADs or DADs may initiate other problems in the heart:

- The weaker second contraction affects the efficiency of heart contraction and the subsequent blood pressure. This may result in thrombus formation which can cause

coronary artery occlusion and subsequent myocardial infarction.

- The second AP prolongs the repolarisation of myocytes when other myocytes are in a polarised state. Thus, a regular propagated SR beat after an EAD or DAD may lead to conduction block at the site of prolongation. This will affect the synchronisation of systole across the domain.
- An EAD while calcium ions have not been fully pumped back in to the SR or out of the cell may result in a greater local concentration of calcium ions, causing a stronger contraction. Over time, a net increase of calcium concentration in myocytes occur, leading to stronger contractions. This may lead to remodelling of the heart which increases general arrhythmia susceptibility.

Action potential duration, diastolic interval, restitution and alternans

The *Action Potential Duration* (APD) is the time between depolarisation and end of repolarisation. In practice, it is hard to define the APD on experimental data as a typical action potential in phase 3 will decay to the resting potential slowly, so the crossover between the end of phase 3 and start of phase 4 is ambiguous. A commonly used measure is *APD90*, which is the time taken for the transmembrane voltage to drop by 90% of its full depolarisation amplitude.

The *Refractory Period* (RP) defines the temporal duration following depolarisation, during which the myocyte cannot be excited to initiate a ‘complete’ action potential. Sub-classifications of the refractory period are used to distinguish further electrical properties of myocytes. The *Effective Refractory Period* (ERP) refers to the length of time during which the myocyte is completely unexcitable. A cardiac myocyte not in its ERP but still repolarising is *relatively refractory*. If stimulated during this period, they myocyte may depolarise again but with a shorter and qualitatively different action potential. The

subsequent contraction is also correspondingly less strong.

In programmed electrical stimulation of cardiac myocytes with a given *cycle length* (CL) (or pacing frequency), the *diastolic interval* (DI) refers to the time interval between the end of one action potential and the beginning of another. This can be determined using the equation

$$DI = CL - APD$$

Cardiac cells are known to exhibit *restitution*, where the APD shortens in response to decreasing diastolic intervals. This is an effect of cardiac cells adapting to a change in pacing frequency. The effect of restitution can be examined in single cell experiments or through computer simulation of the action potential, and, where APD is plotted against DI or CL as a *restitution curve*. A slope in the restitution curve with gradient > 1 is considered as a precursor to initiation of complex dynamics, such as alternans [Qu and Weiss, 2006]. Figure 2.6 reproduced from Qu and Weiss [2006] shows a typical restitution curve (filled circles) of a guinea pig AP against a curve of an AP with modified ion channel characteristics (open circles).

Cardiac alternans refer to cardiac tissue exhibiting APs with an alternating sequence of long and short duration [Qu et al., 2000, Qu and Weiss, 2006, ten Tusscher and Panfilov, 2006]. This phenomenon occurs when cardiac tissue is paced at a fast cycle length, and is associated with transition in to arrhythmia such as fibrillation.

2.1.3 Myocardial tissue structure and anatomy

In this subsection, the myocardial architecture of the heart is briefly introduced, with specific reference to structural effects on electrical connectivity, based on structural characterisation studies completed in human and animal tissue.

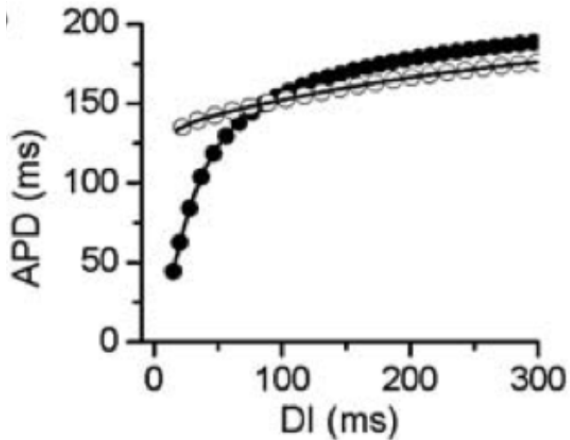


Figure 2.6: A restitution curve plots Action Potential Duration (APD) against Diastolic Interval (DI). This figure shows the restitution of a Luo–Rudy guinea pig AP [Luo and Rudy, 1991] (filled circles) versus an AP with modified ion channels (open circles). The curve typically steepens and terminates when the APD reaches some minimum value. A slope of > 1 is correlated with initiation of complex cardiac dynamics. (Reproduced from Qu and Weiss [2006]).

The heart is a complex 3–dimensional structure comprised of multiple cell types with specific functions. In the ventricles, layered 2D sheets of myocytes are observed through the thickness of the ventricular wall parallel with the epicardium. Each myocardial sheet has its long axes in a primary orientation which varies from endocardium to epicardium. Within each sheet, myocytes are long, thin and aligned with their long axis in similar orientations. Typical dimensions for a ventricular cardiac myocyte are around $100\mu m$ in length, and $20\mu m$ in diameter. and the thickness of the human ventricular wall is in the order of $1 - 2cm$ [Streeter, 1979].

The atrial wall is thinner, in the order of several millimetres and there is no clear alignment of the atrial myocytes in sheets [Ho and Sánchez-Quintana, 2009]. Atrial myocytes are clustered in bundles organised in a complex manner, with myocyte orientation following the local bundle orientation [Sachse, 2004]. Within individual anatomical struc-

tures, there are specific bundle orientations. For example, myocytes on the atria near the sleeves of the pulmonary veins exhibit a circumferential orientation.

Orientation of cells along the long axis in to sheets and fibre bundles leads to *anisotropy* - a directional dependence of electrical conduction velocity in the heart. Electrical wavefronts conduct faster along the long axis of a cell than in other directions. This permits electrical wavefronts to propagate quickly throughout the heart, which then causes muscular contraction in the specified direction.

For detailed anatomical measurements, tissue and microscopic architecture in both human and animal hearts, the reader is referred to models and studies by the Auckland Bioengineering group. In particular, the canine heart is characterised by [LeGrice et al. \[1995\]](#), the tissue microstructure of the rat ventricle is described and modelled by [Hooks \[2002\]](#), and the general effect of cardiac anatomy and structural discontinuities on electrical activation are reviewed by [Smaill et al. \[2004\]](#). This series of studies indicate that anatomical and structural features such as tissue microstructure, cellular arrangement and connectivity, may play an important role in the initiation and maintenance of arrhythmia. This view was first proposed by Madison Spach, who led a series of studies to investigate the effect of anatomical features and structural discontinuities on electrical activation in the heart [[Spach and Heidlage, 1995](#), [Spach, 2001](#), [2003](#), [Spach et al., 1988](#), [Spach and Miller, 1981, 1982](#)].

Other cell types

Myocytes are not the only cell type located within the heart. *Fibroblasts* which are responsible for synthesis of the extracellular matrix and collagen are found in large quantities (50-70% of heart cells) [[Agocha et al., 1997](#)]. Fibroblasts have been found to couple

with cardiac myocytes [Kohl, 2003], and both are embedded within the *extra-cellular matrix* of connective tissue which is formed of collagen, elastin, laminin and fibronectin. Studies of other cell types or the interaction between myocytes and other cell types are not considered within this study.

2.1.4 Gap junctions

Gap junctions (GJs) are low-resistance pathways interlinking cytoplasms of neighbouring cells, which allow small ions and molecules of less than 1 kilo Dalton to pass through. They are thought to be crucial for maintaining speed of action propagation from cell to cell. Gap junctions are formed by channel-forming sub-units known as *connexons* which are normally located in the step-like intercalated disc structure at the end face of the myocyte, and ‘dock’ with a connexon located in a neighbouring myocyte. This can be visualised in Figure 2.7.

Each connexon sub-unit is formed of six *connexin* (Cx) proteins and can be formed of combinations of different connexin isoforms. The most common isoforms found in the human heart are Connexin 40, 43 and 45, with Cx43 being the predominant isoform. Connexons composed of six identical isoforms are called *homomeric*, and are called *heteromeric* if formed by a combination of differing connexin isoforms. Gap junctions which are formed from identical connexon types are *homotypic*, and are *heterotypic* otherwise. The specific properties of each gap junction type is not a primary concern of this thesis; the reader is referred to Severs 2008 for a comprehensive review [Severs et al., 2008].

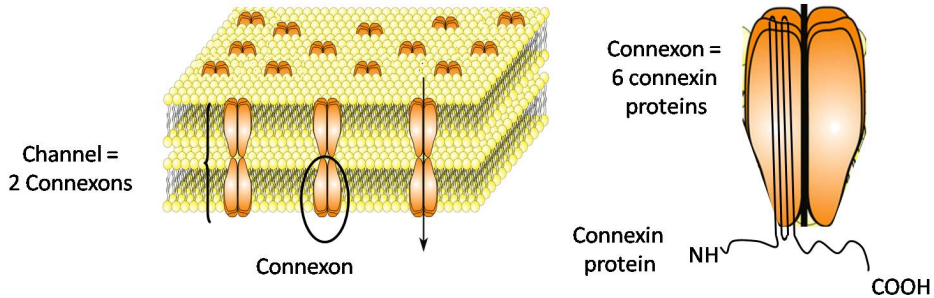


Figure 2.7: Diagrammatic view of a gap junctional channel. Each channel is made of two connexons, with each connexon formed by 6 connexin proteins in a circular arrangement. A connexin protein consists of four transmembrane domains, with the hydrophobic C-terminus and N-terminus at the docking interface. Image reproduced courtesy of Dr Rasheda Chowdhury.

2.2 Effects of structure and function on initiation of arrhythmia

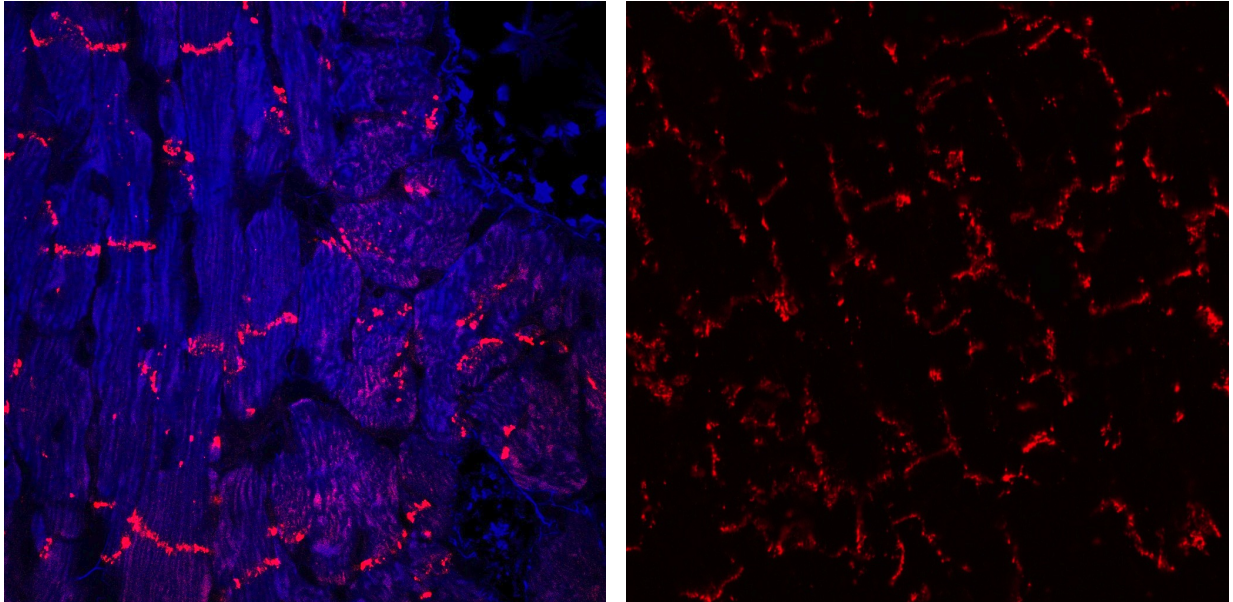
In this section, the effects of cardiac structure and function on the initiation of arrhythmias are explored in more detail. In particular, the focus is on mechanisms underlying changes in the conduction velocity of excitable wavefronts, which leads to complicated behaviours and potential arrhythmogenesis.

Lateralisation

As described in the previous section, gap junctions are low-resistance pathways interlinking cytoplasms of neighbouring cells, which in healthy cardiac tissue, are primarily located at the step-like intercalated disc structures at the end face of myocytes, perpendicular to the long axis. This can be seen in a sectioned image of healthy tissue shown in Figure 2.8a in which Cx43 protein has been labelled red via immunolabelling.

It has been shown [Peters et al., 1997], [Severs et al., 2008] that in diseased myocardium such as in recovered areas following myocardial infarction, gap junctions ap-

pear in the lateral part of the cell membrane (known as *lateralisation*). This is thought to alter spatial heterogeneity in cell conductivity, which changes the anisotropy of the myocardial substrate and makes the heart more pro-arrhythmic through subsequently affecting electrical conduction velocities.



(a) In healthy cardiac tissue, Cx43 (red) is aggregated in step-like structures within the intercalated disc, located at the end faces of myocytes. The cytoplasm is labelled in blue indicating the primary fibre direction.

(b) In diseased cardiac tissue, GJ-forming Cx43 protein (red) are located along the lateral membrane of myocytes in addition to the end faces. This is known as Cx43 *lateralisation*. The direction of the myocytes is similar to a).

Figure 2.8: Distribution of Cx43 protein in healthy (a) and diseased (b) canine ventricular tissue as a marker of gap junction localisation. Cx43 are labelled in red and cytoplasm in blue, using immuno-labelling. Images courtesy of Mrs Pravina Patel [[Patel et al., 2001](#)], and adapted for visualisation purposes.

2.2.1 Initiation of action potential upstroke and conduction slowing

Initiation of the cardiac action potential from its polarised resting phase is due to complex interaction of several factors including both structural and functional [[Kléber and Rudy, 2004](#)]. Initiation alters the shape of the foot of the AP upstroke curve, and is

closely correlated with conduction slowing; a shallow foot indicates slow conduction of excitation. Reduced conduction speed is considered pro-arrhythmic as it can either lead to conduction block, or shorten the wavelength of electrical excitation, which permits multiple wavefronts and re-entry to be sustained within the cardiac substrate (see Section 2.1.1). The effects of structural and functional factors governing initiation of the AP upstroke and conduction slowing is summarised in the following section.

Safety factor

The safety factor of conduction is related to source sink relationships [Rohr et al., 1997] and defines success of action potential propagation. It is defined in Shaw and Rudy [1997] and Wang and Rudy [2000] to be given as the ratio between charge generated to an charge consumed by an area of excitable tissue. Mathematically, it is described as:

$$SF = \frac{\int_A I_c dt + \int_A I_{out} dt}{\int_A I_{in} dt} \quad A|Q_m > 0. \quad (2.4)$$

I_c is the capacitative current of the tissue, and I_{in} , I_{out} are the axial currents entering and departing the tissue respectively. The charge Q of each term can be determined by the time integral of the current over an interval A , during which net membrane charge Q_m is positive. At the resting potential, $Q_m = 0$. However, a depolarising region consumes charge (sink) and Q_m increases to a positive peak. As the tissue discharges excitation by depolarising downstream tissue, Q_m decreases back to zero, and has completed its sink-source cycle defined by the interval $A|Q_m > 0$.

The safety factor is thus the quotient of total charge that the tissue receives (Q_{in}) plus the charge generated by the tissue via depolarisation Q_c , over charge used to depolarise downstream cells (Q_{out}). A SF of > 1 characterises successful conduction in a linear system with uniform cellular properties. The key determinants of charge in and out are

given [Kléber and Rudy, 2004] by contributions of gap junctional resistance, contribution of different ion currents or the cell dimensions.

Sodium (Na) channel excitability

Reduced availability of sodium channels leading to reduction in excitability occurs in acute ischemia, tachycardia and in certain electrical remodelling [Kleber, 2005]. Shaw and Rudy [1997] simulated the effects of progressive reduction of sodium excitability (by reduction in the density of available sodium channels), on the conduction velocity (CV) and the safety factor (SF) of conduction. They found that velocity and SF decreased monotonically as membrane excitability was reduced. Conduction failure occurred when SF decreased below 1, and the slowest CV recorded was 17cm/s .

Gap junctional coupling

The role of gap junctions (GJs) in propagation have been explored in theoretical and numerical studies [Rudy and Quan, 1987, Shaw and Rudy, 1997, Spach and Heidlage, 1995]. In simulations of 1D cells Shaw and Rudy [1997], normal gap junctional conductance was reported as $g_j = 2.5\mu S$, with a typical conduction velocity of 54cm/s . Normal conduction time across the $100\mu\text{m}$ myocyte was $0.1ms$, which was similar across gap junctions across the intercellular boundary that was 80\AA , indicating that even in normal conduction, propagation is discontinuous at cellular level with 50% of total conduction time being due to junctional delay. A ten-fold decrease of g_j increased intercellular conduction delay and decreased intracellular conduction time, resulting in gap junction dominance of the overall macroscopic conduction velocity.

The additional effect of transverse propagation present in multicellular strands acted to attenuate the junctional delay from 50% of total conduction time down to $\sim 20\%$ [Fast

and Kléber, 1993], suggesting that in three dimensions, inhomogeneities during propagation due to GJ delays smooths to an extent that 3D propagation can be considered continuous under normal GJ coupling.

Cell size was also found to be a parameter affecting the ratio of junctional delays to total delay [Joyner, 1982]. In a recent optical mapping study with a neonatal rat ventricular myocyte (NRVM) cell culture preparation, cytoplasmic conduction time was $38\mu s$ compared with $80\mu s$ at cell ends [Fast and Kléber, 1993].

It was also found by Shaw and Rudy [1997] that decreasing intercellular coupling initially increased the maximum rate of action potential upstroke dV/dt_{max} in a discontinuous model of conduction before decreasing sharply immediately preceding conduction block, but was unchanged in a continuous model. Peak sodium channel excitability g_{Na} was monotonically decreased by decreased intercellular coupling, explained by an extended sub threshold depolarisation providing time for sodium channel inactivation before activation threshold can be reached, resulting in reduced channel availability and thus a smaller g_{Na} . Further discussion by Kleber [2005] has discussed the relative role of L-type calcium channels compared to sodium channels in supporting slow conduction at high GJ coupling, although this is not covered in the scope of this thesis.

2.3 Detection and measurement of electrical activity

This section introduces some existing methodologies for measurement of electrical activity within the *ex-vivo* framework. Improved diagnostic capabilities from *in-vivo* cardiac electrical measurements derive from better understanding of the underlying biological mechanisms, which occurs as we derive further insights from *in-vivo* and *ex-vivo* mea-

surements. This is a long and complicated process of experimental design, testing and feedback, and *in-silico* modelling is a key component that can reduce the time and cost of this process.

The electrocardiogram (ECG) is a ‘first glance’ technique for diagnosis of arrhythmias [Hampton, 2003] via electrical recordings from external electrodes placed on the body surface. The ECG records summated activity from the heart, but cannot provide a detailed spatial map of cell electrophysiology. More advanced tools are used to obtain better spatial resolution on the epi- and endocardium of the heart. Each technique has different spatial and temporal resolutions, and is often used in separate contexts. Devices used *in vivo* are limited by size and their impact on the patient, and give a poorer spatial resolution which is an issue when treating arrhythmias such as atrial fibrillation. However *ex-vivo* devices with better spatial resolution are more cumbersome and dangerous to use in the clinic. A deterministic way to correlate data obtained using these different measurement techniques could make laboratory results more clinically relevant and provide some way of translating observed electrophysiology phenomena in patients in to questions that can be answered in the laboratory.

2.3.1 Unipolar, bipolar electrodes and cardiac catheters

A unipolar electrode refers to an electrode placed in proximity or in contact with the object of measurement. The subsequent unipolar electrogram records electrical activity with reference to a far field reference potential. Simplistically, an activation wave front moving towards the electrode produces a positive deflection on the electrogram, and a negative deflection is recorded as the wave front moves away from the signal. This biphasic signal on a unipolar electrode from a uniform propagating wavefront was mathematically modelled by Clark and Plonsey, and Geslowitz in a series of papers on the core

conductor model in the 1960s [[Clark and Plonsey, 1966, 1968, Geselowitz, 1966](#)]. They derived a theoretical expression relating the measured electrical signal to the second spatial derivative of the transmembrane potential in space and time.

The unipolar electrode in its most general definition includes any experimental setup with a single electrode that measures current relative to a far field. Thus several leads of the ECG are types of unipolar electrodes, as are a range of other electrode set ups including plunge electrodes [[Wang, 1995](#)] and the micro-electrode array described below. Within clinical cardiac electrophysiology however, the unipolar electrogram refers to cardiac electrical data acquired via *in-vivo* measurement of the endocardial heart surface, using electrodes embedded within cardiac catheters, which are inserted in to the heart via the femoral vein in the groin. Catheter embedded band electrodes are typically cylindrical in shape, with a height of 1mm and a diameter of 1mm.

A bipolar electrode measures local electrical activation, via potential differences between two proximally located electrodes.

Variations of cardiac catheters exist for specific diagnostic and treatment procedures. In a typical electrophysiology procedure, several catheters will be used in conjunction with the 12 lead ECG, to record electrical activities at specific locations. Treatment in EP procedures involve the delivery of radio-frequency or cryo-ablations to the tissue via specialised ablation catheters which can also record electrical data.

More complicated catheters have up to twenty embedded unipolar electrodes, which can be used to probe the sequence of electrical activation via either unipolar or bipolar electrogram recordings. Other catheters include balloon or basket catheters containing

multiple unipolar electrodes, which are capable of recording simultaneous low-resolution spatial information in 3D closer to global coverage, compared to sequential data recorded using simpler catheters. These multi-array catheters represent current state-of-the-art in *in-vivo* human EP studies and are generating significant scientific interest, with [Narayan et al. \[2011, 2012b,a\]](#) identifying the presence of spiral waves and rotors, previously undetected in human *in-vivo* recordings .

2.3.2 Multi-electrode arrays

Multi- or micro-electrode arrays (MEAs) describe smaller unipolar electrodes, typical $30 - 50\mu m$ in size, which are arranged within a regular array. These are typically used in *ex-vivo* experiments on cardiac tissue or cells, and can provide higher level of spatial accuracy compared to cardiac catheters which have greater electrode diameter and inter-electrode distance. More detail on MEAs will be presented in Chapter 6.

2.3.3 Microelectrodes

Microelectrodes describe glass electrodes with a sharp micropipette tip, which is used to impale a myocyte membrane and record the subsequent intracellular action potential. The impaled micropipette contains potassium chloride (KCl) solution, and the recorded data are the potential difference between the micropipette and a far field reference electrode also containing KCl solution. This technique may be used to obtain very accurate transmembrane potential data of single cells, and forms the basis for experimental results on guinea pig tissue obtained by Dr Paramdeep Dhillon, which is presented within Chapter 4.

2.3.4 Optical mapping

Optical mapping is a common *ex-vivo* technique for imaging spatial-temporal variations in biological data, and is a common experimental modality for whole heart [Efimov, 2004], and cell culture studies [Himel et al., 2012]. The imaged substrate is infused with a voltage-sensitive dye which binds to the cell membrane. The dye alters its fluorescence emission spectra depending on the voltage at the cell surface. Upon excitation by the chosen wavelength, the dye emits light at a lower wavelength which is detected by a CCD or CMOS digital camera. This permits both spatial (conduction) and functional (optical action potential) properties of the tissue to be measured, which are not detectable via unipolar electrodes. Additionally, dyes can be developed to examine other transient properties, such as intracellular calcium cycling [Lee et al., 2011, 2012].

Each pixel on the camera records a voxel of information, which represents averaged electrical information over that voxel. Thus, the dimensions of the voxel represent the limit of spatial resolution of the optical data. The size of the voxel is dependent on the diffusive properties of the substrate being studied. The diffusion problem of optical mapping has been theoretically studied by Hyatt et al. [2008], and depth-specific optical mapping techniques have been developed by the group of Walton et al. [2010].

Optical mapping is a useful tool for measuring acute electrophysiological information, and many studies are published using this technique [Akar et al., 2001, Kucera et al., 2001, Rohr et al., 1997, Fedorov et al., 2010]. However, long-term studies are not always feasible due to toxicity effects of the specific voltage sensitive dyes, and the costs of using voltage sensitive dyes. Additionally, it is unlikely that optical mapping can be used in *in-vivo* human studies, due to logistical, ethical and financial complications.

2.4 Modelling in cardiac electrophysiology

This section outlines the development of mathematical models to describe the biophysics of cardiac electrophysiology, and highlights the key challenges that remain in the field. In particular, the challenge of modelling pathophysiological changes is discussed.

2.4.1 Functional models of the single cardiac myocyte

The theoretical cardiac electrophysiology field initiated following the pioneering work by Hodgkin and Huxley on membrane excitability within the squid nerve axon [[Hodgkin and Huxley, 1952](#)]. The nerve axon is a single elongated cell; Hodgkin and Huxley separated the propagation of electrical excitation in the axon in to two coupled components: the functional electrical characteristics of the nerve cell described by transmembrane action potential activity (the Hodgkin–Huxley action potential model), and passive propagation of local dipole currents along the axon, from which cable theory and the cable equation was introduced.

Within the Hodgkin–Huxley cell model, three ionic currents are described to determine the AP: a sodium (Na) current, potassium (K) current and a leakage current due to natural membrane permeability. The model contains four variables: the transmembrane voltage, the activation and inactivation variables of the sodium channel and the inactivation variable of the potassium current.

The Hodgkin–Huxley model paved the way for two types of subsequent model development of the single cell: mathematically simplified models which captured gross ‘phenomenological’ behaviour (e.g. FitzHugh–Nagumo [[Fitzhugh, 1961](#)]) and more biophysically detailed models (Noble SA node model [[Noble, 1962](#)]), which sought to characterise

accurately excitable behaviour in the single cell.

The development of the patch clamp technique in the 1980s brought further understanding of the ionic mechanisms within the single cell [Liem et al., 1995]. Subsequent biophysical studies have built both on these experimental developments and on existing cardiac cell models, via introduction of additional ionic currents and modified equations to match with experimental data. The Beeler–Reuter model [Beeler and Reuter, 1977], a generic ventricular myocyte model, is such an example, whilst other studies have sought to characterise the AP of cells of specific species and anatomical location, such as guinea pig ventricle [Luo and Rudy, 1991, 1994], human ventricle [Bueno-Orovio et al., 2008, O’Hara and Rudy, 2012, ten Tusscher et al., 2004], and human atrium [Courtemanche et al., 1998]. Many modern biophysical models include complicated dynamical behaviour to capture intracellular calcium cycling and other cellular mechanisms, such as the sodium calcium exchanger and ion pumps, which makes these models highly complex and computationally demanding to solve [Lines et al., 2003].

The additional complexity and computational cost of such detailed biophysical models can be considered a disadvantage [Clayton et al., 2010]. Thus, development of simple phenomenological models of the AP has continued alongside the emergence of more detailed biophysical models. Simple phenomenological models aim to correctly capture the main properties of the physiology, such as the AP shape, APD and its restitution. The FitzHugh–Nagumo model [Fitzhugh, 1961] mentioned above, is a simplification of the four variable Hodgkin–Huxley model in to two variables - a membrane potential (V) and a lumped recovery variable (w). The Aliev–Panfilov model [Aliev and Panfilov, 1996] and the Fenton–Karma models [Fenton and Karma, 1998] are examples of simpler 2 to 4 variable models that capture APD and restitution properties of more complicated mod-

els, with appropriate tuning of its parameters.

Single cell AP models permit investigation into arrhythmias initiated or maintained due to abnormal automaticity of cardiomyocytes, such as long QT syndrome [Viswanathan et al., 1999]. Mechanisms determining the onset of cardiac alternans can be modelled, and functional studies using these single cell models can be performed to understand properties of specific cell types under pharmacological modulation.

Cellular Automata

Simple rule based models of the action potential have been described using cellular automata (CA) [Moe et al., 1964, Bub and Shrier, 2002]. A ‘cell’ representing single or a cluster of real cells assumes one of several discrete states, which may correspond to the phases of the AP. The state of a cell changes in strict sequence, depending on simple factors such as the state of its neighbours, rather than on complex ion channel behaviour. This permits a more computationally efficient approach to simulating excitable media, and can be used to examine behaviours of large domains of tissue (e.g. in 3D [Sachse, 2004]), which would be more challenging with a traditional biophysical model.

CA models have been used to model simple cardiac behaviour, and aid mechanistic understanding in multidisciplinary translational research teams. Work by Spector et al. [2011] has used CA models, coupled with a simple action potential, to demonstrate reentrant behaviour and propagation failure due to wavefront curvature.

2.4.2 Models of excitable cardiac tissue

The excitation of cardiac tissue presents a different physical problem to excitation in a nerve axon, but analogies can be drawn between the two systems, which leads to the

fundamental equations of excitation in cardiac tissue. Mathematically describing the local continuous or discontinuous excitation of tissue at different spatial scales is the focus of this section.

Tissue modelling - Continuum approach

As described in the previous section, the Hodgkin–Huxley studies [Hodgkin and Huxley, 1952] considered a single elongated nerve axon, and propagation of local membrane currents within the single cell. Cardiac myocytes *in-vivo* differ from nerve axons in their shape and size, being approximately cylindrical of around $100\mu m$ in length and $20\mu m$ in diameter, as detailed in Section 2.1.3.

Propagation in a thin cylindrical bundle of cardiac tissue comprising of aligned myocytes in the long–axis of the bundle is considered. Theoretical studies of propagation in cylindrical bundles have been completed [Henriquez et al., 1988, Henriquez and Plonsey, 1990, Roth, 1991]. Because of the relative scale of the myocyte’s length to its radial length, the *core-conductor assumption* [Clark and Plonsey, 1966], which assumes that potential of the cell depends only on the length variable and not its radial or azimuthal variable, can be applied [Keener and Sneyd, 2009, p.177] to reduce the problem to one dimension.

Despite the structural differences between cardiac tissue and nerve axons, well coupled cardiomyocytes are known to behave in a syncytial manner [Clayton and Panfilov, 2008, Keener and Sneyd, 2009, Kléber and Rudy, 2004]. At a macroscopic tissue scale, an excitation wavefront across the domain occurs at speeds of $> 40cm/s$ [Keener and Sneyd, 2009, p. 251]. Defining the space constant λ as the distance for the potential at a point of the cell to decay by a factor of e , it can be calculated that for healthy well

coupled tissue, the space constant is much greater than the length of a single cell [Keener and Sneyd, 2009]. Thus, the discrete cellular cytoplasmic resistance and GJ resistances can be lumped in to an diffusion coefficient using a mathematical process known as *homogenisation*, which transforms the discrete tissue structure in to an effective continuum [Keener and Sneyd, 2009, Neu and Krassowska, 1993]. The effect of homogenisation is to average the behaviour of many cells at each point in space, so that the potential at each point represents the net potential of many myocytes. In this case, the cable equation forms a continuum approximation for propagation of excitation in cardiac tissue. The cable equation will be derived and presented in Section 3.4.1.

Using cable theory, two primary continuum models of tissue excitation have been described - the monodomain and bidomain models [Pullan et al., 2005, Sachse, 2004]. The monodomain considers the spatial-temporal behaviour of a single variable - the transmembrane potential (V_m). The bidomain model considers two variables coexisting at each point in space and time - typically the extracellular potential V_e and the transmembrane potential V_m . The monodomain model is a limiting case of the bidomain model, and the theoretical *homogenisation* process of deriving the bidomain model from first principles has been completed by Neu and Krassowska [1993].

The equations for both models will be presented in Chapter 3.

Tissue modelling - Discrete approaches

The effect of discontinuous structure of cardiac tissue on conduction on a microscopic scale has been explored experimentally. Spach and Miller [1981] examined discontinuous propagation in canine cardiac tissue, and this was explored in preparations of cell monolayers by Kucera et al. [2001]. In these studies, it was reported that whilst conduction speed was constant across the length of a myocyte, local conduction delays occurred

across cell boundaries between cells.

This discontinuous conduction is described as ‘saltatory’, and was studied theoretically by [Henriquez and Plonsey \[1987\]](#) and [Rudy and Quan \[1987\]](#), among others, using a discrete approach of modelling individual cells, coupled via gap junctions. [Keener and Sneyd \[2009\]](#) completed elegant analytical studies of discontinuous conduction in passive cells with no realistic ion channels, and this will be presented in detail in Chapter 7.

The cellular automata (CA) models outlined in the previous section can be used to describe cardiac tissue. Using each ‘cell’ to represent single or a cluster of myocytes, a tiled arrangement of cells can be arranged to represent cardiac tissue, with rules governing excitation of a cell based on the states of its neighbours. This is a natural discrete description of cardiac tissue, and studies using this model have been completed by [Moe et al. \[1964\]](#), [Gerhardt et al. \[1990\]](#) and [Bub and Shrier \[2002\]](#).

Continuum vs discrete models

In normal cardiac excitation, the longitudinal space constant λ , explained in detail in Section 3.4.1, is much greater than the length of a single myocyte ($\lambda = 1\text{mm}$ [[Plonsey and Barr, 2007](#)] or $\lambda \sim 1.5\text{mm}$ [[Akar et al., 2001](#)], compared with the average myocyte length of 0.1mm). This implies that there is very little variation in potential over the length of a single cell, and thus *homogenisation* of the tissue to a continuum representation, ignoring the variation over the length of a single cell, is a valid approximation.

Continuum representations of tissue excitation ignore spatial variation on the level of the single myocyte, and are thus computationally less expensive to solve than detailed discrete models. Over the last twenty years, cardiac EP modelling has been focussed towards

modelling patient specific whole heart models, which require significant computational resources [Clayton et al., 2010, Trayanova, 2011]. This has necessitated a demand for computationally efficient models, and thus continuum tissue models are currently widely used in theoretical cardiac electrophysiology [Lines et al., 2003, Sachse, 2004].

For pathophysiological conditions however, phenomena such as conduction slowing or unidirectional conduction block may arise, which reduce the size of the space constant. A small space constant means that homogenisation is no longer valid, and the discrete, saltatory nature of conduction becomes important. Thus, discrete models of electrophysiology have remained an important area of research since the work of Spach and Dolber [1986]. Studies by Trayanova [1996], Roth [1991] and Keener and Sneyd [2009] have analysed discrete tissue models with passive ion channel coupling. The group of Henriquez has published a series of work on discrete models [Henriquez and Plonsey, 1987, Henriquez et al., 2001, 2004], which will be discussed in more detail in Chapter 7.

2.4.3 Challenges of electrophysiology modelling

Creating accurate, useful *in-silico* models of electrophysiology is a long and challenging process. The long term aims of electrophysiology modelling are to aid understanding of basic mechanisms, and subsequently to make future predictions to inform future experimental studies and protocols in clinical intervention [Pullan et al., 2005]. Multiple challenges and open questions remain [Clayton et al., 2010], some of which are briefly discussed in this section.

Reproducing the correct physiology

The electrical function of the heart is due to complex interactions between cardiac structure and function [José Jalife and Kalifa, 2009]. The key challenge in EP modelling is to

capture the correct electrophysiological features, specific to the question being addressed. The difficulties in addressing this challenge is due to several limiting factors:

- **Limitations of experimental data:** Certain experimental data have been acquired in simple, ‘reductionist’ systems. For example, patch clamp studies are performed on single cells not on multicellular preparation, and conduction studies using cell monolayers ignore the complexity of other cell types present in the heart such as fibroblasts. Certain biological assumptions or parameters may not be valid in a more complex setting; there may exist more emergent biological mechanisms at tissue or whole heart level, which do not surface in simple experiments.
- **Limitations of experimental measurement:** Natural variability in biological data forms a limitation in experimental measurement. This variability cannot be captured easily using deterministic mathematical models, which might predict changes in behaviour at critical parameter values.
- **Basic mechanisms have not been established experimentally** Certain basic mechanisms cannot be easily measured experimentally. For example, patch clamp in coupled cell pairs is the primary method of measuring gap junction functionality [Beauchamp et al., 2012], but no experimental techniques exist for high fidelity measurement of this behaviour in myocyte monolayers or in cardiac tissue, such that one can only extrapolate parameter choices from simpler systems.
- **Limitations of mathematical modelling** Mathematical models are idealised systems of biological behaviour, and thus have many limitations. Models are generally constructed to reproduce behaviour informed by experimental researchers, and thus simulation results may be self-satisfying the hypotheses that the model was created to test. There is a danger of omitting important phenomena, over-exaggerating behaviour which is normally irrelevant, or investigating parameter

ranges that are outside the physiological range. Biological parameters may be at the parameter limit of numerical stability of a described mathematical model, such that simulated results may be uninterpretable, due to introduced numerical error and model instability.

The ability to predict emergent phenomena that is not explicitly considered within the simple models, yet appear upon interactions of these models is one way to ensure the model behaves correctly.

- **Validation against experimental data is difficult** Validation of theory to experiment is often difficult due to differences and mismatches between study hypotheses and assumptions. Study assumptions are different between mathematical and experimental models, and are acquired at different levels of spatial and temporal resolution. For example, correlating whole heart simulation results against in-vivo clinical data is difficult due to the limited spatial resolution from in-vivo recording tools. Conversely, it can be challenging to check experimental data against mathematical models due to a lack of critical parameters in the mathematical models, which themselves require validation. Although both theoretical and experimental models are built using reductionist approaches, the number of adjustable parameters and variables that exist in biology makes mathematical models of realistic systems (which can exhibit sensitivity to initial conditions in just 2 parameter systems) highly non-linear and difficult to create and validate.

Mutual expectation of theoretical or experimental capabilities between researchers of different disciplines can be misplaced, such that experimental researchers expect a fully developed mathematical model to inform all aspects of experimental design, whereas mathematical modellers rely on experimental work to establish fundamental parameters for each aspect of the model.

Accuracy and error of modelling

Continuum electrophysiological models assume the behaviour of cardiac tissue as a functional syncytium, which permits a partial differential equation (PDE) approximation for the diffusion of the cardiac potential in space. Computational electrophysiology equations are notoriously difficult to solve due to the stiffness of the underlying partial differential equations describing diffusion, and the additional complication of the steepness of the action potential upstroke which requires a very fine temporal discretisation to capture [Bordas et al., 2010, Hunter and Pullan, 2003, Clayton et al., 2010].

Choosing a suitable spatial and temporal discretisation method for solving the coupled PDE and ODE system, and an suitable level of discretisation parameters have significant effects on the accuracy of the simulation [Clayton et al., 2010]. Methods for solution of cardiac electrophysiology equations are discussed in more detail in Section 3.5.1, but choice of suitable discretisation parameters is discussed here.

In brief, physiological outputs of the cardiac electrophysiology model such as conduction velocity (CV) and action potential duration (APD) are known to exhibit sensitivity to spatial and temporal resolution [Courtemanche, 1996, Cherry et al., 2003]. Typical values used in large tissue volumes use a resolution of $0.1 - 0.2\text{mm}$ to solve the PDE, and a time step of $0.01 - 0.02\text{ms}$ for the diffusion of the ODE model [Clayton et al., 2010]. Larger spatial resolutions may lead to convergence issues and also the development of unwanted features, such as sharp corners on curved activation wavefronts in 2D where elliptical wavefronts are expected [Clayton et al., 2010], whilst a small time step is required to guarantee stability for the diffusion operator.

Run time of large-scale simulations is large, due to the number of spatial nodes in the domain [Lines et al., 2003]. Simulations are computationally demanding on processing

time and memory, and a $500ms$ simulation, which contains single heartbeat simulation may take over 12 hours to compute, depending on discretisation parameters and methods chosen. Reentrant behaviour may develop over several heartbeats, which increases the simulation time further. Thus there is a tradeoff between reducing computation time, yet maintaining accuracy of the model.

The complexity of the cell ODE models, included with the size and complex structure of the myocardium means a large number of experimental parameters are included within each simulation. Evaluating the reproducibility, stability and uniqueness of the simulations, subject to small changes in model parameters is a challenging task [[Livshitz and Rudy, 2009](#)]. Benchmark studies that compare the accuracy of simulations between studies are limited, with [Niederer et al. \[2011\]](#) beginning to verify the different cardiac EP solvers and methods in research use.

In summary, normal tissue behaviour has been characterised through modelling, and this has led to investigation and simulation of whole heart studies, but there remain numerical challenges in solving the electrophysiology equations quickly and accurately. Additionally, there are additional numerical and interpretational challenges to modelling pathophysiological changes such as fibrosis, infarct border zones or transmural heterogeneities in action potential characteristics through the heart wall.

In this thesis, simple models of cardiac conduction in 1D will be considered and compared, which will allow investigation and simulation at a high spatial resolution, with fewer worries about computation time and trade-off against accuracy.

Chapter 3

Numerical solution of cardiac electrophysiology equations

3.1 Introduction

Electrical excitation in the heart can be mathematically modelled in a continuum manner as a reaction–diffusion process. Mathematical approximations represent the electrochemical processes that occur within individual cardiac myocytes (*reaction*) and from cell to cell (*diffusion*). The parameters for these models are typically fitted from experimental data: single cell voltage clamp recordings are used to obtain critical values governing ion channel behaviour, which are used to construct the ordinary differential equations describing the ion channels of a single cell. The diffusion of the electrical potential at tissue–scale can be detected in *in-vitro* experiments of cardiac tissue, using recording techniques such as extra-cellular electrograms or optical mapping using voltage-sensitive dyes.

This chapter sets out the common mathematical equations and models used throughout the thesis, as well as the numerical methods implemented in this work for finding

solutions to these equations. The quantitative time-dependent mathematical descriptions of select single cell action potential models are introduced, along with an efficient numerical method for solving these equations. Next, the partial differential equations which describe the diffusion of the cardiac potential in space are described, along with the solution methods used to solve these equations. The final section outlines the equation for generating a virtual electogram and implementation details.

3.2 Single cell action potential models

Theoretical models of cardiac excitation cover spatial scales from sub-cellular to macro-scale whole heart level, as described in Section 2.4. In this thesis, the primary focus is to examine multi-scale factors affecting AP propagation and conduction. Thus, the re-polarisation phase of the AP and its restitution behaviour is of secondary importance in constructing the overall model. This determines the criterion for selecting AP models: to choose models with simple biophysical behaviour that grossly re-creates the AP shape of the experimental study in question. To this end, two existing models were selected for implementation in this thesis. The Cherry–Fenton phenomenological model [Cherry and Fenton, 2004], which was used for implementation and validation studies, and the Luo–Rudy I biophysical model [Luo and Rudy, 1991] which was used for the physiological studies. Both models are briefly described below.

3.2.1 The Cherry–Fenton phenomenological model

The Cherry–Fenton model is a modification of the Fenton–Karma model [Fenton and Karma, 1998], a phenomenological model which seeks to reproduce the heuristic properties of complicated action potential systems (such as AP shape, APD restitution), by combining the contribution of multiple ionic channels and expressing them as three

lumped ‘channels’, fast–inward, slow–inward and slow–outward respectively. The behaviour of each ‘channel’ is given by a mathematical equation which is a function of the transmembrane variable and gating variables. The model contains two gating variables v and w which follow first–order ODEs in time. For simplicity, the model considers a rescaled transmembrane voltage, which is a function of the maximum amplitude and resting transmembrane potential. Parameters for the model can be chosen to best fit properties of individual action potential models, and modification of the equations describing the currents and gating variables can be similarly made.

Many modifications of the original Fenton–Karma model have been published for specific applications and investigations [Bueno-Orovio et al., 2008, Cherry et al., 2007, Cherry and Fenton, 2004, Fenton et al., 2002]. In particular, the Cherry–Fenton model [Cherry and Fenton, 2004] is used for investigating the effect of APD restitution and cardiac ‘memory’ on the initiation of pro–arrhythmic phenomena such as alternans and conduction block. The computational efficiency, and versatility of the model in reproducing gross action potential properties (such as shape and restitution) of many commonly used biophysical models, make it attractive to adopt as a simple model of action potential behaviour, and is thus described below in further detail.

In the Cherry–Fenton model, two gating variables v and w are used, similar to the Fenton–Karma model. The voltage V is normalised from the normal transmembrane potential V_m via $V_m = 100V - 85$, with V varying between 0 and 1.4. The gating variables are given by:

$$\frac{dV}{dt} = -(I_{fi} + I_{si} + I_{so}), \quad (3.1)$$

$$\frac{dv}{dt} = \frac{(1-p)(1-v)}{\tau_v^-} - \frac{pv}{\tau_v^+}, \quad (3.2)$$

$$\frac{dw}{dt} = \frac{(1-p)(1-w)}{\tau_w^-} - \frac{pw}{\tau_w^+}, \quad (3.3)$$

(3.4)

where I_{fi} is a lumped fast inward current, I_{si} is a lumped slow inward current, and I_{so} is a lumped slow outward current. Also,

$$\tau_v^- = (1-q)\tau_{v1}^- + q\tau_{v2}^-, \quad (3.5)$$

$$\tau_w^- = (1-q)\tau_{w1}^- + q\tau_{w2}^-, \quad (3.6)$$

and p, q, r are related to Heaviside functions:

$$p = \begin{cases} 0 & V < V_c \\ 1 & V \geq V_c \end{cases}, \quad (3.7)$$

$$q = \begin{cases} 0 & V < V_v \\ 1 & V \geq V_v \end{cases}, \quad (3.8)$$

$$r = \begin{cases} 0 & V < V_r \\ 1 & V \geq V_r \end{cases}. \quad (3.9)$$

The transmembrane currents are subsequently calculated with the following equations:

$$I_{fi} = \frac{-vp(V - V_{fi})(1 - V)}{\tau_d}, \quad (3.10)$$

$$I_{si} = -\frac{w[1 + \tanh(k_1(V - V_c^{si}))]}{2\tau_{si}}, \quad (3.11)$$

$$I_{so} = \frac{V(1 - r)(1 - vk_2)}{\tau_o} + \frac{r}{\tau_r}. \quad (3.12)$$

Parameter values for this model can be obtained from the original paper. The parameter values for Model 2a was used as described in the paper. An example AP of Model 2a is presented in Figure 3.1.

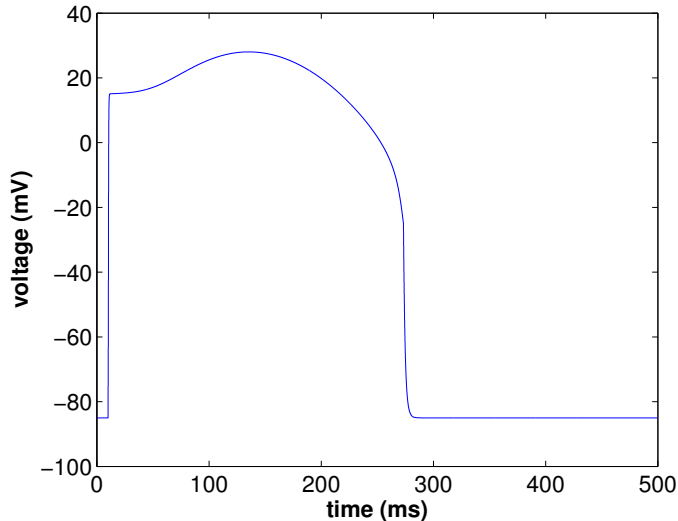


Figure 3.1: A sample action potential from the Cherry–Fenton model 2a [Cherry and Fenton, 2004]. The AP does not contain an initial repolarisation spike common in more biophysically detailed AP models.

3.2.2 The Luo–Rudy I ventricular myocyte model

The Luo–Rudy I model [Luo and Rudy, 1991] is an eight–variable model that describes the action potential of a guinea pig ventricular myocyte. It is a modification of the

Beeler–Reuter model [Beeler and Reuter, 1977], which describes a generic mammalian ventricular action potential, and is one of the most widely cited AP models in the literature [Lines et al., 2003, Kléber and Rudy, 2004].

The model contains two inward currents, sodium (I_{Na}) and a slow inward (calcium) current (I_{si}), and four outward currents, time-dependent potassium (I_K), time-independent potassium (I_{K1}), plateau potassium (I_{Kp}) and background (I_b) currents, as shown in Equation (3.13):

$$C_m \frac{dV_m}{dt} = I_{Na} + I_{si} + I_K + I_{K1} + I_{Kp} + I_b. \quad (3.13)$$

The three time-independent outward currents are sometimes presented as a lumped total time-independent potassium current $I_{K1(T)}$ (where T denotes ‘total’), given by

$$I_{K1(T)} = I_{K1} + I_{Kp} + I_b.$$

Each current with the relevant rate constants are presented in Appendix A, with the parameters for the currents given in Table A.1.

An example AP of the Luo–Rudy I model is presented in Figure 3.2.

3.3 Numerical integration of action potential models

Numerical solution of the coupled ODE systems representing cellular action potential behaviour can be computed using standard ODE solution techniques such as Euler or Runge–Kutta methods [Pullan et al., 2005, Sachse, 2004]. There is a large variation in the characteristic time period during which ion channels within cardiac cells are active,

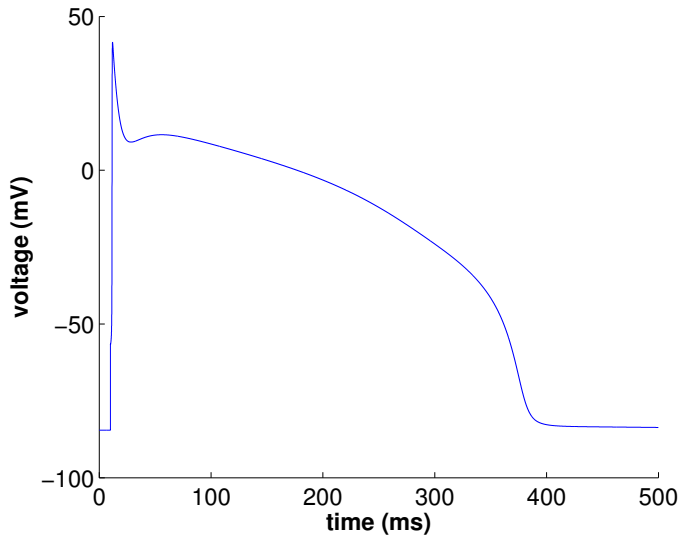


Figure 3.2: A sample AP of a single cell, from the Luo–Rudy I model [Luo and Rudy, 1991], which is modelled on a guinea pig ventricular myocyte.

and this may lead to numerical inaccuracy in discretising and solving these ODEs.

3.3.1 The Rush–Larsen algorithm

The Rush–Larsen algorithm [Rush and Larsen, 1978] is a method developed specifically for fast solution of cardiac cellular ODE equations. The fundamental assumption for the Rush–Larsen algorithm is that the rate constants are constant over the time step of integration, assuming that the time step is small.

For a single cell with N ionic currents, an injected stimulus current entering the cell is equal to the sum of ionic currents crossing the cell membrane, due to Kirchoff's laws. This can be expressed as:

$$I_s = C \frac{dV}{dt} + \sum_{k=1}^N g_k(V - V_k) \quad (3.14)$$

The conductance g_k of ion channel k are expressed as a function of gating variables:

$$g_k = \bar{g}_k f_k(y_1, y_2, \dots), \quad (3.15)$$

where \bar{g}_k is the maximum conductance and f_k is a function which varies between 0 and 1, thus scaling the conductance. Each gating variable y_i satisfies

$$\frac{dy_i}{dt} = \alpha_{y_i}(1 - y_i) - \beta_{y_i}y_i. \quad (3.16)$$

Rate constants α_i and β_i are voltage dependent terms such that $\alpha_{y_i} = \alpha_{y_i}(V)$ and $\beta_{y_i} = \beta_{y_i}(V)$. This equation can be rewritten as:

$$\frac{dy_i}{dt} = \alpha_{y_i} - y_i(\alpha_{y_i} + \beta_{y_i}), \quad (3.17)$$

which permits an exponential solution for constant α and β . At steady state as $t \Rightarrow \infty$, y_i is a constant and thus $dy_i/dt = 0$ and $y_i(\infty) = \alpha_{y_i}/(\alpha_{y_i} + \beta_{y_i})$.

The complete solution to this system can be solved by separation of variables. Using $y_i(0)$ to denote the initial condition and incorporating the steady state assumption $y_i(\infty) = \alpha_{y_i}/(\alpha_{y_i} + \beta_{y_i})$, the following equation can be obtained:

$$y_i = y_i(\infty) - (y_i(\infty) - y_i(0))e^{-\Delta t/\tau_i}, \quad (3.18)$$

where the time constant $\tau_i = 1/(\alpha_{y_i} + \beta_{y_i})$, for α and β constant.

The algorithm can be summarised using Fig. 3.3, and is briefly outlined below. Equation (3.18) is assumed to be accurate over one time increment, and is rewritten in discretised form for time points $n, n + 1, \dots$, as required. $y_i(0)$, the value of the gating

variable at time n , is written x_n . $y_i(\infty)$ the asymptotic value of y_i , is denoted x_∞ and is a function of the current value of V , denoted $V(n)$.

The rate constants $\alpha_{x_n(V_n)}$ $\beta_{x_n(V_n)}$ are calculated using V evaluated at time step n . Then, the new value of gating variable x at time $n + 1$ (denoted x_{n+1}) can be calculated as follows:

$$x_{n+1} = x_\infty(V_n) + (x_n - x_\infty(V(n)))e^{-\Delta t/\tau_x(V_n)}, \quad (3.19)$$

where

$$\tau_x(V_n) = \frac{1}{\alpha_{x_n}(V_n) + \beta_{x_n}(V_n)}, \quad x_\infty(V_n) = \frac{\alpha_{x_n}(V_n)}{\alpha_{x_n}(V_n) + \beta_{x_n}(V_n)}.$$

From Equation (3.19), it is possible to calculate all the gating variables at the new time step, and the subsequent ionic currents and membrane voltage. The accuracy of the method is still first order similar to Forward Euler, but the algorithm allows for larger time discretisation compared to existing methods [Clayton and Panfilov, 2008].

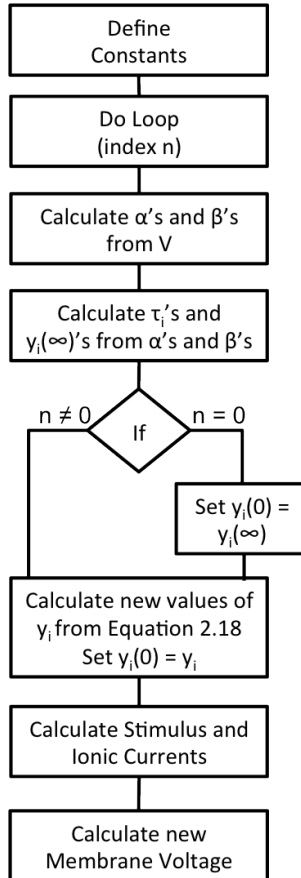


Figure 3.3: The Rush–Larsen algorithm is a fast algorithm for accurate numerical simulation of coupled ODE systems representing ionic channels within the cardiac cell. The algorithm exploits the assumption that rate constants α_{y_i} and β_{y_i} for an ion channel y_i are constant over the time period of integration, and calculates the updated ionic currents and membrane voltage. (Adapted from [Rush and Larsen \[1978\]](#)).

3.4 Tissue models

The previous section introduced single cell AP models, modelled by systems of ODEs. These may be coupled to PDEs which describe the diffusion of the single cell properties in space and time. These PDEs represent models of passive tissue.

In this section, the passive 1D cable equation is derived and presented. Using this derivation, the standard formulations for the monodomain and bidomain models are

given, as extensions or variations of the cable equation.

3.4.1 Derivation of the cable equation

Consider a long thin cylindrical excitable cell of radius a and of infinite length. The cell has a specific resistivity of R_l (Ωcm), a membrane resistance of R_m (Ωcm^2) and a membrane capacitance of C_m ($\mu F/cm^2$). These membrane properties can be converted in to properties per unit length, via the following conversions:

$$r_l = R_l/\pi a^2$$

$$r_m = R_l/2\pi a$$

$$c_m = C_m * 2\pi a$$

The current flux across the area of cell membrane at x is given by the current at the membrane over the surface area of the section, $2\pi a \Delta x$.

Denoting the membrane potential $\Delta V_m = \phi_i - \phi_e$, the change in V_m with small distance Δx is given by $\Delta V_m = -i_l r_l \Delta x$, where r_l is the cell cytoplasm resistance per unit length, and i_l is the current along the membrane. Then, letting $\Delta x \rightarrow 0$,

$$\frac{\partial V_m}{\partial x} = -i_l r_l.$$

The current along the membrane is given by $\Delta i_l = -i_m \Delta x$, where i_m is the transmembrane current per unit length. Again, letting $\Delta x \rightarrow 0$,

$$\frac{\partial i_l}{\partial x} = -i_m.$$

The transmembrane current at each point x is a combination of capacitance current i_c

and leakage current due to membrane resistance i_r . The capacitance current across a membrane area with given capacitance is given by

$$i_c = c_m \frac{\partial V_m}{\partial t}$$

And the current due to membrane resistance is given by using Ohm's law:

$$i_r = \frac{V_m}{R_m}$$

Combining these two terms:

$$i_m = c_m \frac{\partial V_m}{\partial t} + \frac{V_m}{R_m}$$

Then, substituting these terms, the following expression is obtained:

$$\frac{\partial i_l}{\partial x} = \frac{\partial}{\partial x} \left(-\frac{1}{r_l} \frac{\partial V_m}{\partial x} \right) = -\frac{1}{r_l} \frac{\partial^2 V_m}{\partial x^2} = -\left(c_m \frac{\partial V_m}{\partial t} + \frac{V_m}{R_m} \right) \quad (3.20)$$

Rearranging, the passive cable equation can be written as:

$$\sigma_i \frac{\partial^2 V_m}{\partial x^2} = c_m \frac{\partial V_m}{\partial t} + \frac{V_m}{R_m}, \quad (3.21)$$

where $\sigma_i = \frac{1}{r_l}$ the intracellular conductivity is commonly defined.

Further algebraic manipulation of the passive cable equation reduces the numbers of parameters in the equation to two important parameters. The *space constant* λ of the passive cable equation is defined as:

$$\lambda = \sqrt{r_m \sigma_i} = \sqrt{\frac{r_m}{r_l}}, \quad (3.22)$$

which determines the distance along the cell over which an injected potential drops by a

factor of e . The *time constant* τ , defined as

$$\tau = r_m c_m, \quad (3.23)$$

determines the time duration for an injected potential to drop by a factor of e . The space and time constants are useful parameters which are used to measure and characterise properties of specific excitable tissue [Roth, 1997].

Instead of passive membrane resistance, currents due to active ion channels may be substituted in place of the passive transmembrane current: such that:

$$i_r = \sum i_{ions},$$

where each i_{ion} represents transmembrane current due to the movement of specific ion types carrying charge. Then, the passive cable equation can be rewritten as

$$\sigma_i \frac{\partial^2 V_m}{\partial x^2} = c_m \frac{\partial V_m}{\partial t} + \sum i_{ions}. \quad (3.24)$$

3.4.2 The monodomain model

The monodomain equation for the transmembrane potential $V_m(x, t)$ is an extension of the *cable equation*, presented in the previous section, due to the work of Hodgkin and Huxley on the giant squid axon [Hodgkin and Huxley, 1952]. The equation relates the spatial diffusion of the transmembrane potential with the reaction terms that govern the transmembrane potential locally. In one dimension, the monodomain equation coupled with time-dependent active ion channel kinetics $I_{ion}(t)$ and external stimulus $I_{stim}(t)$,

can be described as follows:

$$\sigma_i \frac{\partial^2 V_m}{\partial x^2} = \beta \left(C_m \frac{\partial V_m}{\partial t} + I_{ion}(t) - I_{stim}(t) \right), \quad (3.25)$$

where σ_i is the effective intracellular conductivity, β is the surface to volume ratio of the tissue and $C_m = 1\mu F/cm^2$ is the capacitance of the membrane. The equation can be simplified by reducing the number of parameters; this can be done by dividing through by β and C_m , and defining

$$D = \frac{\sigma_i}{\beta C_m},$$

$$D \frac{\partial^2 V_m}{\partial x^2} = \frac{\partial V_m}{\partial t} + \frac{1}{C_m} (I_{ion}(t) - I_{stim}(t)), \quad (3.26)$$

The monodomain equation is frequently presented in this form, and D is described as the *diffusion coefficient*, with a typical value of $0.001 cm^2/ms$. This diffusion coefficient is also defined in [Kléber and Rudy, 2004, p.440], as $D = \frac{1}{C_m \beta R_i}$, where R_i is the effective intracellular resistivity. Simulations of the 1D monodomain model have been described by the group of Yoram Rudy [Rudy and Quan, 1987, 1991, Shaw and Rudy, 1997].

Gap junctions are not treated explicitly within this model; for a detailed discussion of gap junctions within cable models see a detailed exploration by [Shaw and Rudy \[1997\]](#) and Chapter 7. Within the monodomain model, gap junctional resistivity is assumed to be homogenised over the length of the cell, resulting in the effective diffusion coefficient D .

3.4.3 The bidomain model

The bidomain model [Henriquez, 1993] [Tung, 1978] is a phenomenological model which attempts to encapsulate single cell ion channel behaviour within a homogenised representation of cardiac tissue which covers a large number of identical myocytes. The assumption of the model is that two continuous domains co-exist at every spatial point: an intra- and an extra-cellular potential, which are vector fields in space and time. A rigorous mathematical derivation of the bidomain model has been carried out by Neu and Krassowska [1993]. There are alternative mathematical formulations of the bidomain equations; the standard version, presented here, is from Henriquez [1993]. Let $\sigma_{i,e}$ represent the conductances of the intracellular and extracellular space respectively, and using the notation above for the types of electrical potential, we have the following expressions for current density \mathbf{J} in each domain from Ohm's law:

$$\mathbf{J}_{i,e} = -\sigma_{i,e} \nabla \phi_{i,e}. \quad (3.27)$$

The change in current density in each domain is equal to the current flow across the membrane.

$$-\nabla \cdot \mathbf{J}_i = \nabla \cdot \mathbf{J}_e = A_m I_m, \quad (3.28)$$

where A_m is the surface to volume ratio of the cell membrane, and I_m is the transmembrane current density per unit area. Combining both above equations:

$$\nabla \cdot (\sigma_i \nabla \phi_i) = A_m I_m, \quad (3.29)$$

$$\nabla \cdot (\sigma_e \nabla \phi_e) = -A_m I_m. \quad (3.30)$$

The left hand side of these equations sum to zero, giving an expression:

$$\nabla \cdot (\sigma_i \nabla \phi_i) = -\nabla \cdot (\sigma_e \nabla \phi_e). \quad (3.31)$$

Subtract $\nabla \cdot (\sigma_i \nabla \phi_e)$ from both sides, giving

$$\nabla \cdot (\sigma_i \nabla \phi_i) - \nabla \cdot (\sigma_i \nabla \phi_e) = -\nabla \cdot (\sigma_e \nabla \phi_e) - \nabla \cdot (\sigma_i \nabla \phi_e) \quad (3.32)$$

, then, using the notation $V_m = \phi_i - \phi_e$:

$$\nabla \cdot (\sigma_i \nabla V_m) = -\nabla \cdot ((\sigma_i + \sigma_e) \nabla \phi_e). \quad (3.33)$$

Then, substituting Equation (3.29) in to the monodomain equation given by Equation (3.25):

$$\nabla \cdot (\sigma_i \nabla \phi_e) = \beta(C_m \frac{\partial V_m}{\partial t} + I_{ion}). \quad (3.34)$$

Subtracting and adding $\nabla \cdot (\sigma_i \nabla \phi_e)$, and again using $V_m = \phi_i - \phi_e$:

$$\nabla \cdot (\sigma_i \nabla V_m) = \beta(C_m \frac{\partial V_m}{\partial t} + I_{ion}). \quad (3.35)$$

Combining these two results from Equations (3.33) and (3.35) and including the option to add a time and space dependent stimulus $I_s(x, t)$ from either the extracellular or transmembrane domain, the bidomain model is obtained:

$$\nabla \cdot (\sigma_i \nabla V_m) = -\nabla \cdot ((\sigma_i + \sigma_e) \nabla \phi_e) + I_{s_1}, \quad (3.36)$$

$$\nabla \cdot (\sigma_i \nabla V_m) = \beta(C_m \frac{\partial V_m}{\partial t} + I_{ion}) - I_{s_2}, \quad (3.37)$$

where β is the surface to volume ratio of the cell membrane, $\sigma_{i,e}$ are the intracellular and

extracellular conductivities, C_m is a membrane capacitance per unit area, I_{ion} is the sum of all ionic currents calculated from a cellular AP model (see Section 2.4.1), and I_{s_i} is the external stimulus.

It should be noted that the bidomain model can be reduced to the monodomain model under two special cases: when the extracellular potential can be ignored due to an infinite extracellular conductivity, and when the anisotropy ratios between effective intracellular and extracellular conductivities are identical [Hunter and Pullan, 2003]. In this latter case, the intracellular and extracellular conductivities are proportional, and can be related via:

$$\sigma_e = \lambda \sigma_i$$

Then, substituting in to Equation (3.36), the following expression is obtained:

$$\nabla \cdot \left(\frac{\lambda}{1 + \lambda} \sigma_i \nabla V_m \right) = \beta \left(C_m \frac{\partial V_m}{\partial t} + I_{ion} \right) - I_{s_2}, \quad (3.38)$$

which is identical to the monodomain equation if one chooses an effective conductivity $\sigma = \frac{\lambda}{1 + \lambda} \sigma_i$.

Similar to the monodomain model, the bidomain model does not explicitly model gap junctional conductances. GJ conductances are combined with cytoplasmic resistivity to obtain an effective diffusivity. In Chapter 7, an alternative ‘bidomain’ type model of discrete cells will be described, which separates gap junctional resistivity from cytoplasmic resistivity.

3.5 Numerical implementation

In this section, some discussion underlying the choice of numerical method is presented, followed by an outline of the finite difference implementation used in this thesis.

3.5.1 Numerical methods for continuum cardiac tissue models

Computing the solution of continuum tissue models, such as the monodomain and bidomain equations, are applications of numerical solutions to Poisson's Equation [Clayton et al., 2010], coupled with inhomogeneous source terms representing the transmembrane voltage change at each point in space due to membrane capacitance, the sum of ionic currents and an optional external stimulus current.

Numerical techniques for solution of the cardiac tissue model in a continuous domain are briefly introduced in the sections below.

Finite difference method

The finite difference method (FDM) subdivides the domain in to a grid of points, with some spacing Δx which may vary over the domain. The solution is defined at each point, and a discrete approximation to differential operators such as ∇ and ∇^2 may be constructed at every point, based on a Taylor series expansion of the solution. At domain boundaries, techniques such as ghost pointing or one sided derivatives are used in approximating boundary conditions such as a no-flux boundary condition.

FDM is the most straightforward numerical method to implement due to its simplicity, and many cardiac electrophysiology modelling studies utilise the method in regular shaped, static domains such as slabs or strands of cardiac tissue [Shaw and Rudy, 1997].

The FDM is difficult to implement in irregular shaped domains, as it is a challenge to accurately represent domain boundaries.

Finite element method

The Galerkin finite element method (FEM) subdivides the domain in to a grid of small elements (typically regular shapes such has triangles and quadrilaterals in 2D, and tetrahedrons and hexahedrons in 3D) which vary in shape and size. Within each element, the function is assumed to be smooth and differentiable, and permits a solution which is constructed from a set of basis functions of a given order, which spans the solution space. At the boundaries between internal elements in the domain, the solution is assumed to be continuous.

The FEM is a widely used technique on which most commercial structural mechanics tools are based. It is used in preference to FDM for solving problems on complex geometries, as it is more straightforward to work with irregular grids. However, the setup time and cost to construct an FEM model is higher than for an FDM implementation. Studies that utilise the FEM are typically carried out using bespoke numerical packages developed by research units in collaboration, such as the Henriquez group [[Jacquemet et al., 2009](#), [Stinstra et al., 2006](#)] with CardioWave, CHASTE by University of Oxford [[Mirams et al., 2013](#)] and CARP [[Vigmond et al., 2003](#)].

Finite volume method

The finite volume method (FVM) subdivides the domain in to small volume elements, similar to that of FEM. Volume integrals of the partial differential equation with a divergence component are converted to surface integrals via the divergence theorem, and fluxes are obtained on the surface of each element. The flux leaving one volume element

and entering the adjacent element are identical, which allows conservation laws to be applied. Finite volume methods have been used in cardiac EP modelling, by the groups of Henriquez [[Harrild and Henriquez, 1997](#)] and Johnston et al [[Johnston, 2010](#)].

Spectral/ hp element method

Higher order finite element methods are recently developed numerical techniques for solving partial differential equations [[Karniadakis and Sherwin, 1999](#)]. They also known as Spectral or hp element methods, where h refers to the ability to refine the mesh size, and p refers to using higher order polynomials to approximate the solution within each element. Higher order polynomials exponentially converge to the final solution, which can offer a significant time saving in computation time. However, setup time using these methods are higher than simple FDM or FEM method.

Implementation of spectral/ hp methods in 3D have recently been published by [Cantwell et al. \[2011a,b\]](#); the work of [Arthurs et al. \[2012\]](#) indicates that higher order finite element methods may become a regular tool for solving the equations of cardiac electrophysiology.

Computation cost and challenges

Within the theoretical cardiac electrophysiology field, the focus on 3D whole heart modelling has led to an increase in demand for computational resources [[Clayton et al., 2010](#), [Lines et al., 2003](#), [Trayanova, 2011](#)]. Simulations of a single heartbeat in a whole heart model require hours of computation, and thus new efficient computational methods or methods to simplify cardiac EP equations form important topics of research [[Sundnes et al., 2009](#), [Qu and Garfinkel, 1999](#), [Johnston, 2005](#)].

It remains important, however, to validate the results from computation simulations

to real data. Many assumptions are made in large-scale tissue models, which need to be addressed in order to make computational results physiologically significant. These include, for example, the assumption that identical cell types exist across the entire heart, and the absence of other cell types such as fibroblasts or myofibroblasts, which are known to couple with tissue. The effects of computational mesh size on propagation dynamics (conduction velocity) is also significant [Clayton et al., 2010], and it is important to choose a spatial discretisation that does not impact on the physiological result.

3.5.2 Monodomain implementation

The monodomain equation is discretised using a central difference spatial scheme and implicit (backward Euler) time solver, with time steps of Δt and space steps of Δx respectively. The finite difference stencil is shown in Figure 3.4.

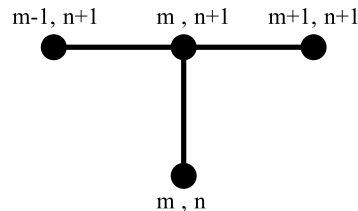


Figure 3.4: Finite difference stencil used in monodomain solver

Membrane currents are calculated at each time point using the Rush–Larsen algorithm in the previous section. Defining the parameters:

$$\epsilon = \frac{\Delta t}{C_m}, \quad D' = \frac{\sigma_i \Delta t}{\beta C_m (\Delta x)^2},$$

the monodomain equation (3.25) is discretised into the following system:

$$-D' u_{m+1}^{n+1} + (1 + 2D') u_m^{n+1} - D' u_{m-1}^{n+1} = u_m^n - \epsilon (I_{ion_m}^{n+1} - I_{stim}^{n+1}) \quad (3.39)$$

$I_{ion_m}^{n+1}$ is the sum of various ionic currents within the cell ODE model at point m and time $n + 1$, and I_{stim}^{n+1} is the stimulus current in the cable. An initial stimulus of $200mV$ lasting $0.5ms$ is applied to the first ‘cell’ in the cable.

To avoid acute fluctuations in action potential behaviour due to changes in pacing rate, every ‘cell’ within the cable is set to initial conditions obtained by ‘pre-pacing’ a single cell to steady state at $2Hz$ [Sato et al., 2009], and using the parameter output from the final iteration. This reduces the simulation time required to pace the cable to a steady state solution.

Boundary conditions are modelled as no-flux conditions at the beginning and the end of the cable. Simulations are implemented in Matlab, for a chain of n cells of length $120\mu m$. Spatial and temporal discretisation of the domain were varied when investigating the numerical accuracy of the system. For physiological investigations, a spatial discretisation of $\Delta x = 6\mu m$ and temporal discretisation of $\Delta t = 0.02ms$ was used. Within the literature, a spatial discretisation of $125 - 250\mu m$ temporal discretisation of $0.01 - 0.1ms$ is used [Sato et al., 2009].

Setting up the finite difference matrix

For the Laplacian operator, the 2nd order central difference approximation is used.

$$\frac{\partial^2 V_j}{\partial x^2} \approx \frac{V_{j+1} - 2V_j + V_{j-1}}{(\Delta x)^2},$$

where $V_{j,m}$ denotes the potential V_j , $j = i, e$ at the point m . Then, at steady state ($\frac{\partial V}{\partial t} = 0$), the discretised equation with constant transmembrane resistance $I_{ion} = (V_i - V_m)/R_m$

becomes for any given point m ,

$$V_{im} - V_{em} = \frac{R_m}{pr_i} \frac{V_{im+1} - 2V_{im} + V_{im-1}}{(\Delta x)^2} = -\frac{R_m}{pr_e} \frac{V_{em+1} - 2V_{em} + V_{em-1}}{(\Delta x)^2} \quad (3.40)$$

The standard central difference stencil with tri-diagonal bands is used to set up the initial mass matrix for both the intracellular voltage V_i and the extracellular voltage V_e ,

$$\begin{pmatrix} -2 & 1 & & & \\ 1 & -2 & 1 & & \\ & 1 & -2 & 1 & \\ & & \ddots & & \\ & & 1 & -2 & 1 \\ & & & 1 & -2 & 1 \\ & & & & 1 & -2 \end{pmatrix}$$

The no-flux boundary conditions at either end of the cable are implemented by considering a ghost point on the outside of the domain. Thus letting subscript 1 represent the end of the domain and subscript 0 the ghost point, the no-flux condition can be approximated:

$$\frac{\partial V}{\partial x} = 0 = \frac{V_0 - V_1}{\Delta x} \Rightarrow V_0 - V_1 = 0$$

The expression $V_0 = V_1$ is incorporated within the Laplacian mass matrix, and similarly at the end of the domain. Thus the new mass matrix becomes:

$$\begin{pmatrix} -1 & 1 & & & \\ 1 & -2 & 1 & & \\ & 1 & -2 & 1 & \\ & & \ddots & & \\ & & 1 & -2 & 1 \\ & & & 1 & -2 & 1 \\ & & & & 1 & -1 \end{pmatrix}$$

3.6 Post-processing

This section discusses and describes the numerical algorithms used to post process the simulation results in to data which can be interpreted physiologically.

3.6.1 Calculation of the virtual electrogram

Derivation of the formula for the virtual electrogram is presented in [Plonsey and Barr \[2007\]](#), based on Poisson's equations for a continuous smooth domain. The expression used to calculate the virtual electrogram within this thesis is from [Sato et al. \[2009\]](#). For a domain with a smoothly varying transmembrane potential $V(\mathbf{x}, t)$, the virtual electrogram at time t' can be measured at point $\mathbf{x} = (x', y', z')$. The equation is given by:

$$\Phi(x', y', z', t') = \int_L D(\nabla V(\mathbf{x}, t'))(\nabla(1/R))dx, \quad (3.41)$$

where R is Euclidean distance of each point from the location of the virtual electrode.

3.6.2 Determining electrical properties of the tissue

Determining the cardiac conductivity to use as a parameter in monodomain or bidomain simulations is important to correctly model cardiac conduction. There have been a wide range of values reported for these parameters in experiments on mammalian ventricular tissue, e.g. from [Clerc \[1976\]](#) and [Roberts et al. \[1979\]](#), [Roberts and Scher \[1982\]](#), with no clear consensus on the appropriate value [\[Roth, 1997\]](#).

Multiple theoretical approaches have sought to determine these parameters through simulation. [Hand et al. \[2009\]](#) looked to estimate the cardiac conductivity via homogenisation of regularly structured microscopic domains with gap junctions, and obtained values dependent on the lattice structure chosen. [Stinstra et al. \[2005\]](#) constructed a finite element model of passive coupled cells in extracellular spaces, and simulated current flow due to an external electrical field - these were used to build the effective conductivity tensors. These theoretical models used experimentally measured cytoplasmic conductivities combined with gap junctional conductances reported in literature; the effective intracellular conductivities were shown to be sensitive to the cytoplasmic conductivity, average length and cross sectional area of the myocytes chosen, which are parameters not considered in continuum models.

Several of the different electrical conductivities reported in the literature are reported in Table 3.1. As can be seen, there is a wide range of values reported, and the anisotropy ratios in both intracellular and extracellular conductivities also vary between publication.

Reference	$\sigma_{i,l}$	$\sigma_{i,t}$	$\sigma_{e,l}$	$\sigma_{e,t}$
Clerc [1976]	1.7	0.2	6.3	2.4
Hand et al. [2009] (Aligned)	1.01	0.03	3.0	1.56
Hand et al. [2009] (Brick-like)	1.40	0.03	3.0	1.56
Stinstra et al. [2005]	1.6	0.05	2.1	0.6
Hooks [2007]	2.63	0.263	2.63	2.45
MacLachlan et al. [2005]	3.0	1.0	2.0	1.65
Roberts and Scher [1982]	3.4	0.60	1.2	0.8
Roberts et al. [1979]	2.8	0.26	2.2	1.3
Roth [1997]*relative dimensionless values	1.0	0.1	1.00	0.40

Table 3.1: Intracellular (σ_i) and extracellular (σ_e) longitudinal (l) and transverse (t) conductivities values reported in different theoretical and experimental publications. Units are in mS/cm , except the parameters reported by Roth in the final row which are dimensionless.

3.7 Discussion

In this section, the theoretical background for models of cardiac electrophysiology was established, including the introduction of single cell action potential models and the continuum tissue model.

Two existing models of single cell electrical activity were presented - the phenomenological Cherry–Fenton model [Cherry and Fenton, 2004] and the Luo–Rudy I model [Luo and Rudy, 1991]. The Cherry–Fenton model was used to establish and test the accuracy and efficiency of the numerical PDE solver developed in Chapter 5, whilst the Luo–Rudy I model was subsequently used in the primary physiological investigation. The Rush–Larsen algorithm for fast simulation of single cell ODE models was presented.

Continuum models of excitable tissue were then described, after an initial derivation of the cable equation, leading to description of the monodomain and bidomain equations. These two representations of cardiac tissue are the primary models used within the com-

putational cardiology literature [Clayton et al., 2010]. The existing numerical methods for solution of the monodomain and bidomain equation was discussed, before an outline of the second order finite difference solver implemented in the thesis was presented. This code formed the basis for the investigations in Chapter 5 and 7.

The post-processing of the virtual electrogram was briefly outlined and described, as the primary method to translate and compare between theoretical simulation and clinical data. Finally, the challenges of accurately determining physiological parameters for use in theoretical simulations of cardiac tissue was discussed, with a large variation in reported values within the literature. The lack of consensus between published literature formed a motivation for the experimental work in the following Chapter, to measure and determine macroscopic conduction properties in samples of guinea pig cardiac tissue.

Part I

**Measuring and calculating
macroscopic conduction properties
in intact myocardial tissue**

4 Measuring conduction properties in a guinea pig papillary muscle model	87
4.1 Introduction	87
4.2 Materials and methods	88
4.2.1 Materials	88
4.2.2 Preparation of papillary muscle samples	89
4.2.3 Impedance dish design and setup	91
4.2.4 Protocol for measuring tissue impedance properties	93
4.3 Microelectrode recordings	97
4.3.1 Description of setup	99
4.3.2 Measurement of intracellular action potentials	100
4.3.3 Measurement of longitudinal conduction velocity	102
4.3.4 Calculation of intracellular resistivity	102
4.3.5 Effect of carbenoxolone on longitudinal conduction velocity	102
4.4 Results	103
4.4.1 Impedance measurements	103
4.4.2 Intracellular recordings	105
4.4.3 The effect of modulating resistivity on conduction velocity	106
4.5 Discussion	108
4.5.1 Measured passive tissue resistivity	109
4.5.2 Physiological range of resistivities from carbenoxolone modulation	110
4.5.3 Physiological range of conduction and breakdown of cable theory	110
5 The effect of modulating conductivity in a continuum model of conduction	112
5.1 Introduction	112
5.2 Methods	114
5.2.1 Implementation of numerical model	114
5.3 Results	116
5.3.1 Simulation duration and accuracy	116
5.3.2 Modulation of physiological parameters	118
5.3.3 Action potential foot τ_{ap}	122
5.3.4 Electrogram	122
5.4 Discussion	123
5.4.1 Numerical accuracy	123
5.4.2 Modulation of physiological parameters	124
5.4.3 Range of parameter modulation compared with experiment	125

Chapter 4

Measuring conduction properties in a guinea pig papillary muscle model

4.1 Introduction

In this chapter, the impedance of normal guinea pig (GP) papillary muscle, a cylindrical shaped tissue found on the endocardial surface, is analysed using impedance spectroscopy [Macdonald, 1992] within an oil-gap experimental setup [Cooklin et al., 1997], in order to obtain physiological parameters for the averaged intracellular resistivity described in the passive 1D cable equation. This aims to validate the intracellular resistivity values reported in the literature, and to investigate the natural variation of resistivity values, within the physiological range. This data was collected with the assistance of Dr Paramdeep Dhillon (Imperial College London), Ms Samantha Salvage (University of Surrey) and Prof Chris Fry (University of Surrey). The values obtained are combined with functional AP studies using the micro-electrode impalement technique, carried out by Dr Paramdeep Dhillon, to form a basis for theoretical investigation of action potential propagation in a 1D cable of tissue in the next chapter.

4.2 Materials and methods

This section outlines the materials and methods used for impedance measurements of guinea pig papillary muscle. Measurements were carried out using a three-chambered impedance dish filled with either Tyrode's solution or mineral oil. All experimental work in this chapter was carried out at University of Surrey, unless otherwise stated.

4.2.1 Materials

Solutions

A Tyrode's solution was used for dissection, incubation and superfusion of the papillary muscle. Table 4.1 details the composition of the solution. All chemicals were obtained from Sigma-Aldrich, unless otherwise stated. The solution was made as a 10x stock solution and diluted to 1x prior to use. The final solution was bubbled with a mixture of 95% O_2 /5% CO_2 , pH 7.35 at $36 \pm 0.5^\circ C$.

Compound	Concentration (mM)
$NaCl$	118
KCl	4.0
$NaHCO_3$	24
$NaH_2PO_4H_2O$	0.4
$MgCl_26H_2O$	1.8
Glucose	6.1
Sodium pyruvate	5.0
$CaCl_2H_2O$	1.88

Table 4.1: Composition of Tyrode's solution .

Animals

Male Dunkin–Hartley guinea pigs, weighing 420-550g, were culled by cervical dislocation in accordance with the Guidance on the Operation of the Animals (Scientific Procedures)

Act 1986. The heart was quickly excised and placed in warm oxygenated Tyrode's solution and transported to the laboratory for dissection.

Carbenoxolone

Carbenoxolone is a synthetic derivative of glycyrrhetic acid, previously shown to be a successful gap junction uncoupler [Dhein, 2004]. It has been used in recent studies to reduce conduction velocity without alteration of ion currents [De Groot et al., 2003, Ng, 2011]. In the present study, carbenoxolone (CBX) was used as a tool for pharmacological uncoupling of GJs, to examine the relationship between GJ conductance and conduction velocity (CV).

Carbenoxolone sodium (Sigma, USA) was dissolved in Tyrode's solution to a concentration of between 10 to 50 μM .

4.2.2 Preparation of papillary muscle samples

Following sacrifice, the heart was transferred to a dissection dish containing warm oxygenated Tyrode's solution, fixed to the silicone elastomer base (Sylgard 184; Dow Corning, East Kilbride, Glasgow) and placed under a dissection microscope (Nikon). The dish was refreshed every 5–10 minutes with clean Tyrode's solution, during the dissection process.

The interior of the left ventricle was exposed by identifying the inter-ventricular septum and dissecting through the posterior ventricular wall following lines lateral to the septum. The resultant flap of left ventricular free wall was secured to the silicone base, which exposed the papillary muscles on the endocardial surface, attached to the chordae tendinae network of the mitral valve. This is shown in Figure 4.1.

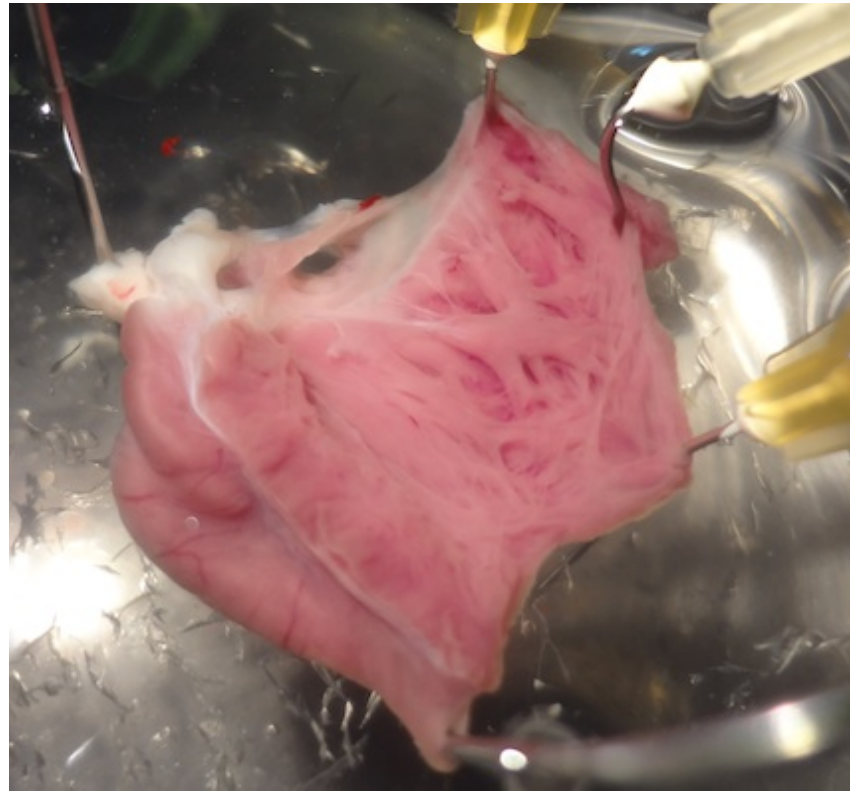


Figure 4.1: The interior of the left ventricle was exposed to extract papillary muscle preparations within the guinea pig. The papillary muscles, roughly cylindrical in shape, are intertwined and are attached to the white chordae tendinae of the mitral valve along the base of the left ventricle.

Suitable papillary muscle preparations were identified and trimmed along the diameter of the muscle where appropriate. Silk tie (D1550, Dixey Instruments Ltd, UK) was slid under each papillary muscle and a knot was tied on each end of the muscle, to be used for subsequent tissue mounting. Following this, the papillary muscle was extracted from the ventricle by dissecting through the chordae tendinae and the end of the muscle near the apex of ventricle. The final preparations were approximately cylindrical in shape, with a length of 5 – 7mm and < 1mm in diameter (Figure 4.2).



Figure 4.2: A guinea pig papillary muscle preparation. The preparations were approximately cylindrical in shape, length of $5 - 7\text{mm}$ and $< 1\text{mm}$ in diameter.

4.2.3 Impedance dish design and setup

Papillary muscle preparations were transferred to a three-chambered tissue bath for measurement of intracellular impedance (see Figure 4.3).

The dish consisted of two Perspex three-sided chambers ($1\text{cm} \times 1.5\text{cm} \times 2\text{cm}$), to which a rubber membrane (Latex glove tip, Semper guard, Semperit, Vienna) was attached, creating a natural fourth side. The two chambers were filled with Tyrode's solution and placed on a brass bass plate with an adjustable positioning screw, separated by a narrow Perspex partition spacer, which formed the central chamber (Figure 4.4). Two tight holes were punctured in the rubber membranes, and the preparation was pulled through these holes, such that it spanned the central chamber, with approximately 1mm of each end lying in the outer chambers containing the Tyrode's solution.

Tissue which was visibly damaged was discarded. Tyrode's solution in the middle chamber was removed and the preparation was coated in mineral oil (Vaseline), creating a high external resistance pathway. The entire dish was placed on a heating block, maintained at $34.5 \pm 1.5^\circ\text{C}$, monitored by a temperature probe.

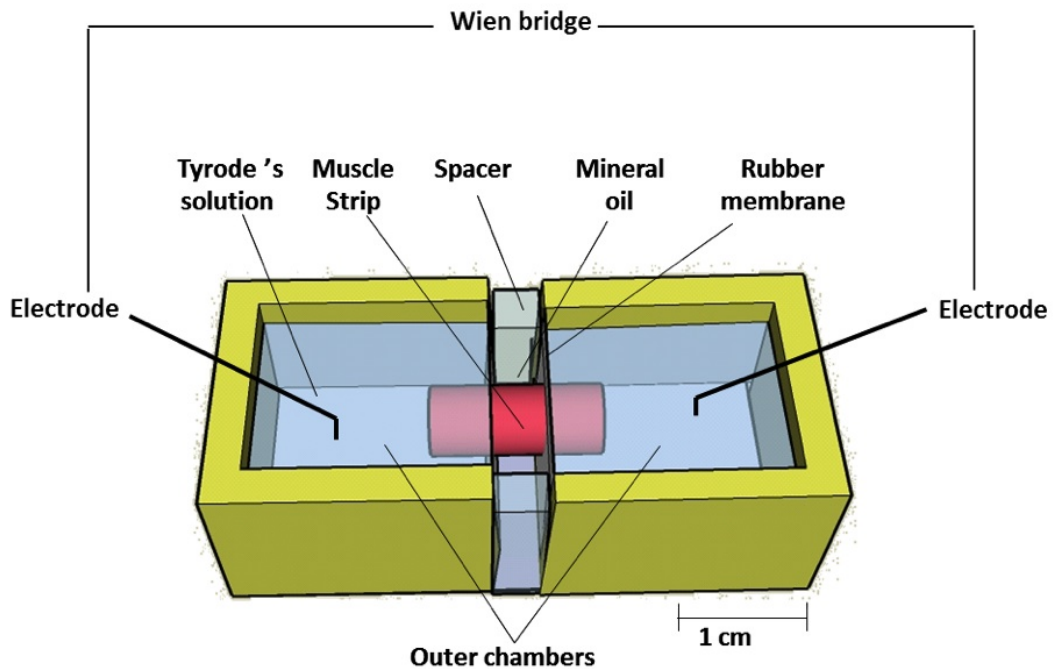


Figure 4.3: The Wien bridge setup is constructed using a three chambered bath as shown in the schematic above. The chambers are separated by rubber membranes through which the muscle preparations are secured. Platinum black electrodes were placed in the outer chambers. Image courtesy of Miss Sam Salvage, University of Surrey.

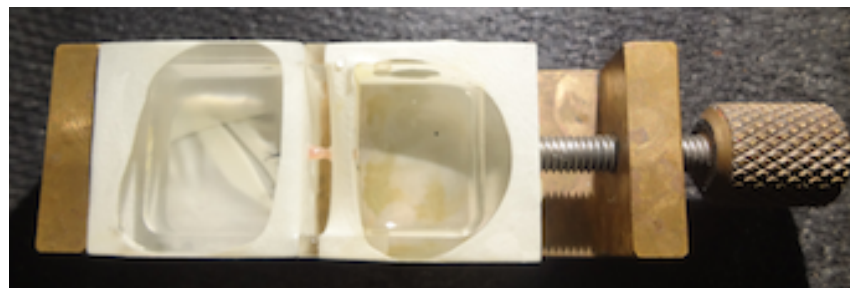


Figure 4.4: The impedance chamber dish with a preparation inserted.

Platinum black electrodes

Platinum wires were coated in platinum chloride to increase its effective surface area and polarisation capacitance. This minimised drift due to build-up of surface charge [Cooklin et al., 1997].

4.2.4 Protocol for measuring tissue impedance properties

Protocol for impedance measurements

Alternating current ($0.2 - 300\text{kHz}$, 10mV peak-to-peak) was applied via platinum black electrodes, described above, to either end of the preparation in the outer chambers. The resistance and capacitance of the system were recorded with a balanced Wien bridge (Wayne Kerr 6430B) [Cooklin et al., 1997]. Measurements were taken across the frequencies returning to 1kHz at regular intervals, which determined the stability of the recording system (Figure 4.5).

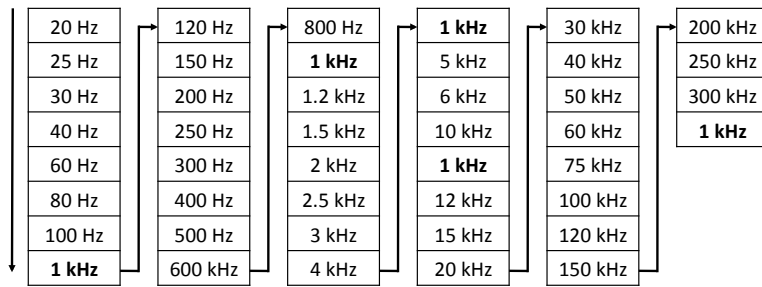


Figure 4.5: Intracellular impedance stimulation protocol.

The protocol was applied twice, several minutes apart. The mean value of the measurements was used. The extracellular shunt of the preparation was measured in the middle chamber, using fine platinum black electrodes placed a known distance apart.

Following the electrical measurements, the length and width of the preparations within the oil-gap were measured under the dissection microscope using a graticule, to determine cross-sectional area [Cooklin et al., 1997]. Platinum black electrode impedance and phase angle measurements were carried out over the same frequency range in a volume of Tyrode's solution at the end of each experiment, for subtraction of electrode properties

from the measurements in post processing of electrical data.

The impedance protocol was conducted using an automated process via the CircleSE v.11 software (JS Young and R Young). CircleSE controlled the Wien bridge and measured programmed frequencies, recorded raw data and carried out correction calculations (see section below) to generate the final values for longitudinal resistance and reactance based on tissue dimensions.

Calculation of intracellular resistive and reactive components

The Wien bridge experimental setup recorded resistance r and capacitance c values for the impedance system. Corrective calculations were required to extract the longitudinal resistivity due to gap junctions r_j , membrane r_m and intracellular conductivity r_c , based on the measured RC circuit being an equivalent circuit of the canonical model [Dhillon \[2010\]](#). The canonical model for the experimental oil–gap chamber preparation is shown in Figure 4.6. Impedance contributions were due to the following:

- The platinum black electrodes z_p , modelled as a series circuit of resistance r_p and capacitance c_p ,
- The intracellular compartment of the preparation z_i , as a cytoplasm resistance r_c in series with a parallel RC circuit consisting of resistance r_j and capacitance c_j ,
- The surface membrane of the preparation z_m , as a parallel RC circuit, with resistance r_m and capacitance c_m ,
- The extracellular resistance shunt around the preparation, r_{ec} .

Resistance and capacitance values for the preparation were measured, and a correction formula was applied to evaluate longitudinal resistivity and capacitance based on the canonical model. The calculation was as follows:

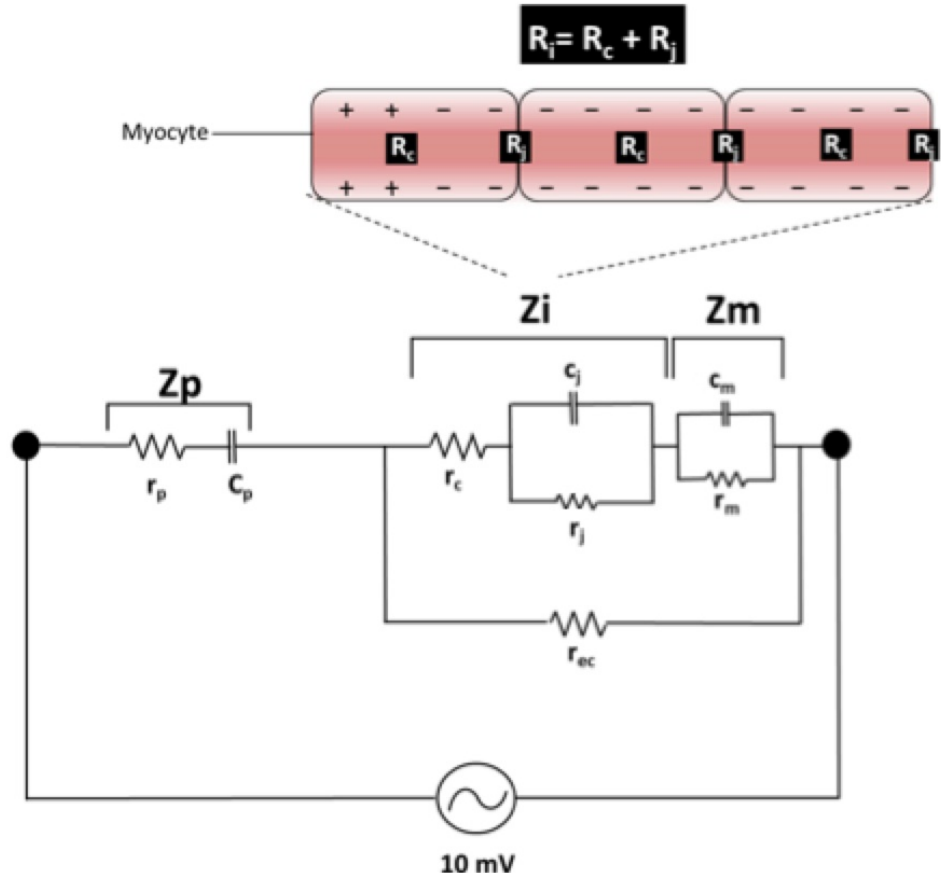


Figure 4.6: Canonical model of the tissue preparation in the oil-gap chamber, showing impedance contributions from the platinum black electrodes z_p , the intracellular compartment of the preparation z_i , the surface membrane of the preparation z_m and extracellular resistance shunt around the preparation, r_{ec} . Platinum black electrodes are modelled as a series circuit of r_p and c_p ; the intracellular impedance is modelled as a cytoplasm resistance r_c in series with a parallel RC circuit consisting of resistance r_j and capacitance c_j . The surface membrane is modelled as a parallel RC circuit, with resistance r_m and capacitance c_m . Image reproduced with permission from Ms Samantha Salvage.

1. The parallel RC circuit resistance r_e and capacitance c_e of the platinum black electrode were measured by the Wien bridge. This was converted to the series circuit r_p and c_p using

$$r_p = \frac{r_e}{(1 + r_e \omega c_e)^2}; c_p = c \left(1 + \frac{1}{(r_e \omega c_e)} \right), \quad (4.1)$$

where $\omega = 2\pi f$ is the radial frequency and f is the measuring frequency.

2. The total tissue impedance across the preparation, z_h , including z_i , z_m and r_{ec} was defined by

$$z_h = r_h + jx_h, \quad (4.2)$$

where j is the complex number $j = \sqrt{-1}$. z_s was defined as the total impedance across the preparation ($z_s = z_i + z_m$), disregarding the contribution of extracellular shunt r_{ec} .

3. Resistance r_h and reactance x_h values of the preparation were calculated from recorded values of r and c by the Wien bridge, using the equations:

$$r_h = \frac{r}{(1 + r\omega c)^2} - r_p, \quad (4.3)$$

$$x_h = \frac{r^2\omega c}{(1 + r\omega c)^2} - \frac{1}{\omega c_p}, \quad (4.4)$$

where $\omega = 2\pi f$ is the radial frequency and f is the measuring frequency.

4. The reactance component of tissue impedance contains contributions from junctional and membrane capacitative components c_j and c_m .
5. The impedance due to extracellular shunt r_{ec} is considered to be in parallel with z_s . Thus, the measured r_{ec} , along with the total tissue impedance z_h was used to determine z_s :

$$z_h = \frac{z_s \cdot r_{ec}}{z_s + r_{ec}}. \quad (4.5)$$

6. The value of z_s (Ω/cm) was converted to specific value Z_s (Ωcm), independent of tissue dimensions via scaling to the cross sectional area (CSA) of each preparation, and the preparation of CSA occupied by muscle. The non-muscle fraction of CSA,

CSA_{ec} was calculated from the value of r_{ec} using the formula

$$CSA_{ec}[cm^2] = \frac{49[\Omega cm]}{r_{ec}[\Omega/cm]}, \quad (4.6)$$

assuming it exclusively contained Tyrode's solution with resistivity $49\Omega cm$ [Cooklin et al., 1997]. Specific values are denoted by upper case letters, R (Ωcm) and C (F/cm^2).

7. Values of Z_s were converted to R_s and $-X_s$ values, and plotted on a graph of R_s against $-X_s$ to generate a semi-circular dispersion.
8. A curve was fitted to the data by the equation of a circle:

$$(R_s - a)^2 + (X_s - b)^2 = c^2, \quad (4.7)$$

where a, b are constants giving the offsets of the centre of the circle from the origin in the $R_s - X_s$ plane, and c is the radius of the circle.

9. The two intercept values with the R_s axis were estimated. The value corresponding to the higher frequency intercept (lower resistivity) returned R_c and the lower frequency (higher resistivity) returned R_i .
10. As $R_i = R_c + R_j$, the value of R_j was calculated as the difference between the two values.

The full protocol is summarised in Figure 4.7.

4.3 Microelectrode recordings

The following experimental work described in this subsection was completed by Dr Paramdeep Dhillon [Dhillon, 2010] at Imperial College London and presented here, to

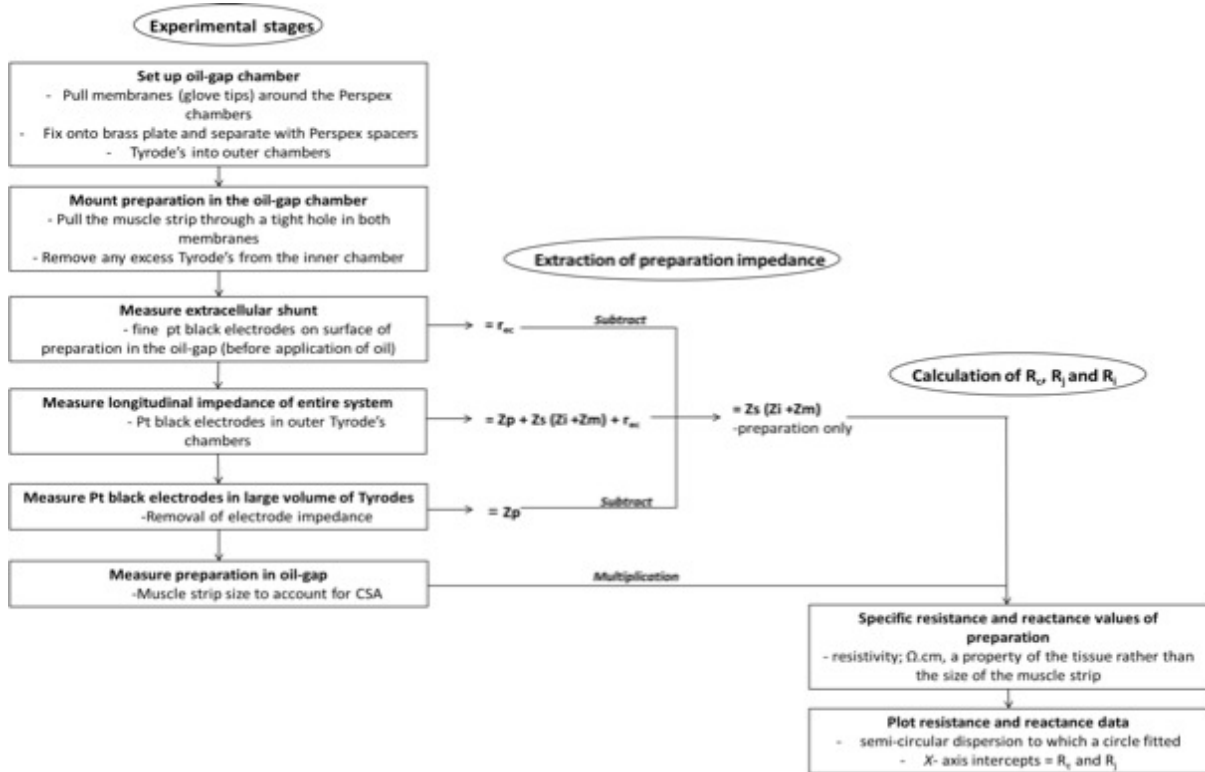


Figure 4.7: Summary of the impedance measurement protocol, and post processing of impedance values. CSA is the cross sectional area of the tissue. Image reproduced with permission from Ms Samantha Salvage.

investigate and compare results and assumptions between theoretical and experimental studies.

A microelectrode technique was established, with the aim to modulate gap junction (GJ) resistivity pharmacologically, and correlate corresponding conduction velocity measurements in guinea-pig ventricular myocardium. This was based on cable theory (Section 2.4.2) that a linear relationship exists between effective conductance and conduction velocity (CV) of excitation in myocardium.

4.3.1 Description of setup

The micro electrode recording method is summarised here; for more details please refer to [Dhillon \[2010\]](#). The experimental setup is depicted in Figure 4.8. The preparation was attached to the fixed hook and to the isometric tension transducer (Statham UC2, USA), which was mounted on a micromanipulator (Prior Instruments, UK). Preparations were superfused with Tyrode's solution through a channel 5mm in diameter. Solutions were maintained at $37 \pm 0.5^\circ C$ and bubbled with 95% O_2 /5% CO_2 . The warm Tyrode's solution was channeled through the preparation at a flow rate of 5ml/min and drained directly.

$Ag/AgCl$ electrodes were made in-house. The reference electrode was placed inside polyvinyl chloride tubing filled with 3M KCl solution and closed at one end. The stimulating electrode consisted of $Ag/AgCl$ electrodes in to each barrel of a double-barrelled glass pipette. Tips were extended beyond the end of the pipette.

Recording glass micro electrodes were constructed using a horizontal micropipette puller (Flaming/Brown P-87, Suttter Instruments Co, California), made from borosilicate glass papillaries with tip impedance of 10 – 18M Ω when filled with 3M KCl.

Preparations were either field or point stimulated. Field stimulation used flattened platinum electrodes placed in contact with the preparation. The stimulator (Digitimer DS 2, Digitimer Ltd, UK) could deliver square pulses of variable voltage; supra threshold voltages of 6 – 15V of pulse duration 1ms was used to stimulate the tissue. Point stimulation was performed using $Ag/AgCl$ wires to generate longitudinal excitation propagation, and pulse durations were kept to a minimum to reduce stimulation artefact. Samples were stimulated at 1.5 \times threshold.

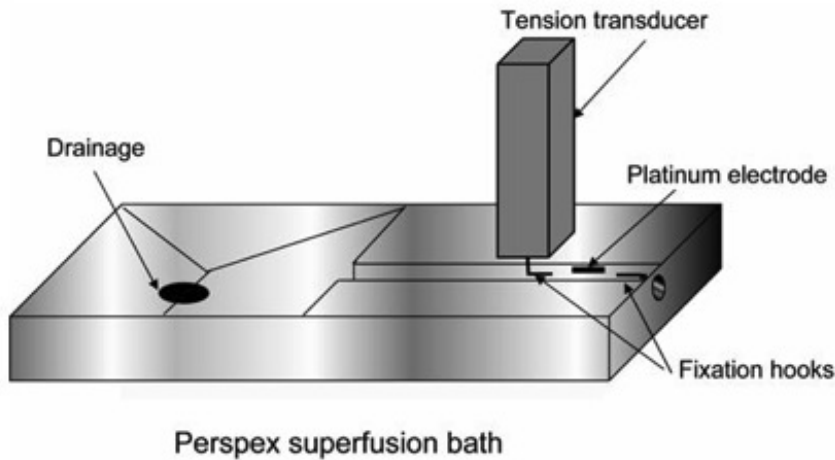
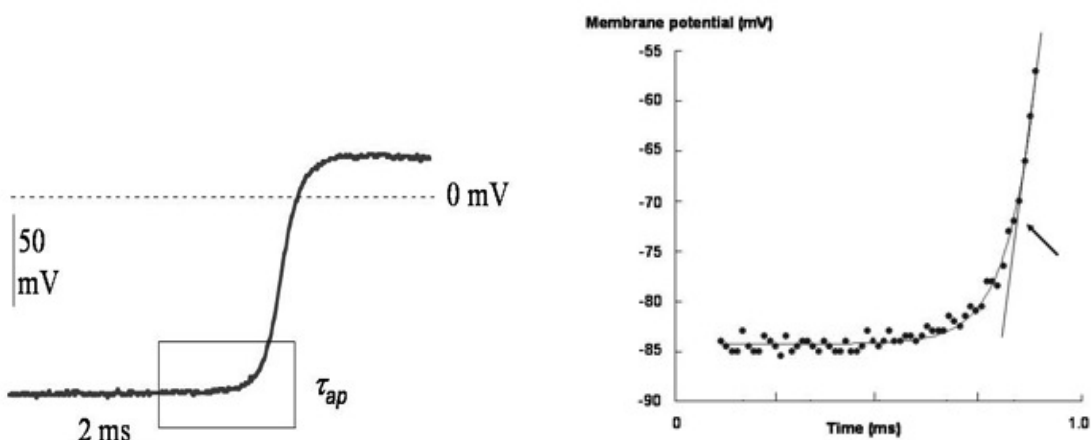


Figure 4.8: Schematic of the micro electrode setup, not to scale. Samples were attached between the two fixation hooks, with one fixed and the other connected to an isometric tension transducer. Tyrode's solution was fed through a small hole in to the bath and drained naturally. Image reproduced with permission from Dr Paramdeep Dhillon.

4.3.2 Measurement of intracellular action potentials

Following field or point stimulation, the KCl microelectrode was immersed in the superfusate, and impaled in to a cell in the muscle surface. Action potentials were measured by the potential difference between the intracellular microelectrode and the 3M KCl reference electrode in the same chamber. Potentials were recorded and amplified; outputs were stored in digitised form using the Transition software package. Noise was minimised by shielding the apparatus with a wire mesh and grounding to a common earth. A minimum of three APs were recorded at impalement sites and at least ten implements were made to measure conduction velocity. APs were recorded between frequencies of 0.2 and 2Hz.

Action potential durations at 50, 75 and 95% repolarisation (APD_{50} , APD_{75} and APD_{95}) were measured, based on AP amplitude defined as the difference between minimum and maximum values reached on phase 0 of the AP. The foot (subthreshold) of the AP was used to estimate the time constant of the upstroke, τ_{ap} . This was calculated by fitting the exponential function $V = A \exp(t/\tau_{ap})$ to the rising phase of the AP, where the membrane potential was $< -70mV$. A is a scaling constant; V is the membrane potential and t is time. The threshold potential V_{th} was calculated from the intercept between the exponential rise of the action potential foot and the linear upstroke of the AP (see Figure 4.9).



(a) The zoomed upstroke of the guinea pig; the box indicates the portion used to determine time constant of AP upstroke τ_{ap} .

(b) Threshold potential V_{th} is at the intercept (arrow) between the exponential rise of AP foot and the linear upstroke.

Figure 4.9: Calculation of τ_{ap} and V_{th} using the upstroke of recorded intracellular potentials. Images reproduced courtesy of Dr Paramdeep Dhillon.

dV/dt_{max} , the max rate of the AP upstroke was obtained by analogue differentiation of the AP upstroke.

4.3.3 Measurement of longitudinal conduction velocity

Conduction velocity (CV) along the longitudinal axis was measured by stimulating the muscle at 1Hz at $1.5\times$ threshold to minimise extracellular current spread. APs were recorded at distances $d > 1\text{mm}$ from the stimulation site. The delay t between stimulus artefact and AP upstroke was recorded. Distance d was measured with a Vernier scale on the micro manipulator and checked with an eyepiece under $40\times$ magnification. Longitudinal CV was calculated from a plot of d vs t over several values of d . Control experiments when recordings were made transverse to the long axis for fixed d showed no variation; indicating conduction was longitudinal only.

4.3.4 Calculation of intracellular resistvity

The effective intracellular resistivity R_i was calculated using the conduction velocity, θ , and the time constant of AP depolarisation, τ_{ap} by rearranging the root of the one dimensional cable equation [Dhillon, 2010, p.35]:

$$\theta^2 = \frac{a}{2R_i C_m \tau_{ap}}, \quad (4.8)$$

where a is the cell radius, and $C_m = 1\mu\text{F}/\text{cm}^2$ is the specific membrane capacitance. R_i and C_m are derived from r_a , the intracellular resistance per unit length, and c_m , the membrane capacitance per unit length, via the following conversion: $R_i = r_a \pi a^2$, $C_m = c_m / 2\pi a$.

4.3.5 Effect of carbenoxolone on longitudinal conduction velocity

$20\mu\text{M}$ Carbenoxolone (CBX) was added to Tyrode's solution, to examine the effect on conduction velocity (CV).

4.4 Results

4.4.1 Impedance measurements

Papillary muscle was extracted from the guinea pig left ventricle and inserted in to the oil gap chamber as described in Section 4.2, and impedance measurements were recorded. Data was collected under the supervision and assistance of Dr Paramdeep Dhillon (Imperial College London) and Ms Samantha Salvage (University of Surrey).

An example of the measurements recorded by the Wien bridge is shown in Figure 4.10. The Wien bridge measured impedance magnitude z as a function of increasing alternating current frequency ($0.2 - 300\text{kHz}$). The graph below shows the plot of final tissue resistance (R_s) against tissue reactance ($-X_s$) following correction for extracellular shunt resistance and the platinum black electrode. The intercept of the semicircular fitted curve (red) through the x -axis returns the values for the effective total resistivity of the tissue R_i (higher resistance) and cytoplasmic resistivity R_c (lower resistance).

Effective resistivity (R_i), and cytoplasmic resistivity (R_c) values were calculated, and the junctional resistivity R_j was evaluated by taking the difference of the two. The measured values are presented in Table 4.2. Junctional resistivity R_j constitutes 73% of the total effective resistivity.

	Mean (Ωcm)	SD (Ωcm)
Effective resistivity R_i	524	45
Cytoplasmic resistivity R_c	141	27
Junctional resistivity R_j	383	17

Table 4.2: Values of effective (R_i), cytoplasmic (R_c) and junctional (R_j) resistivities in guinea pig left ventricular papillary muscle, $n = 6$.

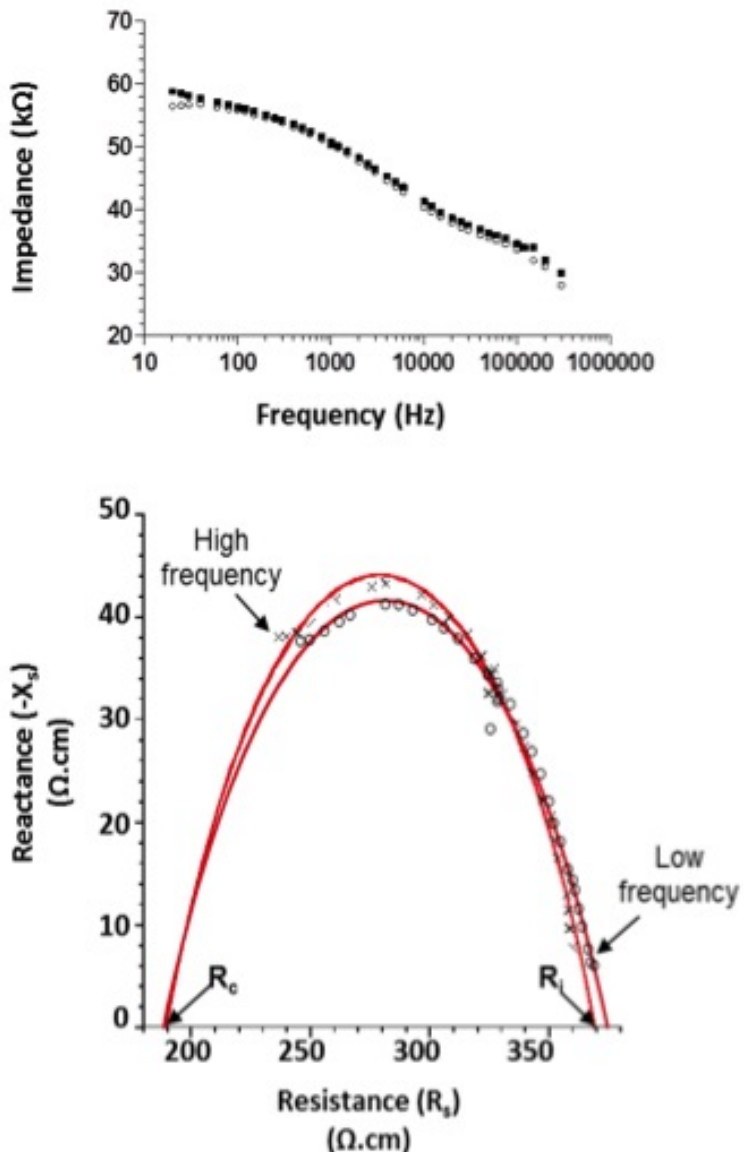


Figure 4.10: Example resistance–reactance graph plotted on Kaleida Graph software. The graph above shows impedance magnitude as a function of AC current frequency. The graph below shows two data tissue resistance (R_s) against tissue reactance ($-X_s$). The intercept of the fitted curve (red) through the x -axis returns the values for the effective total resistivity of the tissue R_i (higher resistance) and cytoplasmic resistivity R_c (lower resistance). Image reproduced with permission from Ms Samantha Salvage.

The effect of carbenoxolone on resistivity

Further resistivity and impedance measurements were carried out by Dr Paramdeep Dhillon at Imperial College London, to assess the effects of $20\mu\text{m}$ carbenoxolone (CBX)

	Left ventricle	Left atrium	Right atrium
Control			
$R_i, \Omega cm$	525 ± 50	270 ± 7	230 ± 21
$R_j, \Omega cm$	393 ± 51	147 ± 9	114 ± 21
$R_c, \Omega cm$	133 ± 13	124 ± 13	116 ± 10
20 μM CBX			
$R_i, \Omega cm$	$654 \pm 43*$	$331 \pm 22*$	$271 \pm 15*$
$R_j, \Omega cm$	$502 \pm 80*$	$187 \pm 27*$	$143 \pm 14*$
$R_c, \Omega cm$	152 ± 41	144 ± 18	127 ± 16

Table 4.3: Guinea pig tissue resistivity, in left ventricle and atrial myocardium, before and following CBX modulation (20 μM). Effective resistivity, R_i , junctional, R_j , cytoplasmic, R_c . Values: mean \pm S.D, n=6. * $p < 0.05$ CBX versus control for corresponding variables. Data courtesy of Dr Paramdep Dhillon.

for 30 minutes. The effect was measured on guinea pig papillary muscle from the left ventricle (LV), left atrium, (LA) and right atrium (RA) , shown in Table 4.3.

R_i and R_j were significantly increased by 20 μm CBX in all preparations ($p < 0.05$), whilst R_c was not significantly increased. The proportion of increase of junctional resistance (% R_j) was similar in all preparations (% $R_j = 26 \pm 16, 25 \pm 14, 28 \pm 9$ for LA, RA, LV respectively). Proportion of increase of effective resistance % R_i : (% $R_i = 22 \pm 8, 18 \pm 11, 25 \pm 10$ for LA, RA, LV respectively).

4.4.2 Intracellular recordings

Intracellular recordings and conduction velocity experiments were carried out by Dr Paramdeep Dhillon. Measurements were made on papillary muscle from guinea pig left ventricle, left atrium and right atrium.

Table 4.4 summarises action potential parameters measured in guinea pig papillary muscle preparations (n = 6). CBX slowed conduction in all preparations with no significant

effect on AP morphology, with a significantly greater slowing in LA compared to RA ($\% \theta = 23 \pm 8$ vs $11 \pm 8\%$). CBX significantly increased peak AP upstroke dV/dt_{max} in LA and LV, which was non significant in RA. τ_{ap} was unaffected.

	LV	LV (CBX)	LA	LA (CBX)	RA	RA (CBX)
V_m, mV	-89 ± 3	-87 ± 4	-75 ± 5	-81 ± 9	-71 ± 5	-72 ± 14
AP_{amp}, ms	117 ± 5	111 ± 7	105 ± 1	$117 \pm 4*$	105 ± 3	110 ± 8
$APD50, ms$	176 ± 13	170 ± 15	—	—	—	—
$APD50, ms$	—	—	57 ± 5	56 ± 7	53 ± 5	53 ± 54
$APD95, ms$	217 ± 12	214 ± 14	—	—	—	—
$dV/dt_{max}, V/s$	224 ± 34	$307 \pm 91*$	269 ± 11	$347 \pm 57*$	190 ± 34	-228 ± 56
τ_{ap}, ms	0.29 ± 0.06	0.28 ± 0.05	0.20 ± 0.02	0.20 ± 0.04	0.33 ± 0.1	0.32 ± 0.09
$\theta, cm/s$	70.9 ± 1.3	$59.2 \pm 3.1*$	78.6 ± 4.9	60.1 ± 6.1	$77.5 \pm 7/4$	$68.9 \pm 6.7*$

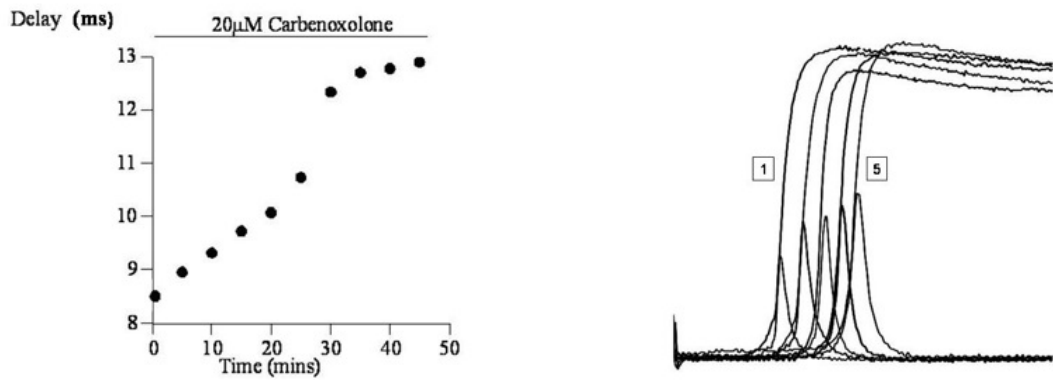
Table 4.4: Action potential parameters from guinea pig papillary muscle (n=6), left ventricle (LV), left atrium (LA) and right atrium (RA), control and after $20\mu M$ carbenoxolone (CBX). V_m : membrane potential AP_{amp} denotes action potential amplitude; $APD50$, $APD75$, $APD95$, action potential duration at 50%, 75% and 95% repolarisation. dV/dt_{max} denotes AP upstroke velocity; τ_{ap} denotes time constant of the action potential foot; θ denotes longitudinal conduction velocity. Data: mean \pm S.D, * $p < 0.05$. Images reproduced courtesy of Dr Paramdeep Dhillon.

The effect of carbenoxolone on conduction delay and action potential morphology

The effects of carbenoxolone (CBX) at different concentrations were studied. CBX was shown to achieve maximum conduction delay with $20\mu M$; concentrations greater than this had no greater effect. CBX slowed CV over a timescale of 30 minutes in all preparations, and effects were fully reversible on washout.

4.4.3 The effect of modulating resistivity on conduction velocity

Measured conduction velocities and other parameters were substituted in to Equation (4.8) to obtain estimates for resistivity values, compared to directly measured resistive



(a) Time course effect of uncoupling by CBX. Conduction delay was stable after 30–35 minutes.

(b) Peak upstroke of AP (dV/dt_{max}) due to CBX modulation, measured at 5 minute intervals.

Figure 4.11: Effect of carbenoxolone: time course effect and AP upstroke. Conduction delay increased after CBX as a function of time, up to 35 minutes. Peak AP upstroke dV/dt_{max} was gradually increased following CBX. Images reproduced courtesy of Dr Paramdeep Dhillon.

values from impedance studies. For each tissue preparation type, the average measured conduction velocity was compared with the average measured tissue resistivity. Figure 4.12 shows the relationship between measured R_i or R_j and the measured parameter a/θ^2 , with $a = 12\mu m$ for guinea pig (GP) ventricles and $a = 6.5\mu m$ in GP atrium. It was assumed that CBX had no effect on cell dimensions. Figure 4.12A shows a best fit linear relationship between a/θ^2 and R_i ; Figure 4.12B shows that GJ resistivity is the primary sub component of R_i that determines its relationship to CV variation. The x -axis intercept on Figure 4.12B is an estimate of cytoplasmic resistivity R_c at $100\Omega cm$, compared to a measured mean value of $133 \pm 19\Omega cm$ from impedance measurements.

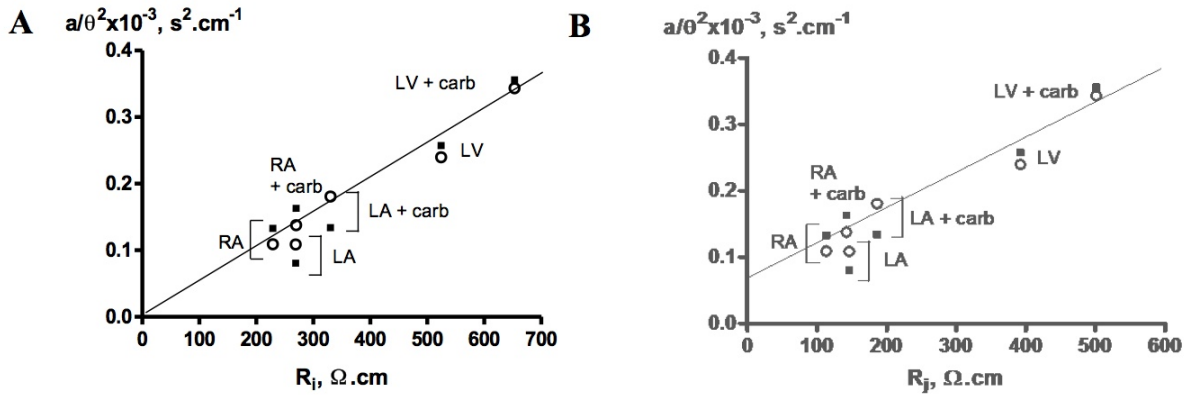


Figure 3.8 The relationship between conduction velocity, θ , and total intracellular resistivity, R_i (part A) and junctional resistivity, R_j (part B) in guinea-pig myocardium. CV is normalized to the ratio a/θ^2 , consistent with continuous cable theory. The straight lines were obtained by least-squares analysis and were extrapolated to the origin and ordinate, respectively. The data points corresponding to the mean values in each myocardial preparation in the presence and absence of carbinoxolone are labelled. The closed squares use a value of r_{ap} , averaged across each preparation; the open circles use a value appropriate to each datum point – see text for details. For graph A there was a significant correlation between data values pre- and post carbinoxolone ($r = 0.83 p=0.05$) but not for values corrected for r_{ap} ($r=0.71 p=0.13$). Values were significant for graph B; $r=0.94 p=0.02$ and $r=0.88 p=0.03$ for both values uncorrected and corrected for r_{ap} respectively.

Figure 4.12: A: Effect of total effective resistivity on conduction velocity in guinea pig (GP) myocardium. B: Effect of junctional resistivity on conduction velocity in GP myocardium. Conduction velocity θ has been normalised to a/θ^2 , where a is the cell radius: $12\mu\text{m}$ for GP ventricle and $6.5\mu\text{m}$ for GP atrium [Dhillon, 2010]. Closed squares: an average value of τ_{ap} was used; open circles, individual values of τ_{ap} was used. Image reproduced with permission from Dr Paramdeep Dhillon.

4.5 Discussion

In this chapter, tissue resistivity and functional AP characteristics were measured in guinea pig papillary muscle, in conjunction with Dr Paramdeep Dhillon and Ms Samantha Salvage. The aim of collecting the data was to present physiological parameters relevant to cable theory models, and to assess the effect of physiological modulation on resistivity and AP characteristics in an experimental setting.

4.5.1 Measured passive tissue resistivity

It was found that electrical excitation in 1D tissue can be considered [Cooklin et al., 1997] as electrically equivalent to a network of a single resistor (due to effective cytoplasmic resistance) placed in series with two parallel RC circuits (due to membrane and gap junction RC circuits respectively). The passive effective, junctional and cytoplasmic resistivity of the tissue were measured using impedance spectroscopy [Macdonald, 1992]. To our knowledge this is the only technique available to measure specific GJ resistivity in tissue preparations.

A range of tissue resistivities have been reported in the literature (see Table 3.1). Kléber and Rudy [2004] reported an intracellular cytoplasmic resistivity of $150\Omega cm$, while Stinstra et al. [2005] and Pullan et al. [2005] used $333\Omega cm$. Keener and Sneyd [2009] and [Plonsey and Barr, 2007, p.273] both report $588\Omega cm$ based on frog myocardium measurements from Chapman and Fry [1978], which refers to cytoplasmic resistivity as $282\Omega cm$. Junctional resistivity R_j in the frog constitutes 50% of the total intracellular resistivity.

Resistivity values within the current study were obtained as follows: Effective (R_i): $524 \pm 45\Omega cm$, junctional (R_j): $383 \pm 17\Omega cm$, cytoplasmic (R_c): $141 \pm 27\Omega cm$. R_j formed 73% of the total effective intracellular resistivity, which is a larger proportion than the 50% from Chapman and Fry [1978]. This finding would be a valuable addition to theoretical modelling studies, which have predominantly continued to use results from prior studies.

4.5.2 Physiological range of resistivities from carbenoxolone modulation

In this study, the effect of GJ uncoupler carbenoxolone (CBX) on tissue resistivity was studied. It was reported, whilst CBX led to increased resistivity, increasing CBX dosage did not continue to increase tissue resistivity linearly, and thus $20\mu M$ was the chosen concentration. $20\mu M$ of CBX led to an increase of effective resistivity R_i by 20% in all preparations.

It appears that pharmacological GJ modulators work within a narrow range of concentrations, and have a saturation effect above which further increase in tissue resistance is unfeasible. This differs from theoretical models, where effective resistivity can be modulated to extreme values at will. There is no reported consensus on whether a theoretical or experimental model of resistance modulation best represents the *in-vivo* physiology.

4.5.3 Physiological range of conduction and breakdown of cable theory

The present guinea pig study, along with additional results outside this thesis [Dhillon, 2010] reported a correlation between experimentally recorded resistivity values, and theoretical resistivities calculated by using experimentally recorded conduction velocity values substituted in to the cable equation. A linear best-fit relationship was established between resistivity and CV parameter a/θ^2 .

It should be noted that the values of resistivities and conduction velocities obtained were collated across both atria and left ventricle (LV); the cable theory utilised cell radii of $6.5\mu m$ in the atria and $12\mu m$ in LV. In reality, local CV may vary as the range of cell

radii may overlap. Additionally, both resistivities (inc R_j and R_i) and CV were reported within a specific range: $120 - 650\Omega cm$ for R_j , R_i , and $59 - 78.6 cm/s$ for CV. It is unclear what the behaviour of the relationship would be outside these ranges, and if the cable theory might break down at extreme resistances or under very slow conduction.

Chapter 5

The effect of modulating conductivity in a continuum model of conduction

In this chapter, the relationship between conductivity and the propagation of the action potential is explored numerically, in a classical 1D monodomain model of guinea pig ventricular tissue. This relationship is compared with experimental data presented in Chapter 4, which measured tissue resistivities and action potential propagation in isolated strands of guinea pig ventricular papillary muscle.

5.1 Introduction

The characteristics of AP propagation in healthy tissue have been explored under multiple experimental preparations, including squid axon [Hodgkin and Huxley, 1952], rabbit [Allessie et al., 1977, Knisley and Neuman, 2003], canine [Spach and Miller, 1981, 1982], cultured neonatal rat myocytes [Fast and Kléber, 1994] and in human tissue [Fedorov et al., 2011]. Experimental models have advantages and disadvantages over other prepa-

rations which make that model suitable for exploring particular hypotheses. The differences might include added biological complexity, ethical concerns, financial cost, natural variability within a model, or ease of modulating biological parameters to measure results.

In-silico computational models of cardiac electrophysiology are increasingly attractive tools to complement experimental data and inform experimental design. Computational models are inexpensive to run compared with experimental studies and are less subject to biological variability. Additionally, the simplicity of computational models permit a reductionist approach towards determining causes of specific biological phenomenon, which may not be detectable in an experimental preparation due to complex compensatory mechanisms that may counteract the effect being examined.

In the previous chapter, the experimental relationship between tissue resistivity and speed of action potential propagation was explored using an *ex-vivo* model of ventricular guinea pig papillary muscle, which is a cylindrical shaped tissue found on the endocardial surface. This showed a correlation between tissue resistivity and the parameter a/θ^2 (where a is the radius of the papillary muscle, and θ the conduction velocity through the tissue as defined in the previous Chapter). The aim of this chapter is to construct a computational model of AP propagation through guinea pig ventricular muscle, and to demonstrate the relationship between the diffusivity coefficient D and conduction velocity (CV) of the propagation wavefront. We hypothesise that there is a linear relationship between D and conduction velocity in this model, and that D is correlated to the experimental tissue resistivity discussed previously.

5.2 Methods

The experimental setup in Chapter 4 measured electrical activation through a thin strip of guinea pig ventricular papillary muscle. The thickness of the tissue was $< 1\text{mm}$, compared to the length which was approximately 5mm . Propagation was measured over the length of the tissue and considered instantaneous over the width. This allowed for the assumption of one dimension propagation.

Additionally, as $1\text{mm} \gg 100\mu\text{m}$, the longest dimension of a typical myocyte, there are many myocytes across a single cross section and along the tissue. A continuum approximation was made, which considers the averaged potential over all cells at each point. Combined with the assumption of longitudinal propagation only, a 1D cable model was used to represent this experimental set up, which can be described by the monodomain equation introduced earlier in Equation (3.25). The equation is restated below:

$$D \frac{\partial^2 V_m}{\partial x^2} = C_m \frac{\partial V_m}{\partial t} + I_{ion}(t) - I_{stim}(t), \quad (5.1)$$

The ionic model coupled to the system was the Luo–Rudy I guinea pig ventricular AP model [Luo and Rudy, 1991], which was outlined previously in Chapter 3.

5.2.1 Implementation of numerical model

A cable of length 12mm, represented by the 1D monodomain equation described in the previous Section, was implemented in MATLAB (Mathworks) with a custom code, using a second order finite difference method in space described in Chapter 3. A spatial discretisation of $\Delta x = 6\mu\text{m}$ was used. The ends of each cable were modelled as no flux boundary conditions.

The monodomain model was coupled to the Luo–Rudy I guinea pig ventricular action

potential model [Luo and Rudy, 1991]. The non-linear ionic currents at each time point were calculated using the Rush Larsen algorithm described in Section 3.3.1, and a first order implicit time integration scheme was used to forward march the solution $V(x, t)$ in time, with $\Delta t = 0.02ms$.

Pre-pacing and stimulation

To eliminate the effects of previous rate-dependent pacing history affecting the dynamics of the ionic currents in the model, a single cell representation of the LR1 ODE model was numerically paced until steady state was reached (no observable variation in consecutive action potentials). The final values of the gating variables at resting membrane potential, and the resting potential were input as initial conditions throughout the tissue at all points.

The tissue was subject to a time-dependent stimulus at one end of the cable, over a region representing the length of a single cell $120\mu m$. The stimulus duration was $0.5ms$ and the stimulation amplitude was 1.2 times the minimal activation threshold to trigger an action potential.

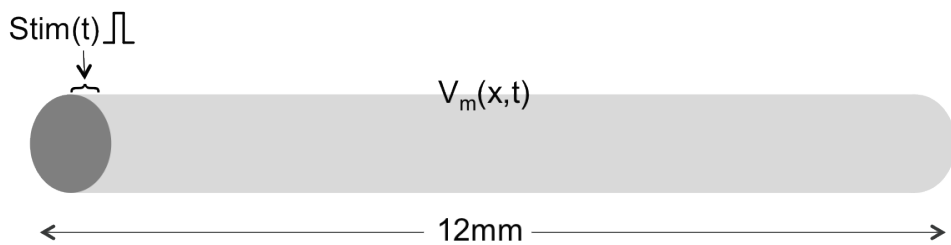


Figure 5.1: A schematic depiction of the simulated cable. A $12mm$ cable was coupled with the Luo–Rudy I action potential model, and stimulated at one end of the cable. The numerical solution $V_m(x, t)$ was evaluated.

Post Processing

The final solution was post processed to find physiological determinants of the model, including conduction velocity (CV) and action potential duration (APD).

The activation time at point x was defined by the first time point T such that $V(x, T) \geq -60mV$, and was determined at two points close to the beginning and end of the cable, from which the conduction velocity CV was calculated.

The action potential duration (APD) was determined using APD90, the time duration for a point to repolarise 90% of its amplitude after depolarisation.

Point virtual electrograms were calculated as described in Section 3.6.1. The electrode was assumed to be at the minimum distance of one cell radius away from the cable.

5.3 Results

5.3.1 Simulation duration and accuracy

The 1D monodomain equation implemented above computed in $20 - 240s$ on a MacBook Pro with a 2.6GHz i7 processor and 16GB of memory, depending on the spatial and temporal discretisation chosen.

Numerical accuracy of the simulation was studied by systematically varying the numerical parameters Δx and Δt . The accuracy was evaluated by comparing the simulation (for chosen Δx and Δt) at a single time point for all points on the domain, against a simulation calculated using a very fine discretisation in time and space ($\Delta x = 1.2\mu m$, $\Delta t = 0.001ms$). The L2 error norm was used to evaluate the error between the solutions.

The error of the solution varied depending on the single time point chosen relative to the time of the action potential wavefront being initiated in the tissue. Taking a time point close to the start of AP initiation (within $5ms$) caused a larger magnitude error due to the difficulty of capturing the steep spatial gradient of the AP upstroke in the depolarisation phase. Taking a time point when most of the tissue was in the recovery phase of the AP produced a smaller magnitude of error. Error curves had similar shape and behaviour for both choices of time points.

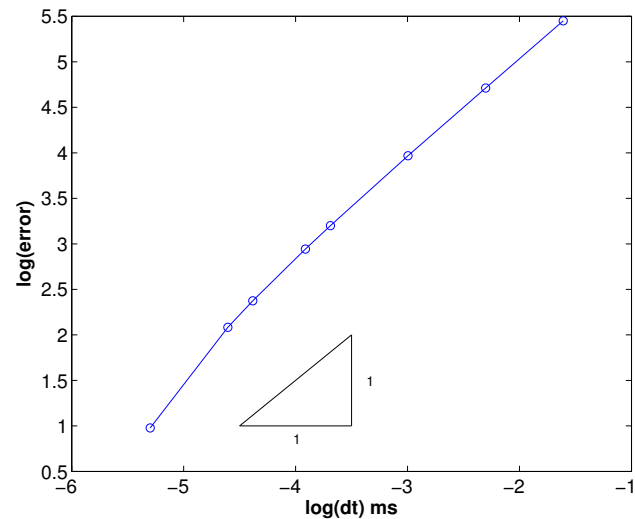


Figure 5.2: A log graph showing the numerical error of the implementation against Δt , 15ms after a stimulus was initiated in the cable. The code tends to first order accuracy, as expected for a first order implicit time scheme.

The code demonstrated first order error in time as shown in Fig. 5.2, and second order error in space as shown in Fig. 5.3. The time point was evaluated at 15ms post stimulus.

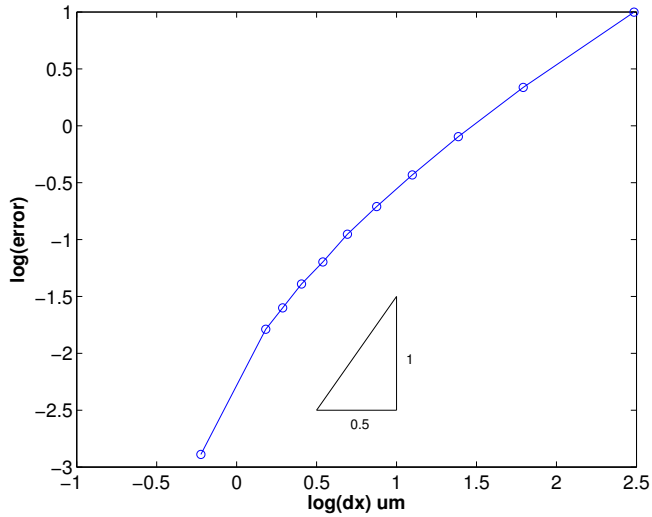


Figure 5.3: A log graph showing the numerical error of the implementation against Δx , 15ms after a stimulus was initiated in the cable. The code tends to second order accuracy, as expected for a second order central difference discretisation.

5.3.2 Modulation of physiological parameters

The effect of modulating conductivity on conduction velocity

The effect of modulating the diffusion coefficient D , also known as the conductivity of the tissue, is presented in Table 5.1. The baseline coefficient D was chosen as $D = 0.001 \text{ cm}^2/\text{ms}$ from literature [Sachse, 2004].

The table shows that decreasing D by a factor of 2 produces a decrease in CV of approximately 1.4, which demonstrates a linear power law relationship between D and CV . This can be demonstrated more clearly by plotting a log graph, in Figure 5.4. The slope of the curve is approximately 0.5.

$D \times$	CV (cm/s)	Ratio of decrease	Ratio from baseline CV
2	87.7		1.40
1	62.6	1.40	1.00
2^{-1}	44.5	1.41	0.71
2^{-2}	31.0	1.44	0.50
2^{-3}	22.2	1.40	0.35
2^{-4}	15.6	1.42	0.25
2^{-5}	11.0	1.42	0.18
2^{-6}	7.86	1.40	0.13
2^{-7}	5.55	1.42	0.09
2^{-8}	3.92	1.42	0.06
2^{-9}	2.77	1.42	0.04
2^{-10}	1.95	1.42	0.03
2^{-11}	1.36	1.43	0.02

Table 5.1: Effect of modulating conductivity D on conduction velocity CV. D is normally given as $0.001\text{ cm}^2/\text{ms}$.

The effect of modulating g_{Na} on CV

It has been demonstrated in theoretical models of AP propagation, that reducing the peak excitability, g_{Na} , of the sodium channel in the action potential model leads to a reduction in conduction velocity of propagation [Kléber and Rudy, 2004]. In this section, g_{Na} was systematically reduced to examine whether the numerical implementation of this model behaved in accordance with published data.

The peak sodium channel excitability g_{Na} parameter was reduced in increments of 10%, for the diffusion coefficient of $D = 0.0005\text{cm}^2/\text{ms}$. The resultant conduction velocity of the system is plotted against the corresponding reduced value of g_{Na} as shown in Fig. 5.5. Conduction block was obtained below 20% peak g_{Na} .

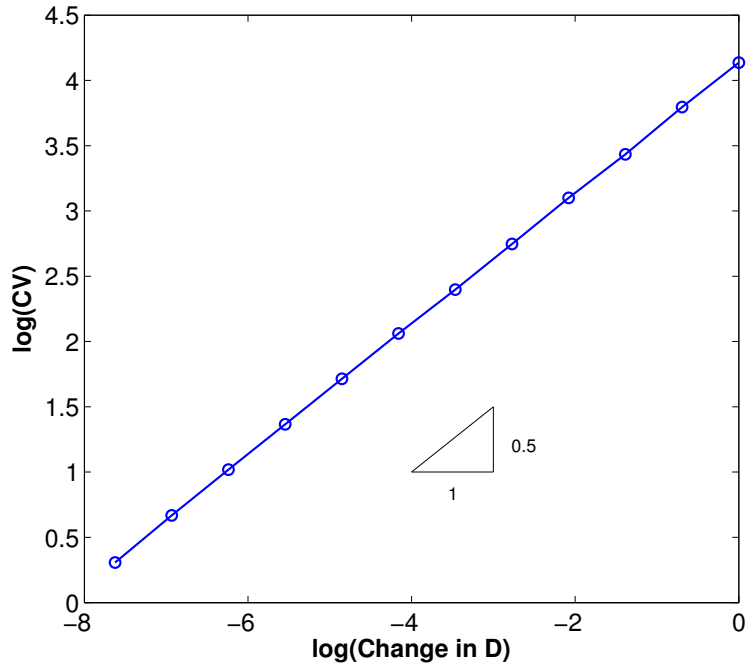


Figure 5.4: The relationship between modulating diffusion coefficient D against the resulting conduction velocity in the 1D monodomain cable model with the LR-1 guinea pig ventricular AP model. The slope of the curve is approximately 0.5, showing a linear power law relationship between the two parameters. D is normally given as $0.001 \text{ cm}^2/\text{ms}$.

$\%g_{Na}$	CV (cm/s)	Ratio of decrease	Ratio from baseline CV
100%	44.5		1.00
90%	43.0	1.03	0.97
80%	41.6	1.03	0.93
70%	39.9	1.04	0.90
60%	37.8	1.06	0.85
50%	35.4	1.07	0.80
40%	32.5	1.09	0.73
30%	28.7	1.13	0.65
20%	23.12	1.24	0.52
10%	Block	Block	Block

Table 5.2: Effect of reducing peak sodium excitability g_{Na} on conduction velocity.

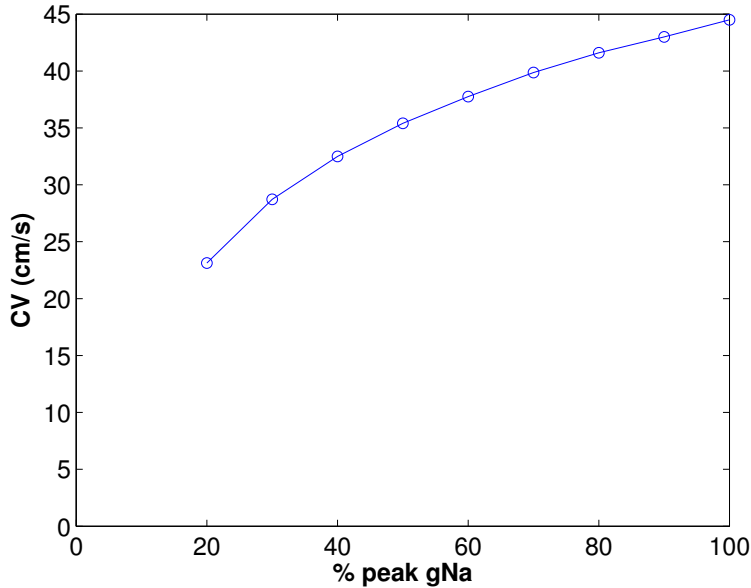
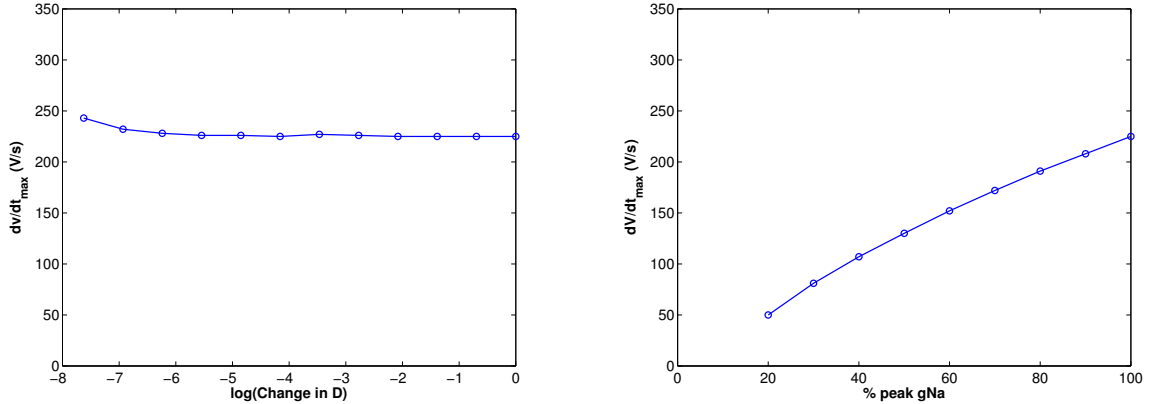


Figure 5.5: The relationship between modulating maximum sodium channel excitability g_{Na} against the resulting conduction velocity in the 1D monodomain cable model with the LR-1 guinea pig ventricular AP model.

Peak upstroke dV/dt_{max}

In Figure 5.6, it can be seen that decreasing effective diffusivity D had no effect on altering the peak AP upstroke dV/dt_{max} . However, modulating peak sodium excitability g_{Na} reduced the max AP upstroke due to reduced sodium channel activity. Conduction block occurred after an 80% reduction in g_{Na} .

It was noted that using a spatial resolution of $6\mu m$ inaccurately resulted in an increase in dV/dt_{max} as D was decreased to small values. This was probably due to numerical error, as discussed in the previous Section 5.3.1. However a spatial resolution of below $2\mu m$ was used to generate the result listed.



(a) Modulating diffusivity D has no effect on max AP upstroke dV/dt . (b) Modulating g_{Na} reduces the max AP upstroke dV/dt .

Figure 5.6: Effect of modulating physiological parameters on max AP upstroke. In the cable model, D the effective diffusivity is independent of the AP upstroke, whereas modulating peak sodium excitability g_{Na} reduces the max AP upstroke.

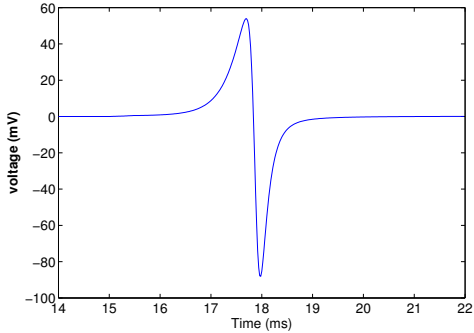
5.3.3 Action potential foot τ_{ap}

The action potential foot τ_{ap} , introduced in the previous chapter, is used as a factor between resistivity and CV. In this study, outputted action potentials on the cable were analysed for different values of diffusion coefficient D corresponding to normal or slow conduction. It was found that τ_{ap} was not significantly different between normal conduction ($CV = 44.5\text{cm}/\text{s}$, $\tau_{ap} = 0.30\text{ms}$) and slow conduction ($CV = 5.5\text{cm}/\text{s}$, $\tau_{ap} = 0.31\text{ms}$).

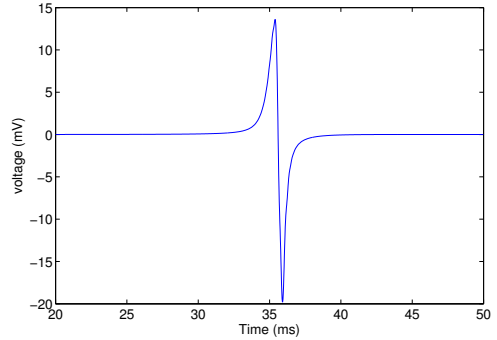
5.3.4 Electrogram

The virtual electrogram (vECG) was simulated for values of diffusion coefficient D which produced ‘normal’ conduction ($> 40\text{cm}/\text{s}$) and ‘slow’ conduction ($< 10\text{cm}/\text{s}$). These are plotted in Figure 5.7.

In normal conduction, the electrogram has a peak to peak amplitude of 142mV and a duration of 2.5ms . In slow cable conduction, the electrogram retained its biphasic morphology, with a smaller amplitude (35mV) and wider duration 5ms .



(a) Normal conduction, $CV = 41.1\text{cm/s}$.



(b) Slow conduction, $CV = 5.5\text{cm/s}$.

Figure 5.7: Virtual electrogram (vECG) of cable model, under normal and slow conduction velocities. vECG normal CV: peak to peak amplitude: 142mV , duration: 2.5ms . vECG slow CV, peak to peak amplitude: 35mV , duration: 5ms .

5.4 Discussion

In this chapter, a 1D cable model was numerically implemented, coupled with the Luo–Rudy I guinea pig ventricular AP model, and subject to analysis of numerical accuracy in space and time. Physiological determinants including conduction velocity (CV) and max AP upstroke (dV/dt_{max}) were calculated from simulations, where effective diffusivity D and peak sodium excitability g_{Na} were modulated.

5.4.1 Numerical accuracy

Convergence studies of the present work indicated that the finite difference in space, backward Euler in time, implementation followed second order accuracy in space and first order accuracy in time. This is in line with convergence rates expected of the schemes chosen. A note here is that spatial discretisation used in the present study is significantly higher resolution (biggest space step = $20\mu\text{m}$) than in published literature, which tends to use $\Delta x = 100\mu\text{m}$ (the approximate length of a single cell) as the smallest space

step. This is due to the motivation in this thesis to examine the physiological parameter limits underlying model validity, both between theoretical models and between theory and experiment. Examination of numerical parameter limits for accuracy of simulation between different theoretical models was not studied in this thesis, but has been reported in literature [Clayton et al. \[2010\]](#).

5.4.2 Modulation of physiological parameters

Investigation of physiological parameters were carried out in the cable model to assess the effects on conduction velocity (CV) and peak AP upstroke - dV/dt_{max} . Diffusion coefficient D and peak sodium channel excitability g_{Na} were modulated. A linear relationship between D and CV was observed, as expected from a 1D cable model implantation. Modulating D did not induce change on max AP upstroke dV/dt_{max} , which agrees with previous studies [\[Shaw and Rudy, 1997\]](#).

For peak sodium excitability g_{Na} , conduction block was observed after 80% reduction in peak g_{Na} . [Shaw and Rudy \[1997\]](#) reported conduction block after 90% reduction, which is lower than than the present study. This may be down to differences in implementation and numerical accuracy. Reducing g_{Na} in the current study reduced dV/dt_{max} , with the value at 80% reduction 50V/s, which is similar to the value reported in [Shaw and Rudy \[1997\]](#).

5.4.3 Range of parameter modulation compared with experiment

It is worth noting the physiological interpretation of D at specific values: $D = 0.001\text{cm}^2/\text{ms}$ corresponds to an effective intracellular resistivity of $R_i = 530\Omega\text{cm}$, based on a cylindrical cell radius of $12\mu\text{m}$ and length $100\mu\text{m}$. The values of D in this study were reduced by up to $2000\times$; even a $2\times$ reduction takes the effective R_i to $> 1000\Omega\text{cm}$, which is outside of the resistivity range measured in the previous chapter.

Thus, it is difficult to directly correlate results between theory and experiment for a simple 1D cable model of conduction: changes in D do not compare with changes in experimental AP data modulated by carbenoxolone. Significant conduction slowing needs to be induced in an experimental model to validate and compare theoretical simulations.

Part II

Development of a framework to examine discrete models of conduction

6 Development of a 1D experimental cell culture model using the HL-1 cell line	129
6.1 Background	130
6.1.1 Choice of a cell-line model	132
6.1.2 The HL-1 cell line	132
6.2 Methods	134
6.2.1 Maintenance of the HL-1 cell line	134
6.2.2 Cryostorage of HL-1 cells	134
6.2.3 Stimulating and recording of extracellular electrograms	135
6.2.4 Cell culture protocol for monolayers on MEA plates	136
6.2.5 Micro-contact printing for cell culture	137
6.2.6 Immunocytochemistry	142
6.3 Results	144
6.3.1 Control of cell seeding density	144
6.3.2 Alignment with electrodes	145
6.3.3 Quality of fibronectin transfer from stamp on to plate	145
6.3.4 Stability of patterns	147
6.3.5 Co-location and cell growth	147
6.3.6 Cell shape and anisotropy	147
6.3.7 Expression of Cx43 in patterned strands	151
6.3.8 Electrical Recording	156
6.4 Discussion	157
6.4.1 Summary of findings	157
6.5 Work in progress: Development of a mathematical model of the HL1-6 action potential	162
7 Developing a 1D mathematical model of conduction in discrete coupled myocytes	163
7.1 Introduction	163
7.2 The discrete cell chain model	165
7.2.1 Analytical solution: steady state passive problem, Dirichlet boundary conditions	167
7.2.2 Analytical solution: steady state passive problem, Neumann boundary conditions	168
7.2.3 Unsteady passive problem, no flux boundary condition with time dependent stimulus	170
7.2.4 Outline of the 1D discrete model with active ion channel kinetics	172
7.3 Results: Implementation and validation of the 1D discrete model	174
7.3.1 Implementation of the Keener and Sneyd model	174
7.3.2 The passive Dirichlet problem	175
7.3.3 The passive Neumann problem	181

7.3.4	No flux (Neumann) boundary conditions, time dependent forcing stimulus	185
7.3.5	Implementation of the full model with active ion channel kinetics	187
7.4	Results: Computation details and numerical sensitivity	187
7.5	Results: Determining physiological factors underlying conduction slowing	192
7.5.1	Gap junctional resistance	192
7.5.2	Cytoplasmic resistivity	195
7.5.3	Membrane capacitance	197
7.5.4	Sodium channel excitability	197
7.6	Results: Discrete model versus Continuum model	199
7.6.1	Effective diffusivity versus gap junction resistance	200
7.6.2	Sodium excitability and composite effects	204
7.6.3	Electrogram	205
7.7	Discussion	205
7.7.1	Summary of findings	205
7.7.2	Numerical sensitivity and stability of the discrete model	207
7.7.3	Physiological insights from the discrete model	208
7.7.4	Differences between the 1D discrete and the 1D cable model	211
7.7.5	Applicability and limitations of the discrete model	213

Chapter 6

Development of a 1D experimental cell culture model using the HL-1 cell line

In Section 1.3, a primary sub aim of developing a discrete framework to model and capture slow electrical conduction was established, along with the aim of developing a parallel and integrated theoretical and experimental approach towards understanding cardiac excitation. The present investigation aimed to develop a novel experimental cell culture model of slow electrical conduction on microelectrode–embedded culture plates, on which the local electrogram can be recorded at high spatial resolution. This model, if established, would provide a source of experimental data, to which results from theoretical models (Chapter 7) can be matched and compared.

This chapter outlines work to design and implement a method for creating custom patterned monolayers of HL-1 cardiac myocytes on glass culture plates with embedded electrodes. The technique is based on the micro–contact printing protocol described by

Camelliti [Camelliti et al., 2006], with the aim to manipulate and control cell shape and alignment in to controllable geometries, on which local electrograms can be recorded.

6.1 Background

In-vitro cell culture studies to examine the electrical conduction properties of coupled cardiomyocytes have used two primary recording methods - optical mapping [Kucera et al., 1998, 2001, Rohr et al., 1997, 1998] and multielectrode arrays [Halbach et al., 2003].

In comparison with multielectrode arrays, optical mapping is the current method of choice for obtaining detailed spatio-temporal information of the electrical excitation wavefront [Efimov, 2004], due to the extra AP information which can be assessed via the optical action potential [Kleber, 2005]. However, within the clinic, it is not currently possible to carry out optical mapping studies at such detailed resolution, due to logistical and technical difficulties. The electrogram signal remains the primary source of electrical conduction data *in-vivo*. In the clinic, multiple electrogram signals are analysed simultaneously, to determine spatial patterns of activation, based on activation times assigned to each electrogram waveform or ‘event’. Other features of the recorded waveform such as the amplitude, duration and morphology are currently not utilised.

Under normal conduction, the sequence of electrical activation in the heart is easy to determine due clear signal waveforms indicating syncytial tissue behaviour. In fibrillation however, complex fractional atrial electrograms (CFAEs) refer to disorganised electrogram behaviour recorded in the atrium, which is not well understood [Nattel, 2008].

The desire to better understand the features of the fractionated electrogram in reen-

trant arrhythmia remains a key challenge within the clinical community, prompting a number of theoretical [Lesh et al., 1988, Correa de Sa et al., 2011, Jacquemet and Henriquez, 2011] and experimental studies [Umapathy et al., 2008, Narayan et al., 2011]. Slowing of electrical excitation conduction is a primary initiator of reentrant arrhythmias [Rohr et al., 1998], and thus experimental models of slow conduction provide a platform for studies of reentrant arrhythmia and associated fractionation.

Within an experimental model, the ability to modulate parameters known to affect conduction properties of tissue, such as geometry, cell size, functional properties including ion channel and gap junction expression is important. An experimental setup to examine factors underlying electrogram fractionation paves the way for a deterministic relationship between these factors to be established using theoretical modelling, which can consequently be used to further inform clinical understanding and experimental design.

Multi- or micro-electrode arrays (MEAs) allows the acquisition of multiple extracellular electrograms from biological preparations situated over the surface of the array. Previous characterisation studies have described novel techniques for seeding simple isotropic monolayers of cells on MEAs, and for measurement of conduction properties in cardiac myocytes using this modality [Dias, 2010, Chowdhury, 2011]. However, simple cell culture monolayers do not mimic geometrical shapes found within *in-vivo* tissue, namely the aspect ratio of cell shape, anisotropy due to the alignment of elongated cardiomyocytes, and the three dimensional structure.

The ability to modulate cell shape and growth have been addressed in other experimental studies, using optical mapping. Kucera et al. [1998] described effects of branching

tissue geometry on glass coverslips, whilst Rohr et al. [1997] used a similar experimental methodology to demonstrate the source–sink effect with a single strand of cultured cells connected to a 2D monolayer. Bursac et al. [2002] described a method for controlling macroscopic anisotropy in cardiomyocyte cultures on coverslips, and Camelliti et al. [2006] published a technique for patterned cell growth on elastic membranes.

No previous studies have demonstrated a method of controlling macroscopic cell growth and anisotropy on MEAs. The aim of the present work was to carry out development of a method for growing reliable cell cultures on MEAs, with the ability to modulate geometrical cell and tissue shape.

6.1.1 Choice of a cell-line model

Primary cell cultures such as neonatal rat ventricular myocytes (NRVMs) are routinely used for in vitro studies [de Diego et al., 2011, Chang et al., 2009, Fast and Kléber, 1994]. However, they can dedifferentiate or undergo apoptosis after a few days in culture, and may contain many cell types or inconsistent proportions, which can introduce additional complications in the model. A cell line allows for consistency of preparations of a single cell type.

6.1.2 The HL-1 cell line

Work to create a cardiac myocyte cell line was carried out by Steinhelper et al. [1990], deriving the AT-1 cell line, which expressed cardiac specific proteins and retained structural features of cardiomyocytes. However, the AT-1 cell line and other attempts to create cardiac cell lines either experienced a gradual loss of the cardiac phenotype, or a loss of proliferation.

Claycomb et al. [1998] established the HL-1 cell line from an AT-1 culture, via careful control of the culture environment. Further characterisation by the same group demonstrated that HL-1 cells expressed cardiac-specific myosin and muscle-specific desmin intermediate filaments, normal myofibril development and gene expression comparable to that of adult atrial myocytes [White, 2003]. Electrophysiological characterisation demonstrated the presence of currents equivalent to sodium, potassium and L-type calcium currents, whilst electron microscopy of cell-cell borders revealed the existence of intercalated discs. These characterisations suggest the suitability of the HL-1 cell line for investigating fundamental mechanisms of cell-cell coupling and cardiac excitation.

HL-1 subclones

A feature of the original HL-1 cell line is the heterogeneity of the line, with genetically identical cultures exhibiting different morphological and contractile characteristics. Dupont and Dias [2010] carried out further work on the HL-1 culture to create six separate sub-clones, named HL1-1, . . . , HL1-6 respectively. The HL1-5 line terminated due to a lack of proliferation. Characterisation of the remaining sub-clones revealed differing connexin expression and contractile characteristics between sub-clones, whilst Western blot analysis also exhibited differing quantities of Cx43 and Cx40 expression from sub-clone to sub-clone [Dias, 2010].

The HL-1 clone 6 has been characterised to express a maximal conduction velocity of 42mm/s in a monolayer paced at $1 - 2\text{Hz}$ [Dias, 2010] and is the main sub-clone used throughout the investigation in this thesis. Any subsequent reference to HL-1 cells refer specifically to the HL-1 clone 6 (also denoted HL1-6) unless stated otherwise. Due to its slow baseline conduction velocity compared to NRVMs, the HL-1 cell line is considered a useful tool for investigating mechanisms of arrhythmogenesis due to intrinsic slow

conduction [Dias, 2010, Chowdhury, 2011].

6.2 Methods

All materials were supplied by Sigma-Aldrich unless otherwise stated.

6.2.1 Maintenance of the HL-1 cell line

HL-1 cells were cultured in Claycomb medium supplemented with 10% foetal bovine serum (FBS), 4*mM* L-Glutamine, 0.1*mM* norepinephrine, and 100*µg/ml* Penicillin/Streptomycin in an incubator at 37°C with 5% CO₂. Culture flasks were pre-coated with 0.02% gelatine and 5*µg/ml* fibronectin.

Confluent flasks were passaged with two washes of phosphate-buffered-saline solution (PBS) followed by incubation with 1*ml* trypsin/EDTA (0.5*mg/ml*, 0.2*mg/ml* EDTA in PBS for 8–12 minutes to loosen the cells from the flask surface. After cells were dislodged, trypsin digestion was terminated using 1*ml* trypsin inhibitor and the solution washed in to a centrifuge tube with PBS and centrifuged at 1000*g* for five minutes. The resulting supernatant was removed and the cells were resuspended in media, diluted between 1/3 and 1/6 and seeded in to a new culture flask.

6.2.2 Cryostorage of HL-1 cells

Freezing

Unused HL-1 cells were preserved in liquid nitrogen for later use. Cells were cultured in T75 flasks using the protocol described in Section 6.2.1. After dislodging and centrifuging, the cells were resuspended in a freezing medium of 95% FBS and 5% dimethyl sulfoxide (DMSO), and aliquoted to cryovials (9 vials per T75 flask). Cells were frozen

at $-80^{\circ}C$ for 24 hours before being transferred to liquid nitrogen.

Thawing

Cryovials were thawed rapidly in a $37^{\circ}C$ water bath, and the contents were centrifuged with 10ml Dulbecco's Modified Eagle Medium (DMEM) for five minutes at 1000G. The supernatant was removed and the cells were resuspended in supplemented Claycomb medium and seeded. The cells were left to attach for 4 – 6 hours, before the medium was replaced. To ensure full recovery from cryostorage, cells underwent two full passages before any use in experiments.

6.2.3 Stimulating and recording of extracellular electrograms

The multielectrode array system

The MEA system produced by Multichannel Systems, Germany is a commercially available system for electrical stimulation, recording and data acquisition.

Microelectrode arrays (MEAs) are reusable arrays of electrodes which permit simultaneous electrical stimulation and recording. The electrodes, made from titanium nitride (TiN), are set in glass, and channels connecting electrodes to pre-amplifier contact points are electrically isolated with silicon nitride (PEVCD). Each electrode is capable of recording voltage and delivering electrical stimuli at physiologically realistic voltages. The system is amplified via a pre-amplifier and a filter amplifier and has an acquisition voltage range of $\pm 4mV$ at $25kHz$, versus optical mapping systems which acquire at $1 - 2.5kHz$. An 8×8 culture MEA plate consists of 60 electrodes (with no corner electrodes), with an electrode diameter of $30\mu m$ and electrode spacing of $200\mu m$ giving a recording area of $1.4mm \times 1.4mm$ (depicted in Figure 6.1)

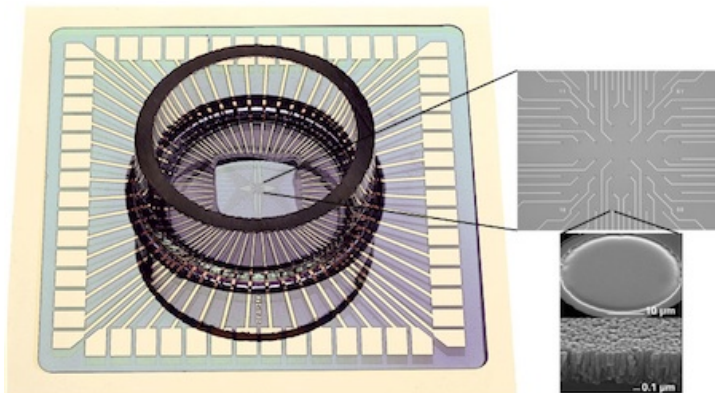


Figure 6.1: A microelectrode array (MEA) plate consists of a square array of electrodes of around $30\mu m$ in diameter with a spacing of between 100 and $500\mu m$. Image from Multichannel Systems.

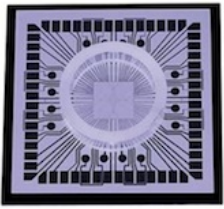
Two types of MEA plates were used, as depicted in Figure 6.2:

- Standard MEA plates were made with a solid ring around the area of the electrodes to hold the culture medium.
- For immunocytochemistry on the same culture plate, flat MEA plates were used with a removable silicone cell culture chamber (Greiner Bio One) to hold media. This ring could be removed post-recording to allow the MEA plate to be imaged on a confocal microscope.

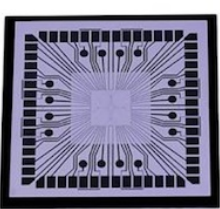
The protocol permitting electrophysiological recordings followed by immunocytochemistry on the same culture plate was devised by Dr R Chowdhury [[Chowdhury, 2011](#)] and reproduced below.

6.2.4 Cell culture protocol for monolayers on MEA plates

Cells in confluent flasks were re-suspended and diluted. Two techniques were used for seeding the cells on the MEA plates, which were pre-coated with fibronectin and washed with Poly-L-Lysine-conjugated Polyethylene Glycol (PLL-PEG):



(a) Standard MEA plate with solid ring



(b) Flat MEA plate without ring



(c) Removable silicone cell culture ring

Figure 6.2: The standard solid ring MEA is used for normal experiments; the flat MEA is used when additional immunocytochemistry is needed. Images reproduced courtesy of Dr Rasheda Chowdhury.

- 10 μ l of medium containing 0.5cm² of cells were dropped precisely on top of the microelectrode array. This was left for 20 minutes to allow cells to settle before topping up with medium.
- The whole culture of the MEA plate was flooded with 0.5cm² of cells, suspended in a larger volume of medium (200 μ l).

Following two pre-washes with Dulbecco's Modified Eagle Medium (DMEM), a second medium change was made between 2-6 hours after seeding to remove dead and loose cells.

Electrical activity within the cells were recorded up to 5 days after seeding. Activity within the cells were either triggered through intrinsic pacemaker activity or via an external biphasic electrical stimulus.

6.2.5 Micro-contact printing for cell culture

During the process of cell culture and MEA recordings, cultured monolayers seeded and formed arbitrary shapes. Required geometrical 1D/2D patterns could not be created using the established seeded monolayer technique. An additional method was sought, that could control overall tissue shape and geometry, and the chosen method to implement

was *micro contact printing*, also known as micropatterning.

Micropatterning techniques have been utilised successfully by several groups, such as Kucera et al [Kucera et al., 1998, Rohr et al., 1998] and Camelliti et al[Camelliti et al., 2006]. The chosen experimental method of creating patterns within this work was based on the micro-patterning protocol of Camelliti et al, with suitable adaptations and modifications.

Overview of the protocol

The micro-contact printing protocol consisted of the following steps (illustrated in Figure 6.3):

- DESIGN - A photomask layout with the desired pattern was created. A transparent ‘mask’ made from soda-lime glass with chrome covering the desired feature was manufactured.
- COATING - The mask was aligned on to a silicon wafer, which was pre-coated with a light sensitive material known as *photoresist*.
- EXPOSURE - The coated wafer was exposed to UV light through the photo mask.
- DEVELOPMENT - the coated wafer was baked and developed to dissolve the unexposed pattern and create the final mould.
- STAMP-MOULDING - PDMS stamps were created through deposition in to relief moulds on the wafer and baked at low temperature.
- STAMPING - The stamp was coated with Alexa488-conjugated fibronectin and pressed on to the substrate, which was then seeded with cells.

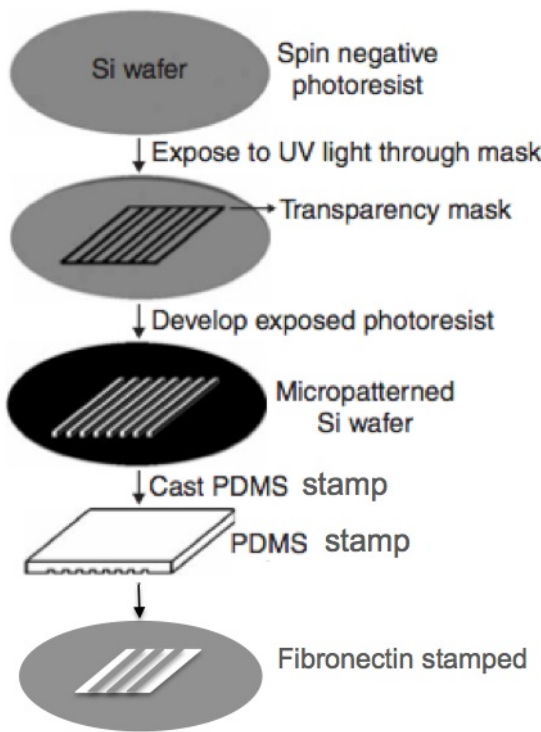


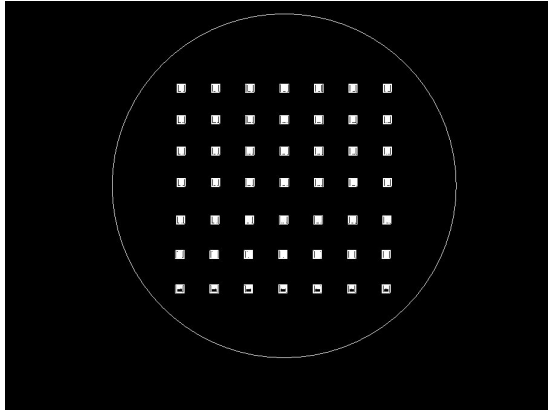
Figure 6.3: An illustration of the micro-contact printing protocol (adapted from [Camelliti et al. \[2006\]](#)).

Designing the transparency mask

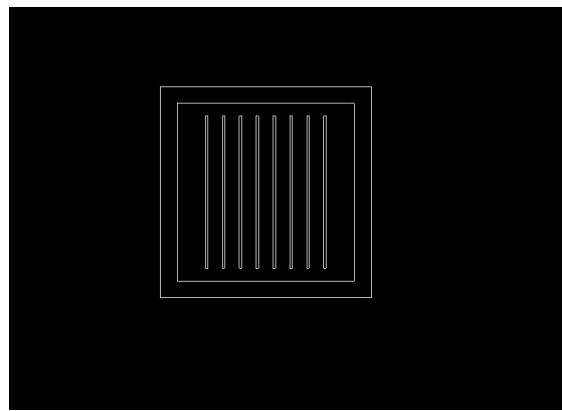
Photomask layouts were created using a CAD multi physics modelling package (COM-SOL), and designs were sent to an external photomask supplier (JD Phototools, UK) for manufacture. 5" × 5" photomasks were manufactured from soda lime, with printed chrome creating opaque features on the mask (Figure 6.4)

Creating the patterned wafer

Photolithography work was undertaken in a controlled clean room environment to reduce contamination of small airborne dust and other contaminates during the manufacturing process. The clean room was based at London Centre for Nanotechnology, UCL, and had a Class 1000 (ISO 6) rating.



(a) Transparency mask layout containing 7×7 features designed on a CAD package.



(b) A designed feature, consisting of 8 strands, width $30\mu m$, length $2000\mu m$.

Figure 6.4: Features were designed on a transparency mask, with a zoomed feature showing a design with long thin strands of width $30\mu m$. Each feature had a square boundary around the border to stabilise the stamp during incubation.

The negative photoresist solvent *SU-8* (Microchem) was used to create coatings of controlled depth. The SU-8 resist was available in several different viscosities, each requiring a modified protocol that resulted in different depths of deposition on the silicon wafer surface. SU-8 2005 was initially used, creating a coated layer with a depth of $\approx 5\mu m$ which was not deep enough to transfer the specific pattern feature cleanly. Instead, SU-8 2025 with a much higher viscosity was chosen, creating a coating of depth $\approx 30\mu m$.

Photolithography was carried out as follows: 4 inch diameter round silicon wafers were coated with SU-8, spun rapidly to create a uniform layer, and baked pre-exposure to minimise remaining solvent concentration, first at $65^{\circ}C$ for pre-baking and then at $95^{\circ}C$ for softbaking. Following this, the wafer was placed on a vacuum controlled mask aligner (Quintel) with the transparency mask overlaid.

The masked wafer was exposed to UV light for a controlled energy dose and this rendered exposed parts of the coating to cross link and become insoluble to developer. Following

exposure, the wafer was post exposure baked (again at 65/95°C) to complete the cross linking process. The wafer was developed in EC Solvent, dissolving the unexposed photoresist, and washed in isopropanol.

A summary of SU-8 photoresist properties and timings for each step of the protocol is presented in Table 6.1.

	Thickness (μm)	Spin Speed (RPM)	Pre Exp Bake Pre/Soft (min)	Exposure (s)	Post Exp Bake Pre/Soft (min)	Development (min)
SU8-2005	5	3000	1 / 2	10	1 / 1	1
SU8-2025	30 – 40	3000	2 / 5	40	1 / 3	5

Table 6.1: Summary of SU-8 photoresist properties and required times for each protocol step. Pre bake was carried out at 65°C, post bake at 95°C

Fabrication and maintenance of PDMS stamps

Polydimethylsiloxane (PDMS) solution was mixed from a commercial elastomer kit (Dow Corning). Sylgard 184 was mixed with a curing agent at a weight ratio of 10:1 [Camelliti et al., 2006] and vacuum pumped to remove air bubbles. The desiccated solution was poured in to pre-cut relief moulds placed on the master mould and baked at 70°C for one hour to form the stamp. This was cleaned via sonication in ethanol and rinsed in distilled water. PDMS stamps were treated in a plasma cleaning system for final cleaning and ionisation before use.

PDMS stamps were sonicated in 70% ethanol and rinsed in distilled water after each use.

Pattern transfer with fibronectin

The stamp was incubated in fibronectin (diluted to 0.2 mg/ml of labelled fibronectin solution) for 1 hour before stamping on to the substrate (either an MEA plate or a glass

coverslip). The substrate was then washed in Poly-L-Lysine conjugated Polyethylene Glycol PEG (0.1mg/ml) before being rinsed and blown dry using nitrogen gas.

Labelling of fibronectin

To look for co-localisation of fibronectin and seeding of cells, the fibronectin solution was pre-conjugated with Alexa-fluor 488, a substance which fluoresces green under excitation from blue fluorescence at a wavelength of 488nm. This was carried out by mixing the Alexa-Fluor reagent with fibronectin, and eluting the resultant solution through a purification column.

The collected volume fractions of labelled fibronectin were diluted at 1/5, before being used as above.

Seeding of cells

HL-1 cells in suspension were seeded at a high density over the feature of interest, at a range of dilutions. Following the seeding, MEA plates were washed with PBS solution at specific time points, to remove dead cells that were adhered to the surface.

Imaging of cells

Cells and patterns were imaged using a Nikon inverted microscope (Eclipse TE200).

6.2.6 Immunocytochemistry

Immunocytochemistry was carried out to identify Cx43 expression in the patterned myocytes. The protocol is outlined below.

Fixing

Cells on the MEA plate were fixed with methanol for five minutes then washed twice for five minutes in PBS and stored at 4°C overnight. All subsequent incubations were carried out at room temperature.

Antibody incubation

Cells were initially incubated with 1% BSA block in PBS for 1 hour (PBS–BSA). Cells were simultaneously incubated with the primary rabbit anti Cx43 and anti N-cadherin antibodies for 2 hours. The anti Cx43 antibody (Zymed) was raised against the rat, and used at a 1:200 dilution in BSA. The anti N-cadherin (Zymed) was raised against the chicken, used at a 1:500 dilution in BSA. Antibody dilutions were made in PBS–BSA.

After washing three times for five minutes with PBS, cells were incubated simultaneously with secondary antibodies: Cx43: anti-rabbit Cy3 at 1:500 dilution, N-cadherin: anti-mouse FITC at 1:500 dilution in BSA for 45 minutes. The cells were then washed three times for five minutes with PBS.

Mounting

The removable rings on the MEA plates were then removed and the plates were dipped in distilled water. The plate edge was blotted on tissue paper. A coverslip was mounted onto the plate using CitiFluor mountant in excess without sealing.

Quantification

Cell size and orientation from confocal images and phase contrast images were manually identified and measured by using Fiji, an open source image analysis software [[Schindelin](#)

et al., 2012]. The method in the confocal image is outlined:

- The image stack was projected to a single plane along the Z axis, taking the max intensity for each pixel across the Z stack.
- Individual cells were identified and a freehand trace around each cell border was performed.
- An ellipse was fitted to each cell using the built-in Fiji tool, and the properties of the ellipse (major axis length, minor axis length and angle of major axis from horizontal) were measured.
- Cell size, anisotropy ratio and orientation was calculated.

Statistics

Comparisons between groups were carried out by one way analysis of variance (ANOVA), with post-hoc Bonferroni's multiple comparison test. p values: * : $p < 0.05$, ** : $p < 0.01$, *** : $p < 0.001$.

6.3 Results

Patterns were designed as eight parallel lines, of length $1500\mu m$, and with variable thickness of $30\mu m$ up to $100\mu m$, with line spacing of $200\mu m$ from centre to centre.

6.3.1 Control of cell seeding density

Chowdhury [2011] established a method for seeding cells in suspension over a specific area: to deposit a small droplet of medium containing a high concentration of suspended cells over the feature of interest: this saturation of cells would lead to a confluent monolayer. The challenge faced for micropatterning purposes was to find a seeding method

which did not saturate the area of interest yet had a high enough concentration of cells per unit area to ensure that cells would bind to each pattern.

It was found through systemic variation of seeding technique and re-suspension concentrations, that a $1/50$ (0.5cm^2 of cells from a 100% confluent T25 flask) concentration, suspended in around $100 - 200\mu\text{l}$ of media, was optimal.

6.3.2 Alignment with electrodes

The stamps created were transparent and cylindrical (5mm diameter), and features were of the order of 1.4mm , to fit with a line of 8 electrodes spaced $200\mu\text{m}$ apart.. To ensure the stamp aligned with the MEA feature, a Z-axis micro-manipulator-controlled clamp was initially used. However, it was found that manual manipulation of the stamp using forceps whilst looking through the microscope eyepiece was sufficient to accurately align the stamp with the electrode.

6.3.3 Quality of fibronectin transfer from stamp on to plate

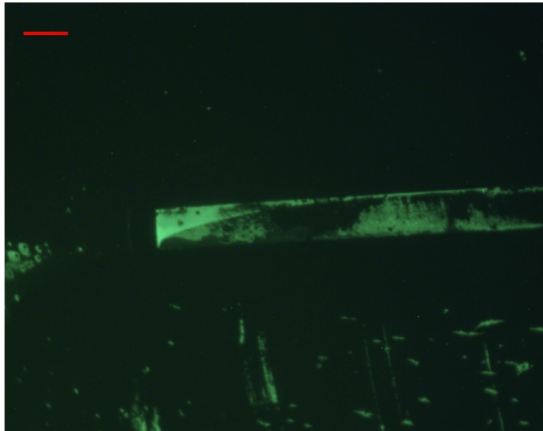
The quality of fibronectin transfer from the PDMS on to the glass plate was assessed by conjugation of Alexa-Fluor 488 with fibronectin, and subsequent analysis of the resultant patterns on glass cover slips using an epifluorescence microscope.

It was initially found that fibronectin transfer on to the plate was inhomogenous, as shown in Figure 6.5. Pattern transfer was preferential on the edges of stamp features and not in the middle of the features. This design and quality of PDMS stamps were improved to include an outer square outside the region of interest for support, and by increasing the depth of the features on the silicon wafer. Additionally, the incubation time of the fibronectin on the stamp was increased to one hour from 20 minutes. This resulted in a

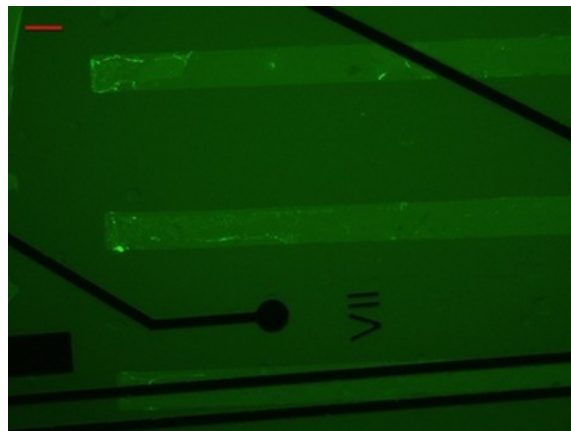
cleaner pattern transfer, as shown in Figure 6.5.

However the condition of each MEA plate was found to have effects on the quality of pattern transfer. New MEA plates require pre-treatment to create a hydrophilic surface; over time the hydrophilic properties of the plate dissipate and this was found to impact on the quality of the transfer. Plasma treatment was found to refresh the hydrophilic properties of the plate.

Additionally, the silicon nitride insulation above electrodes deteriorated over use and this created an uneven plate topography, which also impacted on fibronectin transfer.



(a) Patchiness of fibronectin transfer with initial stamps.



(b) Reliable fibronectin transfer after improvement of protocol.

Figure 6.5: Quality of fibronectin transfer (green) on to MEA plate was improved following modification of the initial protocol. Scale bar: $30\mu m$

6.3.4 Stability of patterns

MEA plates imprinted with Alexa-fluor 488-conjugated fibronectin were imaged daily over a two week period, to examine the stability of the pattern. It was found that the fluorescence pattern retained constant shape and intensity over this time period, indicating that the fibronectin pattern did not deteriorate over time.

6.3.5 Co-location and cell growth

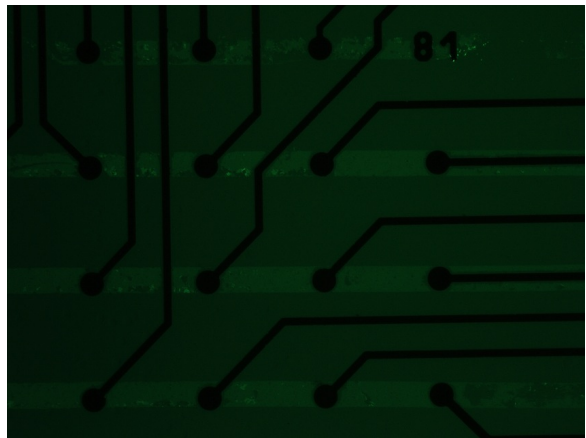
Fibronectin was imprinted on glass MEA plates, for parallel lines of thickness 30 and $100\mu m$. HL-1 cells were seeded according to the cell seeding protocol outlined in Section 6.2.1. Thirty minutes to two hours after seeding, the MEA plate was washed vigorously in PBS solution, to remove dead cells adhered to the MEA plate. The plates were imaged immediately after the PBS wash, and daily subsequently.

Figure 6.6 shows two sets of patterned cultures, for thicknesses of 30 and $100\mu m$ respectively. After seeding, suspended cells settled and attached preferentially to fibronectin patterns. Plates were washed 0.5 – 2 hours post seeding, and imaged (6.6c and 6.6d). One day after seeding, cells began to attach to each other, forming confluent monolayers within the pattern (6.6e and 6.6f).

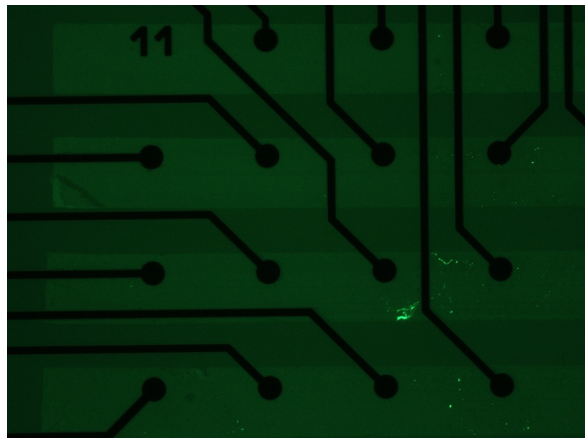
6.3.6 Cell shape and anisotropy

For very thin fibronectin patterns $< 10\mu m$, single cells aligned exactly along lines of fibronectin (Figure 6.7).

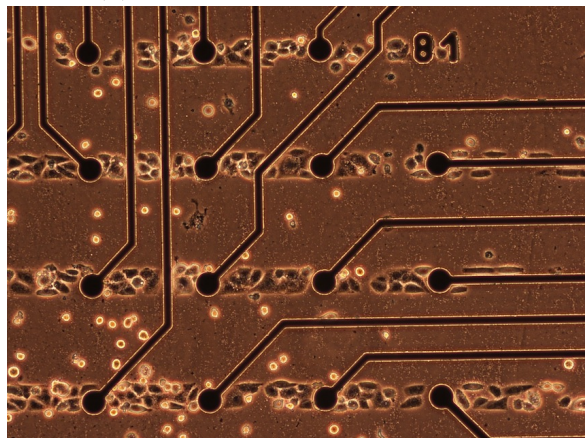
The morphology of HL-1 cells in patterned strands were compared with HL-1 cells seeded in a normal monolayer. Initial visual observation suggested that patterned strands



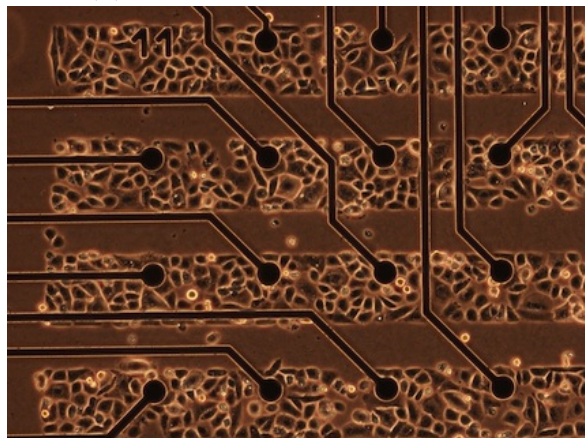
(a) Patterned lines, $30\mu\text{m}$ thick



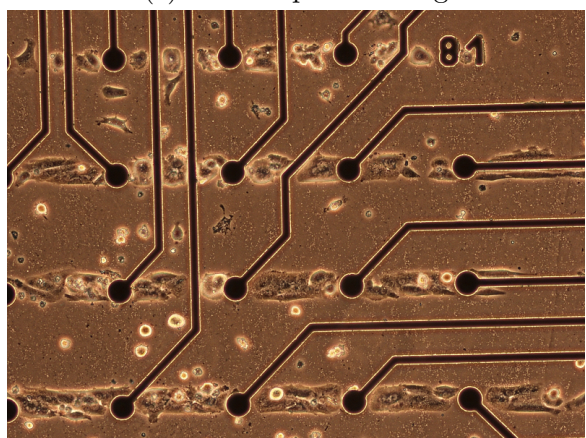
(b) Patterned lines, $100\mu\text{m}$ thick



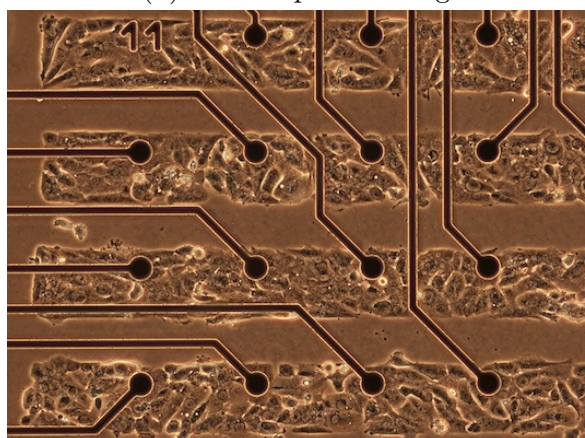
(c) 2 hours post seeding



(d) 2 hours post seeding



(e) Day 1 after seeding



(f) Day 1 after seeding

Figure 6.6: Growth of patterned HL-1 cells on MEA plates. Alexa-Fluor 488-labelled Fibronectin was printed on MEA plates (6.6a and 6.6b). Cells were seeded and washed 0.5 – 2 hours post seeding (6.6c and 6.6d). One day after seeding, cells began to attach to each other, forming confluent monolayers (6.6e and 6.6f).

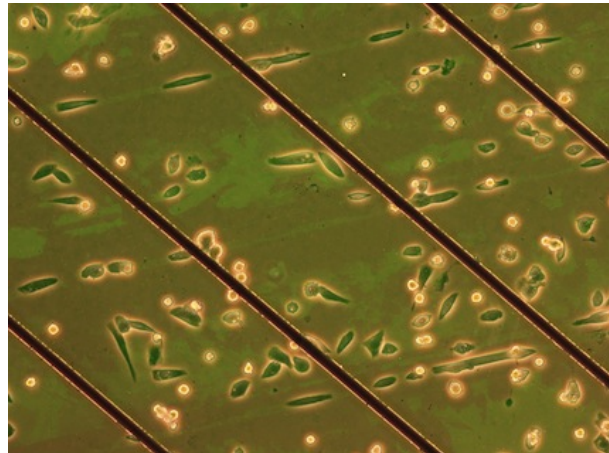


Figure 6.7: Single cell alignment (bright field) overlaid on fibronectin patterns (green). On very thin lines, HL-1 cells elongated exactly along lines of fibronectin. Thickness of electrical lines along diagonal: $10\mu m$.

induced elongation in seeded HL-1 cells compared to non-patterned monolayers (Fig. 6.8).

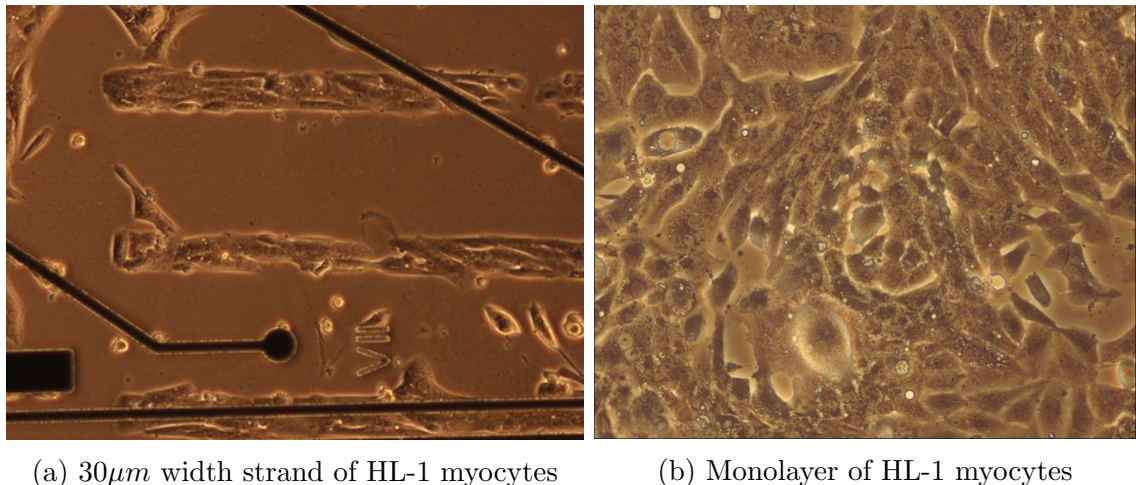
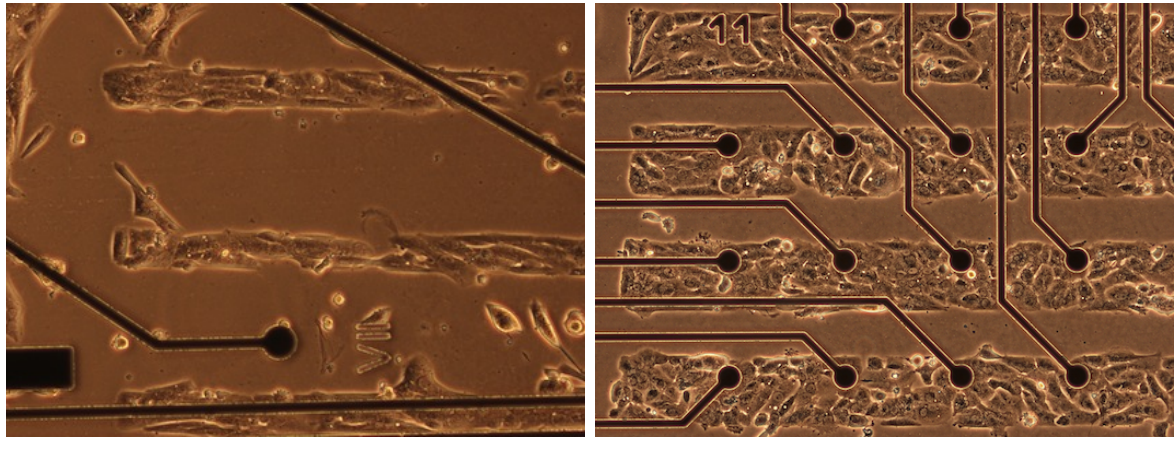


Figure 6.8: HL-1 cells in a patterned strand vs in a monolayer. Cells within pattern are elongated primarily in the direction of the strand. Cells seeded in a 2D monolayer exhibit a range of shapes and orientation.

The morphology of HL-1 cells were compared in thin strands ($30\mu m$) vs thick strands



(a) Thin strands, $30\mu m$ width

(b) Thick strands, $100\mu m$ width

Figure 6.9: Cell orientation in thin vs thick strands, imaged one day post seeding. Elongated cells were more homogeneously orientated in thin strands along the long axis compared to thicker strands.

($100\mu m$), shown in Figure 6.9. There was no visual difference between degree of cell elongation in thinner strands ($30\mu m$) versus thicker strands ($100\mu m$), due to confluence of monolayers, and further quantitative analysis was carried out.

Quantitative analysis on cell morphology and orientation was carried out on thick and thin strands as described in Section 6.2.6, by manually fitting ellipses to individual myocytes identified on phase contrast and Cx43–labelled confocal images of patterned culture. Cell length and width, anisotropy ratio and mean orientation from horizontal were calculated, and presented in Table 6.2. Morphological parameters are compared in Figure 6.10.

In single cells on patterned lines, cells had an average anisotropy of 4.4 and were closely aligned to the pattern. In patterned strands, the cells became significantly less elongated as strand thickness was increased; the anisotropy ratio of cell long axis to short axis decreased from 4.4 down to 1.9, as cells exhibited a less anisotropic profile. The

Width	n	Long axis (μm)	Short axis (μm)	Anisotropy	Angle ($^\circ$)
Single line	8	29.0 ± 2.5	6.8 ± 1.0	4.4 ± 0.6	0 ± 4
$30\mu m$	28	20.8 ± 8.0	6.7 ± 2.3	3.2 ± 0.9	-4 ± 12
$100\mu m$	52	19.4 ± 4.8	11.8 ± 2.9	1.9 ± 0.6	15 ± 51

Table 6.2: Cell morphology was measured in strands of different thickness, by fitting ellipses to cells. Long/short axis lengths, anisotropy between long and short axis, and deviation of the long axis from the horizontal are presented.

distribution of cell orientation from the horizontal axis was more heterogeneous as width of patterned strand increased, from single cell thickness strands (S.D. 4°) to $30\mu m$ (S.D. 12°) to the $100\mu m$ strand (S.D. 51°), as shown in Figure 6.11.

Overgrowth of patterned shapes

Patterned shapes were found only to retain the pattern for a period of 1-2 days after seeding. Proliferation of HL-1 cells continued over incubation period, such that cells would overgrow the features of the pattern and form new connections with other features by day 3 and 4, as shown in Figure 6.12.

6.3.7 Expression of Cx43 in patterned strands

Immunocytochemistry was carried out ($n=1$ of each strand), fixed 3 days after seeding, to determine cell shape and Cx43 expression on patterned culture. The image was acquired on a confocal microscope along the Z-axis. Each slice had a thickness of $1.2\mu m$. A sample slice through the preparation is shown in Figure 6.13.

Cx43 labelling identified Cx43 in HL-1 cells seeded on patterned MEA plates (Figure 6.13b). The intensity of labelling was greater on cell membranes compared to intracellular space, indicating possible existence of gap junctions on the cell membrane. Elongated cells exhibited labelling along both membrane axes.

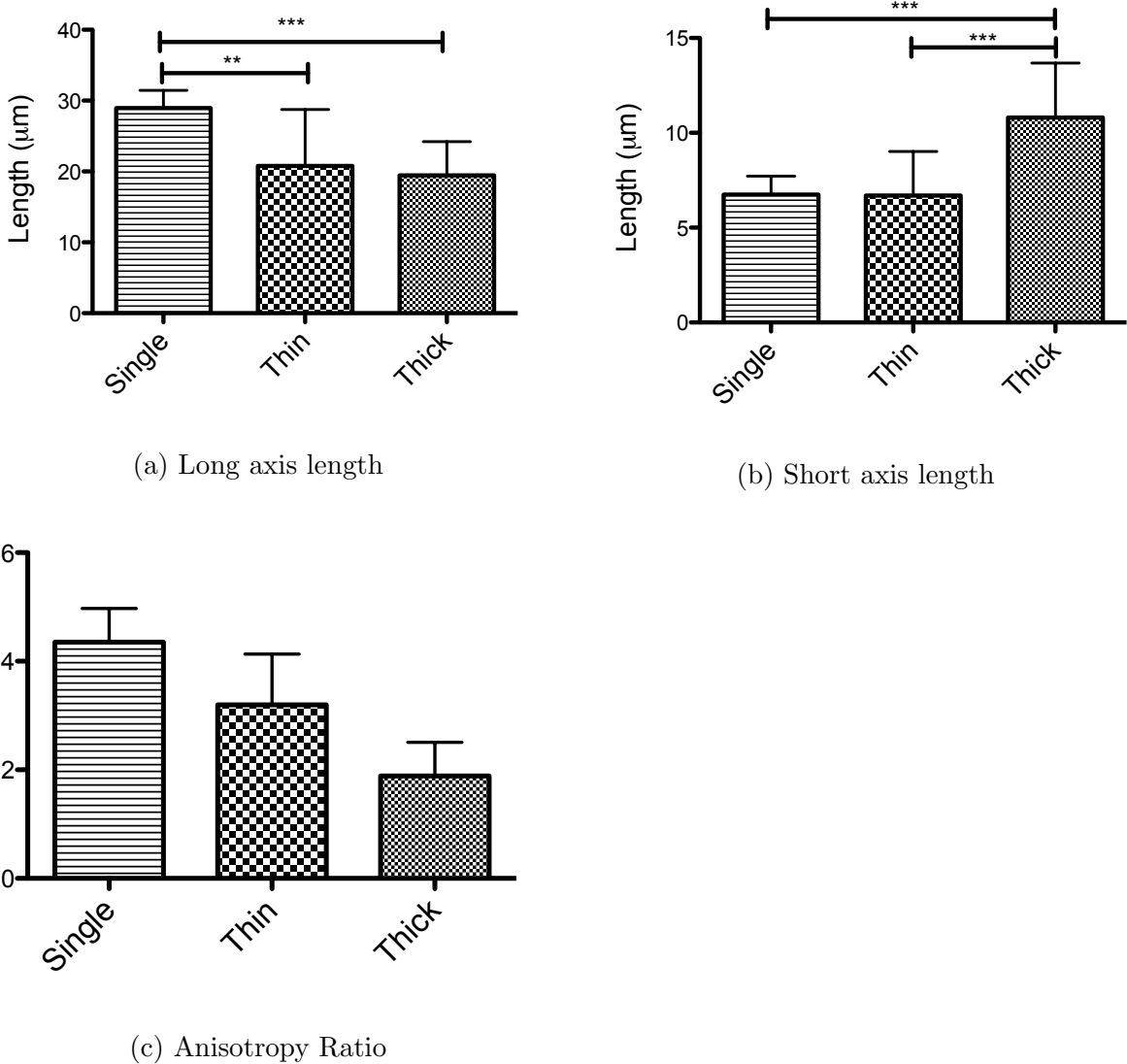
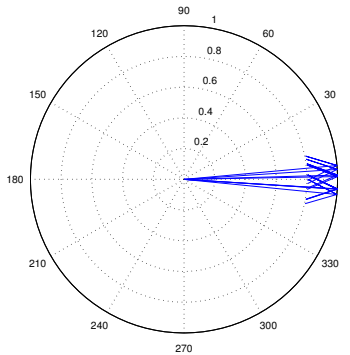
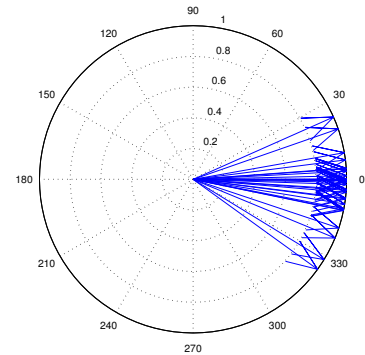


Figure 6.10: Comparison of cell morphology in different strand thickness, by manual fitting of ellipses to cells and measuring their properties. Bar graphs: mean \pm SD. There was no significant difference in mean long axis between $100\mu\text{m}$ (Thick) and $30\mu\text{m}$ (Thin) strand, but significant differences between thick and single cell–thick (Single) ($p < 0.001$), and between Thin and Single ($p < 0.01$). The mean short axis length was not significantly different between Single and Thin strands, but significant difference between Single and Thick ($p < 0.001$), and between Thick and Thin strands ($p < 0.001$). Finally there was significant difference in anisotropy ratios between all three pairs (all $p < 0.001$).

(a) Single cell thickness



(b) Thin strand



(c) Thick strand

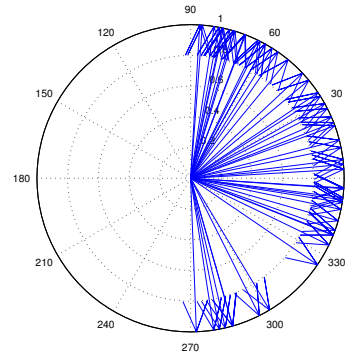
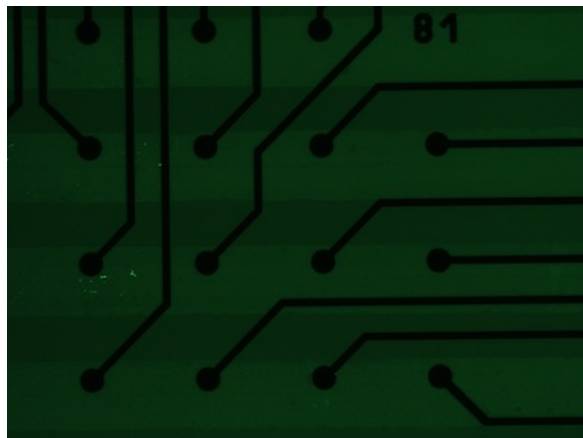
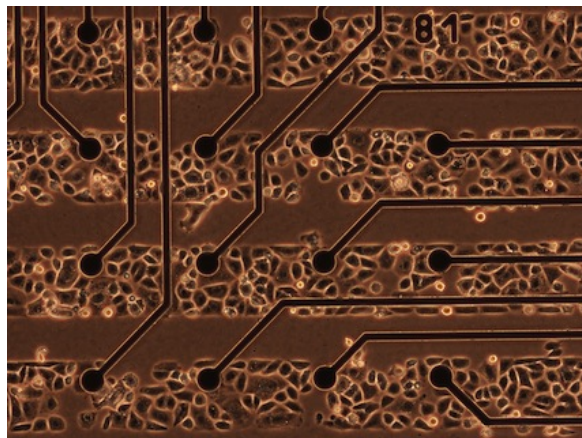


Figure 6.11: Orientation of patterned cells from horizontal. Cells on a pattern $< 10\mu\text{m}$ were aligned with pattern ($n = 8$), while mean orientation on a thin pattern had a small deviation from the horizontal ($n = 28$). Cells within a thick strand had a wide range of orientations ($n = 52$).

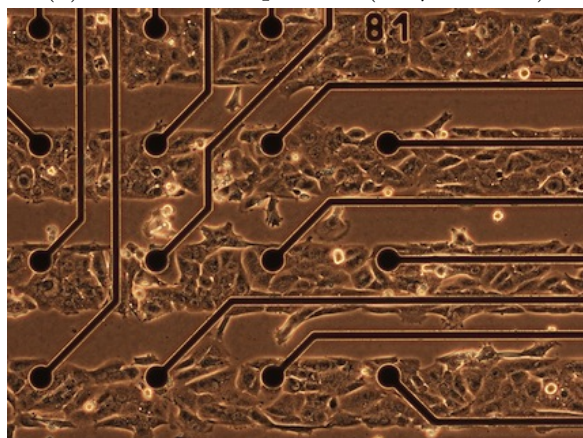
Sequential confocal images acquired through the Z-depth of the sample revealed the existence of proliferated cells above the primary monolayer (Figure 6.14). Slice 9 reveals autofluorescence of the embedded electrodes. The maximum intensity of Cx43 labelling was projected along the Z axis was projected on to a single plane shown in Figure 6.15, which reveals the mean elongation and orientation of cells in thinner strands compared with the thick strand. Cx43 labelling occurred uniformly along both long and short axis of HL-1 cells in both strand thicknesses.



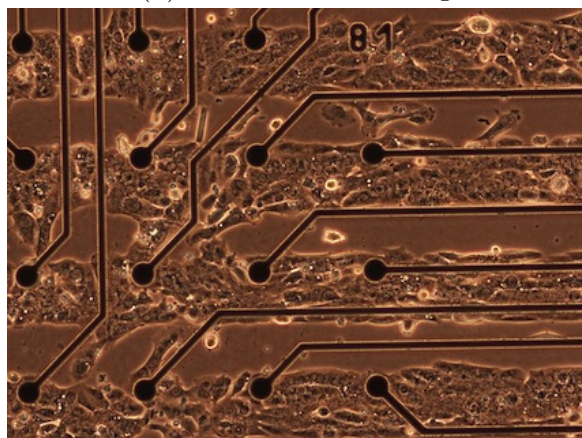
(a) Fluorescence pattern ($100\mu\text{m}$ thick)



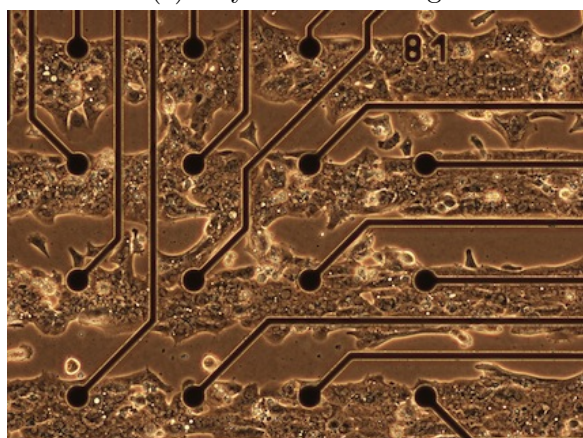
(b) 2 hours after seeding



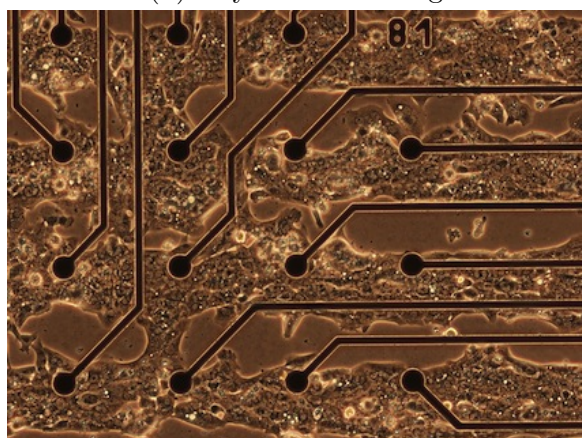
(c) Day 1 after seeding



(d) Day 2 after seeding

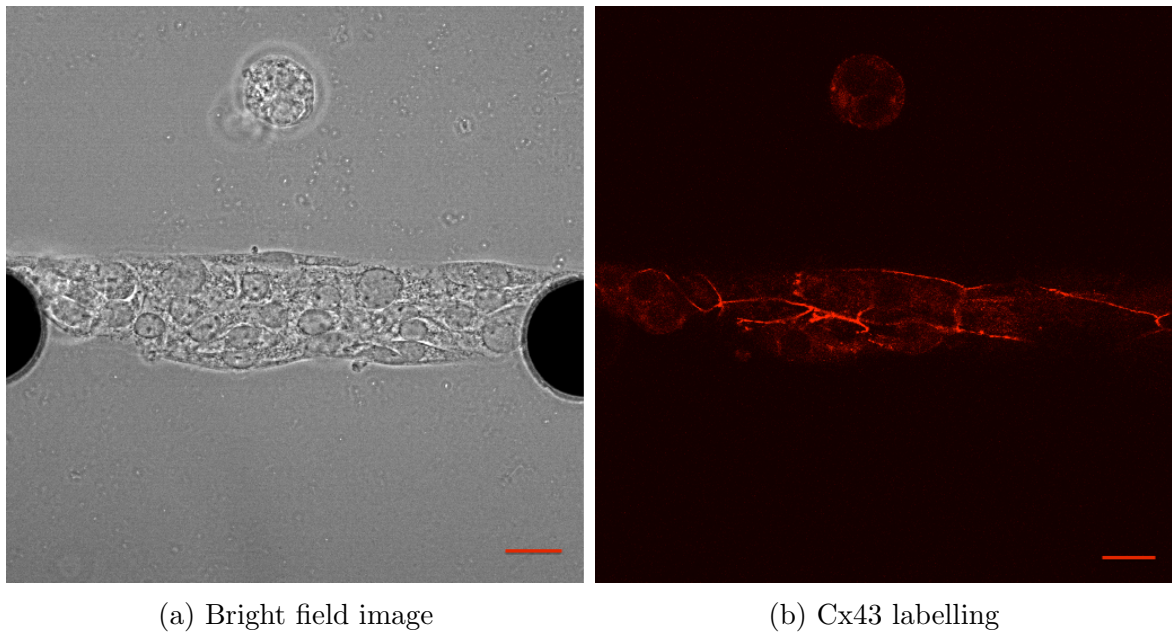


(e) Day 3 after seeding



(f) Day 4 after seeding

Figure 6.12: Micro-patterned HL-1 cells initially adhere to pattern (6.12b and 6.12c), but then start to overgrow the pattern and connect with other lines (6.12e and 6.12f).



(a) Bright field image

(b) Cx43 labelling

Figure 6.13: Cx43 labelling of patterned HL-1 myocytes on MEA plate. 6.13a is a bright field image showing the elongation of HL-1 cells in to an anisotropic shape along the line of the strand. 6.13b shows the distribution of Cx43 labelling within the cell and along the membrane, around the middle Z slice through the thickness of the preparation (10 $12\mu m$). Z-slice resolution: $1.2\mu m$. Scale bar: $15\mu m$.

A double labelling protocol for *Cx43* and for intercalated disc–protein N–Cadherin was carried out, and the overlaid labelled images are presented in Figure 6.16, with sites of co-localisation appearing purple. This indicated that lines of high Cx43 intensity are localised within the intercalated disc on the cell membrane.

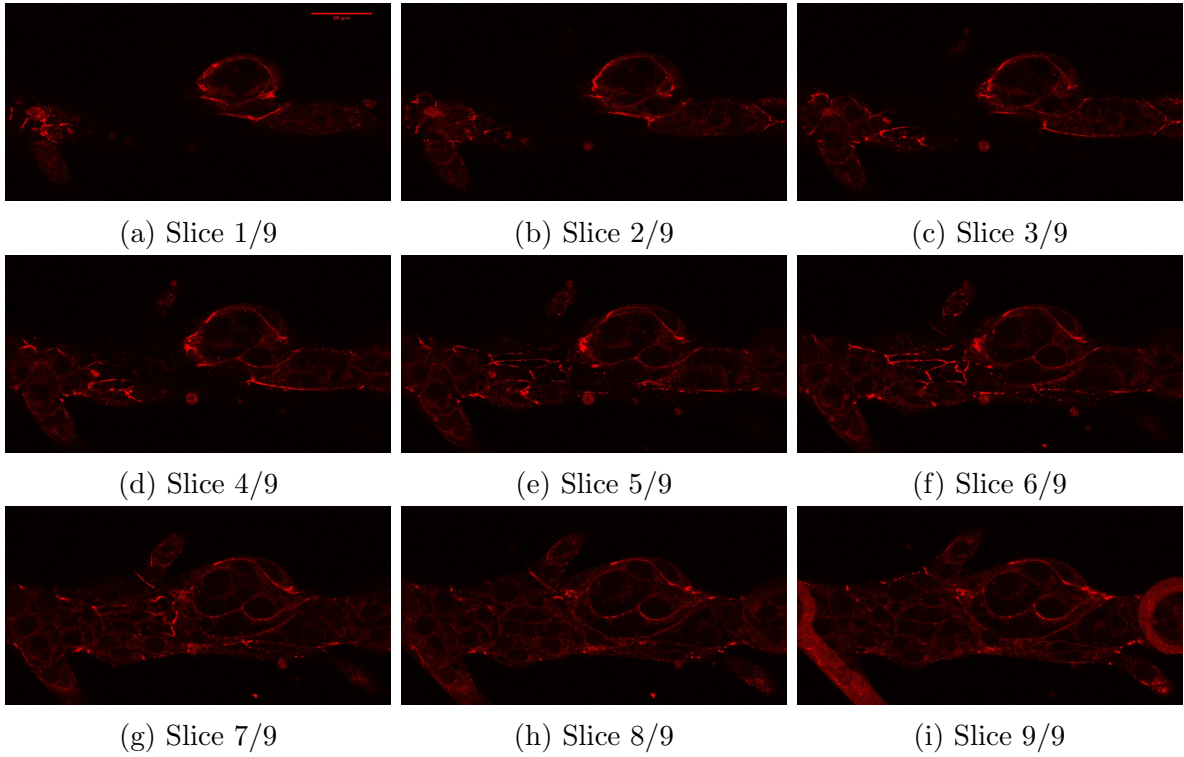
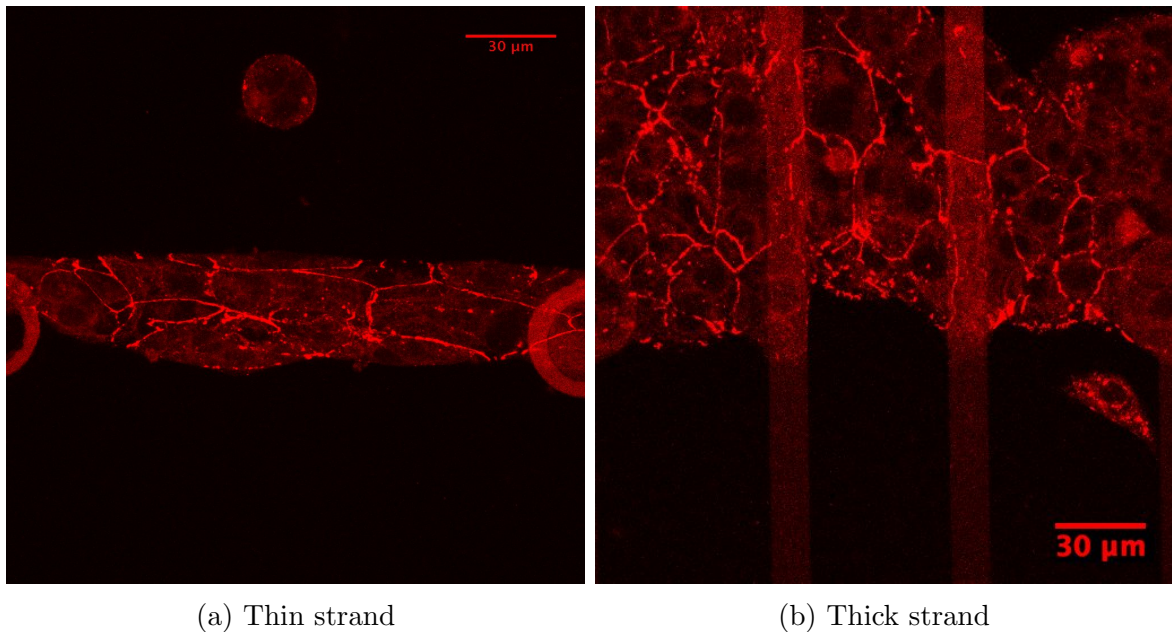


Figure 6.14: Z stack of Cx43 labelling in patterned strand reveals height profile of HL-1 cells. A second layer of proliferated cells (slices 1–5) can be observed above the monolayer (slices 5–9). Z slice thickness: $1.2\mu m$. Scale bar: $30\mu m$. HL-1 cells have a Z height of approximately $6 – 8\mu m$.

6.3.8 Electrical Recording

Seeded MEA plates were plugged in to the Multichannel recording system, and recordings were taken daily, for both intrinsic activity and paced electrical activity. Cells overgrew designed patterns after 3 days in culture, and thus recordings were only taken for up to 3 days.

No successful electrical recordings, paced or intrinsic, were recorded from the patterned HL-1 cultures within 2-3 days of seeding.



(a) Thin strand

(b) Thick strand

Figure 6.15: Z -projected, max intensity profile of Cx43 labelling reveals shape and orientation of cells on patterned strands, with patterns running east to west. Cells had greater elongation (anisotropy ratio) and smaller deviation of orientation from the horizontal axis in the thin strand. Cx43 labelling was even along all cell borders in both strand types.

6.4 Discussion

6.4.1 Summary of findings

In this chapter, an experimental protocol was described to create designer patterns of cultured cells on glass MEA plates, with the future aim of investigating the morphology of extracellular electrograms in slow conduction of excitation. The HL-1 sub clone was suggested as a suitable experimental for studies of slow conduction. Technique optimisation for patterned cell culture was carried out, and initial results on the viability of the protocol were reported.

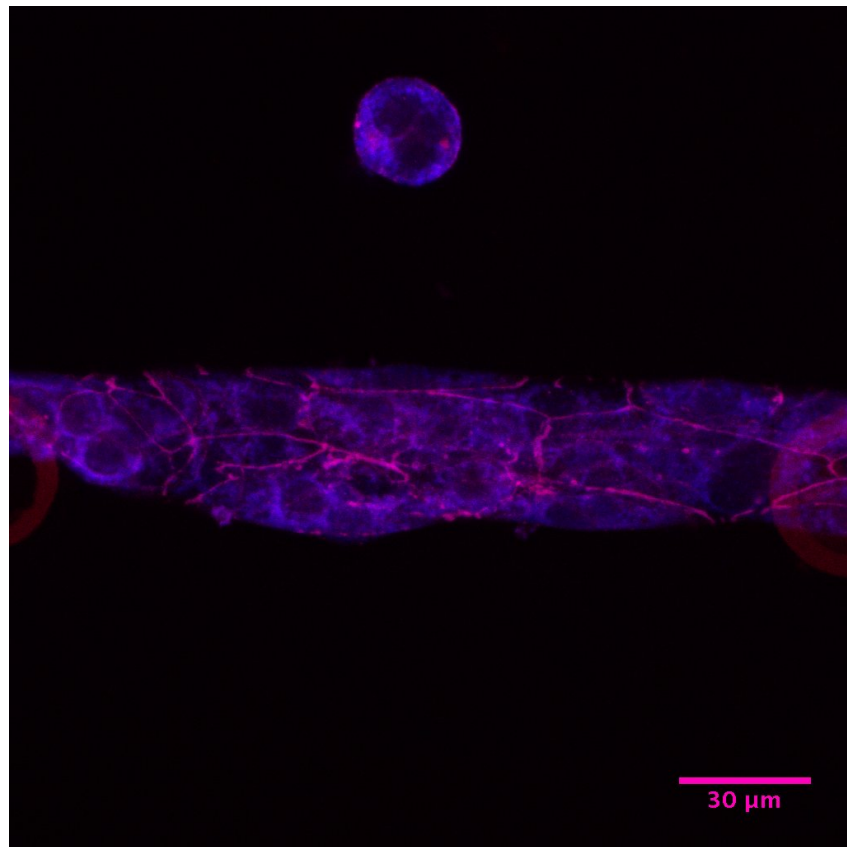


Figure 6.16: Overlaid image of Cx43 (red) and N–Cadherin (blue) labelling, summed over the Z –axis. Sites with co–localisation of Cx43 and N–Cadherin appeared purple

Viability of technique

It was observed in the present study that designer patterns of fibronectin on MEA culture plates successfully induced patterns of cell monolayer. The work was a novel attempt to implement a micro–contact printing protocol for use on commercially available glass MEA culture plates. Previous reported patterned cell cultures on cardiomyocytes have been completed on disposable coated cover-slips [Kucera et al., 2001, Rohr et al., 1998, Bursac et al., 2002, Badie, 2010], or on elastic grooved PDMS membranes [Camelliti et al., 2006, Motlagh et al., 2003].

The technical challenge in replicating this culture technique was in obtaining reliable

fibronectin transfer on to reusable glass plates; fibronectin patterns on MEAs were found to stable over a period of several weeks. Reproducing this technique reliably requires access to plasma coating facilities and an increased turnover of reusable MEA plates due to the necessity for an even surface topography on plates with deteriorating electrode insulation.

Effects of patterned culture on cell and tissue morphology

Creating designer patterns affected the shape and orientation of HL-1 cells seeded on to the pattern, compared to cells seeded in monolayers. Thin strands were observed to induce greater elongation in cells and more homogeneous orientation along the line of the pattern compared to the thicker strands, which had a larger spread of orientations and a more circular profile.

These results were consistent with existing characterisation studies on micro contact printing methods [Badie, 2010, Bursac et al., 2002, Deutsch et al., 2000, Motlagh et al., 2003], which additionally report that creating Z-grooves further assist with promoting alignment of cultured myocytes.

Cx43 distribution in patterned cells

Connexin 43 distribution was assessed on patterned HL-1 cultures via immunocytochemistry labelling on a single MEA plate, fixed 3 days after seeding. Cx43 labelling was found to preferentially locate at cell membranes (identified by co-localisation with membrane-bound N-Cadherin), compared to intracellular space, suggesting that gap junctions (GJ) may exist between neighbouring cells. The functionality of these GJs were not assessed, and further studies may be completed via dye transfer assays.

Previous HL-1 characterisation studies have indicated that connexins are evenly distributed around the cell border of HL-1 cells in monolayers, due to their lack of structured shape and orientation [Dias, 2010, p.188], [Chowdhury, 2011]. In the current work, analysis of Cx43 distribution via immunocytochemistry did not reveal any conclusive evidence to suggest that the anisotropic cell shape, induced by patterned cell culture, led to increased Cx43 labelling along the cell short axis, as is conventional in normal myocardium. Other optimisation studies have reported limited success in inducing gap junctional cell end localisation in otherwise-anisotropic cell culture designer patterns [Badie, 2010, p.62], compared to tissue sections. This suggests that modifying cell shape and orientation alone in designer cell cultures may not be sufficient to mimic gap junctional distributions in real myocardium.

The current work looked only at expression of Cx43 in HL-1 cells, although it has been reported that Cx40 and Cx45 are also present [Dias, 2010], which may be worth targeting in further studies.

Electrogram recording of HL-1 on patterned strands

No electrical response could be recorded on patterned strands of HL-1 cells, up to and including 3 days after seeding. It has been reported in previous characterisation studies [Chowdhury, 2011] that monolayers of HL-1 cell line require up to 7 days in culture to fully develop electrical excitability and peak conduction velocity of $30 - 40\text{mm/s}$, with conduction velocity dependent upon the day of culture. This indicates several key problems in attempting to use the HL-1 cell line for patterned cell culture:

- Electrical conduction in 1D patterned strands can only be reliably correlated to 1D conduction models if strands remain disconnected. The time duration for HL-1 myocytes to develop electrical activity is greater than the time duration by which

cell proliferation leads to overgrowth of cells outside the pattern and in the Z-direction.

- The signal to noise ratio of recording activity in thin patterned strands is necessarily lower than ratios obtained from full monolayers. Future theoretical studies may be undertaken to assess the minimum strand width to generate a signal large enough to be captured on existing systems. Optical mapping has been successfully used in previous functional studies of patterned cell culture [[Kucera et al., 2001](#)], which suggest the signal to noise ratio is not an insurmountable challenge.

Summary and future applications

The technique of creating patterned cell culture on commercial MEA plates described in this chapter is novel method for measuring extracellular electrograms using a non-toxic, non-invasive method. However, many technical hurdles still exist and further quantitative studies will be needed to fully develop the utility of the technique. The technique may assist topics for further study, such as the following:

- Conduction within neonatal rat ventricular myocytes (NRVMs) may be studied using this technique, as NRVMs exhibit higher baseline speeds of electrical conduction [[Meiry et al., 2001](#)].
- Questions involving interfaces of different cardiac cell types can conceivably be studied through patterned cell growth, such as *in-vitro* analysis of conduction and electrogram properties within the transmural wall, from endocardium to epicardium.
- Source-sink based problems [[Rohr et al., 1997](#)] have long been studied using designer cultures, and have continued to be studied in recent years [[de Lange and Kucera, 2009](#)].

6.5 Work in progress: Development of a mathematical model of the HL1–6 action potential

A primary aim within this chapter was to establish an experimental model of slow conduction, to which theoretical models could be compared. The HL1–6 has previously been shown to exhibit slow baseline conduction velocity [Dias, 2010, Chowdhury, 2011]. However no current mathematical models of the murine HL–1 action potential exist in the literature. Establishment of a mathematical model of the HL–1 action potential would allow electrophysiology and conduction experiments using the HL–1 cell line to be reproduced *in-silico* with a monodomain or bidomain tissue coupled with the HL–1 AP model.

Initial work to develop a mathematical model of an HL-1 sub clone cell line was undertaken during the present period of research, and is presented in Appendix B. The work includes evaluation of the literature concerning functional characteristics of the mouse atrial myocyte, and existing mathematical models of rodent, murine or atrial action potentials. An initial mathematical model was proposed based on these findings and on experimental data, with the resoling AP morphology in a single cell matching experimental AP curves. However, other properties did not match experimental data.

Investigation and refinement of the model is a work in progress, and hence the initial results are presented in the Appendix for reference.

Chapter 7

Developing a 1D mathematical model of conduction in discrete coupled myocytes

7.1 Introduction

This chapter outlines the development and implementation of a model of discrete coupled myocytes in one dimension. The model breaks from the continuum assumption that electrical behaviour in tissue can be averaged over many cells, instead addressing single myocytes, each modelled as a continuum, which are coupled together via conditions on the cell boundaries that represent gap junctions. The aim of this study was to compare this model with continuum models to assess under what conditions the latter can still be considered a valid approximation.

A histologically detailed approach has been considered in other studies. Keener and Sneyd [2009] derived analytical solutions for a passive 1D case, whilst numerically Shaw

and Rudy [1997] have numerically implemented a 1D chain of ‘coupled’ myocytes, by adopting an alternative junctional resistance at periodic intervals within a cable model. A 3D computational model, described by Stinstra et al. [2010] coupled with the LR–1 model represents the most histologically representative model, with an additional capacitance term co-located at cell ends with gap junctions. However, the full 3D model is very computationally intensive, and a simpler model may provide additional insights to existing literature without significant computational resources. A 1D fully discrete myocytes with active ion channels following the description of Stinstra has not been fully explored within the literature and will be the focus of the present work. The outline of the chapter is given below.

A simple mathematical monodomain model of voltage potential in cells coupled by gap junctions and a membrane capacitance was explored, as a preliminary study to investigate the analytical behaviour of simple cells to a boundary stimulus. The mathematical and physiological insights from this work, presented in Appendix C, was subsequently applied to the main results presented in this chapter.

The passive 1D problem outlined in section 12.3.1 of Keener and Sneyd’s *Mathematical Physiology* [Keener and Sneyd, 2009] is introduced, implemented numerically and validated against the theoretical solution. From this, the full 1D discrete model is described, based on the 3D discrete model described by Stinstra et al. [2010] and the Keener and Sneyd model outlined. Capacitance and ionic channel kinetics are added to the model, physiological extensions to the model are posed and implemented, and the results are presented. Finally, simulation results of the discrete model are compared with results from a continuum model, the details of which have been presented earlier. Physiological parameters are modulated and the effect on conduction velocity, action potential upstroke

and the virtual electrogram are presented and compared.

7.2 The discrete cell chain model

Consider a line of connected cylindrical myocytes of length L and radius a , contained within extracellular space. Myocytes are coupled end-to-end via gap junctions, as described in Keener and Sneyd [2009]. A cylindrical coordinate system $\mathbf{x} = (r, \theta, x)$ is defined with x in the direction of the myocyte long axis. The extracellular space has cross sectional area $\Omega(x)$ which varies in the x direction. The intracellular potential $v_i(\mathbf{x}, t)$ is defined within the myocytes and the extracellular potential $v_e(\mathbf{x}, t)$ within the extracellular space. A one dimensional bidomain model is constructed by defining the average intracellular and extracellular potentials $V_i(x, t)$ and $V_e(x, t)$ for given x , and the resulting transmembrane potential $V_m(x, t) = V_i - V_e$.

At point x , the average cross sectional intracellular potential V_i is given by

$$V_i = \frac{1}{\pi a^2} \int v_i dA$$

and the average cross sectional extracellular potential is

$$V_e = \frac{1}{A_e(x)} \int_{\Omega(x)} v_e dA$$

Then, the cable equation within each cell is given by:

$$p \left(C_m \frac{\partial V_m}{\partial t} + I_{ion} \right) = \frac{\partial}{\partial x} \left(\frac{1}{r_i} \frac{\partial V_i}{\partial x} \right) = - \frac{\partial}{\partial x} \left(\frac{1}{r_e} \frac{\partial V_e}{\partial x} \right) \quad (7.1)$$

with $r_i = \frac{R_i}{A_i}$ and $r_e = \frac{R_e}{A_e}$, where R_i, R_e are the resistivities of intracellular and extracellular space, $A_i = \pi a^2$ and A_e are the average cellular intracellular and extracellular

cross-section areas, and $p = 2\pi a$ is the circumference of the cell. There is a jump in intracellular potential at the ends of the cell where the gap junctions are located. The intracellular current is given by $-\frac{1}{r_i} \frac{\partial V_i}{\partial x}$ and is continuous within the cell.

Assuming that the gap junctions behave like ohmic resistors, the drop in potential across the junction is proportional to the current through the junction. Then:

$$\frac{[V_i]}{r_j} = \frac{1}{r_i} \frac{\partial V_i}{\partial x}, \quad (7.2)$$

with $[V_i]$ the jump in the intracellular potential across the gap junctions and r_j the effective gap junctional resistance.

I_{ion} is taken to be a constant applied current across the cell membrane at every point, i.e.

$$I_{ion} = \frac{V_m}{R_m} = \frac{V_i - V_e}{R_m}. \quad (7.3)$$

To calculate the space constant in this problem, Keener and Sneyd sought to find the steady state solution to the problem by application of suitable boundary conditions on the cable which simulate a held potential or current at one end of the cable. This solution was then used to obtain a relation between the space constant and the effective non-dimensional gap junctional resistance.

Keener and Sneyd obtained a steady state solution to this problem, which is presented in the subsection 7.2.1. This steady state solution is plotted in Matlab, and the problem is simulated by iterating a time-dependent implementation of the system above to a steady state solution. Following on from this, the constant transmembrane currents in the

system is adapted with voltage and time dependent transmembrane currents representing a mathematical action potential model, to simulate action potential propagation across discrete cells.

7.2.1 Analytical solution: steady state passive problem, Dirichlet boundary conditions

In this section, we describe the steady state solution developed by [Keener and Sneyd \[2009\]](#). For a constant stimulus on one end of the cable (Dirichlet boundary condition), assume a geometrically decaying solution, with $V_i(x + L) = \mu V_i(x)$, $V_e(x + L) = \mu V_e(x)$ for a decay constant $\mu < 1$. The decay constant is related to the space constant λ_g by the following expression:

$$\mu = e^{-L/\lambda_g} \quad (7.4)$$

The analytical solution to this steady-state problem for a given cell can be found, which is briefly summarised below. For the n -th cell, the solution is proportional to

$$\begin{pmatrix} V_i \\ V_e \end{pmatrix}_n = \mu^n \Phi(\mu, x) = \mu^n \begin{pmatrix} \phi_i \\ \phi_e \end{pmatrix} \quad (7.5)$$

and thus at steady state, Equation (7.1) can be rewritten as:

$$\frac{\partial}{\partial x} \left(\frac{1}{r_i + r_e} \frac{\partial \phi_m}{\partial x} \right) - \frac{p \phi_m}{R_m} = 0, \quad \phi_m = \phi_i - \phi_e. \quad (7.6)$$

The solution to this equation is given by:

$$\phi_m = \alpha_1 \exp(\lambda x) + \alpha_2 \exp(-\lambda x), \quad (7.7)$$

where $\lambda^2 = \frac{p}{R_m}(r_i + r_e)$, then the solutions are given by:

$$\phi_i = \frac{r_i}{r_i + r_e} \phi(x) + \beta, \quad \phi_e = -\frac{r_e}{r_i + r_e} \phi(x) + \beta. \quad (7.8)$$

Using the boundary conditions of continuity of current, continuity of extracellular potential and the jump condition for the intracellular potential at the gap junction, the constants are determined by:

$$\alpha_1 = \mu - \frac{1}{E}, \quad \alpha_2 = \mu - E, \quad \beta = 2 \frac{r_e}{r_i + r_e} \frac{(\mu - E)(\mu - \frac{1}{E})}{\mu - 1}, \quad E = e^{\lambda L} \quad (7.9)$$

where μ is the root of the characteristic equation:

$$\frac{r_j \lambda}{r_i + r_e} = \frac{R_j}{\lambda L} = 2 \frac{(\mu - \frac{1}{E})(\mu - E)}{\mu(E - \frac{1}{E})} \quad (7.10)$$

with $R_j = \frac{L p r_j}{R_m}$ being the effective non-dimensional gap-junctional resistance. The plot of the analytical solution is reproduced in Figure 7.1:

As shown, the intracellular potential V_i decays geometrically with jumps at cell-cell boundaries due to gap junctional resistance, whilst the extracellular potential V_e decays smoothly. Numerical implementation of this model will be presented in Section 7.3.2.

7.2.2 Analytical solution: steady state passive problem, Neumann boundary conditions

The previous section considered the analytical solution for a line of passive cells coupled by gap junctions, with a constant potential held on one end of the cells. This constant potential boundary condition is a first approximation to the passive problem, and more realistic boundary conditions may be considered. The alternative boundary value problem, also considered by [Keener and Sneyd \[2009\]](#), models the problem with a current

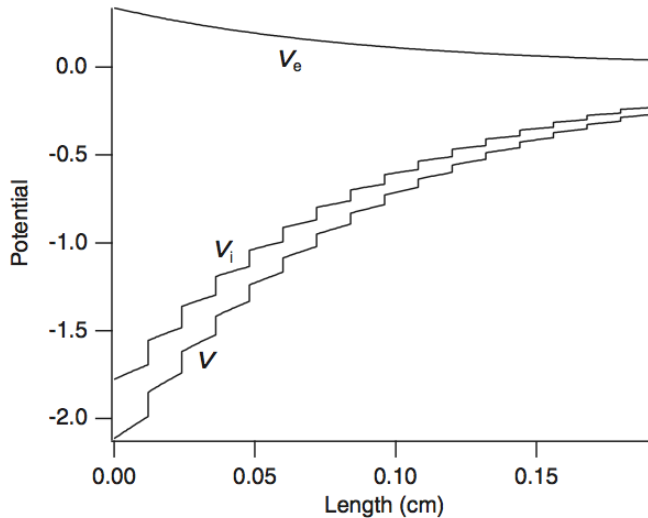


Figure 12.22 Plot of intracellular, extracellular and transmembrane potentials as functions of space, with a constant subthreshold potential maintained at a single point. For this plot cells had $L = 0.012 \text{ cm}$, $A_i = 4.0 \times 10^{-6} \text{ cm}^2$, and a space constant $\lambda_g = 0.09 \text{ cm}$. $R_m = 7000 \Omega\text{cm}^2$, $R_c = 150 \Omega\text{cm}$, $q_e = 0.5q_i$, $q_i = 5.47 \times 10^{-3}$, where $q_j = \frac{L^2\rho}{R_m}r_j$, $j = i, e$. The vertical scale on this plot is arbitrary.

Figure 7.1: Analytical solution, Dirichlet boundary conditions, from [Keener and Sneyd, 2009, p.556]

injection in to the extracellular space instead of direct current flow in to the intracellular space. This is a Neumann problem and the boundary conditions are given by:

$$-\frac{1}{r_e} \frac{dV_e}{dx} = I, \quad \frac{1}{r_i} \frac{dV_i}{dx} = 0, \quad (7.11)$$

at the ends of the cable, $x = 0, l$. The solution to this on the interior of the cells is given by:

$$\begin{pmatrix} V_i \\ V_e \end{pmatrix}_n = \frac{1}{r_e + r_i} \begin{pmatrix} r_i \\ -r_e \end{pmatrix} V_n + \begin{pmatrix} 1 \\ 1 \end{pmatrix} (-\beta Ix + \gamma_n), \quad (7.12)$$

and $V_n = (A_n + \frac{r_e}{\lambda} I) \sinh \lambda x + B_n \cosh \lambda x$, for $n = 0, 1, \dots, N - 1$, where

$$A_n = \frac{-S}{1-\mu}(\mu c_1 - c_2)f_n, \quad (7.13)$$

$$B_n = \frac{\mu c_1 - c_2}{1-\mu} \left(C f_n + \frac{1-\mu^N}{1-\mu^{2N}} (\mu^{n+1} + \mu^{N-n-1}) \right) - \frac{c_1 - \mu c_2}{1-\mu}, \quad (7.14)$$

$$f_n = \frac{1 - \mu^{N-n} - \mu^n + \mu^{N+n} + \mu^{2N-n} - \mu^{2N}}{1 - \mu^{2N}}, \quad (7.15)$$

$$\gamma_{n+1} = \gamma_n - L\beta I + \frac{\beta}{r_i} K_g \left(\frac{r_e}{\lambda} I(C-1) + A_n C + B_n S \right), \quad (7.16)$$

$$C = \cosh \lambda L, \quad S = \sinh \lambda L, \quad c_i = \frac{S(1-\eta_i) + \eta_i K_g(1-C)}{S(2 + K_g \eta_i + K_g C)}, \quad (7.17)$$

with $\eta_1 = \frac{1}{\mu}$, $\eta_2 = \mu$, where $\mu < 1$ is the root of the characteristic equation (7.10), and $k_g = \frac{r_j \lambda}{r_i + r_e} = \frac{R_j}{\lambda L}$, $\beta = \frac{r_i r_e}{r_i + r_e}$. The analytical solution of the transmembrane potential V_m from [Keener and Sneyd \[2009\]](#) is reproduced in Figure 7.2:

This produces a ‘sawtooth’ potential, showing inter-cell jumps in the transmembrane potential V_m . The global behaviour of V_m differs from the Dirichlet problem, in that the solution to the Dirichlet problem exhibits an exponential drop, whereas the greatest V_m variations in the Neumann problem occur near the cable boundaries, with little variation in mean V_m in the centre of the cable.

Results from the implementation of this model will be presented in Section 7.3.3.

7.2.3 Unsteady passive problem, no flux boundary condition with time dependent stimulus

Neumann boundary conditions represent fixed currents on the cable ends. Here, the Neumann conditions are adopted to create a cable with zero current (no-flux) conditions on both ends of the cable. The model still contains the passive transmembrane current $I_{ion} = \frac{V_m}{R_m}$. In order to alter the model to represent a sealed cable with an injected current

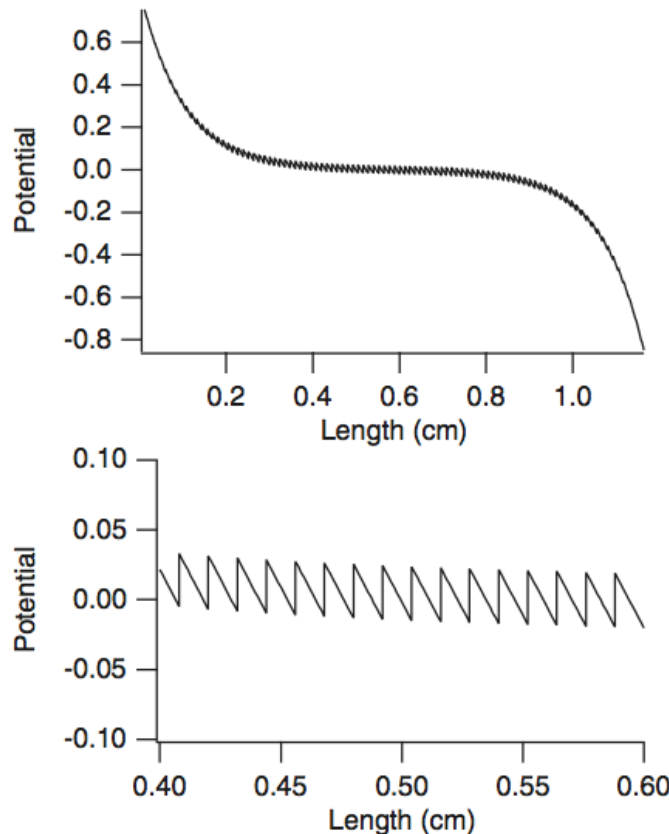


Figure 12.23 Plot of transmembrane potential as a function of space, with a constant applied current. For this plot cells had $L = 0.012 \text{ cm}$, $A_i = 4.0 \times 10^{-6} \text{ cm}^2$, and a space constant $\lambda_g = 0.09 \text{ cm}$. $R_m = 7000 \Omega\text{cm}^2$, $R_c = 150 \Omega\text{cm}$, $q_e = 0.5q_i$, $q_i = 5.47 \times 10^{-3}$, where $q_j = \frac{L^2 p}{R_m} r_j$, $j = i, e$. The vertical scale on this plot is arbitrary.

Figure 7.2: Analytical transmembrane solution, Neumann boundary conditions from [Keener and Sneyd, 2009, p.559]

near one end, a time dependent forcing stimulus on the several cells at one end of the cable is implemented, via addition of non-zero, time varying forcing terms to the right of the system equations (I_{stim}).

$$A \begin{pmatrix} V_i \\ V_e \end{pmatrix}_{n+1} = B \begin{pmatrix} V_i \\ V_e \end{pmatrix}_n + I_{stim} \quad (7.18)$$

The problem was solved numerically for 84 cells (approximately 1cm of cells). Numerical implementation of this model will be presented in 7.3.4.

7.2.4 Outline of the 1D discrete model with active ion channel kinetics

The 1D analytical model outlined by [Keener and Sneyd \[2009\]](#) predicts steady state solutions for discrete passive cells coupled by gap junctions. It does not offer detailed physiological insight for biophysical cardiac cells with active ion channel kinetics.

Such a model has been described mathematically in 3D by the Henriquez group at Duke University, notably by the PhD work of [Roberts \[2009\]](#) and the work of [Stinstra et al. \[2010\]](#). Their ‘micro domain’ model describes a histologically influenced 3D computer model to study propagation at a multicellular model. Several ‘slices’ of randomly generated myocyte cross-sections, are extruded in the z -axis to create a 3D block of 64 myocytes, on which the bidomain equations are solved with the LR-1 guinea pig ventricular cell model [[Luo and Rudy, 1991](#)].

Three types of boundary conditions were used, modelling the intracellular-intracellular coupling, extracellular-intracellular boundaries and also the periodic boundary conditions at the edges of the tissue block. The model was used to examine the effect of non-uniform interstitial loading, and on the validity of using a continuum versus micro domain model in 3D.

The micro domain model described by Stinstra is extremely computationally intensive; it required 36 hours to solve the full 3D problem incorporating a $1mm \times 0.06mm \times 0.092mm$ size domain. Thus a simpler 1D model based on this micro domain model may

offer a significant reduction in computation resources, whilst still providing physiological insight into models of discrete cells.

Thus, a novel 1D discrete model coupled with active ion channel kinetics was proposed to be an improved model for simulating discrete propagation, compared to the existing 1D models. This was initially based on the Keener and Sneyd model, but was altered to more closely resemble the micro domain model outlined by Stinstra.

Notably, the cell-cell boundary was modelled to include membrane capacitance C_m alongside gap junctional resistance R_j . Also, the passive membrane resistance term, was replaced by the Luo Rudy-1 ion channel kinetics (Section 3.2.2). The full model for a pair of cells is proposed and outlined below:

$$p \left(C_m \frac{\partial V_m}{\partial t} + I_{ion} + I_{stim} \right) = \frac{\partial}{\partial x} \left(\frac{1}{r_c} \frac{\partial V_i}{\partial x} \right) = - \frac{\partial}{\partial x} \left(\frac{1}{r_e} \frac{\partial V_e}{\partial x} \right) \quad (7.19)$$

$$\sigma_e \frac{\partial^2 V_e}{\partial x^2} = 0 \quad (7.20)$$

where $V_m = V_i - V_e$, the difference between intracellular and extracellular potentials. The equations are subject to the following boundary conditions between adjacent cells 1 and 2:

$$\left(\frac{1}{r_c} \nabla V_{i1} \right) \cdot \hat{n} = C_m \frac{\partial V_{i1} - V_{i2}}{\partial t} + R_j (V_{i1} - V_{i2}), \quad (7.21)$$

$$\left(\frac{1}{r_e} \nabla V_{i2} \right) \cdot \hat{n} = -C_m \frac{\partial V_{i1} - V_{i2}}{\partial t} - R_j (V_{i1} - V_{i2}), \quad (7.22)$$

where $p = 2\pi a$ is the cross sectional circumference of the cell, r_c and r_e the intracellular and extracellular resistivities, and R_j the the resistance due to gap junctions. V_{i1} denotes

the intracellular potential on the end of cell 1 and V_{i2} denotes the intracellular potential on the start of cell 2. No flux boundary conditions were modelled on both the intracellular and extracellular ends of the cable. There is a jump in intracellular potential at the ends of the cell where the gap junctions are located.

Implementation details are provided in Section 7.3.5.

7.3 Results: Implementation and validation of the 1D discrete model

The numerical implementation of Keener and Sneyd [2009] was compared against the analytical solution described, and subsequently adapted to the full 1D discrete model described in Section 7.2.4.

7.3.1 Implementation of the Keener and Sneyd model

Equation (7.1) was solved in MATLAB using a finite difference method. A second order central difference scheme was used for the diffusion, with an implicit backward Euler scheme to march the solution forward in time. For the full model with ion channel kinetics, an explicit forward Euler scheme with the Rush–Larsen algorithm [Rush and Larsen, 1978] was used to obtain gating variables and the ionic currents at future time steps.

The domain was divided into cardiac cells of length L , and each cell was divided into N points, giving a spatial discretisation of $\Delta x = L/Ncm$. Due to this finite difference discretisation, there is an inter-cell spacing of length Δx between each cell, which tends to 0 as $\Delta x \rightarrow 0$.

The following system parameters were used [Keener and Sneyd, 2009]:

Parameter	Value	Description	Unit
L	0.012	Length of cell	cm
A_i	4×10^{-6}	Average intracellular cross sectional area	cm ²
λ_g	0.09	Space constant	cm
R_m	7000	Membrane resistance	Ωcm ²
R_i	150	Resistivity of intracellular space	Ωcm
R_e	75	Resistivity of extracellular space	Ωcm

Table 7.1: Parameters used in [Keener and Sneyd \[2009\]](#) for discrete model.

Discretisation of gap junctional boundary conditions

A second order one-sided derivative stencil was used to approximate the gap junctional boundary condition (7.2) via Taylor expansion of the boundary condition. For two cells discretised in to points $1, \dots, N, N+1, \dots, 2N$ respectively, the gap junctional boundary condition at point N , the end of the first cell, $N+1$, the start of the second cell, respectively is approximated by

$$\frac{\partial V_i}{\partial x} = \frac{r_j}{2r_i\Delta x}(V_i^{N-2} - 4V_i^{N-1} + 3V_i^N) \quad (7.23)$$

on cell 1,

$$\frac{\partial V_i}{\partial x} = -\frac{r_j}{2r_i\Delta x}(3V_i^{N+1} - 4V_i^{N+2} + V_i^{N+3}) \quad (7.24)$$

on cell 2.

Choice of boundary conditions

This is discussed in detail in the following sections for each of the problems.

7.3.2 The passive Dirichlet problem

The numerical implementation was followed as above, to compare and validate the numerical model against the theoretical solution predicted by Keener and Sneyd.

Steady state model

The analytic solution described earlier is plotted, against which other solutions will be validated. The value of the transmembrane potential at $x = 0$ is determined by the boundary

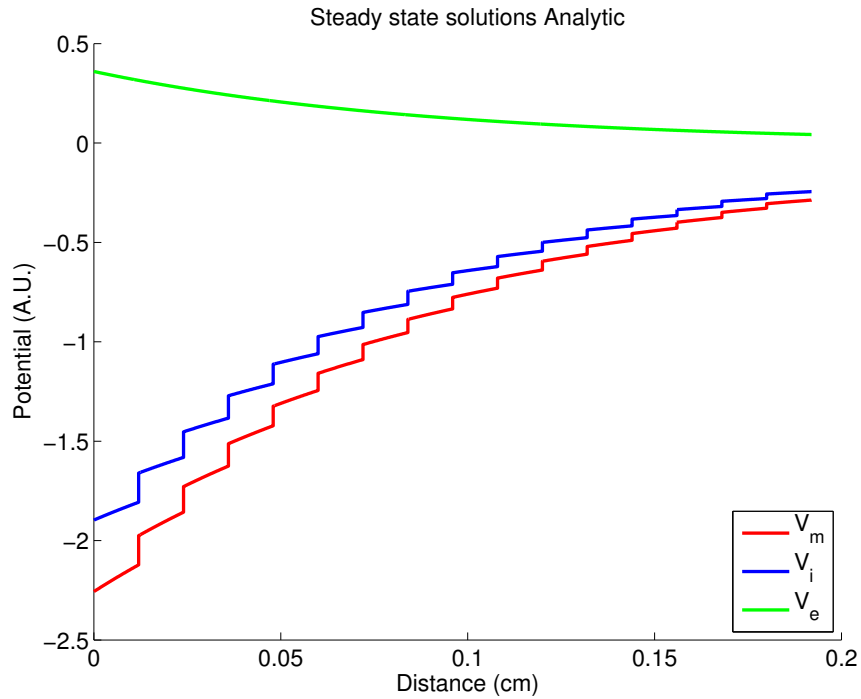


Figure 7.3: Analytical solutions for 16 cells at steady state, held at fixed potential at both ends of the cable.

conditions of the analytic solution found earlier, obtaining that $V_m(0) = 2\mu$. With the choice of parameters in this problem, this gave boundary conditions of $V_i(0) = -1.8969$ and $V_e(0) = 0.3598$.

In the numerical implementation of the gap junctions, three discretisations are implemented for the jump in intracellular potential $[V_i]$ (7.2) across the gap junction between cell pairs:

- Version 1: $[V_i] = V_i^N - V_i^{N+1}$ on cell 1, $[V_i] = V_i^N - V_i^{N+1}$ on cell 2, denoted SSV1.
- Version 2: $[V_i] = V_i^{N-1} - V_i^{N+1}$ on cell 1, $[V_i] = V_i^N - V_i^{N+2}$ on cell 2, denoted

SSV2.

- Version 3: $[V_i] = V_i^{N-1} - V_i^{N+2}$ on cell 1, $[V_i] = V_i^{N-1} - V_i^{N+2}$ on cell 2, denoted SSV3.

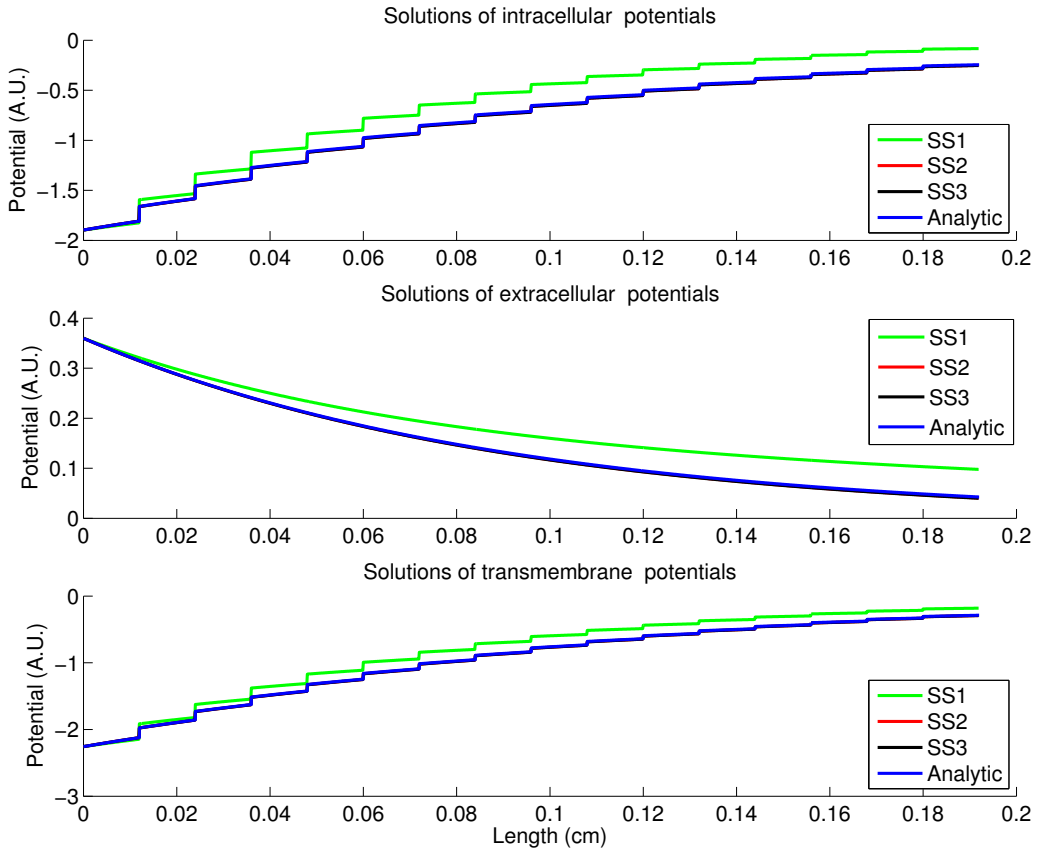


Figure 7.4: Three different steady state implementations of the trans-junctional jump, plotted against the analytic solution. SSV2 and SSV3 are behind the analytic curve and cannot be observed.

Fig. 7.4 shows the numerical solutions match closely to the analytic solution, for each of the three domains V_i , V_e and V_m . Zooming in to the transmembrane potential V_m as shown in Fig. 7.5, the SSV2 and SSV3 implementations are very close to the analytic solution and cannot be observed.

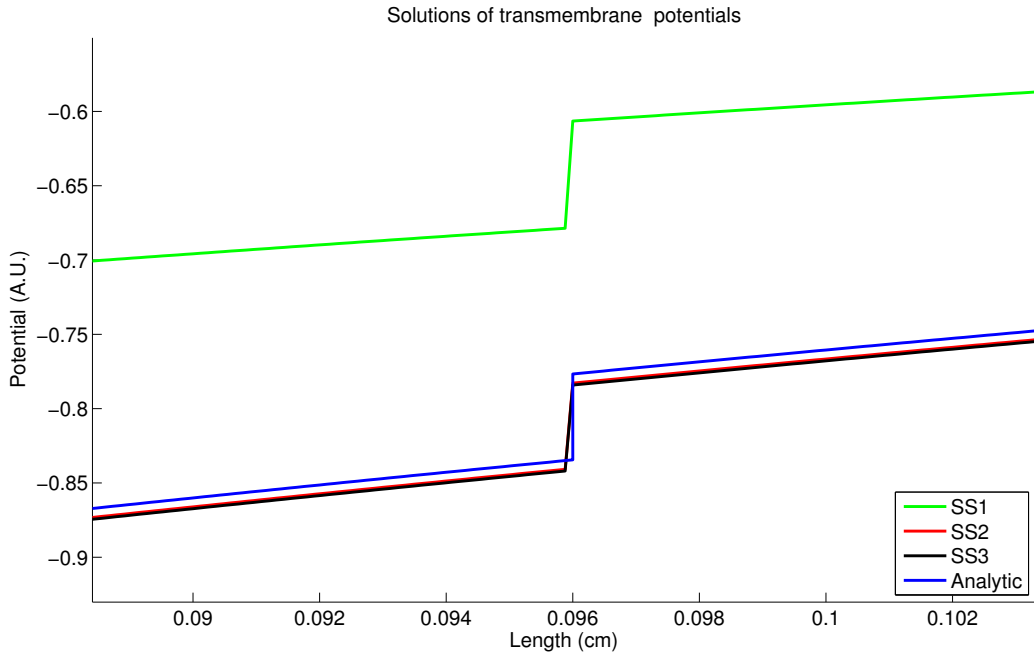


Figure 7.5: Transmembrane solutions for all cases, zoomed

The difference in the solution at this resolution is due to the discretisation differences: the analytic solution plots the potential behaviour over a single cell and this decays by a factor of μ^{K-1} for each K th cell, allowing for a vertical discontinuity or jump at the end and beginning of cells.. The numerical solution is finite difference and hence there is a gradient between the solutions in different cells.

Step size error versus analytical solution

To investigate the error of the numerical solution, the mean squared error was compared between the numerical steady state solution version 2 (SSV2) and the analytic solution, and plotted this against decreasing step size Δx .

As shown in Fig. 7.6, the accuracy of the numerical solution improves with decreasing Δx (h), with the steepest gradient of around 2 initially - this indicates initial second

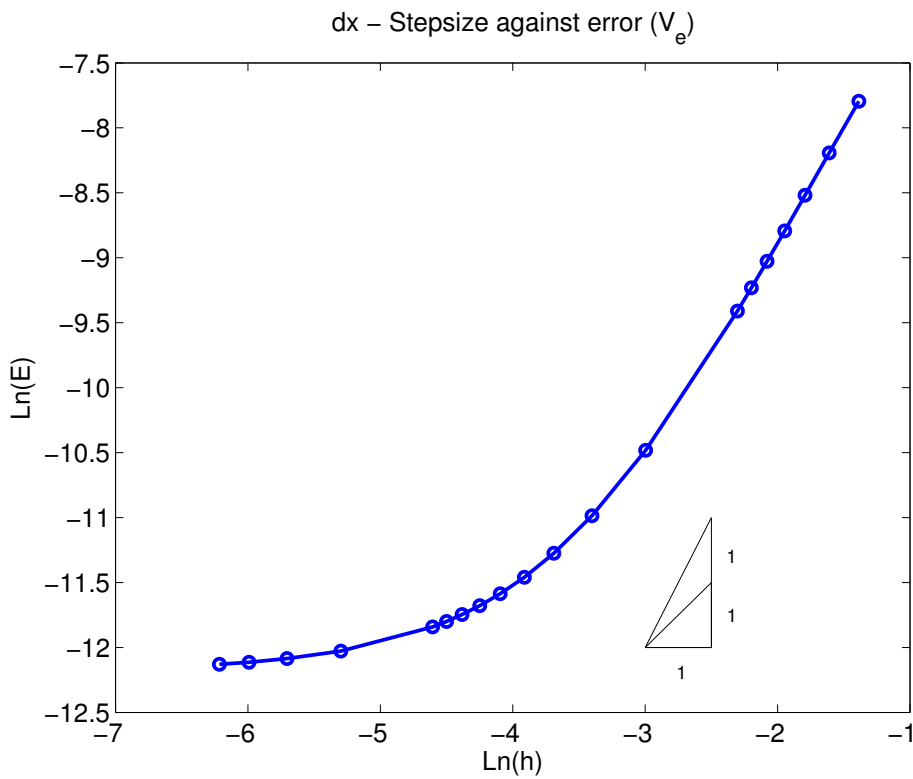


Figure 7.6: $\ln \Delta x$ (h) against \ln error (E)

order convergence. The rate of convergence slows and suggests that the solution reaches machine precision for small Δx .

Time dependent model

Equation (7.1) was implemented with a time dependent solution. Using a backward Euler implicit discretisation for time, where $V_{j_m}^i$ denotes the potential of V_j at space point i at time point m , the following discretised equation was obtained:

$$\begin{aligned}
\frac{R_m C_m}{\Delta t} [(V_{i,m+1}^i - V_{e,m+1}^i) & - (V_{i,m}^i - V_{e,m}^i)] + V_{i,m+1}^i - V_{e,m+1}^i, \\
& = \frac{R_m}{pr_i} \frac{V_{i,m+1}^{i+1} - 2V_{i,m+1}^i + V_{i,m+1}^{i-1}}{(\Delta x)^2}, \\
& = -\frac{R_m}{pr_e} \frac{V_{e,m+1}^{i+1} - 2V_{e,m+1}^i + V_{e,m+1}^{i-1}}{(\Delta x)^2}.
\end{aligned} \tag{7.25}$$

The boundary conditions were kept the same as in the steady state implementation in the previous section. A parameter $\xi = \frac{R_m C_m}{\Delta t}$ was defined in the implementation, and used to calculate the final solution. $C_m = 1e^{-6}\mu F/cm^2$ was taken in initial calculations. Fig. 7.7 shows the numerical time dependent solution at steady state (outputted at $5ms$) against the SSv2 solution plotted earlier. The solutions are qualitatively similar.

Convergence checking

A convergence analysis was performed for decreasing Δt with the expectation that reducing the size of temporal discretisation should improve the accuracy of the model. The simulation was run for time steps up to a timepoint of $5ms$ and the solution was compared with the steady state solution earlier. Figure 7.8 shows the dependence of $\log dt$ against $\log error$. There is a negative power law relationship with a gradient of around -2 , which imply that decreasing dt increases the error of the solution. However the actual value of the errors are very small, and this result may be meaningless. It was observed that at this capacitance value, the solution reached steady state within one or two time steps, regardless of the temporal discretisation.

A larger capacitance $C_m = 5e^{-6}\mu F/cm^2$ was considered to slow down the physical problem. This was compared to $C_m = 1e^{-6}\mu F/cm^2$ and the rate of convergence at several time points prior to the steady state solution was considered, the results of which are

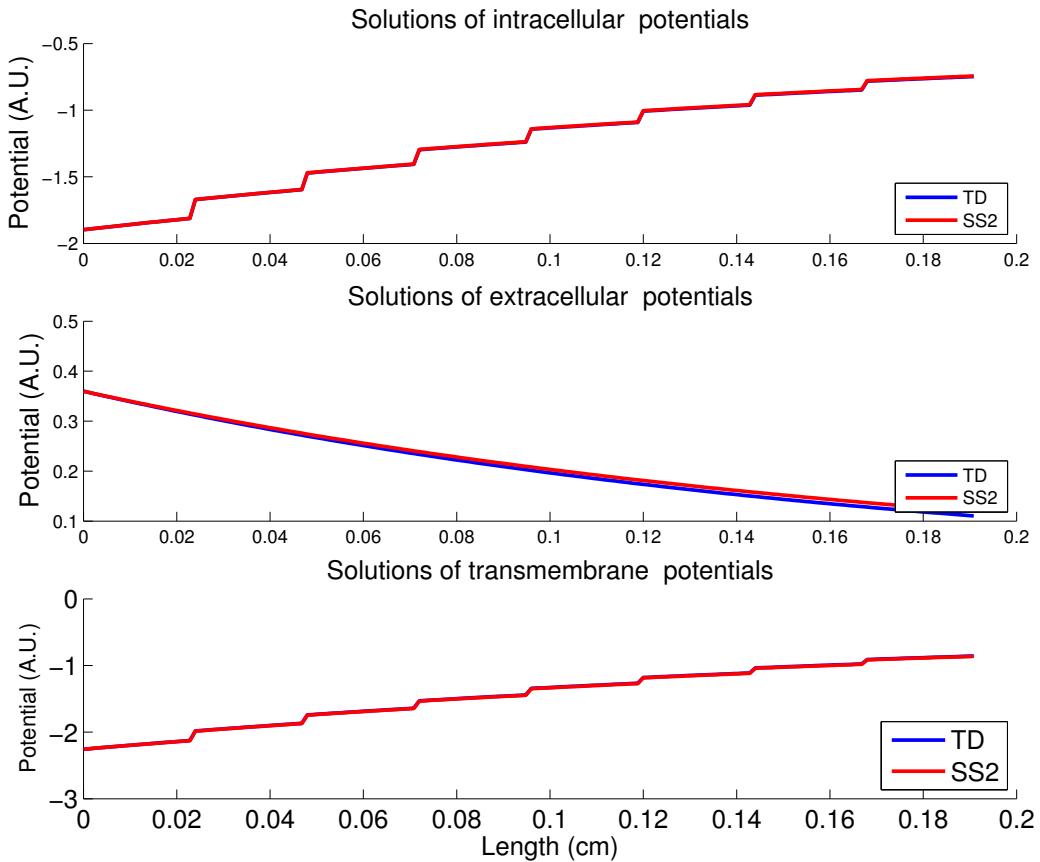


Figure 7.7: Time dependent numerical solution against Steady State solution (V2).

plotted in Fig. 7.9.

For this value of C_m , it can be seen that accuracy initially improves with decreasing dt , for the first few time steps, but that the solution again becomes less accurate for $\log dt \approx 3.5$.

7.3.3 The passive Neumann problem

The second analytical problem presented earlier consists of Neumann boundary conditions representing current flow in and out of the extracellular space at the ends of the

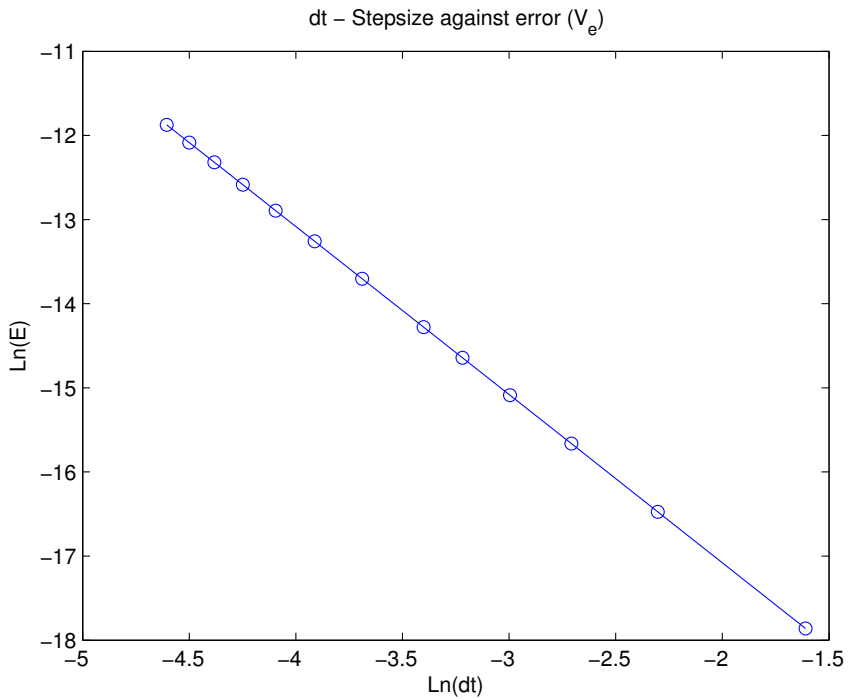


Figure 7.8: $\text{Ln } dt$ against Ln error, at steady state ($t=5\text{ms}$).

cable, and no flux conditions in and out of the intracellular space on the boundaries of the domain.

This was implemented with first order spatial derivatives:

$$V_{em}^i - V_{em}^{i+1} = r_e \Delta x I \quad (7.26)$$

$$V_{im}^i - V_{im}^{i+1} = 0 \quad (7.27)$$

However, using a fully set of Neumann boundary conditions makes the mass matrix non-invertible. Thus, on the end of the cable (around 1cm), Dirichlet boundary conditions $V_e(1\text{cm}) = 0$ were imposed, to pin a unique solution. The injected current on the extracellular space on the left end of the cable was simulated by taking $I = -4e^{-7}$ (non dim.); this value was obtained by tweaking input conditions to produce matching values from

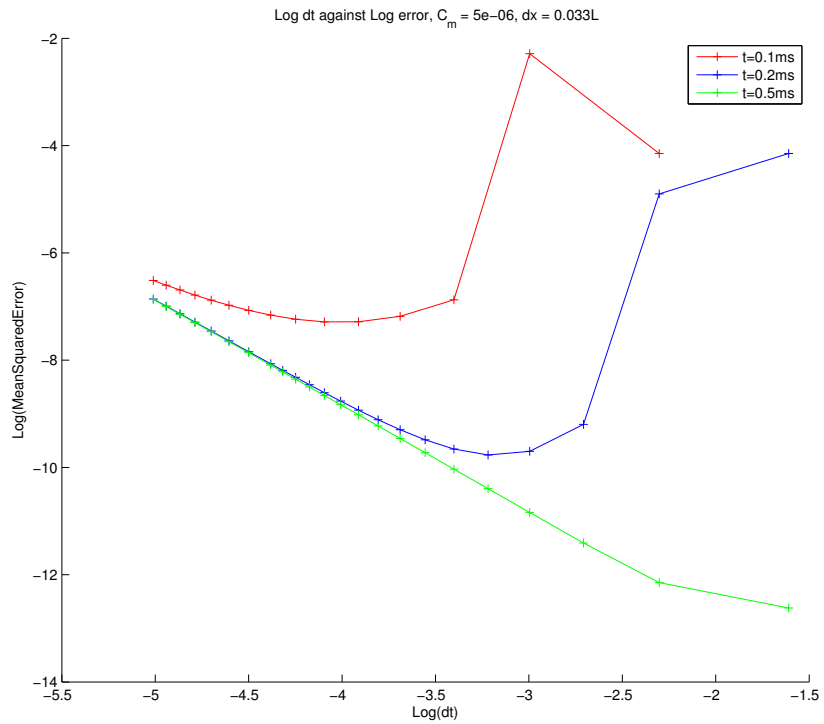


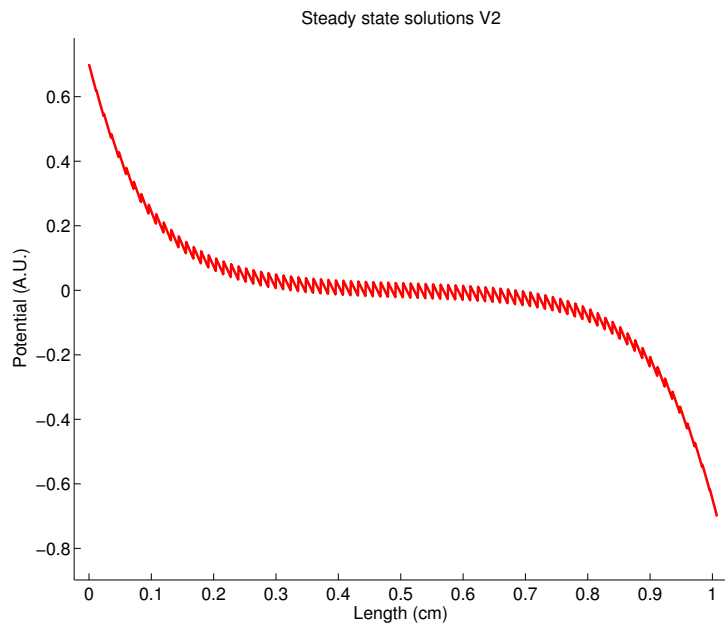
Figure 7.9: Log dt against Log error, for several time steps.

the analytic solution.

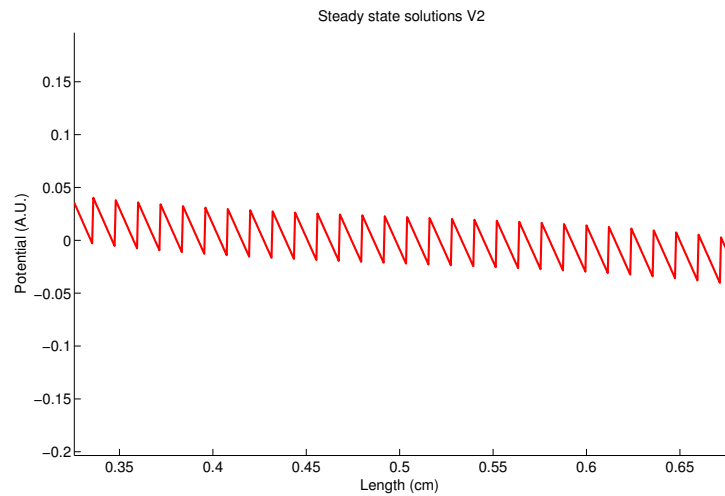
The steady state solution is plotted in Fig. 7.10, which is qualitatively similar to the analytic solution predicted by Keener and Sneyd (Fig. 7.2).

Neumann boundary conditions, time dependent forcing stimulus

A time dependent solution of this model is implemented and the output is displayed in Fig: 7.11:

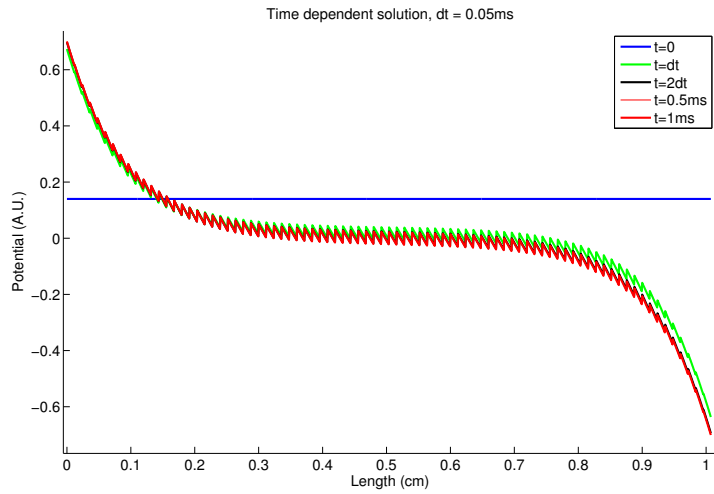


(a) Steady state transmembrane solution,

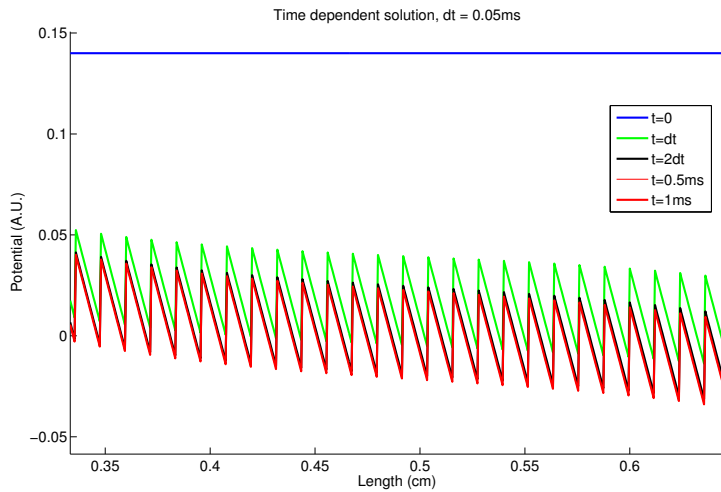


(b) Transmembrane solution zoomed in; sawtooth solution.

Figure 7.10: Steady state solution, transmembrane potential V_m . Compare with Figure 7.2.



(a) Time dependent transmembrane solution,

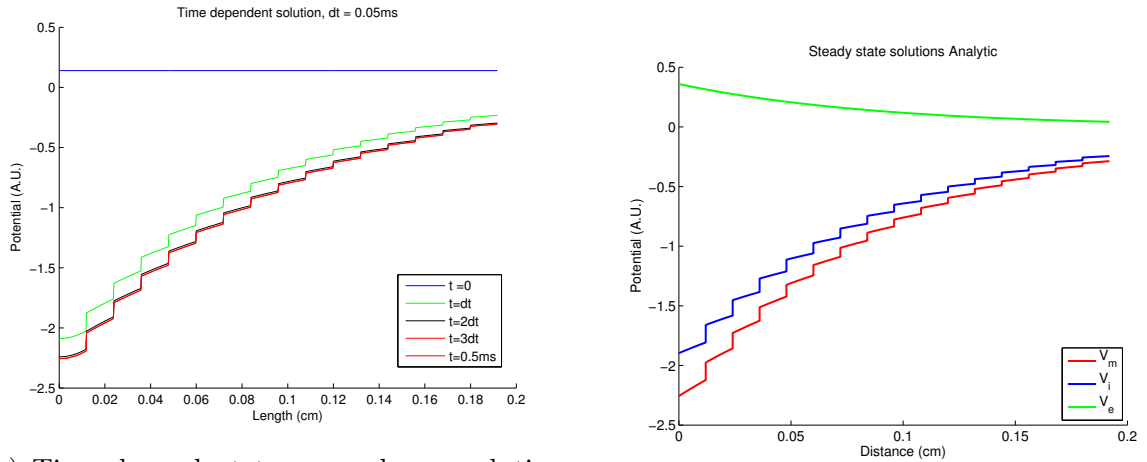


(b) Transmembrane solution zoomed in, showing the sawtooth solution.

Figure 7.11: Time dependent stimulus, transmembrane potential V_m .

7.3.4 No flux (Neumann) boundary conditions, time dependent forcing stimulus

The domain was set up with no flux boundary conditions representing sealed end of cables. Within this, a time dependent forcing stimulus was injected in to the first cell of the chain. This gives the following solution in Fig. 7.12a.



(a) Time dependent transmembrane solution, no flux boundary conditions for 0.5ms , with one cell stimulated on the left hand side for 0.5ms .

(b) Analytical solution for Dirichlet problem, reproduced from Figure 7.3. The transmembrane solution V_m is denoted in red.

Figure 7.12: Simulation of no flux boundary conditions and a time dependent injected current stimulus (7.12a) tends to the transmembrane profile (red line) in the Dirichlet problem (7.12b).

Contrary to the Neumann boundary condition solution with varying forcing stimulus on the boundary of the cell, Figure 7.12a shows that using no flux boundary conditions with a time dependent stimulus within the domain produces a steady state potential similar to the Dirichlet problem solution (Figure 7.12b).

7.3.5 Implementation of the full model with active ion channel kinetics

Following from the numerical analysis carried out in the previous Section, the model was altered to that described by Equation (7.19). The intracellular (cytoplasmic) space has resistivity R_c , and the extracellular space, R_e . Boundary conditions on the domain were chosen as follows: no flux boundary conditions on the intracellular domain and one end of the extracellular domain. The end of the extracellular domain had a Dirichlet boundary condition implemented to prevent non-uniqueness of the problem.

Within each cell, the passive membrane resistance term from the Keener model was removed, and the Luo Rudy-I ion channel kinetics was implemented along the edge of the cell (Section 3.2.2). A normal gap junctional resistance of $R_j = 0.0015k\Omega cm$ [[Stinstra et al., 2010](#)] was implemented on the end of each cell, in parallel with a cell membrane capacitance of $1\mu F/cm^2$. The equivalent circuit diagram for the domain is shown in Figure 7.13.

A domain consisting of 80 cells each of length $120\mu m$ was created with a discretisation of Δx of $6\mu m$ or smaller. The domain was stimulated from the first cell using a stimulus pulse of $0.2ms$ duration and greater than 1.2 times the stimulus threshold.

7.4 Results: Computation details and numerical sensitivity

In the previous subsections, the accuracy of the numerical solution is compared with the analytical solution for the passive coupled problem. For the full 1D problem coupled with

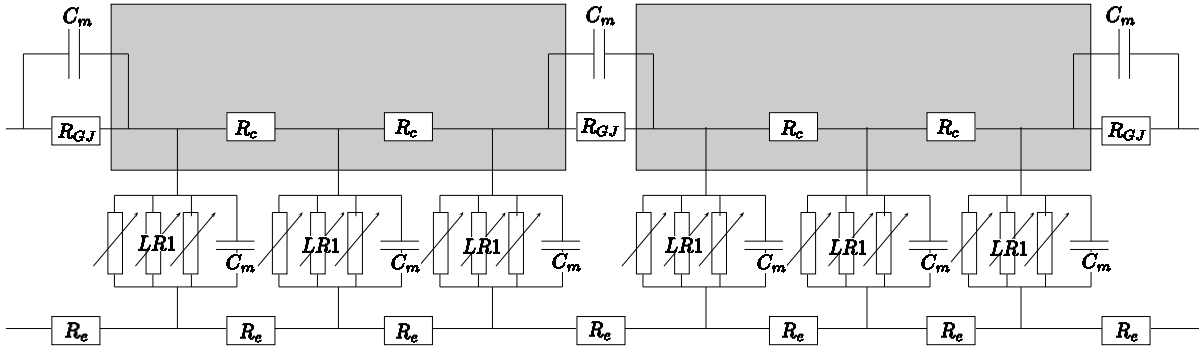


Figure 7.13: Equivalent circuit diagram of the 1D discrete cell model. Each discrete cell is a continuous intracellular domain, with Luo–Rudy I (LR–1) ion channel kinetics connecting intracellular and extracellular space. The intracellular (cytoplasmic) space has resistivity R_c , and the extracellular space has resistivity R_e . At intercellular borders, a parallel RC circuit couples neighbouring cells, with a gap junctional resistance R_j and membrane capacitance C_m .

ionic channels, the ionic channel ODE models are non-linear and there are no analytical solutions. It is difficult to fully validate results from the numerical simulations against an analytical solution. There are published numerical benchmark tests for standard numerical solutions to bidomain and monodomain models [Niederer et al., 2011], but no published solutions for the discrete 1D model that has been described. Investigations into the numerical sensitivity for the model compared against a finely resolved solution in space and time, to evaluate the largest space and time discretisation permissible for efficient yet accurate simulations.

Computation details

Equation (7.19) was solved numerically using the finite difference method (FDM). A second order central difference scheme in space was used to discretise the domain (see Chapter 3), with second order one-sided finite difference derivatives used to model boundary conditions at cell ends, and at the ends of the domain.

The gating variables were updated at each time step using a combination of the Rush Larsen method and the forward Euler method. A fully implicit backward Euler method was used to march the solution forward in time. All code was written in Matlab (Mathworks).

A $500ms$ simulation on a $9.6mm$ cable, with $\Delta x = 6\mu m$ and $\Delta t = 0.02ms$ took $42s$ to compute on a MacBook Pro with a 2.6GHz i7 processor and 16GB of memory. A discrete model simulation on a similar size domain took $225s$.

Spatial sensitivity

For investigating spatial sensitivity of the discrete model, a domain of 50 cells ($0.6cm$) was simulated with a fixed temporal discretisation of $0.02ms$. The size of Δx was varied from $20\mu m$ (largest) down to $0.6\mu m$ (smallest). The domain was stimulated after $15ms$, with a stimulus duration of $0.2ms$, and the simulation was run for $500ms$.

The transmembrane solution V_m was outputted $15ms$ after the injected stimulus (i.e. at $t = 30ms$). Only the transmembrane solution of the first 20 cells of the domain were compared, to eliminate any boundary effects from the end of the cable. Conduction velocity was measured between cells 5 and 20,to eliminate stimulus artefact distorting the upstroke. Different spatial resolutions were compared with the most detailed spatial resolution, with the L2 norm calculated. Simulations at higher spatial resolutions were downsampled to the lowest spatial resolution, to match the number of the spatial points in the domain being compared. The L2 norm is plotted in Figure 7.14.

It can be seen from Figure 7.14 that the implementation was second order accurate in space. The spatial resolution was very fine, with the largest discretisation being $6\mu m$.

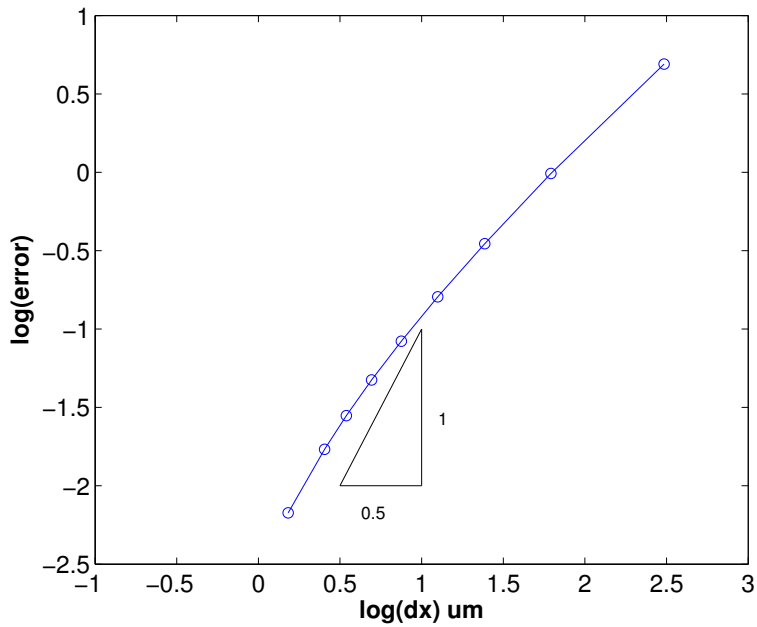


Figure 7.14: Spatial sensitivity: L2 error norm of discrete model at 15ms after stimulus. Decreasing the size of Δx reduces the error. The slope of the curve is 2, indicating second order accuracy.

Temporal sensitivity

For investigating temporal sensitivity of the discrete model, a domain of 50 cells (0.6cm) was simulated with a fixed spatial discretisation of $\Delta x = 1.2\mu\text{m}$. The range of temporal discretisation varied between $\Delta t = 0.1\text{ms}$ (largest) and $\Delta t = 0.0125\text{ms}$ (smallest). The domain was stimulated after 15ms, with a stimulus duration of 0.2ms, and the simulation was run for 500ms.

The transmembrane solution V_m was outputted 15ms after the injected stimulus (i.e. at $t = 30\text{ms}$). Only the transmembrane solution of the first 20 cells of the domain were compared, to eliminate any boundary effects from the end of the cable. Different temporal resolutions were compared with the most detailed temporal resolution, with the L2 norm calculated. Simulations at higher temporal resolutions were downsampled to the lowest

temporal resolution, to match the number of the temporal points being compared. The L2 norm is plotted in Figure 7.15.

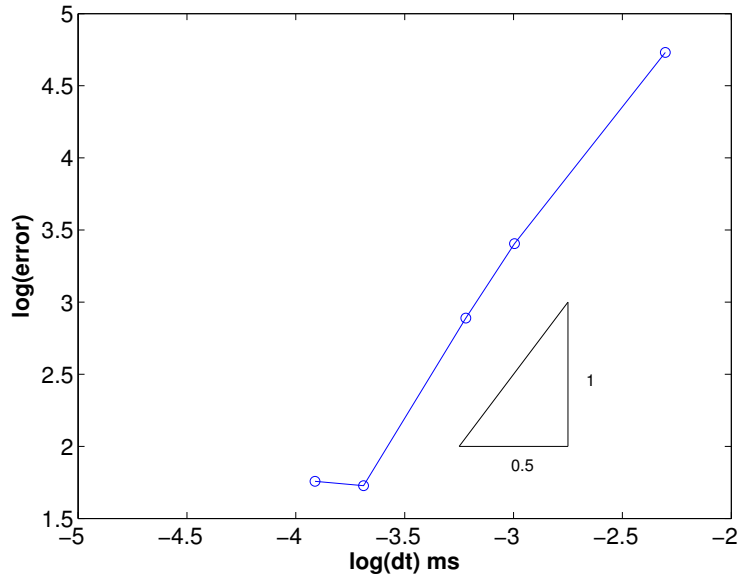


Figure 7.15: Temporal sensitivity: L2 error norm of discrete model at $15ms$ after stimulus. Decreasing the size of Δt reduces the error. The slope of the curve is 2, indicating second order accuracy. The magnitude of the error is very large, which indicates the solution is highly sensitive to the size of Δt .

From Figure 7.15, it would suggest that the implementation was second order accurate in time. However, a first order Backward Euler method was used which should only have first order accuracy. It was also noted that the magnitude of the error was very large, suggesting that the solution is highly sensitive to the choice of Δt .

Several temporal discretisations of $\Delta t < 0.0125ms$ were attempted. These resulted in divergent numerical solutions, which were discarded. This suggests that the optimal temporal discretisation was between $0.0125 - 0.02ms$. In all subsequent investigations, simulations were carried out using a discretisation of $\Delta t = 0.02ms$.

7.5 Results: Determining physiological factors underlying conduction slowing

Within the discrete model, there are a number of physiological parameters which may alter the properties of action potential propagation. These include parameters modulating the passive properties of the tissue (cytoplasmic conductivity R_c , extracellular conductivity R_e and gap junctional resistivity R_j), as well as parameters altering the functional properties - these are contained within the specific action potential model which is coupled with the passive tissue model.

The effects of some of these parameters are well explored within the computational and experimental literature [Kléber and Rudy, 2004], and thus these parameters form the basis for the present investigation. Each parameter is varied in turn on the discrete model, to examine its effects on conduction and the action potential upstroke.

7.5.1 Gap junctional resistance

In this section, the effect of altering cell-cell coupling via gap junctional resistance is considered. The 1D discrete model, coupled with the LR-1 action potential is simulated, and the effect on resulting conduction velocities, activation waveform and action potentials are calculated and presented.

Effect on conduction velocity

The effect of modulating gap junctional resistivity R_j on conduction velocity is shown in Table 7.2. As shown in the table, reducing the GJ resistivity R_j (or equivalently, increasing GJ conductance σ_j) from baseline had a minimal impact on conduction velocity, with a $2\times$ reduction in resistivity only resulting in a 5% increase in conduction velocity.

$R_j \times$	CV (cm/s)	Ratio of decrease	Ratio from baseline
0.5	40.5		1.05
1	38.5	1.05	1.00
2	35.3	1.09	0.92
4	30.6	1.15	0.79
8	24.4	1.25	0.63
16	17.3	1.41	0.45
32	10.9	1.59	0.28
64	6.03	1.81	0.16
128	2.73	2.21	0.07
256	Block	Block	Block

Table 7.2: Effect of increasing R_j from baseline ($\times 1$).

An increase in R_j (decrease in σ_j) reduced conduction velocity, in a complex, non-linear manner. At larger increases above $16\times$, doubling R_j decreased CV by greater than a factor of 1.4. This factor increased until conduction block occurred for a $256\times$ increase - this occurred below $3\text{cm}/\text{s}$.

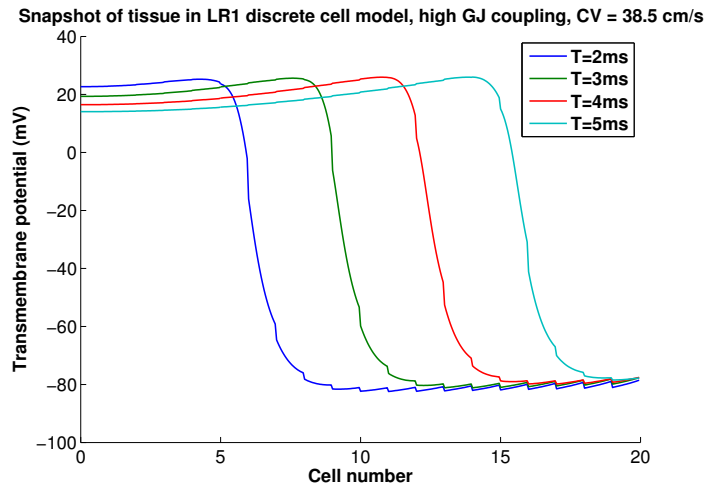
Effect on activation wavefront

The transmembrane potential V_m wavefront is plotted versus space in Figure 7.16.

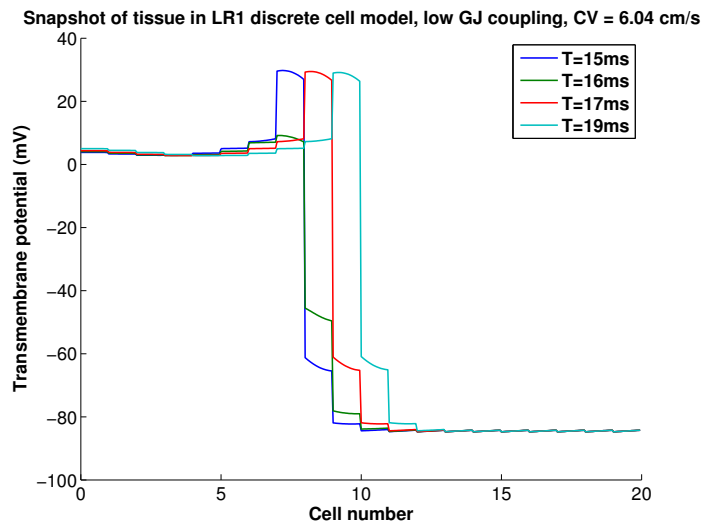
As shown in the Figure, normal conduction ($38.5\text{cm}/\text{s}$) resulted in a smooth spatial activation wavefront. As the conduction velocity decreases, the activation wavefront changes appearance. For slow conduction, activation occurs quickly within each cell, with long time delays at intercellular junctions causing the jagged profile of the activation wavefront.

Effects on the action potential

The transmembrane potential V_m is plotted versus time in Figure 7.17.



(a) Normal conduction



(b) Slow conduction

Figure 7.16: V_m spatial profile for different gap junctional resistivities. Normal propagation was defined for 38.5cm/s , and slow propagation at 6.04cm/s . The spatial activation wavefront loses its smooth shape for lower CV and activation is fast within each cell, with long delays at intercellular junctions.

As shown in the figure, normal conduction results in an action potential upstroke which reaches a peak at 25ms , with the spike and dome morphology preserved. In slow conduction, the action potential spike reaches a peak of over 40ms , which is comparable with the original LR-1 model for a single cell [Luo and Rudy, 1991].

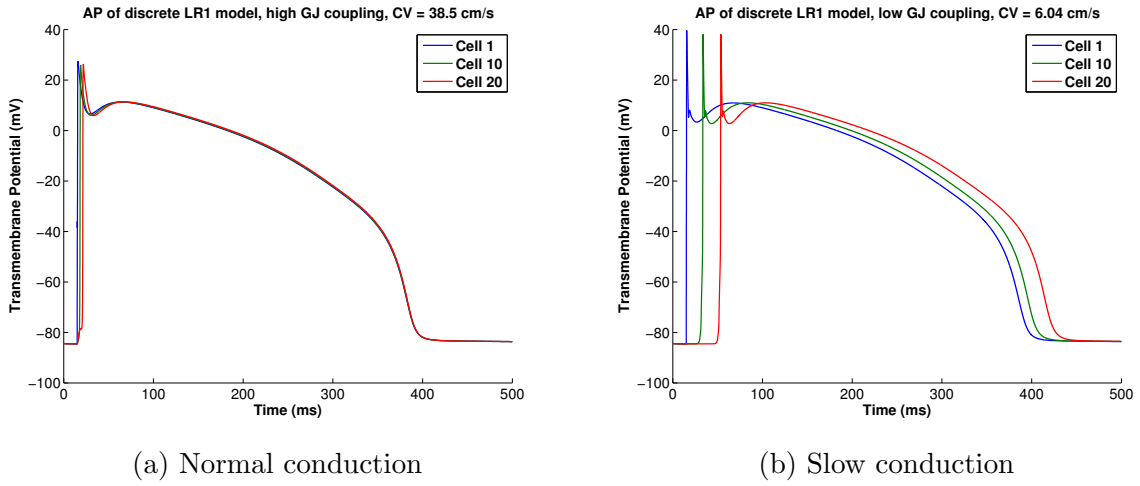
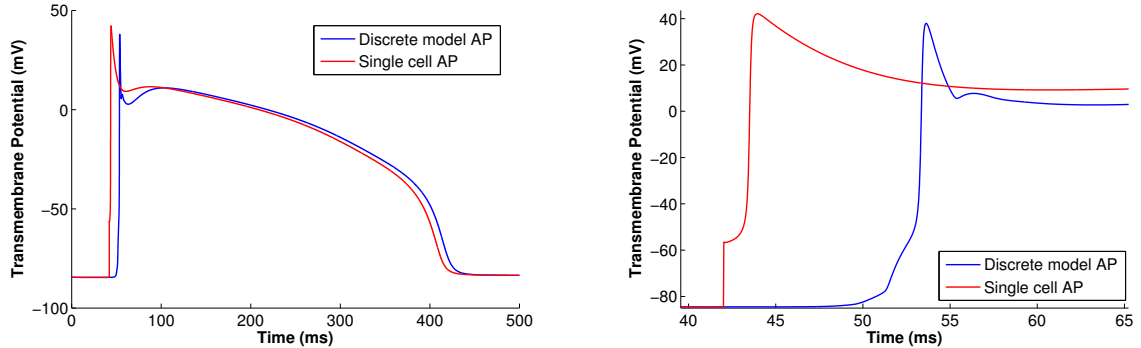


Figure 7.17: Effect of modulating R_j on V_m versus time

The foot of the activation wavefront (τ_{ap}) becomes more pronounced as the gap junctional resistance R_j is increased. Compared to a single cell model which is stimulated via direct addition of a stimulus current, a curved action potential foot is created (Figure 7.18), which is due to diffusion of the intracellular potential from the upstream neighbouring cell.

7.5.2 Cytoplasmic resistivity

In this section, the effect of altering cytoplasmic resistivity on conduction is considered. Cytoplasmic resistivity is normally considered constant in experimental studies; however this study provided an opportunity to alter this value and evaluate the effects this might have on conduction. The 1D discrete model, coupled with the LR-1 action potential is simulated, and the resulting conduction velocities and action potentials are calculated and presented.



(a) Morphology of the LR-1 AP in a single cell simulation versus discrete coupled cell simulation

(b) AP upstroke, zoomed in. The AP is triggered when transmembrane potential exceeds -60mV

Figure 7.18: Morphology of the LR-1 AP in single cell versus discrete coupled cells. In slow conduction, the AP shape in a discrete cell model closely resembles AP from a single cell simulation. The AP upstroke is different; the single cell is stimulated from a point stimulus, whereas the coupled cell receives its stimulus via diffusion from its neighbour, to create a curved foot of action potential τ_{ap} .

$R_c \times$	CV (cm/s)	Ratio of decrease	Ratio from baseline
0.33	52.63		1.28
0.5	49.18	1.07	1.20
1	41.10	1.20	1.00
2	31.9	1.29	0.78
4	23.81	1.34	0.58
8	17.14	1.39	0.42
16	12.00	1.43	0.29
32	8.13	1.48	0.20
64	5.24	1.55	0.13
128	3.09	1.69	0.08
256	1.41	2.19	0.03
512	Block	Block	Block

Table 7.3: Effect of increasing R_c from baseline ($\times 1$).

Effect on conduction velocity

Increasing cytoplasmic resistance decreased conduction velocity, as seen in Table 7.3. At larger increases above $64\times$, doubling R_j decreased CV by greater than a factor of 1.5.

This factor increased until conduction block occurred for a $512\times$ increase - this occurred below $3\text{cm}/\text{s}$.

Effect on activation wavefront

The activation wavefront changes in a different way compared to modulation of cytoplasmic resistance, as shown in Figure 7.19. For slow conduction caused by higher cytoplasmic resistance, activation through the cell is slower with a longer delay. The difference between intracellular delay and intercellular delay is reduced.

Effect on action potential

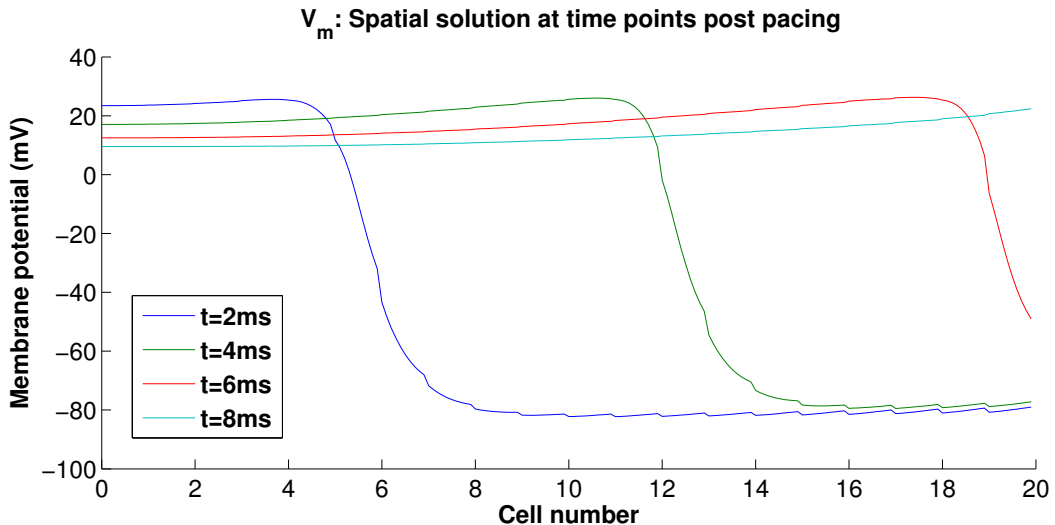
No qualitative difference was observed between the AP from modulating R_c in a discrete cell chain simulation, from the cable model simulation.

7.5.3 Membrane capacitance

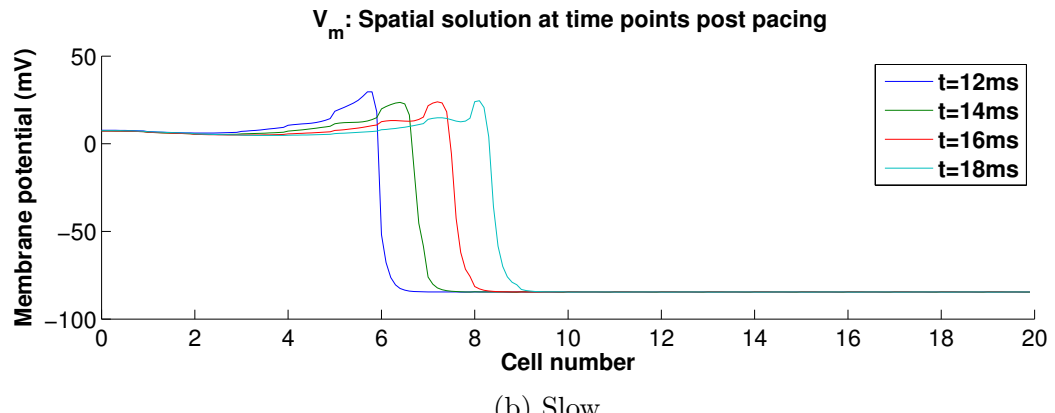
The effects of altering local membrane capacitance on action potential propagation was not investigated in detail. However, preliminary results shown in Section 7.3.2 suggested that small changes in membrane capacitance may induce changes in the numerical model. It is known that membrane capacitance is a determinant of conduction velocity in a continuous cable model [Dhillon, 2010]. Thus, local changes in membrane capacitance at the cell ends (compared to the local membrane capacitance along the long axis) were a potential cause for conduction slowing, although this was not investigated.

7.5.4 Sodium channel excitability

In this section, g_{Na} was systematically reduced to examine whether the numerical implementation of this model behaved in accordance with published data.



(a) Fast



(b) Slow

Figure 7.19: Effect of modulating R_c on V_m activation wavefront. The activation wavefront is smooth due to the increased intracellular delay caused by increased cytoplasmic resistance.

The peak sodium channel excitability g_{Na} parameter was reduced in increments of 10%, for the control diffusivity parameter of $D = 5e^{-4}cm^2/ms$. Conduction velocity decreased monotonically with a conduction block after 70% reduction in g_{Na} . The resultant conduction velocity of the system is plotted against the corresponding reduced value of g_{Na} as shown in Fig. 7.20, with the raw data provided in Table 7.4.

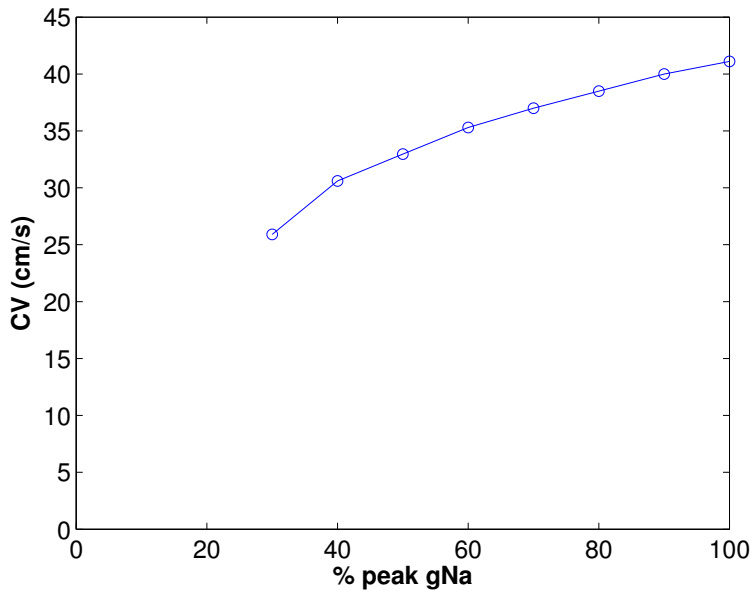


Figure 7.20: A log graph showing the relationship between modulating maximum sodium channel excitability g_{Na} against the resulting conduction velocity in the 1D discrete cell model with the LR-1 guinea pig ventricular AP model.

% g_{Na}	CV (cm/s)	Ratio of decrease	Ratio from baseline	dv/dt_{max} (V/s)
100%	38.5		1.00	245
90%	37.5	1.03	0.97	227
80%	36.1	1.04	0.94	209
70%	34.5	1.04	0.90	189
60%	33.3	1.05	0.86	169
50%	31.2	1.07	0.80	146
40%	29.1	1.08	0.74	121
30%	25.9	1.18	0.63	93
20%	Block	Block	Block	Block

Table 7.4: Effect of reducing peak sodium excitability g_{Na} on conduction velocity

7.6 Results: Discrete model versus Continuum model

In this section, the differences and similarities between the continuum cable model and the discrete cell model were compared, under similar physiological conditions, such as conduction velocity or peak sodium excitability.

$\%g_{Na}$	CV (cm/s)	Ratio of decrease	Ratio from baseline	dv/dt_{max} (V/s)
100%	24.40		1.00	334
90%	23.62	1.03	0.97	312
80%	22.90	1.03	0.94	284
70%	21.90	1.05	0.90	259
60%	20.69	1.06	0.85	228
50%	19.48	1.06	0.80	196
40%	17.86	1.09	0.73	170
30%	15.87	1.13	0.65	120
20%	13.16	1.21	0.54	74
10%	6.49	2.03	0.27	10
5%	Block	Block	Block	Block

Table 7.5: Effect of reducing peak sodium excitability g_{Na} on conduction velocity for $R_j \times 8$

7.6.1 Effective diffusivity versus gap junction resistance

Parameters modulating conduction in cable and discrete models were compared, to examine the effect on conduction velocity (CV) and in max dV/dt . The approach taken in this study was to match similar conduction velocities across cable and discrete models via adjustment of the relevant parameter which controlled speed of excitation.

Conduction Velocity

In Figure 7.21, CV is calculated in simulations for both cable and discrete models, following modulation of parameters affecting primarily CV: effective diffusivity D for the cable model, and gap junctional resistance R_j and cytoplasmic resistance R_c for the discrete model. These values were reported in Tables 5.1, 7.2 and 7.3

The cable model exhibited a linear power law relationship between effective diffusivity D and CV. No conduction block was observed under modulation of D ; propagation of $1.36 cm/s$ was achieved. Under increase of GJ resistance R_j (decrease in σ_j), conduction velocity decreased in a non-linear fashion. Conduction block occurred after $2.73 cm/s$ at $128R_j$. Interestingly, increasing σ_j beyond the normal value did not result in an increase

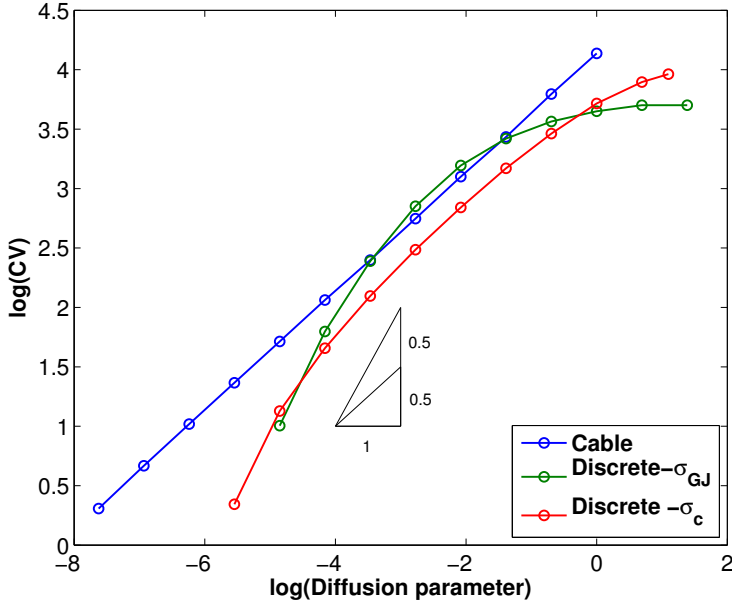


Figure 7.21: Conduction velocity (CV) against diffusion parameters: diffusivity (D) for cable model, and gap junctional conductance (σ_j) and cytoplasmic conductance (σ_c) for discrete model. Normal values: $D = 0.001\text{cm}^2/\text{ms}$, $\sigma_c = 0.003\text{S}/\text{cm}$, σ_j (denoted as σ_{GJ})

in CV, whereas increasing D in the cable model continued to increase CV.

For the parameter of cytoplasmic conductance σ_c (resistance R_c), decreasing the conductance led to a decrease in CV , also with a non-linear power law relationship. Very slow conduction of 1.40cm/s was observed.

Maximum dV/dt

The gradient of the AP upstroke dV/dt is calculated in simulations for both cable and discrete models, following modulation of diffusivity parameters: effective diffusivity D for the cable model, and gap junctional resistance R_j and cytoplasmic resistance R_c for the discrete model. The max upstroke for the cable model and for R_j is plotted in Figure 7.22 for each modulation (R_c is omitted).

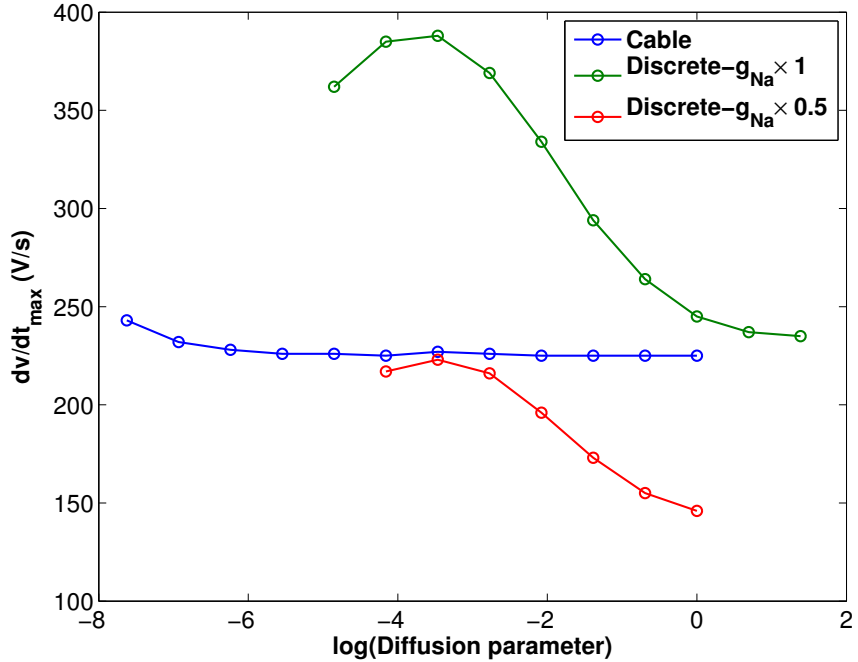


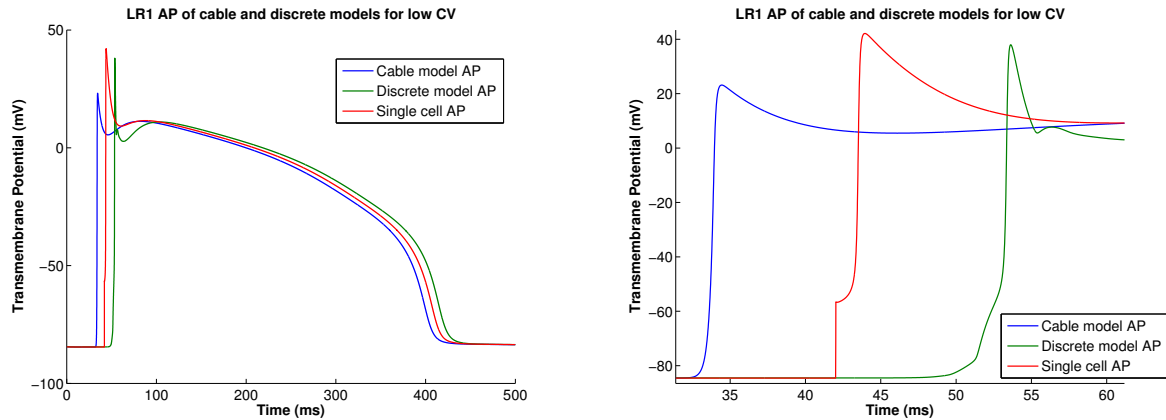
Figure 7.22: Maximum dV/dt as a function of diffusivity. In the cable model, dV/dt_{max} was independent of diffusivity. In the discrete model (both normal and reduced g_{Na}), increasing R_j led to an increase in dV/dt_{max} to an initial peak, which dips immediately prior to conduction block.

As shown in Figure 7.22, modulating effective diffusivity D within the cable model did not alter the max AP upstroke. dV/dt_{max} remained similar for different levels of diffusivity D . The dV/dt_{max} initially increased in the discrete model for increased R_j (decreased σ_j , from 225V/s for normal R_j to 388V/s for $32 \times R_j$) (11cm/s). After this, dV/dt_{max} decreased slightly down to 362V/s at $128 \times R_j$, before conduction block.

The discrete model was simulated for different R_j values with a fixed 50% reduction in peak g_{Na} , to examine the effects of decreased sodium channel activity and increased GJ resistance. As shown in the Figure, dV/dt_{max} also increased when R_j was increased, and peaked at $R_j \times 32$ (8.31cm/s), before a slight decrease immediately at 4.29cm/s prior to conduction block.

Action potential upstroke τ_{ap}

The shape of the action potential upstroke τ_{ap} was plotted for slow conduction in both cable and discrete models. Figure 7.23 shows the LR-1 action potential for a single cell



(a) Simulated LR-1 action potentials under slow conduction for cable and discrete models, alongside a single cell simulation.

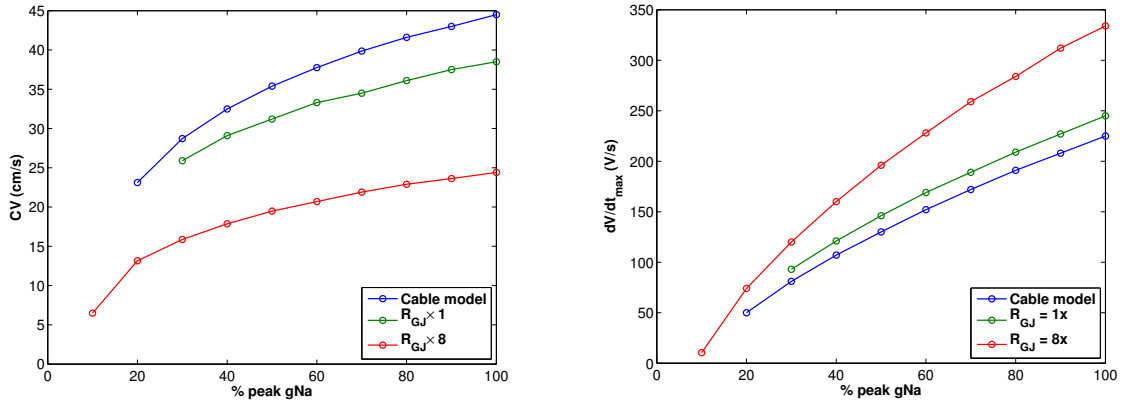
(b) The AP upstroke to the LR-1 action potentials for cable and discrete models, alongside a single cell simulation.

Figure 7.23: Simulated action potentials in cable, discrete cells and a single cell model. Single cell (red): stimulated via an injected current (vertical notch) and has no τ_{ap} . AP from cable model (blue): τ_{ap} is around 1.3ms . Discrete model AP (green): a double notched deflection indicates a lengthened τ_{ap} duration, due to diffusion of intracellular potential from upstream neighbouring cells.

simulation, and also cable and discrete tissue models under slow conduction. The single cell (red) is stimulated via an injected current stimulus and has no action potential foot (τ_{ap}) due to the vertical stimulus spike. In the AP from the cable model, τ_{ap} is around 1.3ms (compared to 0.29ms in experimental measurements of normal tissue (see Chapter 4)). In the discrete model AP however, a double notched deflection indicates the presence of τ_{ap} of lengthened temporal duration, due to diffusion of intracellular potential from upstream neighbouring cells.

7.6.2 Sodium excitability and composite effects

The effects of peak sodium channel excitability g_{Na} on CV and max dV/dt are plotted in Figure 7.24. Under reduction of g_{Na} , dV/dt_{max} decreases in both continuum and discrete



(a) Conduction velocity (CV) as a function of peak sodium excitability (g_{Na}). (b) $\frac{dV}{dt}_{max}$ as a function of peak sodium excitability (g_{Na}).

Figure 7.24: Discrete versus continuum model – modulation of g_{Na} . Under reduction of g_{Na} , dV/dt_{max} decreases in both continuum and discrete models (7.24b). Cable model: conduction block after 80% g_{Na} reduction, discrete mode: 70% reduction. For $R_j \times 8$ in the discrete model, conduction block only occurs after 90% g_{Na} reduction.

models (7.24b). In the cable model, this leads to conduction block after an 80% reduction in g_{Na} , and after 70% reduction in the discrete model. However, when GJ resistance is increased by 8× in the discrete model, the increased dV/dt_{max} attenuates the effect of g_{Na} reduction, leading to sustained slow conduction (6.49cm/s) at 90% knockout, and conduction block after this. The dV/dt_{max} at this point was 10.36V/s.

This phenomena was not reproduced in the cable model of propagation, as altering the diffusivity D did not induce a change in dV/dt_{max} .

7.6.3 Electrogram

The virtual electrogram (vECG, Section 3.6.1) was simulated in both cable and discrete models, for normal CV ($38 - 41\text{cm/s}$) and for low CV ($5 - 6\text{cm/s}$), and plotted in Figure 7.25.

On the left panel, there is little difference between vECGs for the cable (Fig. 7.25a) and discrete models (Fig. 7.25c) under normal CV. However on the right panel, at low CV, vECG exhibit different morphologies and amplitude: the cable model (Fig. 7.25b) has a smaller amplitude and wider duration than for normal CV; in the discrete models (Fig. 7.25d) and (Fig. 7.25e), non biphasic waveforms are observed with a wide duration and large difference in amplitude. This may be due to the large intercellular delays and fast intracellular conduction when R_j is modulated, compared to the sharp smaller intercellular delays and slower intracellular conduction when R_c is modulated.

7.7 Discussion

7.7.1 Summary of findings

In this chapter, a 1D discrete bi-domain model of identical myocytes coupled by passive resistors, representing gap junctions, was presented. The model was coupled to either a passive transmembrane resistance, or a biophysically detailed ionic current model (Luo-Rudy I).

Analytical solutions to the discrete model were considered, and compared with a FDM numerical implementation of the model, to determine the sensitivity and stability of the discrete model. Numerical simulations of the discrete model, coupled to the Luo-Rudy I AP, were computed, to investigate the effects of modulating physiological parameters on

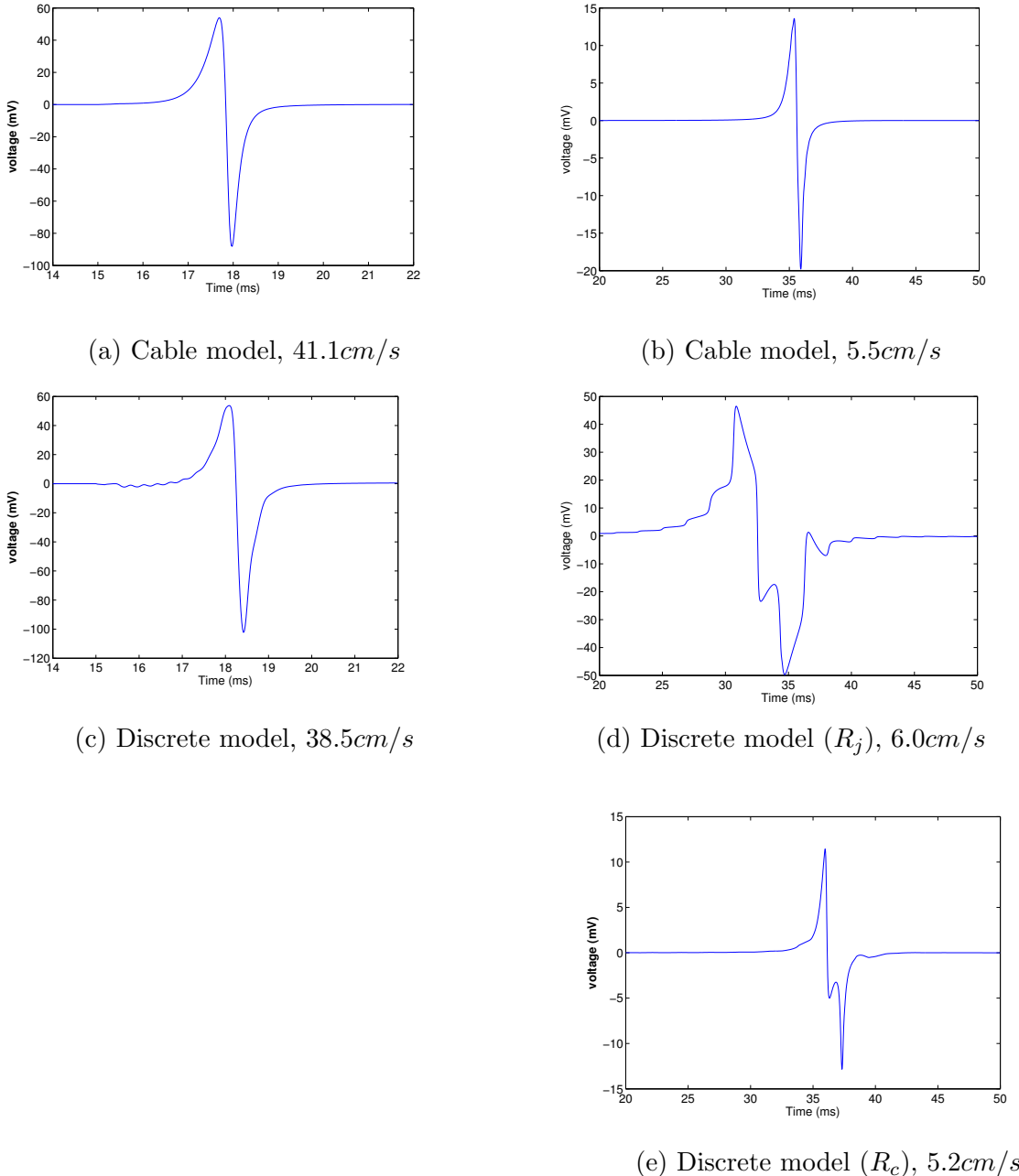


Figure 7.25: Virtual ECGs generated from cable and discrete models. There is little difference between vECGs for cable (7.25a) and discrete models (7.25c) under normal CV. However at low CV, vECG exhibit different morphologies and amplitude: the cable model (7.25b) has a smaller amplitude and wider duration than for normal CV; in the discrete models (7.25d) and (7.25e), non biphasic waveforms are observed with a wide duration and difference in amplitude.

AP propagation in the model.

The continuous cable model and discrete models were compared using several metrics. Parameters were chosen in each model which matched conduction velocities between the models, and the relationship between these parameters were compared. Other physiological features resulting from numerical simulations were compared between the models, as well as the virtual electrogram in normal versus slow conduction.

7.7.2 Numerical sensitivity and stability of the discrete model

The 1D discrete cell chain model was implemented numerically in Matlab, and results were compared with analytical solutions using the passive 1D model proposed by [Keener and Sneyd \[2009\]](#). It was found that steady state numerical implementations matched closely to the analytical solution for multiple types of boundary conditions, subject to the choice of finite difference approximation for the intracellular boundary flux due to GJ located at cell ends. The implementation exhibited second order accuracy in space.

Under time dependent conditions, the passive discrete model tended to steady state within one or two time steps. It appeared that increasing the temporal resolution reduced temporal accuracy.

The discrete model was then coupled with the LR–1 ion channel model, a well characterised and widely used model within the literature [[Pullan et al., 2005](#)]. The novelty of this 1D discrete cell model made it difficult to compare the numerical results against published solutions or benchmarks (e.g. [Niederer et al. \[2011\]](#)), and thus a numerical sensitivity analysis was performed by comparing with a finely resolved model.

It was found that the spatial resolution of the implementation followed second order

accuracy, as expected for a 2nd order FDM implementation. However, despite appearing to exhibit second order accuracy in time, the model was shown to be highly sensitive to choice of temporal discretisation, with large errors introduced for large time steps $> 0.02ms$, and divergent solutions for $< 0.01ms$. This may be due to the choice of a first order implicit backward Euler scheme; it is known that implicit schemes are stable for longer time steps but are very computationally expensive [Clayton et al., 2010]. It may be that using time marching schemes such as Crank–Nicholson [Crank and Nicolson, 1947] or semi-implicit IMEX schemes [Ethier and Bourgault, 2008] may resolve this issue.

7.7.3 Physiological insights from the discrete model

It was found that gap junctional resistance R_j and cytoplasmic resistance R_c had effects on AP propagation when increased to large values. Increasing the cytoplasmic resistance R_c reduced CV,, also seen for increase in the GJ resistance R_j . Additionally, increasing R_j altered the spatial activation wavefront and led to alterations in the peak dV/dt of the AP upstroke and on τ_{ap} .

High levels of R_j led to a ‘staircase’ activation wavefront, with cells activating near-instantaneously within each cell, and long trans-junctional delays between neighbouring cells ($2ms$ at $6cm/s$), especially at the foot of the activation wavefront. It should be noted that this cable was not at steady state and this could potentially be only a transient effect. This simulation replicates the experimental result observed by Beauchamp [2004], where a 96% knockout of intercellular GJ conductance led to a reduction of CV from $52cm/s$ to $2.1cm/s$. This effect of discontinuous propagation is also reported by Kucera et al. [2001]. Rohr et al. [1998] reported long transjunctional delays at very slow conduction ($0.54 – 4.52ms$, mean $2.69ms$). Rohr defined slow conduction between $1 – 8.5cm/s$ and ultra-slow conduction $< 1cm/s$. the present study did not observe ultra-slow conduc-

tion as conduction block occurred before reaching 1cm/s in discrete cells, an effect not observed in the cable model. [Spach and Miller \[1981, 1982\]](#) defined slow conduction as around $5 - 12\text{cm/s}$, although his experimental work was carried out in papillary muscle with a lower spatial resolution compared to Kucera and Rohr.

Theoretical studies by [Rudy and Quan \[1987\]](#), [Wang and Rudy \[2000\]](#) also analysed the effect of 1D discrete cells. They similarly found that dV/dt_{max} initially increases as GJ resistance increases before a decrease that leads to conduction block, which is also reported by [Shaw and Rudy \[1997\]](#). This increase in dV/dt_{max} was explained by [Kléber and Rudy \[2004\]](#), as being due to partial reflection of local axial current from cellular boundaries, resulting in a current-to-load mismatch, reducing the density of current per unit membrane area exciting downstream cells. In normal propagation, Wang et al found propagation delay of $100\mu\text{s}$ across the intracellular space, and also $100\mu\text{s}$ across the gap junction. When GJ resistance was increased, a delay of 1ms was observed across the gap junction.

They discuss that these effects are not observed ‘globally’ and that their simulated extracellular potential (virtual electrogram) does not detect these localised changes in conduction delay. This is different to the virtual electrogram result shown in the present study, where the biphasic electrogram morphology is altered for slow conduction using the discrete model. However, the model of Rudy and Wang only considered a localised increase in resistance at the gap junction, but junctional capacitance was not included. Additionally a different cell model type was used ([Beeler and Reuter \[1977\]](#) vs Luo–Rudy I) which may have led to the differences in observation.

The difference in electrogram morphology seen in this model is supported by [Rudy and Quan \[1991\]](#), who argue that each depolarisation in neighbouring cells are sufficiently

separated in time, such that they are reflected as distinct deflections in the morphology of the extracellular electrogram.

The role of sodium excitability in propagation was studied using the discrete model. It was found that reducing sodium excitability decreased CV and also dV/dt_{max} , with 70% reduction leading to $CV = 26cm/s$ and $dV/dt_{max} = 93V/s$, with conduction block occurring for 80% reduction. This trend has previously been reported by [Shaw and Rudy \[1997\]](#), who have shown that conduction continues up to and including 90% knockout of g_{Na} . Their study was used the Luo–Rudy dynamic model (LR–D) , and carried out on a ‘discrete’–like domain, with a different mathematical formulation not including junctional capacitance, which may account for the differences.

A novel feature predicted by the present discrete model study, was of the attenuation mechanism caused by increasing GJ resistance on the effects of decreasing peak sodium excitability. It seems that the initial increase in dV/dt_{max} caused by the enlarged GJ resistance may counteract the decrease in dV/dt_{max} in reduced g_{Na} , which led to slow propagation at 90% g_{Na} knockout and initiation of an action potential with a decreased spike morphology but unaltered AP duration. This result has not been investigated in other studies to our knowledge, although [Shaw and Rudy \[1997\]](#) have found that the presence of L type calcium current in very slow conduction extends the safety factor up to 90% from 80% without, suggesting that the presence of multiple mechanisms responsible for conduction slowing may produce emergent behaviour which is cardioprotective.

7.7.4 Differences between the 1D discrete and the 1D cable model

Several key differences were highlighted between the continuous cable model and the discrete model.

Conduction velocity as a function of resistance

A main feature was the robustness of the linear relationship between resistivity and conduction velocity predicted by cable theory, under large and small effective diffusivity values D . The physiological range supports propagation at least $1m/s$ in specific cardiac tissue types; however it is well characterised experimentally that most mammalian hearts have a theoretical maximum CV.

The discrete model reaches a theoretical maximum despite attempts to further decrease gap junctional resistance, compared to the cable model which does not reach this limit. At the lower end, it was not possible to induce conduction block in the cable model for very finely resolved domains of $1.2\mu m$. A domain of $6\mu m$, which is much smaller than the $250\mu m$ used by most whole heart *in-silico* studies [Trayanova, 2011, p.115] was found to produce inaccurate CV compared to $1.2\mu m$. Conduction block was observed in the cable model at very high GJ resistances (low σ_j), which reproduces experimental data on reduced GJ coupling [Beauchamp et al., 2012, Jansen et al., 2011].

Whilst the cable model is computationally less intensive than the discrete model, and is a well accepted model for simulation normal propagation, the findings above suggest that a more physiologically detailed tissue model should be used when modelling physical problems involving very fast or very slow conduction, or when the size of the domain is small enough for microscopic CV changes to be an important factor [Spach and Heidlage, 1995].

Action potential upstroke

It was observed that under physiological modulation, dV/dt_{max} did not alter significantly in the continuous cable model. By comparison, this had an initial increase followed by a decrease for higher GJ resistances within the discrete model. Both of these phenomena in cable and discrete models are consistent with literature [[Kléber and Rudy, 2004](#), [Shaw and Rudy, 1997](#)].

Whilst this allows separation of parameters affecting structure (conductivity, diffusivity) and function (excitability), the two are intricately linked [[Kléber and Rudy, 2004](#)]. Although the conduction of excitation wavefront is considered independent of the AP repolarisation, there is a complex relationship between AP upstroke and conduction velocity. It has been demonstrated experimentally that reduction of Cx43 (i.e. increase in GJ resistance) is correlated with changes in the peak action potential upstroke dV/dt_{max} [[Dhillon, 2010](#), p.106]. Thus, it is important that physiological changes in dV/dt_{max} following changes in tissue resistivity (effective or local) are captured in the model.

Modelling the action potential foot

In Chapter 4, the use of the τ_{ap} shape to estimate tissue resistivity and conduction parameters in papillary muscle tissue preparations was presented. The presence of τ_{ap} indicates the existence of electrotonic diffusion of a potential into neighbouring cells, thus allowing the excitation wavefront to propagate. The ability to observe τ_{ap} in computational models is important for matching and comparing experimental and theoretical models.

The cable model expressed $\tau_{ap} = 0.30ms$ under slow conduction, and around 0.29 in normal conduction. τ_{ap} was not present in a single cell simulation, due to the direct

‘injection’ of a current stimulus in to the cell. The discrete model however, exhibited a difference in τ_{ap} between normal and slow conduction. In slow conduction, there was a small double notch at the foot of the AP which may be attributable to diffusion of intracellular potential from upstream neighbouring cells. The existence of multiple notches agrees with existing studies on discrete models [Henriquez and Plonsey, 1987], with multiple humps indicating that local response generated at each junction travels down the fibre; this is suggested to be indicative of an electrotonic prepotential.

Summary

One of the aims of the present work was to examine the limitations of continuum tissue models in producing physiologically meaningful predictions. This has remained an open challenge within the research field [Clayton et al., 2010], and this study has sought to re-highlight the importance of discrete modelling in correctly modelling physiological behaviour, in particular slow conduction, and for matching and comparing experimental and theoretical models.

7.7.5 Applicability and limitations of the discrete model

Existing studies have taken more analytic approaches in 1D with passive transmembrane currents in order to derive macroscopic conductivities [Trayanova and Pilkington, 1993, Trayanova, 1996, Hand et al., 2009, Keener and Sneyd, 2009], or have introduced higher dimensional discrete models with detailed ion channel kinetics, often at greater computational cost [Roberts, 2009, Stinstra et al., 2006, 2010].

Many existing studies have worked in 2D. Lesh et al. [1988] described an early computer model for modelling fractionation. Spach and Heidlage [1995] carried out stochastic modelling of propagation based on a 2D model of real myocytes with varying shapes and size. The model had longitudinal propagation at 48cm/s and transverse at 15cm/s , with time

to cross each cell longitudinally as $226 \pm 78\mu s$ and transactional delays of $87 \pm 32\mu s$. Data given as mean $\pm SD$. dV/dt_{max} ranged from $162 \pm 10V/s$ for longitudinal propagation. Cabo and Boyden [2009] examined the effect of extracellular space on GJ remodelling in AP excitation, whilst a series of studies by the Henriquez group (Hubbard et al. [2007], Hubbard [2010], Jacquemet and Henriquez [2011], Kim [2010]) have also analysed the discrete effects of factors such as cell shape, orientation, heterogeneity or GJ distribution to examine effect on AP propagation or fractionation.

The discrete model in the present study is novel from existing studies on discrete cells, as a 1D bidomain model with active ion channel kinetics, containing periodic intracellular domains, coupled end-to-end by both gap junctions and membrane capacitance. As a 1D model, it is inexpensive computationally and can be used to further examine questions related to discrete cell models, such as the effect of altered membrane capacitance at cell ends, or dynamic voltage-gated GJ resistance instead of modelling gap junctions as passive resistors.

However, there are many geometrical effects which cannot be examined in 1D, such as the effect of wavefront curvature, and the existence of re-entrant circuits. The discrete model outlined can conceivably be implemented in 2D, which would hopefully provide additional insight into structural and functional mechanisms underlying AP propagation.

This study has modelled gap junctional conductances as being a fixed intercellular resistance. A further extension to the model could be via implementation of time-dependent dynamic gap junctional resistances, which have been reported in models [Vogel and Weingart, 1998, Henriquez et al., 2001] and measured in cell pairs [Desplantez et al., 2007], but have not been widely studied.

Part III

Conclusions and Comments

Chapter 8

Discussion

The aim of this thesis was to assess the factors affecting the validity of multi scale theoretical and experimental models of cardiac excitation under modulation of tissue conduction properties. This chapter summarises the findings of the thesis, discusses the findings against the stated research aims, and outlines limitations and future directions of study.

8.1 Summary of key findings

In Chapter 4, an experimental model of electrical propagation in a guinea pig papillary muscle was established. Longitudinal tissue resistivity including a linear combination of junctional (R_j) and cytoplasmic (R_c) resistivity was measured using the oil-gap technique and impedance spectroscopy, with R_j contributing greater than half of the total effective resistivity R_i . Microelectrode recordings on papillary muscle were carried out with Dr Paramdeep Dhillon, with a linear relationship established between tissue resistivity and conduction velocity (CV), as predicted by cable theory. The effects of gap junction (GJ) uncoupler carbenoxolone (CBX) on resistivity and CV were assessed.

In Chapter 5, a monodomain tissue model with Luo-Rudy I ion channel kinetics was

introduced in a 1D cable, representing a long strip of guinea pig ventricular papillary muscle. The numerical accuracy of the implementation was verified. Modulation of diffusion coefficient D led to decrease in CV, and no change in dV/dt_{max} , with no conduction block achieved. Reduction in peak sodium excitability g_{Na} decreased CV and dV/dt_{max} , with conduction block after 80% reduction of g_{Na} . No change was induced in the action potential foot τ_{ap} . The resultant electrogram in slow conduction had a smaller amplitude and wider duration than in normal conduction.

Chapter 6 introduced the atrial myocyte-derived immortal cell line *HL* – 1, and the non-invasive multi electrode array (MEA) system, which has potential applications in understanding the electrogram under physiological slow conduction. Development of a 1D experimental cell culture model on this system required the ability to alter the shape of cell monolayers and individual cells, and a novel technique was proposed to create patterned cell culture on MEA plates. The process of technique optimisation was described, and initial proof of concept results suggested that thin fibronectin-patterned strands induced significant elongation and uniform orientation in HL-1 cells on the patterns compared to thicker strands or simple monolayers. Cx43 labelling studies concluded that it was not possible to mimic normal GJ distribution observed *in-vivo*. No electrical recordings were successfully recorded during this technique optimisation.

Chapter 7 on discrete myocytes coupled by GJs formed the primary investigation within the thesis. It was found that analytical 1D passive discrete cell models have been investigated, as have full 3D computational models of active discrete cells in a block of tissue. A novel 1D discrete cell model with active ion channel kinetics was introduced and implemented, with a detailed validation process against analytical passive problems. The numerical implementation was second order accurate in space, but exhibited large

error and high sensitivity to choice of temporal and spatial discretisation. The full model was coupled to the LR-1 guinea pig AP model, and was simulated subject to physiological modulation of GJ resistance R_j , cytoplasmic resistance R_c and peak sodium excitability g_{Na} .

It was found that increasing R_j and R_c both reduced CV, with a non-linear relationship. Slow conduction in R_j produced spatial activation wavefronts with significant trans-junctional delays, which was not observed for increase in R_c . Conduction block in both occurred below $3\text{cm}/\text{s}$. The effect of modulating R_j led to alteration in the morphology of the action potential foot τ_{ap} . dV/dt_{max} increased initially as R_j increased, then decreased immediately before conduction block was observed .

Decreasing peak sodium excitability led to conduction block after 70% knockout as well as decrease in dV/dt_{max} . An interesting result was an increase in R_j attenuated the effect of decreasing g_{Na} on conduction block due to counteracting effects on dV/dt_{max} , with slow conduction supported even at 90% knockout of g_{Na} .

Finally, cable and discrete models were compared to assess predictions using both models for similar propagation characteristics. Whilst no differences were observed for normal conduction, the spatial activation wavefront, dV/dt_{max} , τ_{AP} and the resultant virtual electrogram all differed at parameters simulating slow conduction.

8.2 Addressing the study aims

8.2.1 Developing an integrative theoretical and experimental approach for understanding cardiac conduction

The work in this thesis sought to undertake an integrative approach to research questions concerning cardiac conduction and electrogram fractionation. This involved addressing questions at one spatial scale using both theory and experiment, and also comparing results on different spatial scales for a particular theoretical or experimental investigation.

Cardiac conduction in tissue

Cable theory is an established and accepted model in the literature [Kléber and Rudy, 2004, Plonsey and Barr, 2007], to which any further study or improvement must be compared. The theoretical electrophysiology community has established a benchmark for comparing numerical methods for solving cardiac physiology equations [Niederer et al., 2011]. A key challenge for computational modellers is to obtain physiologically accurate parameters for simulations.

The conductivity tensor D is the primary determinant of electrical conduction velocity in mono domain and bidomain models [Johnston, 2011, Roth, 1997, Moreau-Villeger et al., 2006]. Constructing this tensor based on histology, magnetic resonance angiography or other imaging techniques is a key research area [Clayton et al., 2010, Pop et al., 2009], and this extends to the modelling of fibrosis and infarct border zone.

In the current study, a 1D cable model of conduction in guinea pig papillary muscle was simulated using values of the 1D conductivity tensor D common in the theoretical literature ($0.001\text{cm}^2/\text{ms}$). Experimental measurement of effective and junctional resistiv-

ity in guinea pig revealed the range of physiological resistivities which correspond closely with theoretical values of D . However, these experimental measurements revealed that junctional resistivity contributes a greater proportion (73%) of total effective resistivity in mammalian myocardium than is commonly considered (50%), which is based on data from frog myocardium. The oil-gap and micro electrode techniques are elegant methods for direct measurement of physiological parameters, and combined together, produced a set of linear relationships between resistivity and conductivity which reflect the prediction made by cable theory.

Cardiac conduction in cells

Monolayer mapping of cultured cell monolayers have been used successfully in previous investigations of cardiac conduction [Kucera et al., 2001, Rohr et al., 1997, Bub et al., 2002, Kirkton, 2012, Bursac et al., 2002]. In this study, theoretical and experimental approaches were taken towards creating a simple model of slow conduction.

A sub clone of the HL-1 cell line (HL1-6), with a baseline CV of around $3 - 4\text{cm/s}$, was identified as a novel model for investigating the relationship between slow conduction and electrogram morphology in 1D. This required cells to be grown on glass cell culture plates with embedded micro electrode arrays (MEA plates), which would permit extracellular electrograms to be recorded.

Patterned monolayers of HL1-6 cells were induced by using the micro-contact printing technique. This technique successfully induced significant elongation of cell length and anisotropy ratio of the cells, for ‘thin’ strands of tissue, as well as decreasing the variation of cellular orientations. Cx43 distribution remained even around cell borders despite

elongation of cells. These results have been confirmed by [Badie, 2010, p.62], indicating that modifying cell shape and orientation alone in patterned monolayers is insufficient to mimic gap junction distribution in myocardium.

A novel 1D bidomain model of excitation in discrete cells coupled by a parallel RC circuit representing gap junctions and membrane capacitance was described and validated against an analytical model. The model exhibited cable theory-like behaviour at conduction velocities greater than $> 40\text{cm/s}$, but at extreme slow conduction velocity ($< 6\text{cm/s}$), long delays were seen at intercellular junctions, reproducing results from experimental studies in cell culture [Rohr et al., 1998].

The present work documents proof of concept and optimisation studies in each of the areas listed above. A successful culmination of these three lines of work would ultimately result in both theoretical and experimental descriptions of 1D conduction in elongated cultured cells, with cell morphology similar to real tissue myocardium and with quantifiable biological parameters which can be introduced in to the model. This setup would allow both simulation and direct measurement of the extracellular electrogram, which can then be used to examine the signature of electrogram fractionation in arrhythmic tissue exhibiting slow conduction velocity.

8.2.2 Investigation of the physiological parameter range and limitations of experimental models

The microelectrode and oil-gap techniques are accepted experimental models for deriving physiological parameters for input in to theoretical studies [Chapman and Fry, 1978, Cooklin et al., 1997]. The work carried out in this thesis, with the support and guidance of Dr Paramdeep Dhillon and Ms Samantha Salvage, has measured tissue resistivity, ac-

tion potential characteristics and conduction properties in guinea pig papillary muscle samples.

It was discovered that a linear relationship exists between tissue resistivity and conduction velocity in the papillary muscle samples, as predicted by cable theory. However the pharmacological agent (carbenoxolone) used to induce gap junctional uncoupling, whilst having a time course effect in degree of tissue uncoupling, had no continued or increased effect above a given dosage.

Resistivity and conduction velocity studies observed in the current study showed a $3\times$ change in resistivity for a conduction slowing of 15%. The range and effect of physiological changes appeared to be limited, compared to theoretical studies in Chapter 5 where parameter values can be arbitrarily set. This suggests some limitation in using experimental models and tools to assess physiological behaviour. Emergent phenomena and specificity of pharmacological interventions are all effects which may compensate for a pure mechanism. The experimental studies have suggested that certain biological interventions may be limited to a small range of effects, and also that it is unclear if and how the linear relationship breaks down at extreme limits of pharmacological modulation.

8.2.3 Developing and investigating a discrete framework and approach to understanding slow conduction

The focus in cardiac modelling in recent years has been in developing whole heart models which simulate cardiac behaviour with a large domain and high number of variables [Clayton and Panfilov, 2008, Clayton et al., 2010]. Whilst improving computational speed and numerical methods have become a primary avenue of research [Arthurs et al., 2012, Qu and Garfinkel, 1999, Lines et al., 2003], relatively few studies have worked to analyse the accuracy of simulations [Niederer et al., 2011, Camara et al., 2011] or to investigate

the validity of current models against biological datasets. The group of Henriquez has been active in this latter topic, publishing several articles analysing the effect of detailed cardiac monolayer models [Hubbard, 2010, Roberts, 2009, Stinstra et al., 2010].

The work described in this study sought to examine the effect of slow conduction, which might occur in the areas of high gap junctional uncoupling or lateralisation such as infarct border zone following myocardial ischemia. It has been reported that saltatory conduction from cell-to-cell occurs in slow conduction [Spach and Miller, 1981, 1982, Rohr et al., 1998], and this suggested that modelling on the level of discrete cells would be needed to study this phenomenon.

The mathematical discrete bidomain model described in Chapter 7 models piecewise continuous ‘cables’ of individual cells, connecting to each other via a parallel RC circuit representing resistance due to gap junctions and capacitance, and to a continuous extracellular space via ion channel kinetics. This differs from existing studies: analytic studies did not contain functional ion channel kinetics [Keener and Sneyd, 2009], some models of discrete tissue were in 3D [Stinstra et al., 2010], whilst Shaw and Rudy [1997] only considered resistive coupling between cells in a monodomain model, without the additional capacitance term. The simulations are also more spatially resolved than many prior studies.

The results of the study compares well with publications in the Henriquez group, who reported saltatory conduction, and also observed multiple humps in the action potential upstroke under slow conduction velocity [Henriquez and Plonsey, 1987].

A parallel approach to develop an experimental model of discrete patterned cells in culture was also described, to ultimately record and analyse the extracellular electrogram during slow conduction. This was, to our knowledge, the first attempt in the literature

to apply a patterned cell culture technique on to commercially available multi electrode array (MEA) plates, on which the electrogram of slow conduction can be recorded. The work described suggested proof of concept; further studies are required to fully develop this experimental model.

8.2.4 Assessing the numerical and physiological parameters for which continuum models produce physiologically meaningful predictions

One dimensional models were described at two separate spatial scales - continuum models where the behaviour of many cells are averaged at a single point, versus a discrete model where individual cells were modelled as piecewise continuous cables. At high conduction velocity, the characteristics of the propagation wavefront between the two models were similar. At low conduction velocity, the propagation in the discrete model exhibited a discontinuous, saltatory activation pattern, reproducing results from experimental studies on cell culture [Rohr et al., 1998].

The assumption for validity of the continuum model is that length constant λ is greater than the length of a single myocyte [Keener and Sneyd, 2009]. Experimental studies [Kléber and Rudy, 2004] would suggest, from the discussion of saltatory conduction observed in slow conduction, that λ is reduced under conditions of slow conduction. This supports the finding in the current study that continuum models do not correctly predict physiological behaviour under slow conduction in excitable tissue.

With reference to numerical parameters, it was noted in the current work that key physiological parameters, such as conduction velocity and dV/dt_{max} were dependent on

the spatial discretisation chosen for fixed physiological parameters, as has previously been indicated [Clayton et al., 2010]. To eliminate variability due to numerical error, the models were both simulated at high spatial resolution ($\Delta x < 6\mu m$), smaller than $\Delta x \sim 0.1mm$ described in existing studies [Clayton et al., 2010]. The continuum model did not capture physiological behaviour at slow conduction velocity. This suggests a breakdown in the continuum model exists at a critical conduction velocity that cannot be rectified via further numerical refinement. This leads to the conclusion that the optimum model to capture the physiological behaviour under specific pathophysiological changes is highly sensitive to model assumptions, which need to be readdressed whenever the underlying biology changes.

8.3 Study limitations and future directions

The limitations and future directions of each line of work are summarised below.

8.3.1 Guinea pig work

Within the guinea pig conduction model, conduction slowing was induced using gap junctional uncoupler carbenoxolone. The range of resistivities and conduction velocities (CV) following pharmacological modulation was limited, and thus the physiological effect of tissue resistivity on CV outside this range could only be hypothesised. Further experimental design to carry out further functional studies of AP propagation would be crucial for matching theoretical simulation to experimental data.

8.3.2 Creating patterned strands in cell culture for electrogram recording

The work described on patterned cell culture on MEA plates demonstrated proof of concept, and that thin strands of $< 30\mu m$ induced significant elongation and homogenised orientation of cultured HL-1 cells, which in normal culture, exhibited elliptical or circular profiles with random orientations. The sample size of the study was small across all results, with increased n numbers required to fully document and detail the validity of the technique.

Reproducibility and viability of the patterned technique along with detailed quantification of gap junctional functionality was not fully explored, and there remains room for improvement before the technique can be described to be robust.

The key limitation of the patterned culture model was the failure to capture electrogram recordings in patterned culture cells within several days, after which cells outgrew their pattern. Further work to characterise the signal to noise ratio of the system and the underlying cells would aid completion of the project. Additionally it would be interesting to use other cell lines or primary neonatal rat ventricular myocytes to explore other options for recording electrograms in patterned culture.

8.3.3 Development of an HL-1 sub clone action potential model

An initial mathematical description to describe the action potential of the HL1-6 sub clone was undertaken, although not included within the main results of the thesis. The model was created by fitting to AP characteristics at baseline, but was unable to reproduce restitution properties, notably the maximum experimental pacing rate of $8 - 10Hz$ despite the APD of $20 - 30ms$. Further collaborative work with experimental patch clamp

specialists to ascertain existence and functional properties of further ion channels and gap junctional distributions within the cell line is required, before a careful reconstruction of the action potential model is completed.

Additionally, further work to fit mathematical descriptions of the currents to recorded patch clamp data would aid in a more accurate biophysical description of the model.

8.3.4 Discrete cell model

The discrete cell model compared propagation behaviour via matching conduction velocities that were induced by suitable adjustment of lumped physiological parameters. A more realistic alteration would be to modify physiological parameters using values suggested in literature or by additional experiment. This would truly permit analysis of conduction velocities as a result of physiological changes, as well as gaining further insight to discrete conduction at slow CV.

The full numerical discrete model with ionic channels exhibited high sensitivity to temporal discretisation. Further studies need to be completed, possibly with independent codes and implementations from other external groups to assess and quantify the stability of the model and its accuracy.

It is possible that certain propagation characteristics observed in the work described may have been a feature of the ionic channel model chosen (LR-1 in this case). It would be interesting to couple the discrete model to other existing cell models to explore novel insights due to existence of other currents.

Additionally, extending the model to two dimensions would allow investigation in to

anisotropy ratios and effects of wavefront curvature on conduction slowing and subsequent electrogram fractionation. Consideration of time-dependent dynamic gap junctional resistivity would be a further extension which could provide insight on the effect of gap junction formation and functionality.

8.4 Concluding remarks

This study set out to explore the validity of theoretical and experimental multi scale models of action potential propagation. It described theoretical models of continuum and discrete level cells in 1D and compared the models under physiological modulation. Reduced gap junctional coupling helped to improve the safety factor as membrane sodium excitability was decreased, leading to discontinuous propagation at very slow conduction velocities. It was found that even at high spatial resolution, the continuum models did not reproduce the saltatory conduction observed at low conduction velocity, which was observed in the discrete model. The resultant simulated electrogram waveforms were compared, and potential mechanisms responsible for the morphology of the resultant electrograms were discussed. This study suggests the need to refine the continuous cable model when simulating slow conduction induced by reduced gap junctional coupling or by reduced membrane excitability.

Functional studies in intact guinea pig myocardium were completed to measure effective tissue resistivity and action potential characteristics using a microelectrode impalement technique.

Lastly, development of a technique to create patterned cultures of HL1-6 cells on microelectrode-embedded plates was undertaken, with initial results indicating feasibility of the technique in inducing elongation and orientation of cells. Further work is required to

fully develop an integrated theoretical and experimental model of conduction in discrete cells, which can be used to gain further insight in to understanding the mechanisms underlying electrogram fractionation.

Bibliography

- A Agocha, A V Sigel, and M Eghbali-Webb. Characterization of adult human heart fibroblasts in culture: a comparative study of growth, proliferation and collagen production in human and rabbit cardiac fibroblasts and their response to transforming growth factor-beta1. *Cell and tissue research*, 288(1):87–93, April 1997.
- F G Akar, B J Roth, and D S Rosenbaum. Optical measurement of cell-to-cell coupling in intact heart using subthreshold electrical stimulation. *American journal of physiology Heart and circulatory physiology*, 281(2):H533–42, August 2001.
- RR Aliev and AV Panfilov. A simple two-variable model of cardiac excitation. *Chaos Solitons & Fractals*, 7(3):293–301, 1996.
- M A Allessie, F I Bonke, and F J Schopman. Circus movement in rabbit atrial muscle as a mechanism of tachycardia. III. The "leading circle" concept: a new model of circus movement in cardiac tissue without the involvement of an anatomical obstacle. *Circulation Research*, 41(1):9–18, July 1977.
- C J Arthurs, M J Bishop, and D Kay. Efficient simulation of cardiac electrical propagation using high order finite elements. *Journal of Computational Physics*, 2012.
- Nima Badie. *The Roles of Realistic Cardiac Structure in Conduction and Conduction Block: Studies of Novel Micropatterned Cardiac Cell Cultures*. PhD thesis, Duke University, August 2010.
- P Beauchamp. Electrical Propagation in Synthetic Ventricular Myocyte Strands From Germline Connexin43 Knockout Mice. *Circulation Research*, 95(2):170–178, June 2004.
- P Beauchamp, T Desplantez, M L McCain, W Li, A Asimaki, G Rigoli, K K Parker, JE Saffitz, and A G Kléber. Electrical Coupling and Propagation in Engineered Ventricular Myocardium With Heterogeneous Expression of Connexin43. *Circulation Research*, April 2012.
- G W Beeler and H Reuter. Reconstruction of the action potential of ventricular myocardial fibres. *The Journal of Physiology*, 268(1):177–210, June 1977.
- R Bordas, J Cooper, and A Gurny. A numerical guide to the solution of the bidomain equations of cardiac electrophysiology. *Progress in Biophysics and Molecular Biology*, 2010.
- G Bub and A Shrier. Propagation through heterogeneous substrates in simple excitable media models. *Chaos*, 12(3):747–753, September 2002.
- G Bub, A Shrier, and L Glass. Spiral wave generation in heterogeneous excitable media. *Physical review letters*, 88(5):058101, February 2002.
- A Bueno-Orovio, E M Cherry, and F H Fenton. Minimal model for human ventricular action potentials in tissue. *J Theor Biol*, 253(3):544–560, August 2008.

- N Bursac, K K Parker, S Iravanian, and L Tung. Cardiomyocyte cultures with controlled macroscopic anisotropy: a model for functional electrophysiological studies of cardiac muscle. *Circulation Research*, 91(12):e45–54, December 2002.
- C Cabo and P A Boyden. Extracellular Space Attenuates the Effect of Gap Junctional Remodeling on Wave Propagation: A Computational Study. *Biophys J*, 96(8):3092–3101, April 2009.
- O Camara, M Sermesant, P Lamata, L Wang, M Pop, J Relan, M De Craene, H Delingette, H Liu, S Niederer, A Pashaei, G Plank, D Romero, R Sebastian, K C L Wong, H Zhang, N Ayache, A F Frangi, P Shi, N P Smith, and G A Wright. Inter-model consistency and complementarity: Learning from ex-vivo imaging and electrophysiological data towards an integrated understanding of cardiac physiology. *Progress in Biophysics and Molecular Biology*, 107(1):122–133, October 2011.
- P Camelliti, J O Gallagher, P Kohl, and A D McCulloch. Micropatterned cell cultures on elastic membranes as an in vitro model of myocardium. *Nat Protoc*, 1(3):1379–1391, 2006.
- C D Cantwell, S J Sherwin, R M Kirby, and P H J Kelly. From h to p efficiently: Strategy selection for operator evaluation on hexahedral and tetrahedral elements. *Computers & Fluids*, 43(1):23–28, April 2011a.
- C D Cantwell, S J Sherwin, R M Kirby, and PHJ Kelly. From h to p Efficiently: Selecting the Optimal Spectral/Discretisation in Three Dimensions. *Math. Model. Nat. Phenom.*, 6(3):84–96, 2011b.
- M G Chang, Y Zhang, C Y Chang, L Xu, R Emokpae, L Tung, E Marban, and M R Abraham. Spiral Waves and Reentry Dynamics in an In Vitro Model of the Healed Infarct Border Zone. *Circulation Research*, 105(11):1062–1071, November 2009.
- R A Chapman and C H Fry. An analysis of the cable properties of frog ventricular myocardium. *The Journal of Physiology*, 1978.
- E Cherry, J Ehrlich, and S Nattel. Pulmonary vein reentry—properties and size matter: insights from a computational analysis. *Heart Rhythm*, 2007.
- E M Cherry and F H Fenton. Suppression of alternans and conduction blocks despite steep APD restitution: electrotonic, memory, and conduction velocity restitution effects. *American journal of physiology Heart and circulatory physiology*, 286(6):H2332–41, June 2004.
- E M Cherry, H S Greenside, and C S Henriquez. Efficient simulation of three-dimensional anisotropic cardiac tissue using an adaptive mesh refinement method — Chaos. *Chaos*, 2003.
- R A Chowdhury. *Gap Junction Remodelling and Conduction Abnormalities in the Heart*. PhD thesis, Imperial College London, October 2011.
- J Clark and R Plonsey. A mathematical evaluation of the core conductor model. *Biophysical Journal*, 6 (1):95–112, 1966.
- J Clark and R Plonsey. The extracellular potential field of the single active nerve fiber in a volume conductor. *Biophysical Journal*, 8(7):842–864, 1968.
- W C Claycomb, Jr Lanson, B S Stallworth, D B Egeland, J B Delcarpio, A Bahinski, and Jr Izzo. HL-1 cells: a cardiac muscle cell line that contracts and retains phenotypic characteristics of the adult cardiomyocyte. *Proc Natl Acad Sci U S A*, 95(6):2979–2984, March 1998.
- R H Clayton, O Bernus, E M Cherry, H Dierckx, F H Fenton, L Mirabella, A V Panfilov, F B Sachse, G Seemann, and H Zhang. Models of cardiac tissue electrophysiology: Progress, challenges and open questions. *Progress in Biophysics and Molecular Biology*, pages 1–27, June 2010.

- RH Clayton and AV Panfilov. A guide to modelling cardiac electrical activity in anatomically detailed ventricles. *Progress in Biophysics and Molecular Biology*, 96(1-3):19–43, 2008.
- L Clerc. Directional differences of impulse spread in trabecular muscle from mammalian heart. *The Journal of Physiology*, 1976.
- M Cooklin, W R Wallis, D J Sheridan, and C H Fry. Changes in cell-to-cell electrical coupling associated with left ventricular hypertrophy. *Circulation Research*, 80(6):765–771, June 1997.
- D D Correa de Sa, N Thompson, J Stinnett-Donnelly, P Znojewicz, N Habel, J G Müller, J H T Bates, J S Buzas, and P S Spector. Electrogram Fractionation The Relationship Between Spatiotemporal Variation of Tissue Excitation and Electrode Spatial Resolution. *Circulation: Arrhythmia and Electrophysiology*, 4(6):909–916, 2011.
- M Courtemanche, R J Ramirez, and S Nattel. Ionic mechanisms underlying human atrial action potential properties: insights from a mathematical model. *The American journal of physiology*, 275(1 Pt 2):H301–21, July 1998.
- Marc Courtemanche. Complex spiral wave dynamics in a spatially distributed ionic model of cardiac electrical activity. *Chaos*, 6(4):579–600, December 1996.
- J Crank and P Nicolson. A practical method for numerical evaluation of solutions of partial differential equations of the heat-conduction type. *Mathematical Proceedings of the Cambridge Philosophical Society*, 1947.
- C de Diego, F Chen, Y Xie, R K Pai, L Slavin, J Parker, S T Lamp, Z Qu, J N Weiss, and M Valderrabano. Anisotropic conduction block and reentry in neonatal rat ventricular myocyte monolayers. *AJP: Heart and Circulatory Physiology*, 300(1):H271–H278, January 2011.
- JR De Groot, T Veenstra, AO Verkerk, R Wilders, JPP Smits, FJG Wilms-Schopman, RF Wiegerinck, J Bourier, CNW Belterman, and R Coronel. Conduction slowing by the gap junctional uncoupler carbenoxolone. *Cardiovasc Res*, 60(2):288, 2003.
- E de Lange and Jan P Kucera. The Transfer Functions of Cardiac Tissue during Stochastic Pacing. *Biophys J*, 96(1):294–311, January 2009.
- T Desplantez, E Dupont, N J Severs, and R Weingart. Gap Junction Channels and Cardiac Impulse Propagation. *Journal of Membrane Biology*, 218(1-3):13–28, July 2007.
- J Deutsch, D Motlagh, B Russell, and TA Desai. Fabrication of microtextured membranes for cardiac myocyte attachment and orientation. *Journal of Biomedical Materials Research Part B: Applied Biomaterials*, 53(3):267–275, 2000.
- S Dhein. Pharmacology of gap junctions in the cardiovascular system. *Cardiovasc Res*, 62(2):287–298, May 2004.
- Paramdeep Singh Dhillon. *The Relationship Between Changes in Myocardial Resistivity, Conduction Velocity and Gap-Junction Topology in Diseased Human Myocardium*. PhD thesis, Imperial College London, April 2010.
- Priyanthi Dias. *Influence of Connexin Expression/Co-Expression Levels on Electrical Impulse Propagation Investigated in the HL-1 Cell Model*. PhD thesis, Imperial College London, August 2010.
- I R Efimov. Optical Imaging of the Heart. *Circulation Research*, 95(1):21–33, May 2004.

- M Ethier and Y Bourgault. Semi-Implicit Time-Discretization schemes for the bidomain model. *SIAM Journal on Numerical Analysis*, 46:2443, 2008.
- V G Fast and A G Kléber. Microscopic conduction in cultured strands of neonatal rat heart cells measured with voltage-sensitive dyes. *Circulation Research*, 1993.
- V G Fast and A G Kléber. Anisotropic conduction in monolayers of neonatal rat heart cells cultured on collagen substrate. *Circulation Research*, 75(3):591–595, September 1994.
- V V Fedorov, A V Glukhov, R Chang, G Kostecki, H Aferol, W J Hucker, J P Wuskell, L M Loew, R B Schuessler, N Moazami, and I R Efimov. Optical Mapping of the Isolated Coronary-Perfused Human Sinus Node. *JACC*, 56(17):1386–1394, October 2010.
- V V Fedorov, C M Ambrosi, G Kostecki, W J Hucker, A V Glukhov, J P Wuskell, L M Loew, N Moazami, and I R Efimov. Anatomic Localization and Autonomic Modulation of Atrioventricular Junctional Rhythm in Failing Human Hearts. *Circulation: Arrhythmia and Electrophysiology*, 4(4):515–525, August 2011.
- F Fenton, E Cherry, and H Hastings. Multiple mechanisms of spiral wave breakup in a model of cardiac electrical activity. *Chaos*, 2002.
- Flavio Fenton and Alain Karma. Vortex dynamics in three-dimensional continuous myocardium with fiber rotation: Filament instability and fibrillation. *Chaos*, 8(1):20–47, March 1998.
- R Fitzhugh. Impulses and physiological states in theoretical models of nerve membrane. *Biophysical Journal*, 1(6):445–466, 1961.
- Jocelyn E Manning Fox, Lynn Jones, and Peter E Light. Identification and pharmacological characterization of sarcolemmal ATP-sensitive potassium channels in the murine atrial HL-1 cell line. *Journal of cardiovascular pharmacology*, 45(1):30–35, January 2005.
- W E Garrey. The nature of fibrillary contraction of the heart: its relation to tissue mass and form. *The American journal of physiology*, 1914.
- Martin Gerhardt, Heike Schuster, and John J Tyson. A cellular automaton model of excitable media including curvature and dispersion. *American Association for the Advancement of Science. Science*, 247(4950):1563–1566, 1990.
- DB Geselowitz. Comment on the core conductor model. *Biophysical Journal*, 6(5):691, 1966.
- Dana Goldoni, YouYou Zhao, Brian D Green, Barbara J McDermott, and Anthony Collins. Inward rectifier potassium channels in the HL-1 cardiomyocyte-derived cell line. *Journal of Cellular Physiology*, 225(3):751–756, December 2010.
- M Halbach, U Egert, J Hescheler, and K Banach. Estimation of action potential changes from field potential recordings in multicellular mouse cardiac myocyte cultures. *Cell Physiol Biochem*, 13(5):271–284, 2003.
- John R Hampton. *The ECG Made Easy*. Churchill Livingstone, 2003.
- Paul E Hand, Boyce E Griffith, and Charles S Peskin. Deriving Macroscopic Myocardial Conductivities by Homogenization of Microscopic Models. *Bulletin of Mathematical Biology*, 71(7):1707–1726, October 2009.

- D M Harrild and C S Henriquez. A finite volume model of cardiac propagation. *Annals of Biomedical Engineering*, 25(2):315–334, March 1997.
- AP Henriquez, R Vogel, BJ Muller-Borer, Cs Henriquez, R Weingart, and WE Cascio. Influence of dynamic gap junction resistance on impulse propagation in ventricular myocardium: a computer simulation study. *Biophysical Journal*, 81(4):2112–2121, 2001.
- C S Henriquez. Simulating the electrical behavior of cardiac tissue using the bidomain model. *Crit Rev Biomed Eng*, 21(1):1–77, 1993.
- C S Henriquez and R Plonsey. Effect of resistive discontinuities on waveshape and velocity in a single cardiac fibre. *Medical and Biological Engineering and Computing*, 25(4):428–438, July 1987.
- C S Henriquez and R Plonsey. Simulation of propagation along a cylindrical bundle of cardiac tissue-II: Results of simulation. *IEEE Trans Biomed Eng*, 37(9):861–875, 1990.
- C S Henriquez, N Trayanova, and R Plonsey. Potential and current distributions in a cylindrical bundle of cardiac tissue. *Biophys J*, 53(6):907–918, 1988.
- C S Henriquez, J V Tranquillo, and D Weinstein. Three-dimensional propagation in mathematical models: Integrative model of the mouse heart. From Cell to Bedside, 2004.
- B Hille. Ion channels of excitable membranes. 2001.
- Herman D Himel, Gil Bub, Prajapathy Lakireddy, and Nabil El-Sherif. Optical imaging of arrhythmias in the cardiomyocyte monolayer. *Heart Rhythm*, pages 1–6, October 2012.
- SY Ho and D Sánchez-Quintana. The importance of atrial structure and fibers. *Clinical Anatomy*, 22(1):52–63, 2009.
- A L Hodgkin and A F Huxley. A quantitative description of membrane current and its application to conduction and excitation in nerve. 1952. *J. Physiol.*, 117:500–544, 1952.
- D A Hooks. Cardiac Microstructure: Implications for Electrical Propagation and Defibrillation in the Heart. *Circulation Research*, 91(4):331–338, August 2002.
- Darren A Hooks. Myocardial segment-specific model generation for simulating the electrical action of the heart. *Biomedical engineering online*, 6:21, 2007.
- Letitia Hubbard. *The Effect of Structural Microheterogeneity on the Initiation and Propagation of Ectopic Activity in Cardiac Tissue*. PhD thesis, Duke University, April 2010.
- Marjorie Letitia Hubbard, Wenjun Ying, and Craig S Henriquez. Effect of gap junction distribution on impulse propagation in a monolayer of myocytes: a model study. *Europace*, 9 Suppl 6:vi20–vi28, November 2007.
- H V Huikuri, A Castellanos, and R J Myerburg. Sudden death due to cardiac arrhythmias. *New England Journal of Medicine*, 345(20):1473–1482, November 2001.
- P Hunter and A Pullan. Modeling total heart function. *Biomedical Engineering*, 2003.
- CJ Hyatt, CW Zemlin, RM Smith, A Matiukas, AM Pertsov, and O Bernus. Reconstructing subsurface electrical wave orientation from cardiac epi-fluorescence recordings: Monte Carlo versus diffusion approximation. *Optics Express*, 16(18):13758–15772, 2008.

- V Jacquemet and C S Henriquez. Genesis of complex fractionated atrial electrograms in zones of slow conduction: A computer model of microfibrosis. *Heart Rhythm*, 6(6):803–810, January 2011.
- V Jacquemet, B Robinson, and Cs Henriquez. Electrogram fractionation caused by microfibrosis: insights from a microstructure model. *Computers in Cardiology*, 2008, pages 1105–1108, 2009.
- José Jalife. Rotors and spiral waves in atrial fibrillation. *Journal of Cardiovascular Electrophysiology*, 14(7):776–780, July 2003.
- J A Jansen, M Noorman, H Musa, M Stein, S de Jong, R van der Nagel, T J Hund, P J Mohler, M A Vos, T A van Veen, J M de Bakker, M Delmar, and H V van Rijen. Reduced heterogeneous expression of Cx43 results in decreased Nav1.5 expression and reduced sodium current that accounts for arrhythmia vulnerability in conditional Cx43 knockout mice. *Heart Rhythm*, pages 1–9, December 2011.
- Peter R Johnston. The effect of simplifying assumptions in the bidomain model of cardiac tissue: application to ST segment shifts during partial ischaemia. *Mathematical biosciences*, 198(1):97–118, November 2005.
- Peter R Johnston. A finite volume method solution for the bidomain equations and their application to modelling cardiac ischaemia. *Computer Methods in Biomechanics and Biomedical Engineering*, 13(2):157–170, April 2010.
- Peter R Johnston. Cardiac conductivity values—A challenge for experimentalists? *Noninvasive Functional Source Imaging of the Brain and Heart & 2011 8th International Conference on Bioelectromagnetism*, pages 39–43, 2011.
- Mario Delmar Justus Anumonwo Omer Berenfeld José Jalife and Jérôme Kalifa. Basic Cardiac Electrophysiology for the Clinician, Second Edition. pages 1–358, December 2009.
- R W Joyner. Effects of the discrete pattern of electrical coupling on propagation through an electrical syncytium. *Circulation Research*, 50(2):192–200, February 1982.
- G E Karniadakis and S J Sherwin. Spectral/Hp Element Methods for Cfd - George E. M. Karniadakis, Spencer J. Sherwin - Google Books. 1999.
- James Keener and James Sneyd. *Mathematical Physiology*. Springer, second edition, January 2009.
- Jong Kim. *A Discrete Monolayer Cardiac Tissue Model for Tissue Preparation Specific Modeling*. PhD thesis, Duke University, April 2010.
- R D Kirkton. *Genetic Engineering of Excitable Cells for In Vitro Studies of Electrophysiology and Cardiac Cell Therapy*. PhD thesis, Duke University, April 2012.
- A G Kleber. The Shape of the Electrical Action-Potential Upstroke: A New Aspect From Optical Measurements on the Surface of the Heart. *Circulation Research*, 97(3):204–206, July 2005.
- André G Kléber and Yoram Rudy. Basic mechanisms of cardiac impulse propagation and associated arrhythmias. *Physiological Reviews*, 84(2):431–488, April 2004.
- SB Knisley and MR Neuman. Simultaneous electrical and optical mapping in rabbit hearts. *Annals of Biomedical Engineering*, 31(1):32–41, 2003.
- P Kohl. Heterogeneous Cell Coupling in the Heart: An Electrophysiological Role for Fibroblasts. *Circulation Research*, 93(5):381–383, September 2003.

J P Kucera, A G Kléber, and S Rohr. Slow conduction in cardiac tissue, II: effects of branching tissue geometry. *Circulation Research*, 83(8):795–805, October 1998.

J P Kucera, A G Kléber, and S Rohr. Slow conduction in cardiac tissue: insights from optical mapping at the cellular level. *J Electrocardiol*, 34 Suppl:57–64, 2001.

P Lee, C Bollensdorff, T A Quinn, J P Wuskell, L M Loew, and P Kohl. Single-sensor system for spatially resolved, continuous, and multiparametric optical mapping of cardiac tissue. *Heart Rhythm*, 8(9):1482–1491, September 2011.

P Lee, M Klos, C Bollensdorff, L Hou, P Ewart, T J Kamp, J Zhang, A Bizy, G Guerrero-Serna, P Kohl, J Jalife, and T J Herron. Simultaneous Voltage and Calcium Mapping of Genetically Purified Human Induced Pluripotent Stem Cell-Derived Cardiac Myocyte Monolayers. *Circulation Research*, 110(12):1556–1563, June 2012.

I J LeGrice, B H Smaill, L Z Chai, S G Edgar, J B Gavin, and P J Hunter. Laminar structure of the heart: ventricular myocyte arrangement and connective tissue architecture in the dog. *The American journal of physiology*, 269(2 Pt 2):H571–82, August 1995.

MD Lesh, JF Spear, and MB Simson. A computer model of the electrogram: What causes fractionation?*
1. *J Electrocardiol*, 21:S69–S73, 1988.

Leon K Liem, J Marc Simard, Yumin Song, and Kirti Tewari. The Patch Clamp Technique. *Neurosurgery*, 36(2):382, February 1995.

GT Lines, ML Buist, P Grottum, AJ Pullan, J Sundnes, and A Tveito. Mathematical models and numerical methods for the forward problem in cardiac electrophysiology. *Computing and Visualization in Science*, 5(4):215–239, 2003.

Leonid Livshitz and Yoram Rudy. Uniqueness and Stability of Action Potential Models during Rest, Pacing, and Conduction Using Problem-Solving Environment. *Biophysical Journal*, 97(5):1265–1276, September 2009.

CH Luo and Y Rudy. A model of the ventricular cardiac action potential. Depolarization, repolarization, and their interaction. *Circulation Research*, 68(6):1501–1526, June 1991.

CH Luo and Y Rudy. A dynamic model of the cardiac ventricular action potential. I. Simulations of ionic currents and concentration changes. *Circulation Research*, 74(6):1071, 1994.

J R Macdonald. Impedance spectroscopy. *Annals of Biomedical Engineering*, 20(3):289–305, 1992.

M C MacLachlan, J Sundnes, and G T Lines. Simulation of ST Segment Changes During Subendocardial Ischemia Using a Realistic 3-D Cardiac Geometry. *IEEE Trans Biomed Eng*, 52(5):799–807, May 2005.

G Meiry, Y Reisner, Y Feld, S Goldberg, M Rosen, N ZIV, and O Binah. Evolution of action potential propagation and repolarization in cultured neonatal rat ventricular myocytes. *Journal of Cardiovascular Electrophysiology*, 12(11):1269–1277, 2001.

GR Mines. On dynamic equilibrium in the heart. *The Journal of Physiology*, 1913.

Gary R Mirams, Christopher J Arthurs, Miguel O Bernabeu, Rafel Bordas, Jonathan Cooper, Alberto Corrias, Yohan Davit, Sara-Jane Dunn, Alexander G Fletcher, Daniel G Harvey, Megan E Marsh, James M Osborne, Pras Pathmanathan, Joe Pitt-Francis, James Southern, Nejib Zemzemi, and David J Gavaghan. Chaste: An Open Source C++ Library for Computational Physiology and Biology. *PLoS Computational Biology*, 9(3):e1002970, March 2013.

- Gordon K Moe, Werner C Rheinboldt, and J A Abildskov. A computer model of atrial fibrillation. *American heart journal*, 67(2):200–220, February 1964.
- V Moreau-Villeger, H Delingette, M Sermesant, H Ashikaga, E McVeigh, and N Ayache. Building maps of local apparent conductivity of the epicardium with a 2-D electrophysiological model of the heart. *Biomedical Engineering, IEEE Transactions on*, 53(8):1457–1466, 2006.
- J M Morgan, J C Cowan, A J Camm, and J M McComb. Sudden cardiac death: opportunities for prevention. *Heart*, 92(6):721–723, June 2006.
- D Motlagh, TJ Hartman, TA Desai, and B Russell. Microfabricated grooves recapitulate neonatal myocyte connexin43 and Ncadherin expression and localization. *Journal of Biomedical Materials Research Part A*, 67(1):148–157, 2003.
- S M Narayan, M Wright, N Derval, A Jadidi, A Forclaz, I Nault, S Miyazaki, F Sacher, P Bordachar, J Clémenty, P Jaïs, M Haïssaguerre, and M Hocini. Classifying fractionated electrograms in human atrial fibrillation using monophasic action potentials and activation mapping: Evidence for localized drivers, rate acceleration, and nonlocal signal etiologies. *Heart Rhythm*, 8(2):244–253, February 2011.
- Sanjiv M Narayan, David E Krummen, Michael W Enyeart, and Wouter-Jan Rappel. Computational Mapping Identifies Localized Mechanisms for Ablation of Atrial Fibrillation. *PLoS ONE*, 7(9):e46034, September 2012a.
- Sanjiv M Narayan, David E Krummen, and Wouter-Jan Rappel. Clinical Mapping Approach To Diagnose Electrical Rotors and Focal Impulse Sources for Human Atrial Fibrillation. *Journal of Cardiovascular Electrophysiology*, 23(5):447–454, April 2012b.
- S Nattel. Complex fractionated atrial electrograms: Can they be made simple? *Heart rhythm: the official journal of the Heart Rhythm Society*, 5(6):855, 2008.
- Jeanne M Nerbonne and Robert S Kass. Molecular physiology of cardiac repolarization. *Physiological Reviews*, 85(4):1205–1253, October 2005.
- J C Neu and W Krassowska. Homogenization of syncytial tissues. *Crit Rev Biomed Eng*, 21(2):137–199, 1993.
- Fu Siong Ng. *The Effects of Gap Junction Modulation on Myocardial Structure and Function*. PhD thesis, Imperial College London, December 2011.
- Steven A Niederer, Eric Kerfoot, Alan P Benson, Miguel O Bernabeu, Olivier Bernus, Chris Bradley, Elizabeth M Cherry, Richard Clayton, Flavio H Fenton, Alan Garny, Elvio Heidenreich, Sander Land, Mary Maleckar, Pras Pathmanathan, Gernot Plank, José F Rodríguez, Ishani Roy, Frank B Sachse, Gunnar Seemann, Ola Skavhaug, and Nic P Smith. Verification of cardiac tissue electrophysiology simulators using an N-version benchmark. *Philosophical transactions. Series A, Mathematical, physical, and engineering sciences*, 369(1954):4331–4351, November 2011.
- D Noble. A modification of the Hodgkin–Huxley equations applicable to Purkinje fibre action and pace-maker potentials. *The Journal of Physiology*, 160:317–352, February 1962.
- Muriel Nobles, Sonia Sebastian, and Andrew Tinker. HL-1 cells express an inwardly rectifying K⁺ current activated via muscarinic receptors comparable to that in mouse atrial myocytes. *Pflügers Archiv - European Journal of Physiology*, 460(1):99–108, February 2010.

Thomas O'Hara and Yoram Rudy. Quantitative comparison of cardiac ventricular myocyte electrophysiology and response to drugs in human and nonhuman species. *AJP: Heart and Circulatory Physiology*, 302(5):H1023–30, March 2012.

P M Patel, A Plotnikov, P Kanagaratnam, A Shvilkin, C T Sheehan, W Xiong, P Danilo, M R Rosen, and N S Peters. Altering ventricular activation remodels gap junction distribution in canine heart. *Journal of Cardiovascular Electrophysiology*, 12(5):570–577, May 2001.

Nicholas S Peters, James Coromilas, Nicholas J Severs, and Andrew L Wit. Disturbed Connexin43 Gap Junction Distribution Correlates With the Location of Reentrant Circuits in the Epicardial Border Zone of Healing Canine Infarcts That Cause Ventricular Tachycardia. *Circulation*, 95(4):988–996, February 1997.

Robert Plonsey and Roger C Barr. *Bioelectricity: a quantitative approach*. New York, NY, 2007.

Mihaela Pop, Maxime Sermesant, Damien Lepiller, Michael V Truong, Elliot R Mcveigh, Eugene Crystal, Alexander Dick, Herve Delingette, Nicholas Ayache, and Graham A Wright. Fusion of optical imaging and MRI for the evaluation and adjustment of macroscopic models of cardiac electrophysiology: A feasibility study. *Medical Image Analysis*, 13(2):370–380, April 2009.

A J Pullan, L K Cheng, and M L Buist. *Mathematically Modeling the Electrical Activity of the Heart: From Cell to ... - Andrew J. Pullan, Leo K. Cheng, Martin L. Buist*. World Scientific Publishing Co. Pte. Ltd., 2005.

Z Qu and A Garfinkel. An advanced algorithm for solving partial differential equation in cardiac conduction. *Biomedical Engineering, IEEE Transactions on*, 46(9):1166–1168, 1999.

Z Qu, A Garfinkel, P S Chen, and J N Weiss. Mechanisms of discordant alternans and induction of reentry in simulated cardiac tissue. *Circulation*, 102(14):1664–1670, October 2000.

Zhilin Qu and James N Weiss. Dynamics and cardiac arrhythmias. *Journal of Cardiovascular Electrophysiology*, 17(9):1042–1049, September 2006.

D E Roberts and A M Scher. Effect of tissue anisotropy on extracellular potential fields in canine myocardium in situ. *Circulation Research*, 50(3):342–351, March 1982.

D E Roberts, L T Hersh, and A M Scher. Influence of cardiac fiber orientation on wavefront voltage, conduction velocity, and tissue resistivity in the dog. *Circulation Research*, 44(5):701–712, May 1979.

Sarah Roberts. *Non-uniform Interstitial Loading in Cardiac Microstructure During Impulse Propagation*. PhD thesis, Duke University, April 2009.

S Rohr, JP Kucera, VG Fast, and AG Kleber. Paradoxical improvement of impulse conduction in cardiac tissue by partial cellular uncoupling. *American Association for the Advancement of Science. Science*, 275(5301):841, 1997.

S Rohr, J P Kucera, and A G Kléber. Slow conduction in cardiac tissue, I: effects of a reduction of excitability versus a reduction of electrical coupling on microconduction. *Circulation Research*, 83(8):781–794, October 1998.

B J Roth. Action potential propagation in a thick strand of cardiac muscle. *Circulation Research*, 68(1):162–173, January 1991.

B J Roth. Electrical conductivity values used with the bidomain model of cardiac tissue. *IEEE Trans Biomed Eng*, 44(4):326–328, April 1997.

- Y Rudy and W Quan. Propagation delays across cardiac gap junctions and their reflection in extracellular potentials: a simulation study. *Journal of Cardiovascular Electrophysiology*, 2(4):299–315, 1991.
- Y Rudy and WL Quan. A model study of the effects of the discrete cellular structure on electrical propagation in cardiac tissue. *Circulation Research*, 61(6):815, 1987.
- S Rush and H Larsen. A practical algorithm for solving dynamic membrane equations. *Biomedical Engineering, IEEE Transactions on*, (4):389–392, 1978.
- Frank B Sachse. *Computational Cardiology*. Modeling of Anatomy, Electrophysiology, and Mechanics. Springer, May 2004.
- L Sartiani, P Bochet, E Cerbai, A Mugelli, and R Fischmeister. Functional expression of the hyperpolarization-activated, non-selective cation current If in immortalized HL-1 cardiomyocytes. *The Journal of Physiology*, 545(1):81–92, September 2002.
- D Sato, LH Xie, AA Sovari, DX Tran, N Morita, F Xie, H Karagueuzian, A Garfinkel, JN Weiss, and Z Qu. Synchronization of chaotic early afterdepolarizations in the genesis of cardiac arrhythmias. *Proceedings of the National Academy of Sciences*, 106(9):2983, 2009.
- Johannes Schindelin, Ignacio Arganda-Carreras, Erwin Frise, Verena Kaynig, Mark Longair, Tobias Pietzsch, Stephan Preibisch, Curtis Rueden, Stephan Saalfeld, Benjamin Schmid, Jean-Yves Tinevez, Daniel James White, Volker Hartenstein, Kevin Eliceiri, Pavel Tomancak, and Albert Cardona. Fiji: an open-source platform for biological-image analysis. *Nature methods*, 9(7):676–682, July 2012.
- S M Schumacher, D P McEwen, L Zhang, K L Arendt, K M Van Genderen, and J R Martens. Antiarrhythmic Drug-Induced Internalization of the Atrial-Specific K⁺ Channel Kv1.5. *Circulation Research*, 104(12):1390–1398, June 2009.
- Nicholas J Severs, Alexandra F Bruce, Emmanuel Dupont, and Stephen Rothery. Remodelling of gap junctions and connexin expression in diseased myocardium. *Cardiovasc Res*, 80(1):9–19, October 2008.
- Robin M. Shaw and Yoram Rudy. Ionic Mechanisms of Propagation in Cardiac Tissue : Roles of the Sodium and L-type Calcium Currents During Reduced Excitability and Decreased Gap Junction Coupling. *Circulation Research*, 81(5):727, November 1997.
- BH Smaill, IJ LeGrice, DA Hooks, AJ Pullan, BJ Caldwell, and PJ Hunter. Cardiac structure and electrical activation: models and measurement. *Clinical and Experimental Pharmacology and Physiology*, 31(12):913–919, 2004.
- M S Spach. Mechanisms of the dynamics of reentry in a fibrillating myocardium. Developing a genes-to-rotors paradigm. *Circulation Research*, 88(8):753–755, April 2001.
- M S Spach. Transition From a Continuous to Discontinuous Understanding of Cardiac Conduction. *Circulation Research*, 92(2):125–126, February 2003.
- M S Spach and J F Heidlage. The Stochastic Nature of Cardiac Propagation at a Microscopic Level : Electrical Description of Myocardial Architecture and Its Application to Conduction. *Circulation Research*, 76(3):366–380, March 1995.
- MS Spach and PC Dolber. Relating extracellular potentials and their derivatives to anisotropic propagation at a microscopic level in human cardiac muscle. Evidence for electrical uncoupling of side-to-side fiber connections with increasing age. *Circulation Research*, 58(3):356, 1986.

MS Spach and W T Miller. The functional role of structural complexities in the propagation of depolarization in the atrium of the dog. Cardiac conduction disturbances due to discontinuities of effective axial resistivity. *Circulation Research*, 50(2):175, 1982.

MS Spach and WT Miller. The discontinuous nature of propagation in normal canine cardiac muscle. Evidence for recurrent discontinuities of intracellular resistance that affect the membrane currents. *Circulation Research*, 48(1):39, 1981.

MS Spach, PC Dolber, and JF Heidlage. Influence of the passive anisotropic properties on directional differences in propagation following modification of the sodium conductance in human atrial muscle. A model of reentry based on anisotropic discontinuous propagation. *Circulation Research*, 62(4):811, 1988.

Peter S Spector, Nicole Habel, Burton E Sobel, and Jason H T Bates. Emergence of complex behavior: an interactive model of cardiac excitation provides a powerful tool for understanding electric propagation. *Circulation: Arrhythmia and Electrophysiology*, 4(4):586–591, August 2011.

M E Steinheimer, N A Lanson, K P Dresdner, J B Delcarpio, A L Wit, W C Claycomb, and L J Field. Proliferation in vivo and in culture of differentiated adult atrial cardiomyocytes from transgenic mice. *The American journal of physiology*, 259(6 Pt 2):H1826–34, December 1990.

Jeroen Stinstra, Rob Macleod, and Craig Henriquez. Incorporating Histology into a 3D Microscopic Computer Model of Myocardium to Study Propagation at a Cellular Level. *Annals of Biomedical Engineering*, 38(4):1399–1414, April 2010.

Jeroen G Stinstra, Bruce Hoppenfeld, and Rob S Macleod. On the Passive Cardiac Conductivity. *Annals of Biomedical Engineering*, 33(12):1743–1751, December 2005.

JG Stinstra, Sf Roberts, Jb Pormann, RS MacLeod, and Cs Henriquez. A Model of 3D Propagation in Discrete Cardiac Tissue. *Comput Cardiol*, 33:41–44, 2006.

D D Streeter. Gross morphology and fiber geometry of the heart. *Handbook of physiology*, pages 61–112, 1979.

Joakim Sundnes, Robert Artebrant, Ola Skavhaug, and Aslak Tveito. A second-order algorithm for solving dynamic cell membrane equations. *IEEE Trans Biomed Eng*, 56(10):2546–2548, October 2009.

K H W J ten Tusscher and A V Panfilov. Alternans and spiral breakup in a human ventricular tissue model. *American journal of physiology Heart and circulatory physiology*, 291(3):H1088–H1100, September 2006.

K H W J ten Tusscher, D Noble, P J Noble, and A V Panfilov. A model for human ventricular tissue. *American journal of physiology Heart and circulatory physiology*, 286(4):H1573–89, April 2004.

N Trayanova. Discrete versus syncytial tissue behavior in a model of cardiac stimulation—I: Mathematical formulation. *IEEE Trans Biomed Eng*, 43(12):1129–1140, 1996.

N Trayanova and T C Pilkington. A bidomain model with periodic intracellular junctions: a one-dimensional analysis. *IEEE Trans Biomed Eng*, 40(5):424–433, May 1993.

N A Trayanova. Whole-Heart Modeling: Applications to Cardiac Electrophysiology and Electromechanics. *Circulation Research*, 108(1):113–128, January 2011.

L Tung. *A Bidomain Model for Describing Ischemic Myocardial D-C Potentials.* PhD thesis, MIT, Boston, 1978.

Karthikeyan Umapathy, Stephane Masse, Karolina Kolodziejska, George D Veenhuyzen, Vijay S Chauhan, Mansoor Husain, Talha Farid, Eugene Downar, Elias Sevaptsidis, and Kumaraswamy Nanthakumar. Electrogram fractionation in murine HL-1 atrial monolayer model. *Heart Rhythm*, 5(7):1029–1035, July 2008.

Edward J Vigmond, Matt Hughes, G Plank, and L Joshua Leon. Computational tools for modeling electrical activity in cardiac tissue. *J Electrocardiol*, 36 Suppl:69–74, 2003.

P C Viswanathan, R M Shaw, and Y Rudy. Effects of IKr and IKs heterogeneity on action potential duration and its rate dependence: a simulation study. *Circulation*, 99(18):2466–2474, May 1999.

R Vogel and R Weingart. Mathematical model of vertebrate gap junctions derived from electrical measurements on homotypic and heterotypic channels. *The Journal of Physiology*, 510 (Pt 1):177–189, July 1998.

R D Walton, D Benoist, C J Hyatt, S H Gilbert, E White, and O Bernus. Dual excitation wavelength epi-fluorescence imaging of transmural electrophysiological properties in intact hearts. *Heart Rhythm*, pages 1–38, October 2010.

Paul J Wang and N A Mark Estes. *Cardiology patient pages. Supraventricular tachycardia.*, volume 106. Tufts University School of Medicine and Tufts New England Medical Center, Boston, Mass 02111, USA. Pwang1@lifespan.org, December 2002.

Y Wang and Y Rudy. Action potential propagation in inhomogeneous cardiac tissue: safety factor considerations and ionic mechanism. *American journal of physiology Heart and circulatory physiology*, 278(4):H1019–29, April 2000.

Y G Wang. Plunge electrode for recording multiple intramyocardial monophasic action potential. US Patent Office, 1995.

S M White. Cardiac physiology at the cellular level: use of cultured HL-1 cardiomyocytes for studies of cardiac muscle cell structure and function. *AJP: Heart and Circulatory Physiology*, 286(3):823H–829, October 2003.

Cordula M Wolf and Charles I Berul. Molecular mechanisms of inherited arrhythmias. *Current genomics*, 9(3):160–168, May 2008.

M Xia. Functional expression of L- and T-type Ca²⁺ channels in murine HL-1 cells. *Journal of Molecular and Cellular Cardiology*, 36(1):111–119, January 2004.

Zhenjiang Yang, Wangzhen Shen, Jeffrey N Rottman, John P Wikswo, and Katherine T Murray. Rapid stimulation causes electrical remodeling in cultured atrial myocytes. *Journal of Molecular and Cellular Cardiology*, 38(2):299–308, February 2005.

R Zou. Substrate size as a determinant of fibrillatory activity maintenance in a mathematical model of canine atrium. *AJP: Heart and Circulatory Physiology*, 289(3):H1002–H1012, May 2005.

Appendix

Appendix A

The equations of the Luo-Rudy I model

This section presents the equations of the Luo-Rudy I cell model, as outlined in the original paper by Luo et al [Luo and Rudy \[1991\]](#).

Fast sodium Current I_{Na}

$$I_{Na} = g_{Na} \cdot m^3 \cdot h \cdot j \cdot (V - E_{Na})$$

For all V

$$\begin{aligned}\alpha_m &= \frac{-0.32(V + 47.13)}{\exp(-0.1(V + 47.13)) - 1} \\ \beta_m &= 0.08 \exp(-V/11)\end{aligned}$$

$V \geq -40mV$

$$\begin{aligned}\alpha_h &= 0 \\ \beta_h &= \frac{1/0.13}{\exp(\frac{V+10.66}{-11.1}) + 1} \\ \alpha_j &= 0 \\ \beta_j &= 0.3 \cdot \frac{\exp(-2.535 \cdot 10^{-7} \cdot V)}{1 + \exp(-0.1(V + 32))}\end{aligned}$$

$V < -40mV$

$$\begin{aligned}\alpha_h &= 0.135 \cdot \exp((V + 80) / -6.8) \\ \beta_h &= 3.56 \cdot \exp(0.079V) + 3.1 \cdot 10^5 \cdot \exp(0.35V) \\ \alpha_j &= (-1.2714 \cdot 10^5 \cdot \exp(0.2444V) - 3.474 \cdot 10^{-5} \cdot \exp(-0.04391V)) \\ &\quad \times \frac{(V + 37.78)}{1 + \exp(0.311 \cdot (V + 79.23))} \\ \beta_j &= 0.1212 \cdot \frac{\exp(-0.01052 \cdot V)}{1 + \exp(-0.1378 \cdot (V + 40.14))}\end{aligned}$$

Slow inward Current I_{si}

$$\begin{aligned}
I_{si} &= g_{Si} \cdot d \cdot f \cdot (V - E_{Si}) \\
\alpha_d &= \frac{0.0950 \exp(-0.010(V - 5))}{\exp(-0.072(V - 5)) + 1} \\
\beta_d &= \frac{(0.0700 \exp(-0.017(V + 44)))}{\exp(0.05(V + 44)) + 1} \\
\alpha_f &= \frac{(0.0120 \exp(-0.008(V + 28)))}{\exp(0.15(V + 28)) + 1} \\
\beta_f &= \frac{(0.0065 \exp(-0.020(V + 30)))}{\exp(-0.2(V + 30)) + 1}
\end{aligned}$$

Time-dependent potassium Current I_K

$$\begin{aligned}
I_K &= g_K \cdot x \cdot X_i \cdot (V - E_K) \\
\alpha_x &= \frac{0.0005 \cdot \exp(0.0830(V + 50))}{\exp(0.057(V + 50)) + 1} \\
\beta_x &= \frac{0.0013 \cdot \exp(-0.060(V + 20))}{\exp(-0.04(V + 20)) + 1} \\
V > -100mV \\
X_i &= 2.837 \cdot \frac{\exp(0.04(V + 77)) - 1}{(V + 77) \exp(0.04 \cdot (V + 35))} \\
V \leq -100mV \\
X_i &= 1
\end{aligned}$$

Time-independent potassium Current I_{K1}

$$\begin{aligned}
I_{K1} &= g_{K1} \cdot K1_\infty \cdot (V - E_{K1}) \\
\alpha_{K1} &= \frac{1.02}{1 + \exp(0.2385(V - E_{K1} - 59.215))} \\
\beta_{K1} &= \frac{0.49124 \cdot \exp(0.08032(V - E_{K1} + 5.476)) + \exp(0.06175 \cdot (V - E_{K1} - 594.31))}{1 + \exp(-0.5143(V - E_{K1} + 4.753))}
\end{aligned}$$

Plateau potassium Current I_{Kp}

$$\begin{aligned}
I_{Kp} &= 0.0183 \cdot Kp \cdot (V - E_{Kp}) \\
Kp &= \frac{1}{1 + \exp((7.488 - V)/5.98)}
\end{aligned}$$

Background Current I_b

$$I_b = 0.03921(V - E_b)$$

Parameter	Value	Description	Unit
g_{Na}	23	Max conductance of I_{Na}	mS/cm^2
E_{Na}	54.4	Nernst potential of I_{Na}	mV
g_{si}	0.09	Max conductance of I_{si}	mS/cm^2
E_{si}	$7.7 - 13.0287 \ln(Ca_i)$	Nernst potential of I_{si}	mV
g_K	$0.282\sqrt{K_o/5.4}$	Max conductance of I_K	mS/cm^2
E_K	-77.57	Nernst potential of I_K	mV
g_{K1}	$0.6047\sqrt{K_o/5.4}$	Max conductance of I_{K1}	mS/cm^2
E_{K1}	-87.89	Nernst potential of I_{K1}	mV
E_{Kp}	-87.89	Nernst potential of I_{Kp}	mV
E_b	-59.87	Nernst potential of I_b	mV
K_o	5.4	Extracellular potassium concentration	$ mM$

Table A.1: Parameters within the Luo–Rudy I cell model

Appendix B

Developing a mathematical model of the action potential for the HL-1 clone 6 cell line

In this chapter, initial work to develop a mathematical model of an HL-1 sub clone cell line is developed. An initial evaluation of the literature concerning functional characteristics of the mouse atrial myocyte is performed, and existing mathematical models of rodent, murine or atrial action potentials are considered. The model is developed based on experimental data, collected and analysed in collaboration with other group members. Testing and validation of the mathematical model's behaviour is carried out via single cell pacing and pacing of a mono domain model coupled with the model.

B.1 Background

The HL-1 is an immortal cell line derived from mouse atrial myocytes injected with a tumour growth factor, as outlined in Section 6.1.2. The original cell line exhibited high variability in electrical properties from cell to cell, and was subsequently cloned in to 6 stable subclones by Dr Emmanuel Dupont, with each sub clone exhibiting consistent electrical phenotype [Dias, 2010].

The HL-1 cell line has been demonstrated experimentally as a novel *in-vitro* model for studying cell-cell electrical conduction and the effect of pharmacological agents on conduction slowing [Chowdhury, 2011]. Chapter 6 utilised the HL-1 line as a tool for developing a technique of patterned cell culture, with the aim of using the slow intrinsic conduction properties of the line to gain insight in to the electrogram under slow conduction.

There are no published mathematical models of the HL-1 cell line action potential. This chapter documents initial work to develop a simple mathematical model of the single cell electrical behaviour of the HL-1 sub clone 6 (denoted HL1-6) and examine its

behaviour in a monolayer, based on experimental data and published literature.

B.2 Methods: Determining components of the HL-1 action potential

B.2.1 Data from literature

[Claycomb et al. \[1998\]](#), the original creator of the cell line reported existence of a voltage dependent ' I_{Kr} -like' channel, saturating at $+20mV$ and highly sensitive to dofetilide. [Sartiani et al. \[2002\]](#) carried out further characterisation, examining the presence of the funny current I_f in about 30% of HL-1 cells, with a maximal slope conductance of $89.7 \pm 0.4 pSpF^{-1}$, an activation threshold between -50 and -60 mV, and reversal potential at $-20.8 \pm 1.5 mV$. Action potentials were reported to have a triangular morphology, with overshoot at $+15mV$ and max diastolic potential of $-69mV$. Figure B.1 [[White, 2003](#)] summarises the main currents expressed in HL-1 cells up to 2003.

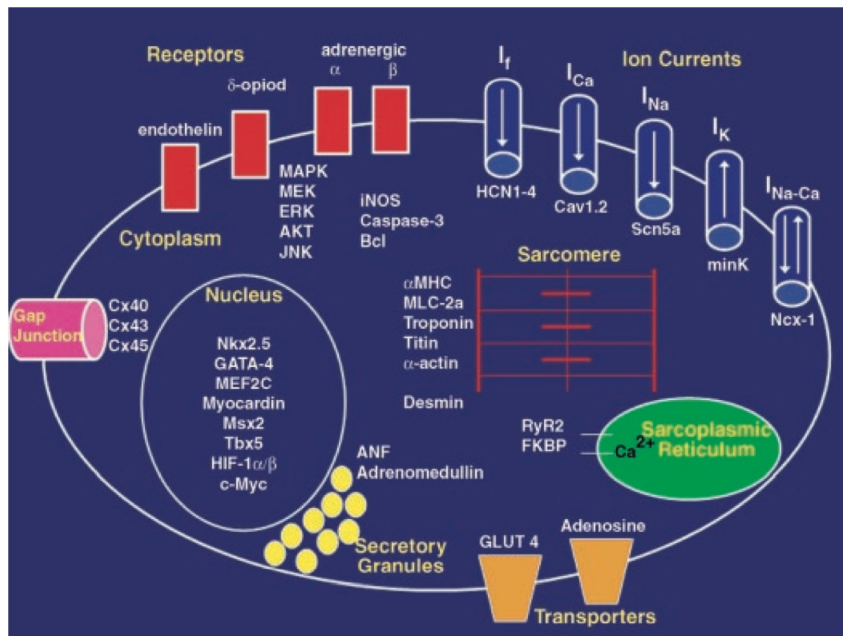


Figure B.1: Schematic depiction of HL-1 features. HL-1 express gap junction-forming proteins Cx40, Cx43, Cx45. In particular, HL-1 cells have been reported to express I_f , I_{Ca} (L and T), I_{Na} , I_K (inc I_{Kr}), and I_{Na-Ca} . Existence of I_{to} , I_{K1} , I_{KATP} currents have been reported since this figure was published. Figure from [White \[2003\]](#).

Further ion channels in HL-1 have been reported. Voltage-dependent Ca^{2+} channels, both L-type and T-type, were reported [Xia \[2004\]](#), although it was noted that both channels were only evident in 30% of cells, with 12% expressing neither channel. Reports on

existence of specific potassium channels differ and no clear consensus has been reached: these include the transient outward current (I_{to}) by Yang et al. [2005] and ATP-sensitive K^+ (I_{KATP}) by Fox et al. [2005], whilst Goldoni et al. [2010] reported and characterised I_{K1} in HL-1 cells. Nobles et al. [2010] reported an inward rectifying K^+ current gated by G proteins, whilst Schumacher et al. [2009] discusses possible existence of the ultra rapid rectifier I_{Kur} .

In summary, experimental literature have indicate presence of a range of ion channels in the native HL-1 cell line, including sodium (I_{Na}), L-type and T-type calcium (I_{CaL}, I_{CaT}), pacemaker (I_f), sodium calcium exchanger (I_{NaCa}) and a wide range of potassium channels, including I_{Kr} , I_{K1} and I_{Kur} and I_{KATP} .

B.2.2 Experimental HL1 subclone characterisation

Specific characterisation of the HL1 subclone cell lines 2 and 6 was carried out by Dias [2010]. Immunoblotting techniques reported HL1-6 cells express Ca^2 handling proteins including the L-type calcium channel, sodium calcium exchanger (NCX) , ryanodine receptor 2 (RyR2) and sarco-endoplasmic reticulum Ca^{2+} -ATPase (SERCA) .

Electrophysiological studies on single cell revealed existence of functional voltage-gated channels, and hyperpolarisation-activated funny current (I_f). In monolayers, sub clones were shown to express rhythmic release of intracellular Ca^{2+} and caffeine-releasable stores indicating functional sarcoplasmic reticulum (SR).

Action potentials of the clone 6 line had a resting potential of $-67mV$, and a mean APD50 of $17 \pm 6ms$ with an overshoot of $28 \pm 5mV$. Individual currents: I_{Na} had a peak activation value of $-85 \pm 14.3pA/pF$ and a reversal potential of $60mV$. L-type calcium currents had a peak activation value of $-0.86 \pm 0.04pA/pF$ obtained at $-10mV$. T-type calcium currents had a peak activation value of $-0.89 \pm 0.03pA/pF$ obtained at $25mV$. I_f had a peak current activation of $-32 \pm pA/pF$ at $-130mV$. A sample AP of the HL-1 clone 6 is shown in Figure B.2.

Extraction of further parameters from *in-vitro* data

Dual cell patch clamp studies of HL1-6 cells were carried out by Dr Thomas Desplantez (private communication). He established the following parameters for the HL1-6 cell: resting potential of $-66 \pm 1.6mV$, amplitude $104 \pm 2.7mV$ and APD90 $32 \pm 12.2ms$.

In monolayers, HL1-6 was reported to have an intrinsic frequency of $1.5 - 2Hz$ Dias [2010]. Maximum pacing rate was not determined by the APD of HL1-6; it was revealed that HL1 – 6 could not be paced above $8Hz$ [Chowdhury, 2011, p.190], indicating a refractory period for $> 100ms$.

Conduction velocity of the HL1-6 cell line was dependent on days after seeding, as

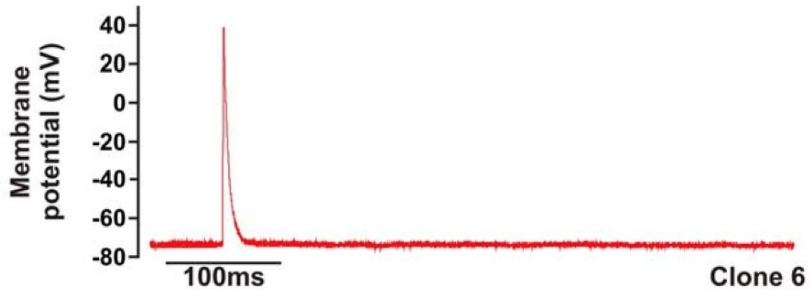


Figure B.2: HL-1 clones 6 action potential, with resting potential of -67mV , an overshoot of $28 \pm 5\text{mV}$ and a mean APD₅₀ of $17 \pm 6\text{ms}$. Figure reproduced with permission from [Dias, 2010, p.123].

monolayers became confluent. CV was reported as $3 - 4\text{cm/s}$ [Dias, 2010] around 3 – 4 days post seeding.

B.3 Results

The aim of developing this model was to create a theoretical AP model, which could be coupled to a tissue or discrete cell model to simulate slow conduction observed in designer experimental preparations, as outlined in Chapter 6. Thus, a requirement of the model was to replicate in detail the AP initiation and upstroke, but to grossly capture the remainder of the AP repolarisation.

B.3.1 Description of initial model

An initial mathematical model was described by adapting the Luo–Rudy I (LR1) model [Luo and Rudy, 1991] described in Appendix A. The model was chosen due to its relative simplicity, compared to other models such as LRD [Luo and Rudy, 1994] which contained more complicated intracellular cycling contributing to the AP repolarisation phase, and increased time of simulation.

Adjustments to the LR1 model were proposed to fit the resultant action potential shape to experimentally recorded HL1-6 APs under patch clamp. The proposed changes are outlined below.

Sodium channel

No change was proposed to the sodium channel of the LR-1 model, which is based on the Beeler Reuter model Beeler and Reuter [1977]. This was based on the assumption of sodium channels being mostly invariant between cell models of different species and function.

Repolarisation currents

Repolarisation currents were adapted to increase the rate of repolarisation, reducing the APD from $350ms$ in the LR1 to $35ms$ in the HL1-6. Additionally, the resting membrane potential in HL1-6 is $-67mV$ compared to -84 in LR1.

The changes were obtained by rescaling parameters within the LR1 potassium channels, and observing the effect on the final AP shape. The final proposed changes were:

- Rescaling the equilibrium potential of the calcium-activated potassium rectifier, (e_K), by a factor of 0.86;
- Rescaling the equilibrium potential of the inward potassium rectifier, (e_{K1}), by a factor of 0.86;
- Increase of the peak potassium rectifier excitability, g_K , by a factor of 5.

Calcium currents

The HL-1 exhibited existence of both L-type and T-type calcium channels, with calcium transients recorded in HL1-6 cells through optical mapping studies [Dias, 2010]. The L-type channel was modelled in the LR1 AP as an effective slow inward current, I_{si} . The HL1-6 line exhibited a significantly shorter APD compared to the LR1 model. Thus the peak slow inward current excitability, g_{si} , was reduced by 90%, to reduce the inward current and decrease the APD. This was achieved by scaling to $0.1 \times$ the value presented from the LR1 paper.

Other currents

The I_f funny current and sodium calcium exchanger NCX were not included in the present model.

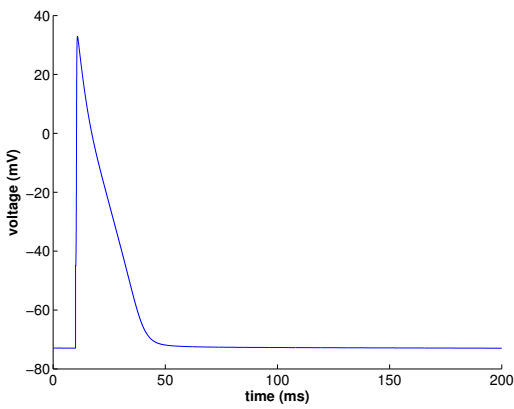
B.3.2 Electrophysiological Properties

Following the suggested changes to the LR-1 model, the proposed AP model, referred to as the HL-1 AP model, was simulated using custom code developed in Matlab. A single cell AP is presented in Figure B.3, along with an HL-1 AP recorded by Dr Thomas Desplantez (private communication).

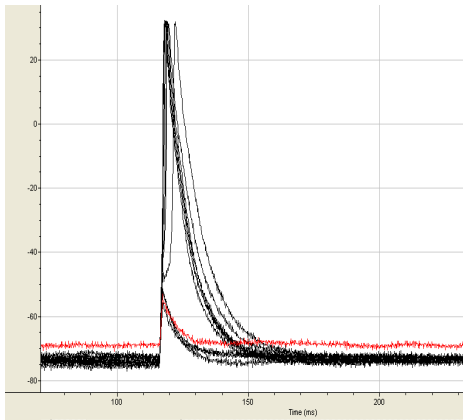
The proposed model matched the resting potential and amplitude of the experimental data, although the $APD90$ was evaluated as $44ms$ at $2Hz$ pacing rate, compared to $32ms$ in experimental models.

B.3.3 APD and restitution properties

The action potential duration at 90% repolarisation to baseline (APD90) was measured as a function of increased pacing frequency in HL1-6 single cell simulations. The resulting



(a) Simulated HL1-6 AP



(b) Recorded HL1-6 AP

Figure B.3: B.3a) Simulated HL1-6 AP in a single cell model. The cell was subject to a 0.02ms stimulus at $t = 10\text{ms}$, with the stimulus $> 1.2 \times$ stimulation threshold. The simulated amplitude and resting potential were similar to experimentally recorded HL1-6 APs in B.3b). Experimental AP reproduced courtesy of Dr Thomas Desplantez.

restitution curve is shown in Figure B.4, with pacing frequency = 1/cycle length (CL). It was found that the APD90 reduced from 44ms at 2Hz down to below 30ms at 20Hz

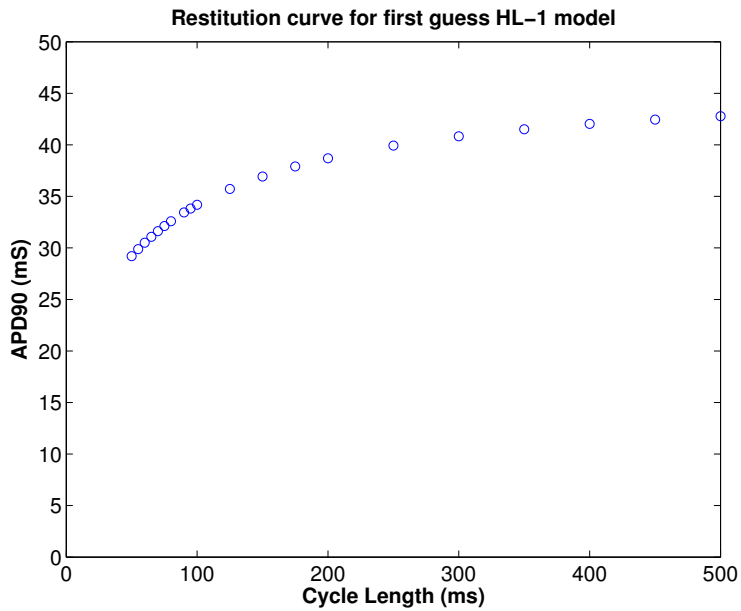


Figure B.4: Simulated single cell HL1-6 restitution curve for pacing frequency between $2 - 20\text{Hz}$. No loss of capture was recorded up to and including 20Hz .

pacing rate. Simulating pacing at up to $20Hz$ did not result in loss of capture. This was contrary to experimental data where loss of capture was observed above $8Hz$, which indicated a refractory period of $100ms$.

B.3.4 Coupling to the monodomain model

The HL1-6 AP model described above was coupled to a 1D mono domain cable with diffusion coefficient $D = 0.0005cm/s$, and an excitation wavefront was initiated from the beginning of the cable following an injected stimulus.

It was found that simulation of the continuous mono domain cable coupled to an HL1-6 AP model under $D = 0.0005cm^2/ms$ produced conduction velocities (CVs) identical to simulations using the standard LR-1 AP model with the same D , in the order of $> 40cm/s$ (data not shown).

Optical mapping studies of HL1-6 monolayers [Dias \[2010\]](#) have previously characterised baseline CV of $2 - 4cm/s$. Whilst modulating D to match conduction velocities seen in experiments was an option, this was not pursued further in the present study. The physiological interpretation of modulating D was unclear due to the large number of unknown parameters which affect the value of D .

B.4 Discussion

In this chapter, an initial proof of concept attempt to mathematically describe the action potential behaviour of the HL-1 clone 6 cell line was outlined. The literature on functional ion channels in HL-1 cells was explored, and an initial mathematical was proposed, based on adaptation of the LR1 AP model to fit the morphology of the recorded HL1-6 AP. The proposed model was coupled within a cable tissue model to test conduction properties.

B.4.1 Choice of currents for the HL1-6 model

Several experimental studies have published accounts of ion channels expressed in the HL-1 cell line, e.g. [Claycomb et al. \[1998\]](#), [Fox et al. \[2005\]](#), [Sartiani et al. \[2002\]](#), [White \[2003\]](#), [Yang et al. \[2005\]](#). Existence or absence of specific potassium channels are the primary cause of discrepancy, with recent studies indicating existence of I_{Kur} [\[Schumacher et al., 2009\]](#), I_{K1} [\[Goldoni et al., 2010\]](#) or I_{KACH} [\[Nobles et al., 2010\]](#).

One common point of existing studies indicated the high variability within the HL-1 cell line, which is indicated by studies which found that the funny current I_f was expressed in only 30% of HL-1 cells [\[Sartiani et al., 2002\]](#). This led to sub-cloning of the line by Dr Dupont as described earlier. However a challenge remains to fully interpret the literature to decide which publications are relevant for the sub clone in question, and

thus which ion channel currents to include within the model.

The HL1-6 AP model presently described used a modified version of the well established LR1 guinea pig ventricular AP model. This was an initial attempt to tweak an existing mathematical model to reproduce experimental result, based on the work of Dias [\[2010\]](#) which indicated presence of sodium, potassium and calcium and funny currents. The aim was to develop a simplistic model which reproduced upstroke and conduction characteristics in detail, but otherwise preserved gross APD and restitution properties.

Whilst the AP shape, and resting potential were closely matched to experimentally measured values, several currents were omitted. The model did not include all ionic features describe in the literature, such as the funny current I_f , the sodium calcium exchanger NCX, and intracellular calcium cycling. Omission of these could lead to key physiological mechanisms being ignored. Additionally, it can be argued that it would be better to adopt an existing atrial model rather than a ventricular model, given the origin of the HL-1 as a mouse atrial myocyte cell line.

Further work should be completed to extensively characterise the existence of particular ion channels within the HL-1 clone 6 cell line before the AP model is finalised.

B.4.2 Restitution properties of the model

A restitution curve generated for the proposed model did not agree with experimental observation of a refractory period of 100ms (8Hz) [\[Chowdhury, 2011\]](#). The present model exhibited a decrease in APD following increase in pacing frequency, but no loss of capture was observed up to 20Hz. This phenomenon may be correlated with lengthened sodium channel inactivity [\[Dias \[2010\]\]](#), which could result in a greater refractory period despite the recovery of the cell to resting potential.

Redesign of the mathematical model to account for the long inactivation period of the sodium channel may refine the model more closely to experiment. Further single cell experimental work to determine a restitution curve for the HL1-6 model would help to inform design of the sodium channel expressed within the sub clone.

B.4.3 Conduction properties of the model

Conduction properties of the AP model was considered by coupling the HL1-6 AP model to a mono domain cable, representing 1D propagation or a planar wavefront along a monolayer.

The conduction velocity obtained in the theoretical simulation was an order of magnitude greater than experimentally recorded CV. In a cable model, CV is modulated by diffusion coefficient D , which is normally estimated from tissue parameters. In order to

correctly capture conduction properties, D requires careful estimation from physiological parameters; however there were several biological unknowns and determinants of D , listed below, which can make its estimation a challenging task:

Cell size and morphology

Cells within natural monolayers exhibit a more circular profile and are not anisotropic. This alters the surface to volume ratio described within the definition of $D = \frac{1}{\beta C_m R_i}$, which may significantly alter the value of D chosen.

Cytoplasmic resistivity

The cytoplasmic resistivity was not measured or estimated in the present study.

Gap junctions not preferentially localised on short cell ends in monolayers

It has been shown [[Chowdhury, 2011](#), [Dias, 2010](#)] that circular profiled cells in culture exhibit even distribution of Cx43 around the entire cellular perimeter. This ‘uniform lateralisation’ –type effect may determine junctional longitudinal and transverse resistivity values (Ωcm), resulting in a change in effective tissue resistivity and subsequent value of D .

Reduced gap junctional conductances within the HL1-6 line

The HL1-6 has been demonstrated to express connexin-making siena, and connexin expression levels were comparable against cells of atrial origin [[Dias, 2010](#), p.163], yet the levels of conductance measured in coupled HL1-6 myocytes were inferior. This could be due to reduced number or functionality of GJ channels at the membrane in cell culture compared to in-vivo systems. Additionally, the connexin composition of GJ channels, which would lead to different GJ types with different unitary conductances, may be different in the HL1-6 line [Dias \[2010\]](#). Further experimental study would help to determine parameter values which can then be used to calculate effective junctional resistivity for use in simulation.

B.4.4 Summary

The model proposed in this chapter constitutes an initial attempt to mathematically describe the functional characteristics of the HL1-6 cell line in a monolayer, based on ion channel behaviour, gap junctional expression and coupling. Further refinement and ongoing collaboration between experimental and theoretical development is required to fully characterise the behaviour of the cell line. Analysis of patch clamp studies and curve fitting would allow a more biophysical characterisation of the HL1-6 action potential model.

Appendix C

A simple mathematical model of discrete coupled cells

A simple mathematical mono domain model of voltage potential in cells coupled by a parallel resistance (representing gap junctions) and membrane capacitance was explored, as a preliminary study to investigate the analytical behaviour of simple cells to a boundary stimulus. Specific boundary conditions coupling the cells are varied to examine the effect on the final solution. The extracellular potential is assumed to be negligible and is omitted from the present work.

Analytical solution of the intracellular potential: An unsteady two cell problem

Consider a coupled pair of cells in 1D, each of length L , with $u_i(x, t)$; $i = 1, 2$, representing the voltage potential for each cell respectively. Aligning the cells together with the first cell beginning at the origin, the intracellular potential is governed by Laplace's equation:

$$\sigma_1 \frac{\partial^2 u_1}{\partial x^2} = 0, \quad (\text{C.1})$$

$$\sigma_2 \frac{\partial^2 u_2}{\partial x^2} = 0, \quad (\text{C.2})$$

with σ_1 and σ_2 the conductivity of the cell. The partial differential equations are subject to the following boundary and matching conditions:

$$u_1 = D(t) \quad \text{at } x = 0 \quad (\text{C.3})$$

$$(\sigma_1 \frac{\partial u_1}{\partial x}) \cdot n = C_m \frac{\partial(u_1 - u_2)}{\partial t} + G(u_1 - u_2) \quad \text{at } x = L \quad (\text{C.4})$$

$$(\sigma_2 \frac{\partial u_2}{\partial x}) \cdot n = -C_m \frac{\partial(u_1 - u_2)}{\partial t} - G(u_1 - u_2) \quad \text{at } x = L \quad (\text{C.5})$$

$$\frac{\partial u_2}{\partial x} = 0 \quad \text{at } x = 2L \quad (\text{C.6})$$

where $D(t)$ is a specified time dependent stimulus, G is the effective resistance due to gap junctions at the boundary and C_m is the capacitance at the boundary.

This admits the solutions:

$$u_1 = \alpha(t)x + \beta(t), \quad (\text{C.7})$$

$$u_2 = \gamma(t)x + \delta(t). \quad (\text{C.8})$$

Applying the boundary conditions at $x = 0, 2L$ we find

$$\beta(t) = D(t) \quad (\text{C.9})$$

$$\gamma(t) = 0 \quad (\text{C.10})$$

The two boundary conditions at $x = L$ become

$$\sigma_1\alpha(t) = C_m(\alpha'L + D' - \delta') + G(\alpha L + D - \delta), \quad (\text{C.11})$$

$$-\sigma_2\gamma(t) = -C_m(\alpha'L + D' - \delta') - G(\alpha L + D - \delta). \quad (\text{C.12})$$

Adding these gives

$$\sigma_1\alpha(t) = \sigma_2\gamma(t) \Rightarrow \alpha(t) = 0 \quad (\text{C.13})$$

Finally, rearrange and are left with the expression:

$$C_m \frac{\partial}{\partial t} (D(t) - \delta(t)) = -G(D(t) - \delta(t)) \quad (\text{C.14})$$

This is a first order ODE for $y = D(t) - \delta(t)$, which we can solve to find:

$$\delta(t) = D(t) - A_1 \exp(-G/C_m)t \quad (\text{C.15})$$

for some constant A_1 . The solution is:

$$u_1 = D(t) \quad (\text{C.16})$$

$$u_2 = D(t) - A_1 \exp(-G/C_m)t \quad (\text{C.17})$$

This implies that u_1 is isopotential within the first cell, varying with $D(t)$, and that within the second cell, u_2 is also isopotential, starts as $D(0) - A_1$ and tends to $D(t)$ as t increases, with a time constant of C_m/G .

n coupled cells, boundary condition at the end

Repeating the above calculation for n cells, we obtain a general solution for u_i :

$$u_1(x, t) = D(t) \quad (\text{C.18})$$

$$u_i(x, t) = D(t) - \left(\sum_{j=1}^{i-1} A_j \right) \exp -(G/C_m)t \quad (\text{C.19})$$

This implies that the solution in each cell is isopotential, with each cell triggering its neighbour to tend towards $D(t)$ with a time constant of C_m/G .

Two coupled cells, mixed boundary condition at the end

A mixed Robin boundary condition is substituted at the end of the last cell to explore the change in the analytical solution.

$$u(x) + k \frac{\partial u}{\partial x} = 0 \text{ at } x = 2L \quad (\text{C.20})$$

Applying this condition to the trial solution $u_i = \alpha_i(t)x + \beta_i(t)$, $i = 1, 2$, a relation can be found between α_2 and β_2 :

$$\beta_2 = -\alpha_2(2L + k) \quad (\text{C.21})$$

Substituting this into the boundary condition at the cell-cell interface,

$$\sigma_1 \alpha_1 = -\sigma_2 \alpha_2 = C_m(\alpha'_1 L + \beta'_1 + \alpha'_2 L + k\alpha'_2) + G(\alpha_1 L + \beta_1 + \alpha_2 L + k\alpha_2). \quad (\text{C.22})$$

Also, it is known from above that:

$$\alpha_1 = \frac{\sigma_2}{\sigma_1} \alpha_2 \quad (\text{C.23})$$

and, using the boundary condition on the first cell to obtain $\beta_1(t) = D(t)$, the following expression is obtained:

$$C_m \left(\left(\frac{\sigma_2}{\sigma_1} L + k + L \right) \alpha'_2 + D' \right) + G \left(\left(\frac{\sigma_2}{\sigma_1} L - \frac{\sigma_2}{G} + k + L \right) \alpha_2 + D \right) = 0 \quad (\text{C.24})$$

Rearranging, and defining:

$$\xi = \frac{\frac{\sigma_2}{\sigma_1} L - \frac{\sigma_2}{G} + k + L}{\frac{\sigma_2}{\sigma_1} L + k + L},$$

a first order ODE is obtained as follows:

$$\alpha'_2 + \frac{\xi G}{C_m} \alpha_2 = -\frac{G}{C_m} D - D' \quad (\text{C.25})$$

Solving this with an integrating factor, this gives:

$$\alpha_2(t) = \exp -\frac{\xi G}{C_m} t \left(\int \exp \frac{\xi G}{C_m} t \left(-\frac{G}{C_m} D - D' \right) dt + B \right)$$

for some initial condition B . The right hand side of this expression can be simplified by integrating the D' term by parts to obtain:

$$\alpha_2(t) = \exp -\frac{\xi G}{C_m} t \left[-[D \exp \frac{\xi G}{C_m} t] - \int D \frac{G}{C_m} (1 - \xi) \exp \frac{\xi G}{C_m} t dt + B \right] \quad (\text{C.26})$$

Simplifying by defining:

$$\eta = \left[-[D \exp \frac{\xi G}{C_m} t] - \int D \frac{G}{C_m} (1 - \xi) \exp \frac{\xi G}{C_m} t dt + B \right],$$

this gives the solution:

$$u_1(x, t) = \eta \frac{\sigma_2}{\sigma_1} \exp(-\frac{\xi G}{C_m} t) x + D(t) \quad (\text{C.27})$$

$$u_2(x, t) = \eta \exp(-\frac{\xi G}{C_m} t) (x - 2L - k) \quad (\text{C.28})$$

This solution is no longer isopotential in each cell, but admits a linear solution with the gradient determined by multiple parameters including the conductivity of each cell, the size of the gap junctional resistance and the capacitance. The solutions belong to a family of solutions due to the constants of integration.

Appendix D

Additional activities

Abstracts

1. *Chang ETY*, Cantwell CD, Roney CH, Siggers JH, Sherwin SJ, Peters NS. Severe Gap Junctional Uncoupling causes Electrogram Fractionation in a Novel 1D Numerical Model of Discrete Myocytes. British Heart Foundation Centre of Research Excellence 13 June 2013.
2. *Chang ETY*, Cantwell CD, Roney CH, Siggers JH, Sherwin SJ, Peters NS. Severe Gap Junctional Uncoupling causes Electrogram Fractionation in a Novel 1D Numerical Model of Discrete Myocytes. European Cardiac Arrhythmia Society Annual Congress 14-16 April 2013 J Interv Cardiac Electrophysiol (2013)
3. Roney CH, Ng FS, *Chang ETY*, Ali R, Cantwell CD, Siggers JH, Peters NS. Determining the resolution of data required for tracking rotors in a downsampled computational model of atrial fibrillation. European Cardiac Arrhythmia Society Annual Congress 14-16 April 2013. J Interv Cardiac Electrophysiol (2013)
4. *Chang ETY*, Ng FS, Chowdhury RA, Inuabasi L, Dupont E, Peters NS. Carbenoxolone limits increase in Connexin43 expression in ischaemic rat ventricular tissue. 33rd Annual Scientific Sessions of the Heart Rhythm Society (HRS), 8 May 2012 - 12 May 2012. Heart Rhythm 9:S403
5. *Chang ETY*, Zhang X, Patel PM, Chowdhury RA, Ng FS, Siggers JH, Peters NS. A Semi-Automated Algorithm for Quantification of Connexin43 Lateralisation in Images of Diseased Myocardium. J Interv Card Electrophysiol 2012; 33(3)
6. Roney CH, Ng FS, Chowdhury RA, *Chang ETY*, Patel PM, Peters FMD, Lyon AL, Siggers JH, Peters NS. Intracellular calcium transient duration restitution shows no significant hysteresis despite hysteresis of action potential duration restitution: a dual optical mapping study. J Interv Cardiac Electrophysiol 2012 33(3): 261-383
7. Roney CH; Ng FS; Chowdhury RA; *Chang ETY*; Patel PM; Lyon AR; Siggers JH; Peters NS. Hysteresis of cardiac action potential duration restitution occurs in the absence of calcium transient duration hysteresis - a dual optical mapping study of

ex vivo rat hearts. 2nd Congress of the Frontiers in Cardiovascular Biology 30 Mar - 1 Apr 2012. Oxford Univ Press 93:S63-S63.

8. Ng FS, Owusu-Agyei AA, *Chang ETY*, Chowdhury RA, Patel PM, Larsen BD, Haugan K, Dupont E, Peters NS. ZP1210, a Novel Gap Junction Modulator, Attenuates Conduction Slowing and Prevents Cx43 Dephosphorylation During Metabolic Stress. American Heart Association (AHA) Scientific Sessions 2010, 13 - 17 Nov 2010. Circulation 122:A13633
9. Ng FS, Lyon AR, Cooper SA, *Chang ETY*, Shadi IT, Chowdhury RA, Patel PM, Dupont E; et al. Conduction slowing in the infarct border zone correlates with ventricular arrhythmia inducibility in a chronic myocardial infarction model. Heart Rhythm Congress 2010, 4 - 6 Oct 2010. Europace 12 (Suppl 2):ii10
10. Ng FS, Lyon AR, Shadi IT, *Chang ETY*, Chowdhury RA, Dupont E, Peters NS. Gap Junction Modulation - An Anti-Arrhythmic Strategy to Prevent Reperfusion VF. 31st Annual Scientific Sessions of the Heart Rhythm Society (HRS), 12 - 15 May 2010. Heart Rhythm 7:S353
11. Ng FS, Lyon AR, Shadi IT, *Chang ETY*, Chowdhury RA, Dupont E, Peters NS. Modulation of gap junctional coupling as an antiarrhythmic strategy to prevent reperfusion ventricular arrhythmias. J Interv Card Electrophysiol 2010; 27(3): 173-174
12. *Chang ETY*, Ng FS, Chowdhury RA, Inuabasi L, Dupont E, Peters NS. Carbenoxolone limits increase in Connexin43 expression in ischaemic rat ventricular tissue. J Interv Card Electrophysiol 2010; 27(3): 234-235

Project Supervision

- Amanda Owusu-Agyei, *The Gap Junction Modulator ZP1210 Prevents Ischaemia-Induced Connexin43 Dephosphorylation*, 2010
- Rheedaa Ali, *Propagation of the cardiac electric signal: Study using Cellular Automaton Methods*, 2011
- Xuhua (John) Zhang, *A semi-automated quantitative system for scoring connexin laterlasation in the myocardium*, 2011
- Yaprak Eminaga, *Numerical Modelling of the Activation Wavefront in the Cardiac Tissue*, 2012
- Qiuzi Zhao, *Modelling Sodium Channel Activity In A Cardiac Myocyte Cell Line*, 2012
- Ibrahim Ahmed, *Modelling cardiac excitation through the thickness of the ventricular wall*, 2013*

GTA work

Fluid Mechanics, 2nd year Bioengineering
Heat & Mass Transfer, 2nd year Bioengineering
Mathematical Methods, 1st year Mathematics
Mathematics, 1st year Bioengineering, 2nd year Aeronautical Engineering, Bioengineering, Chemical Engineering
Modelling in Biology, 3rd/4th year Bioengineering
Multivariate calculus, 2nd year Mathematics
MATLAB, 1st year Mathematics
Ordinary Differential Equations, 2nd year Mathematics
Physiological Fluid Mechanics, 3rd/4th year Bioengineering
Medical Science, 1st year Bioengineering

GSEPS courses

Imperial/Tsinghua summer school in Employability and Entrepreneurship, Beijing June 2012
Career Decisions and Job Choices for PhDs: Physical Scientists, March 2012
GTA training workshop, September 2010
Research Skills Development Residential course, March 2010